1-1-1994

The influence of anisotropy on the stress transfer process between polymeric resins and substrates in planar and cylindrical geometries/

Mario A. Perez
University of Massachusetts Amherst

The Influence of Anisotropy on the Stress Transfer Process Between Polymeric Resins and Substrates in Planar and Cylindrical Geometries

A Dissertation Presented

by

Mario A. Perez

Submitted to the Graduate School of the

University of Massachusetts Amherst in Partial Fulfillment

of the Requirements for the Degree of

DOCTOR OF PHILOSOPHY

September 1994

Department of Polymer Science and Engineering

The Influence of Anisotropy on the Stress Transfer Process Between Polymeric Resins and Substrates in Planar and Cylindrical Geometries

A Dissertation Presented

by

Mario A. Perez

Approved as to style and content by:

Shaw L. Hsu, Co-Chair

Richard J. Farris, Co-Chair

Roger S. Porter, Member

William J. MacKnight, Department Head

Polymer Science and Engineering

To my Wife

Jayashree

ACKNOWLEDGEMENTS

I would like to gratefully acknowledge the opportunity for intellectual advancement provided to me by the Polymer Science and Engineering Department at the University of Massachusetts at Amherst. I am especially indebted to my advisors, Professors Shaw L. Hsu and Richard J. Farris for the constant reshaping and sharpening of my technical abilities in their respective fields of expertise. I want to thank Professor Roger S. Porter for serving as a member my Dissertation Committee and for his enlightenment on topics of polymer anisotropy for my Research Proposal and Dissertation work.

I wish to thank Dr. Allan Waddon and Louis Raboin for their assistance with X-ray and electron diffraction experiments, Dr. Todd Gross for the generation of atomic force micrographs of polyimide films, and Dr. Curt Meuse for helpful advice on matters of external reflection spectroscopy. I am also thankful to Yuan Ren for his advancements in the calculation of isotropic reflection spectra and Dr. Hun-Jan Tao for his valuable input in this work. I am specially grateful to Dr. Robert Jennings for the development of the highly crystalline polyimide powders utilized in the analysis presented in Chapter 4 of this dissertation.

I extend my gratitude to CUMIRP (Center for UMass-Industry Research on Polymers) for their financial support of this research.

Finally, I am indebted to my wife Jayashree for her support, and to my children, Niccola and Elio for their joyous company and the strength and incentive they gave me in bringing this work to fruition.

ABSTRACT

THE INFLUENCE OF ANISOTROPY ON THE STRESS TRANSFER PROCESS BETWEEN POLYMERIC RESINS AND SUBSTRATES IN PLANAR AND CYLINDRICAL GEOMETRIES

SEPTEMBER 1994

MARIO A. PEREZ, B.S., OHIO UNIVERSITY

B.B.A., OHIO UNIVERSITY

M.S., OHIO UNIVERSITY

M.S., UNIVERSITY OF MASSACHUSETTS AMHERST

Ph.D.,UNIVERSITY OF MASSACHUSETTS AMHERST

Directed by : Professor Shaw Ling Hsu and Professor Richard J. Farris

Evaluation of stress transfer mechanisms is critical in the design of composite structures and laminates. Due to anisotropy incurred during production, assessment of stress transfer processes is crucial for polymeric materials. In this study, two cases are evaluated in which parameters governing stress transfer play a critical role. These are: 1) Single fiber composites, and 2) Coatings. The first case examines the consequences of transferring stress from an isotropic matrix to embedded orthotropic fibers. The second case assesses the transferring of stress from anisotropic coatings to isotropic substrates. Fibers used in this investigation are highly oriented high-density polyethylene, poly (paraphenylene terephthalamide), and polydiacetylene [poly(2,4-hexadiyne-1,6-diol bisphenyl urethane)] single crystals. Poly (4,4'-oxydiphenylene pyrromellitimide), known as PMDA-ODA polyimide, is used as the coating material. The investigation of stress transfer was carried out using finite element analysis and analytical solutions. Elastic constants utilized for the analysis were obtained by molecular simulation methodologies.

Crystalline and orientational order of the polymeric coating are characterized. This characterization was accomplished using wide-angle X-ray diffraction, electron diffraction, infrared spectroscopy, and Raman spectroscopy. Also, an external reflection infrared spectroscopic study of ultra-thin polyimide films revealed that molecular anisotropy remained higher and molecular packing lower for films thinner than 150 Å.

Results from these two case studies indicate that stress transfer observed at the ends of fibers or at the edges of coatings, is influenced by increases in the degree of material anisotropy. Assumptions of isotropy in polymeric materials undergoing analysis may lead to serious error in the characterization of stress transfer. Stress transferred from the isotropic matrix to anisotropic fibers leads to a state of radial compression near the fiber ends. Transverse stresses approach the value of the transverse strength of anisotropic fibers when strained uniaxially. For coatings, a complicated state of stress develops at the edges, at which out-of-plane and shear stresses are significant. Shear stress distributions near the ends, and equal in-plane stress, exhibit a slower decay when the degree of anisotropy is higher.

TABLE OF CONTENTS

LIST OF TABLES

LIST OF FIGURES

CHAPTER 1

INTRODUCTION

1.1 Objective

Characterization of the influence of anisotropy on the stress transfer process between polymer resins and substrates in planar and cylindrical geometries. Specifically, this study focuses on the characterization of PMDA-ODA polyimides, poly(4,4'-oxydiphenylene pyrromellitimide), as coatings on hard substrates and the stress analysis of single fiber model composites. The reinforcing fibers used in the study were: poly(phenylene terephthalamide), polydiacetylene [poly(2,4-hexadiyne-1,6-diol bisphenyl urethane)] single crystals, and highly oriented polyethylene.

1.2 Overview of Dissertation and Scope

This dissertation consists of nine chapters and its purpose is to analyze two major cases of stress transfer situations involving polymeric materials. In each case, the need for analysis exists because most preceding efforts have neglected to explain any anisotropic effects in these systems.[1-5] Due to the unavailability of a full set of elastic constants or because of the practical constraints in analyzing the more complicated

anisotropic cases, the assumption of full isotropy has been frequently made. However, as it will be explained below, this assumption is inadequate when dealing with anisotropic polymeric materials. In coating and fiber geometries macromolecules are arranged in a manner that produces non-isotropic macroscopic behavior. Thus, this work investigates the influence of anisotropy on the stress transfer process which occurs in cylindrical and planar geometries.

Stress transfer plays an important role in the performance and service life of a plastic part.[6] In the case where cylindrical geometries apply, the load bearing ability of a reinforcing fiber is a crucial factor in the composite's design limitations.[7-11] In planar geometries the ability of a polymeric coating to stay attached to its substrate depends greatly on how it is able to handle imposed or residual stresses.[12-16] In both stress transfer situations the preferred macromolecular alignment and the amount of crystalline order in the material cause changes in expansion coefficients and mechanical property magnitude and distribution.[17,18] In coatings, the influence of this ordering phenomena on stress transfer needs to be better understood. For the purpose of the present study, a perfect bond at interfaces was assumed. It is not the purpose of this work to attempt to explore the extensive subjects of adhesion and interfaces. Nor is the study an attempt to explore failure criteria, rather, it is to characterize the influence of anisotropy on the stress transfer phenomena for these two specific geometries but within the limitations of elastic analysis.

In this chapter, an explanation of situations which give rise to the stress transfer phenomena in polymer science has been included. Chapter 2 provides the strategy employed for the stress analysis of problems which can be classified under cylindrical geometries, the most important case being that of a reinforcing fiber embedded in a matrix. Finite element modelling was chosen for the analysis due to the complications which can arise when dealing with anisotropic materials. Comparison with analytical

solutions has also been made. Chapter 3 makes the transition between cylindrical and planar geometries and provides an explanation of which variables may influence anisotropy in a coating. Chapter 4 explains how conformation and crystalline order in PMDA-ODA polyimides can be extracted by molecular simulation and X-ray diffraction. This polyimide is commonly called PMDA-ODA due to the monomers utilized to manufacture its precursor, polyamic acid.[19] PMDA is pyromellitic dianhydride and ODA is di-(4-aminophenyl)ether. The basic reaction scheme to obtain PMDA-ODA is shown in Figure 1.1.

Chapter 5 details the characterization of orientational order and packing disorder of coatings by external reflection infrared spectroscopy and electron diffraction. In Chapter 6, calculation of anisotropic elastic constants of PMDA-ODA and their implications on stress transfer are discussed. Chapter 7 explores the application of these constants to stress transfer problems involving planar geometries. Finally Chapter 8 discusses available methods and the feasibility for measuring out-of-plane displacements at constrained ends of coatings to provide an estimation of stress transfer in planar geometries. Chapter 9 contains the overall conclusions from this dissertation and suggestions for future work.

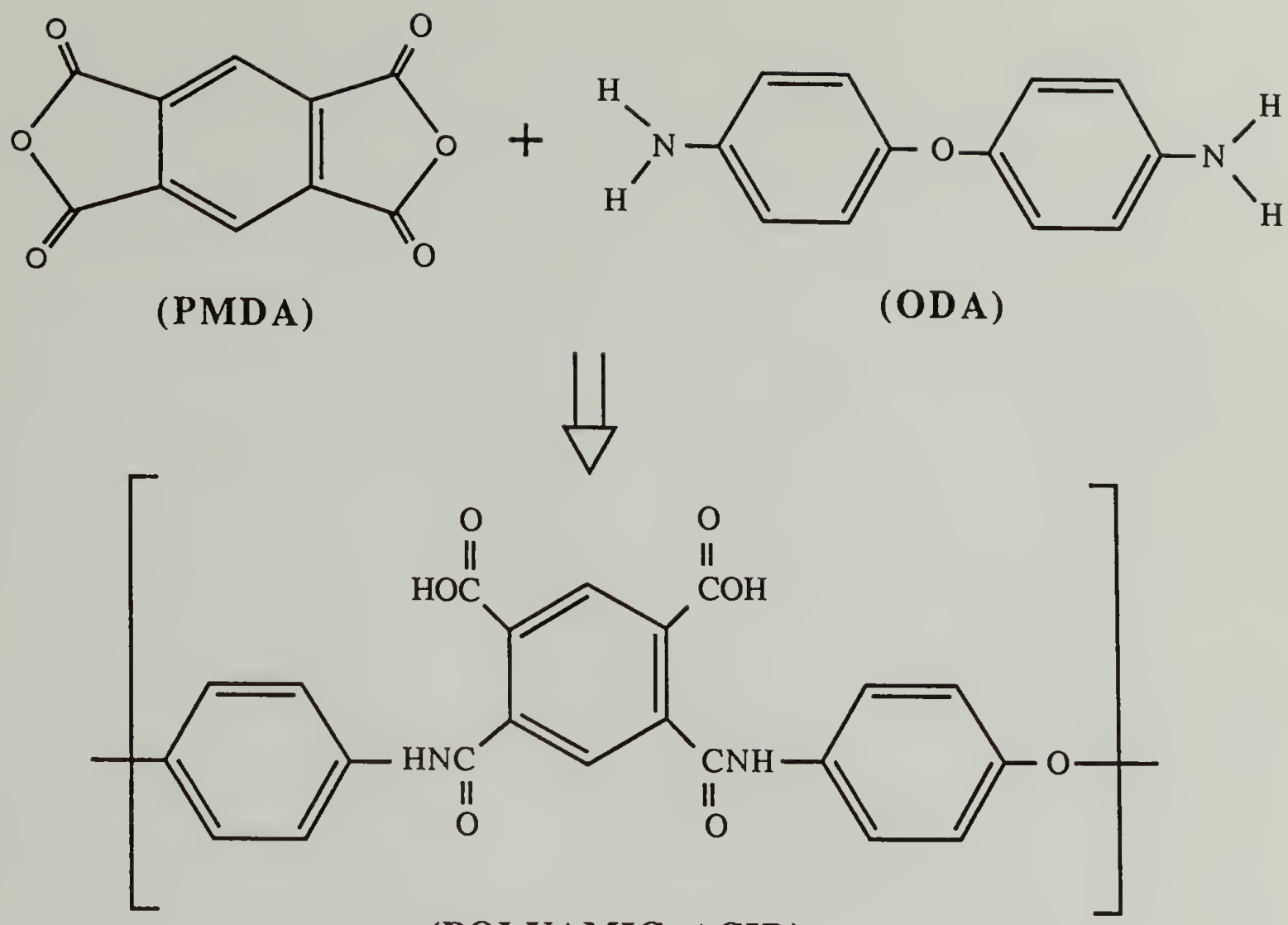

Figure 1.1. Imidization schematic for the formation of PMDA-ODA polyimide.

1.3 Explanation of the Problem

There are numerous cases within the scope of polymer science in which the analysis of the stress transfer process can be of extreme importance. A significant portion of these cases can be classified into two categories, depending on whether their geometries are of cylindrical or planar nature. More specifically, situations in which fibers and coatings interact with their matrices or substrates. Most work to date has focused on the analysis of these situations within the confinements of isotropic material behavior. This has been due to the lack of complete sets of elastic constants or by issues attributed to practical importance. This treatment is inadequate when dealing with these types of anisotropy. Polymer molecules assemble in a manner that yields anisotropic macroscopic behavior in coating and fiber geometries. This work sets out to investigate the influence of this anisotropy on the stress transfer process which takes place in cylindrical and planar geometries while remaining within the limits of elastic analysis.

Mostly, transfer of stress to a fiber occurs at its ends where the shear stresses at the matrix-fiber boundary become greatest. The shear stress decays as the axial stress develops within a few fiber diameters of distance from the ends. The distance from the end of the fiber to where axial stress reaches ~ 97% of its maximum value is called the stress transfer length. The situation is similar in coatings where all stress transfer takes place at the edges. Only at the edges do out-of-plane and shear stresses exist. At a distance from the edges, only in-plane normal stresses persist and in most cases are called "residual stress". These situations are depicted in Figure 1.2.

For those cases mentioned here, highly oriented organic fibers are farthest from representing ideal isotropic behavior. Depending on the fiber's morphology, its anisotropic characteristics can be classified into three categories: radial anisotropy,

circumferential anisotropy and transverse isotropy. In any of these three cases the axial modulus and strength will always be higher than those in any transverse direction. In radial anisotropy the modulus and strength in the radial transverse direction are higher than those in the hoop direction. In circumferential anisotropy, these properties are higher in the hoop than in the radial direction, this is sometimes referred to as an "onion-skin" anisotropy. A transversely isotropic fiber would, accordingly, be one where the moduli and strength do not differ in either of the transverse directions. PPTA is an example of radial anisotropy where hydrogen bonded microfibrilar sheets propagate from the center outwards. Circumferential anisotropy may be observed in the outermost layers of Kevlar fibers due to the last steps in their manufacture. Radial and circumferential anisotropy are also encountered in carbon and graphite fibers. The basal planes of the graphite crystals for example are mostly aligned along the axial direction that gives rise to its high modulus. However, they can have any combination of orientations throughout the cross section depending on processing history. Transverse isotropy is characteristic of polyethylene fibers. Fully isotropic properties can be encountered in glass fibers where there is no mechanical property distinction between the axial and the transverse directions. The next chapter deals directly with the evolution and importance of transverse stress development in orthotropic bodies.

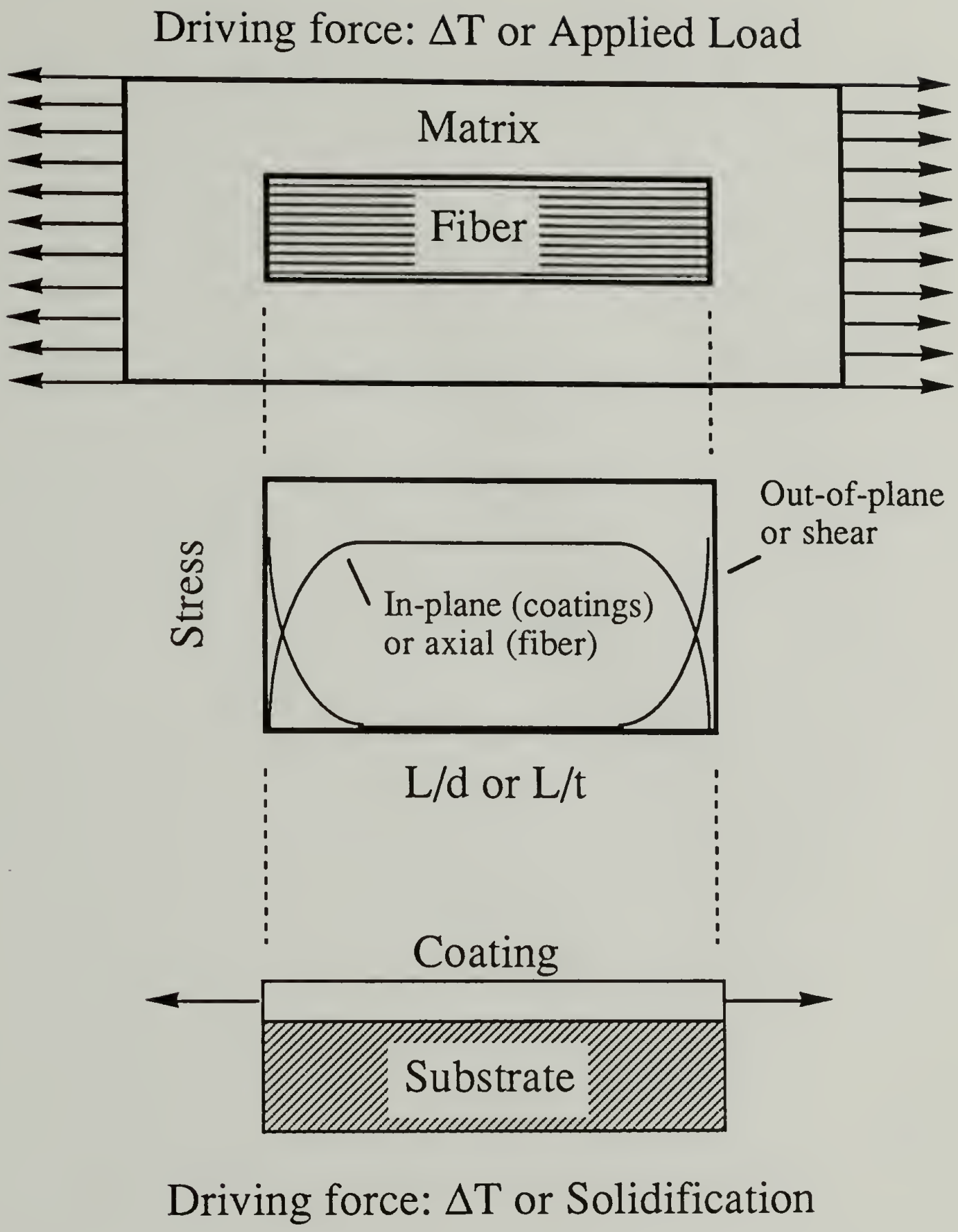

Figure 1.2. Stress transfer in fiber and coating geometries.

1.4 References

(1) Cox, H.L. *British J. of Appl. Phys.* **1952**, *3*, 72.

(2) Outwater, J.O., *Mod. Plast.* **1956**, *March*, 1956.

(3) Rosen, B.W. *Mechanics of Composite Strengthening in Fiber Composite Materials*, ASM Pub., 1964.

(4) Carrara, A.S.; McGarry, F.J. *J. Compos. Mater.* **1968**, *2*, 222.

(5) Agarwal, B.D.; Lifshitz, J.M.; Broutman, L.J. *Fibre Sci. Technol.* **1974**, *7*, 45.

(6) Holister, G.S.; Thomas, C. *Fibre Reinforced Materials*, Elsevier Pub. Co.: N.Y., 1966.

(7) Avery, W.B.; Herakovich, C.T. *J. of Appl. Mech.* **1986**, *53*, 751.

(8) Whitney, J.M.; Drzal, L.T.; *Axisymmetric Stress Distribution Around an Isolated Fiber Fragment. Toughened Composites, ASTM STP 937*, Norman J. Johnston, Ed., Am. Soc. for Test. and Mat., Philadelphia, 179, 1987.

(9) Allen, S.R.; Farris, R.J. *Polym.* **1990**, *31*, 1467.

(10) Dupont, Data Manual for Kevlar® 49 Aramid", E.I. Dupont de Nemours Co., 1986.

(11) Christensen, R.M. *Mechanics of Composite Materials*; Wiley: N.Y., 1979.

(12) Bauer, C.L.; Farris, R.J. *J. of Coatings Technol.* **1988**, *60*, 51.

(13) Goldfarb, J.L.; Farris, R.J. *J. of Adhesion Sci. & Technol.* **1993**, *7*, 8.

(14) Durelli, A.J.; Parks, V.J.; del Río, C.J. *Exp. Mech.* **1967**, *Nov.*, 481.

(15) Chow, T.S.; Liu, C.A.; Penwell, R.C. *J. of Polym. Sci.: Polym. Phys.* **1976**, *14*, 1311.

(16) Elsner, G. *J. of Appl. Polym. Sci.* **1987**, *34*, 815.

(17) Jennings, R.; PhD Dissertation, Dept. of Polym. Sci. and Eng. The University of Massachusetts at Amherst, 1993.

(18) Ree, M.; Nunes, T.L.; Czornyj, G.; Volksen, W. *Polymer* **1992**, *33*, 1228.

(19) Sroog, C.E. *Macromol. Rev.* **1976**, *11*, 161.

CHAPTER 2

ANALYSIS OF CYLINDRICAL GEOMETRIES

2.1 Introduction

The influence of transverse stresses in single fiber model composites was investigated with finite element analysis. Full sets of elastic constants, calculated by molecular simulation, were employed to provide a complete description of the properties of orthotropic fibers. The nature and magnitude of radial and hoop stresses which develop within the fiber, especially at the fiber ends was determined. Also, the dependence of far-field stresses on radial distance and stress behavior at the boundaries of the composite are discussed below.

Stresses in fibers can be categorized into "end" and "far-field" stresses. "Far-field" stresses are simply those that can still be detected away from the fiber ends. For isotropic or transversely isotropic fibers, there are no stress distributions along transverse directions but stresses show increased change in the axial direction near the fiber ends. Isotropic and transversely isotropic fibers cannot exhibit far-field stress distributions along transverse directions.

The origin of the axial dependency of the transverse stresses during unidirectional loading of any type of fiber can be traced to the combined effect of the Poisson's ratios and the stress transfer in the model composite. Far-field transverse stresses that show a

dependency in the transverse direction of a round single fiber loaded axially, and free of defects, can only come from its mechanical anisotropy. Specifically, for the cases discussed above, the fiber must have either circumferential or radially orthotropic properties. A schematic of the characteristic cross section of these orthotropic fibers is shown below in Figure 2.1.

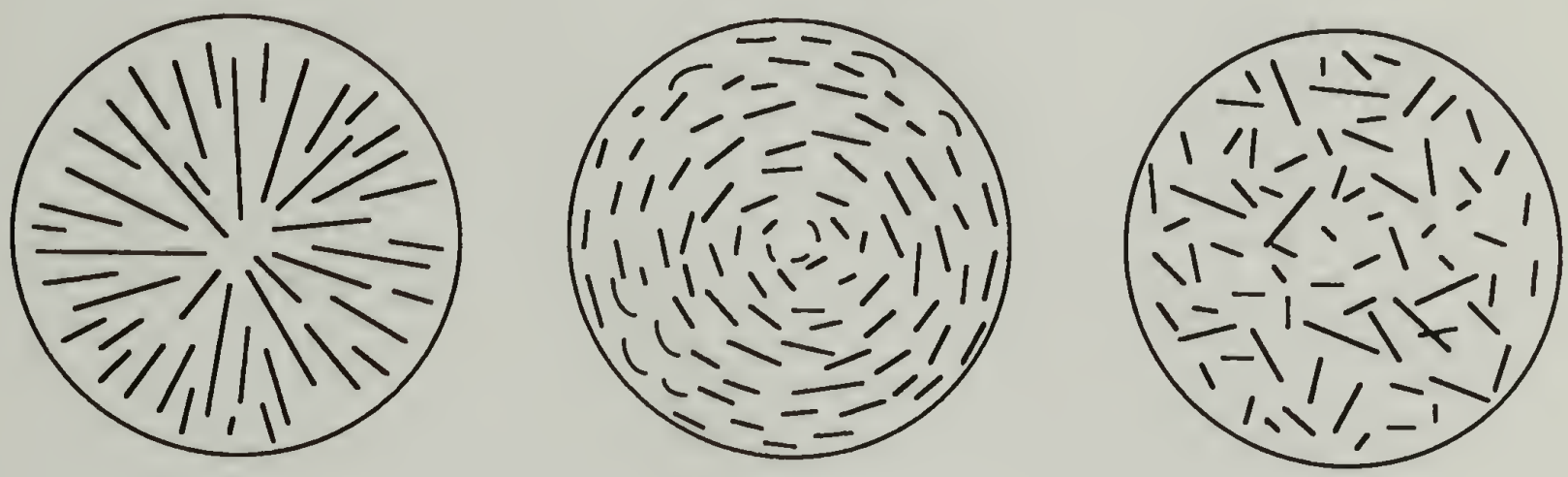

	Radially anisotropic	Circumferentially anisotropic	Transversely Isotropic
E_{axial}	High	High	High
E_{radial}	Moderate	Low	~ to Hoop
E_{hoop}	Low	Moderate	~ to Radial

Figure 2.1. Cross sections describing three cases of fiber orthotropy.

It has been customary in a mechanical analysis of orthotropic bodies to make assumptions which often compromise the validity of the calculation. This is due to the

inability to evaluate stiffness or compliance coefficients for the body under constraint. The experimental evaluation of these coefficients is difficult if not impossible for certain geometrical shapes and sizes.[1] An alternative method for the direct evaluation of these elastic constants is molecular simulation. This technique has gained popularity due to the relative availability of economically feasible computing power. Full sets of elastic constants have now been calculated by this method for organic fibers such as Kevlar and polyethylene (highly oriented), which are good examples of the aforementioned class of materials.[2] Another way has been to scale the elastic constants for a particular fiber based on a known set of these constants obtained from other orthotropic materials such as wood.[3,4,5] All elastic constants utilized in this analysis were obtained in our labs by either one of the these two latter methods. Even very subtle changes in mechanical behavior can be detected when proper elastic constants are utilized. As an example, Figure 2.2 illustrates the radial dependency of the axial stress in an anisotropic fiber of a single fiber model composite. The isotropic fiber showed, of course, no transverse stress distribution.

The structure of highly oriented polymer fibers differs according to the kind of processing steps taken to manufacture them or their precursors. Kevlar fibers as well as some other rigid-rod polymeric fibers, such as poly(para-phenylene benzobisthiazole) (PBZT) and poly(paraphenylene benzobisoxazole) (PFZO) are spun from solutions, coagulated in solvent or water baths and then mechanically tensioned and heat treated. A swollen microfibrilar network is the morphology obtained from the coagulant bath but as the drying process takes place, the microfibrilar network collapses into a more highly ordered and densely pack fibrilar morphology. The microfibrils are para-crystalline structures which grow and exhibit a higher degree of orientation with applied tension and heat treatment.

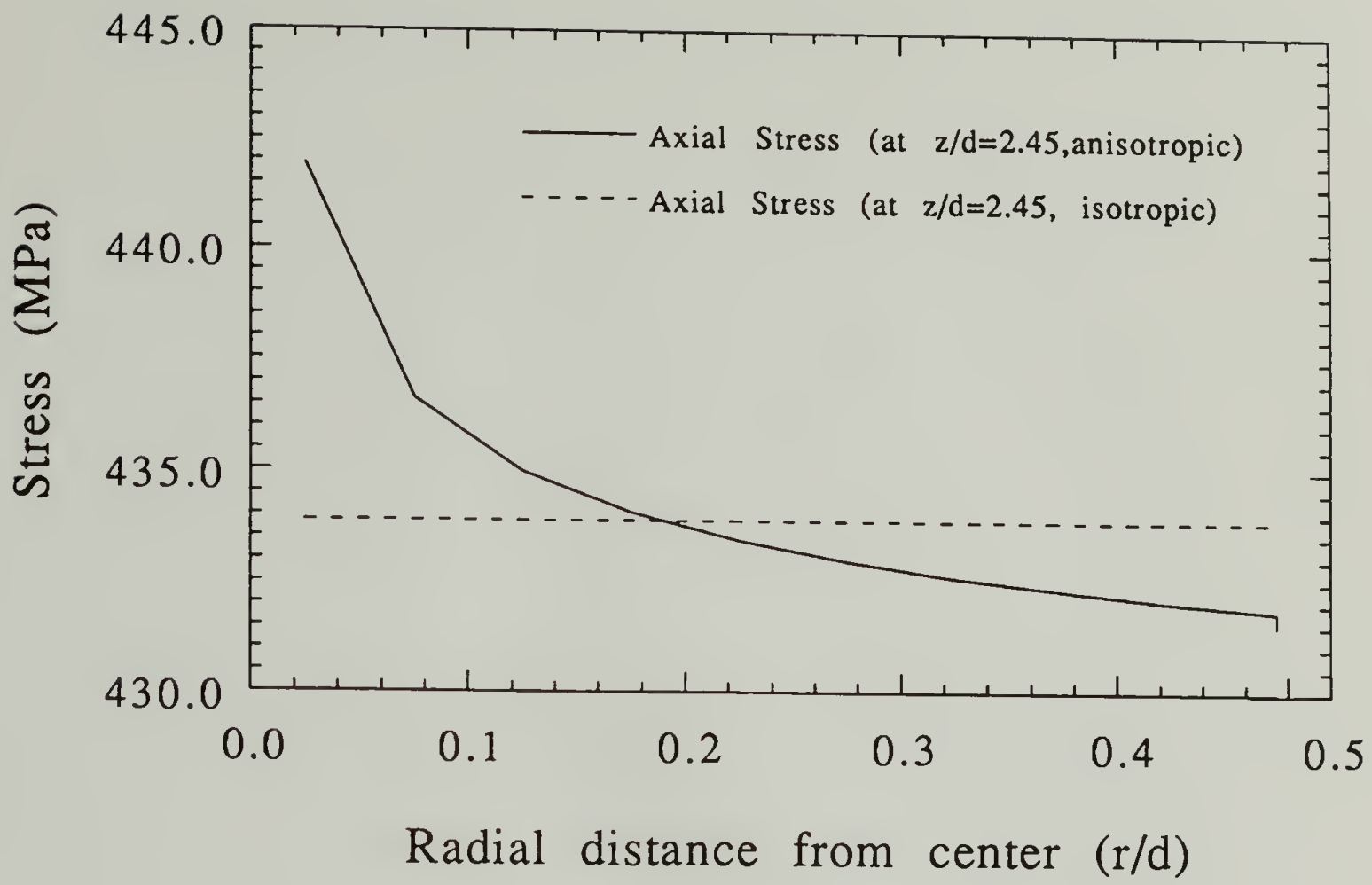

Figure 2.2. Comparison between isotropic and anisotropic far-field axial stress distribution by finite element analysis as a function of radial distance in the fiber.

The cross-section of each microfibril may consist of several crystallites divided by lateral or axial grain boundaries where there are no covalent bonds, although covalent bonding takes place in axial twist boundaries which arise along the axis of the microfibril. Polyethylene fiber morphology may range from a variation of the process described above to elongated spherulites. Polydiacetylene fibers are single crystal morphologies which are solid state polymerized. As a result of these morphologies, high mechanical properties in the axial direction are attained as a result of molecular alignment and covalent bonding, but much weaker properties are to be observed in the other directions since for the most part secondary forces hold the structure together. The role of this anisotropy in the fiber performance is the subject of this chapter.

2.2 Axial Symmetry. Implication on Stress Analysis and Finite Element Solutions

The stress analysis of these orthotropic fibers embedded in an isotropic matrix has been made by assuming an axial symmetry. In this symmetry, a 2-D region can be rotated around the axis to form a solid body of revolution. Geometry, physical properties and loads must be independent of the θ-coordinate. Resulting stresses, strains or displacements are a function of the principal axes, r and z. The z coordinate corresponds to the axial direction and r to the radial direction.

A brief description of the analysis involving these geometries, as extracted from well known mechanics textbooks,[6,7] is given below.

One should expect two non-zero displacement components along the r and z directions,

$u = u(r, z)$ = radial displacement (2.1)

$v = 0$, (θ-direction) (2.2)

$w = w(r, z)$ = axial displacement (2.3)

There are six components of stress and strain:

$\sigma_r (r,z)$ $\varepsilon_r (r,z)$ (2.4)

$\sigma_\theta (r,z)$ $\varepsilon_\theta (r,z)$ (2.5)

$\sigma_z (r,z)$ $\varepsilon_z (r,z)$ (2.6)

$\tau_{rz} (r,z)$ $\gamma_{rz} (r,z)$ (2.7)

$$\tau_{\theta r} = 0 \qquad \gamma_{\theta r} = 0 \tag{2.8}$$

$$\tau_{\theta z} = 0 \qquad \gamma_{\theta z} = 0 \tag{2.9}$$

In general, for cylindrical coordinates the six possible strain-displacement relations are:

$$\varepsilon_r = \frac{\partial u}{\partial r} \tag{2.10}$$

$$\varepsilon_\theta = \frac{1}{r}\frac{\partial v}{\partial \theta} + \frac{u}{r} \tag{2.11}$$

$$\varepsilon_z = \frac{\partial w}{\partial z} \tag{2.12}$$

$$\gamma_{rz} = \frac{\partial w}{\partial r} + \frac{\partial u}{\partial z} \tag{2.13}$$

$$\gamma_{\theta r} = \frac{1}{r}\frac{\partial u}{\partial \theta} + \frac{\partial v}{\partial r} - \frac{v}{r} = 0 \tag{2.14}$$

$$\gamma_{\theta z} = \frac{\partial v}{\partial z} + \frac{1}{r}\frac{\partial w}{\partial \theta} = 0 \tag{2.15}$$

For the axisymmetric problem there are only four non-zero components of strain:

$$\{\varepsilon\} = \begin{Bmatrix} \varepsilon_r \\ \varepsilon_\theta \\ \varepsilon_z \\ \gamma_{rz} \end{Bmatrix} = \begin{Bmatrix} \dfrac{\partial u}{\partial r} \\ \dfrac{u}{r} \\ \dfrac{\partial w}{\partial z} \\ \dfrac{\partial w}{\partial r} + \dfrac{\partial u}{\partial z} \end{Bmatrix} \tag{2.16}$$

The complete equilibrium equations in cylindrical coordinates are:

$$\frac{\partial \sigma_r}{\partial r} + \frac{1}{r}\frac{\partial \tau_{r\theta}}{\partial \theta} + \frac{\partial \tau_{rz}}{\partial z} + \frac{1}{r}(\sigma_r - \sigma_\theta) = -f_r \tag{2.17}$$

$$\frac{\partial \tau_{r\theta}}{\partial r} + \frac{1}{r}\frac{\partial \sigma_\theta}{\partial \theta} + \frac{\partial \tau_{\theta z}}{\partial z} + \frac{2}{r}\tau_{r\theta} = -f_\theta \tag{2.18}$$

$$\frac{\partial \tau_{rz}}{\partial r} + \frac{1}{r}\frac{\partial \tau_{\theta z}}{\partial \theta} + \frac{\partial \sigma_z}{\partial z} + \frac{1}{r}\tau_{rz} = -f_z \tag{2.19}$$

where f_r, f_θ and f_z are body forces such as gravity.

In the absence of body forces and with axisymmetric restrictions, these equations are reduced to:

$$\frac{\partial \tau_{rz}}{\partial r} + \frac{\partial \sigma_z}{\partial z} + \frac{1}{r}\,\tau_{rz} = 0 \tag{2.20}$$

$$\frac{\partial \sigma_r}{\partial r} + \frac{\partial \tau_{rz}}{\partial z} + \frac{1}{r}\,(\sigma_r - \sigma_\theta) = 0 \tag{2.21}$$

Materials that have orthotropic symmetry would have only nine independent elastic constants if the coordinate planes are parallel to the planes of orthotropic symmetry. The principal axes of stress and strain will coincide with the symmetry axis. Three orthogonal planes of symmetry are shown in Figure 2.3.

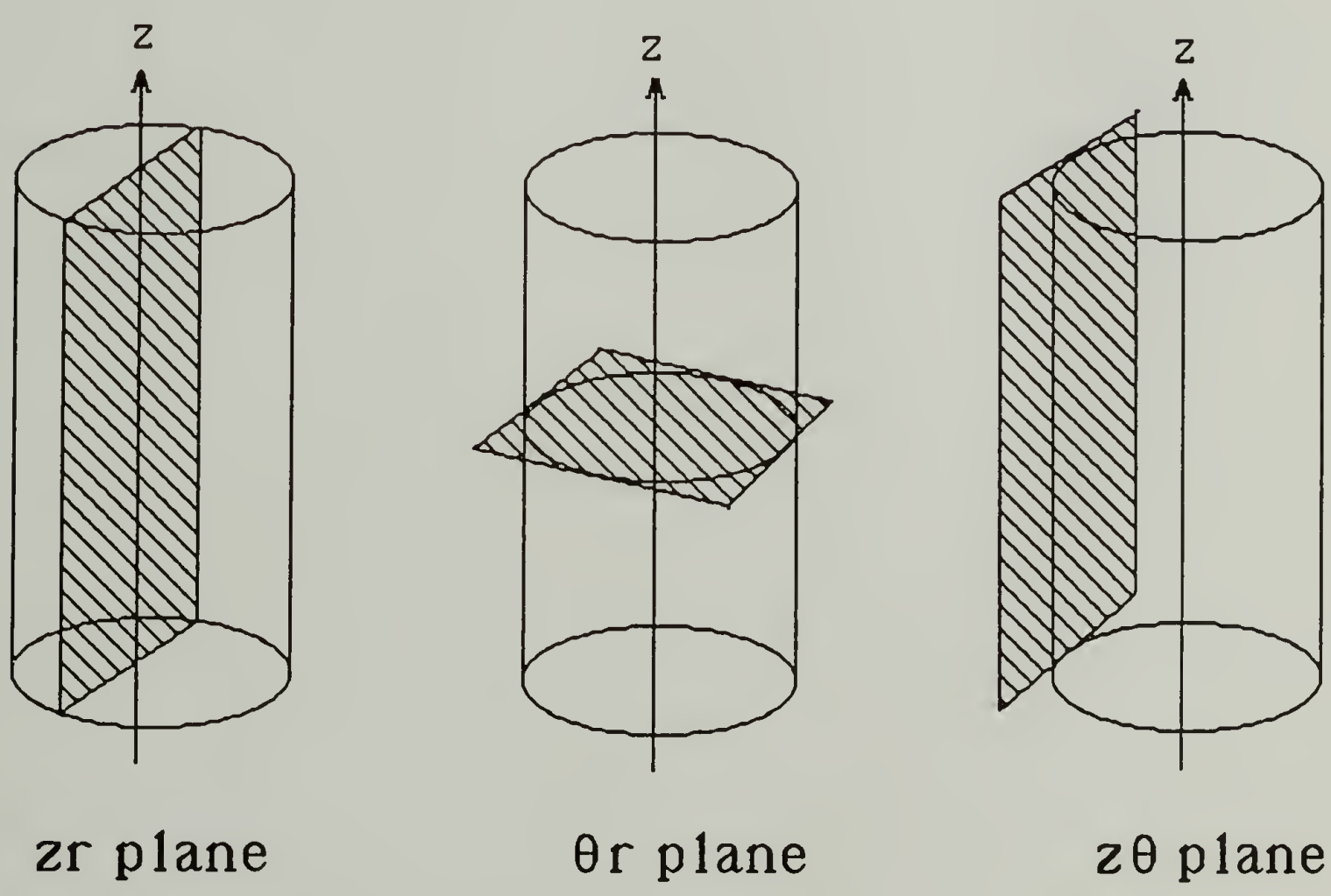

Figure 2.3. Orthotropic symmetry planes.

The elastic constants given in table 2.1 were computed based on energy minimized unit cells. It is important to note that even though periodic boundary conditions simulated the presence of other similar entities around the original cell. It is not a perfect emulation of a particular morphology or microfibrilar structure characteristic of some of these highly oriented organic fibers. The constants as given by molecular simulation reflect the upper limits in mechanical properties which can only rarely be encountered in commercial materials. Nevertheless, these parameters are very suitable for this type of analysis because they are representative of the relative magnitudes of the properties in each direction. The constants were computed in a Cartesian environment, but they can be adapted to axisymmetric problems because all geometry and therefore physical properties must be independent of the hoop direction. As explained above, the problem reduces to that of a two-dimensional situation where displacement, stress and strain are a function of axial and radial coordinates only. The first and second principal axes must lie in the r-z plane and the third principal axis in the θ direction.

The constants for PPTA and PE were computed by the molecular simulation technique and the ones for PDA were scaled according to the anisotropy of wood. A more detailed explanation of the procedure and errors involved in the computation of these constants can be found from references 2-4. For PPTA full sets of elastic constants can also be found in the work of Rutledge and Suter.[8] For PDA one can refer to Leyer, Wegner and Wettling.[9]

Table 2.1. Elastic constants utilized for finite element analysis of model composites.

	PPTA	PE	PDA
E_x	14.9	10.7	2.5
E_y	80.1	8.4	4.9
E_z	335.7	297.5	45.0
G_{yz}	15.4	3.7	3.6
G_{xz}	0.7	1.5	2.9
G_{xy}	5.2	8.3	0.9
ν_{zy}	0.199	0.215	0.390
ν_{zx}	0.496	0.025	0.025
ν_{yx}	0.717	0.472	0.200

E and G, the elastic and shear moduli respectively, are shown above in GPa.
The constants utilized for the isotropic matrix material were E = 4.0 GPa and $\nu = 0.34$

These constants can be related to stress and strain through classical elastic constitutive relationships. One of these relationships is the generalized Hooke's Law equations for the case of cylindrical anisotropy where the elastic constants are shown:[10]

$$\varepsilon_r = \frac{1}{E_r}\sigma_r - \frac{\nu_{\theta r}}{E_\theta}\sigma_\theta - \frac{\nu_{zr}}{E_z}\sigma_z\,, \qquad \gamma_{\theta z} = \frac{1}{G_{\theta z}}\tau_{\theta z}, \tag{2.22}$$

$$\varepsilon_\theta = -\frac{\nu_{r\theta}}{E_r}\sigma_r + \frac{1}{E_\theta}\sigma_\theta - \frac{\nu_{z\theta}}{E_z}\sigma_z\,, \qquad \gamma_{rz} = \frac{1}{G_{rz}}\tau_{rz}\,, \tag{2.23}$$

$$\varepsilon_z = -\frac{\nu_{rz}}{E_r}\sigma_r - \frac{\nu_{\theta z}}{E_\theta}\sigma_\theta + \frac{1}{E_z}\sigma_z\,, \qquad \gamma_{r\theta} = \frac{1}{G_{r\theta}}\tau_{r\theta}\,, \tag{2.24}$$

E_r, E_θ and E_z are the moduli in the three coordinate directions. $\nu_{\theta z}$, ν_{rz}, and $\nu_{r\theta}$ are the Poisson coefficients where the first subscript gives the direction where tension has been applied and the second one provides the direction of its characteristic compression. $G_{\theta z}$, G_{rz} and $G_{r\theta}$ are the shear moduli which characterize the change of the angles in those directions indicated by their respective subscripts. For a transversely isotropic body there is no distinction between the θ and r directions.

2.3 Finite Element Calculations

2.3.1 Boundary Conditions and Assumptions

Since the emphasis of this effort was to investigate the magnitude and origin of transverse stresses which occur due to fiber anisotropy, the availability of a full set of elastic constants such as those mentioned above was crucial. The code utilized for the calculations was Cosmos/M 1.65 from Structural Research and Analysis Corporation. The modeling was done with axisymmetric geometry which allowed for the utilization of only one quarter of the composite. No displacements were allowed along symmetry axes (at r=0, z=0). A 1% strain was applied by using a displacement load at the top of the composite. The other outer edges of the composite had zero shear stress. Some of the assumptions implied by such analysis were: the formation of a perfect bond between fiber

and matrix; load transfer through the fiber ends was allowed; the radius of the composite was large enough so that the lateral edge effects did not impose any significant constraints to the stress distributions around the fiber; perfect elasticity was observed.

The mesh utilized for the calculations is shown in Figures 2.4 and 2.5. A total of 1625 elements and 1716 nodes were employed, doubling the amount of elements in the model did not show a significant improvement in the solution and the increased difficulty in data handling was not justifiable. The element density increase towards the fiber end region is shown in the insert of the same figure. Linear "Plane 2-d" elements with four nodal points suited for axisymmetric analysis were chosen. The longitudinal distance of the composite from its symmetry axis to the loaded end is z/d=30, and the radial distance from its center to the outer boundary is r/d=5. Fiber-matrix boundaries are encountered at z/d=20 and r/d=0.5 . Nine elastic constants were utilized for the description of the material properties in fully orthotropic fibers, but only two were needed for isotropic cases. Those two parameters were the axial modulus and its corresponding Poisson's ratio.

Figure 2.6 shows the axial strain along the z direction for the PDA-matrix composite under an applied load of 1% strain at z = 30. The axial strain distribution at the fiber's boundary, near r/d= 0.475, has been corroborated by Raman spectroscopy and by Ansys, another well known finite element code.[4] The plots provide a perspective on the stress transfer efficiency of the fiber in terms of its critical length, $l_c/2$, but it can also be observed that the fiber strain did not go to zero at z=20. The strain would go to zero at this point in the case where there was no load transfer at the fiber blunt ends. As shown in Figure 2.6, a high strain developed in the matrix side. If our analysis was to focus on this particular region of the matrix, one would be obliged to try a non-linear solution to yield a more appropriate characterization if the plasticity of the matrix was not to be dismissed. The matrix may still be adhered to the blunt end of the fiber but it may already

be beyond its yield point, in which case the values of the strain at this end in the fiber side may be lower than otherwise predicted.

An appropriate set of elastic constants should yield a positive-definite stiffness matrix for the finite element calculation to converge at a true global minimum in strain energy. A positive definite matrix is a Hermitian where all its eigenvalues are real and positive. A Hermitian matrix is one that equals its adjoint or conjugate transpose. It is implied that these matrices are square.

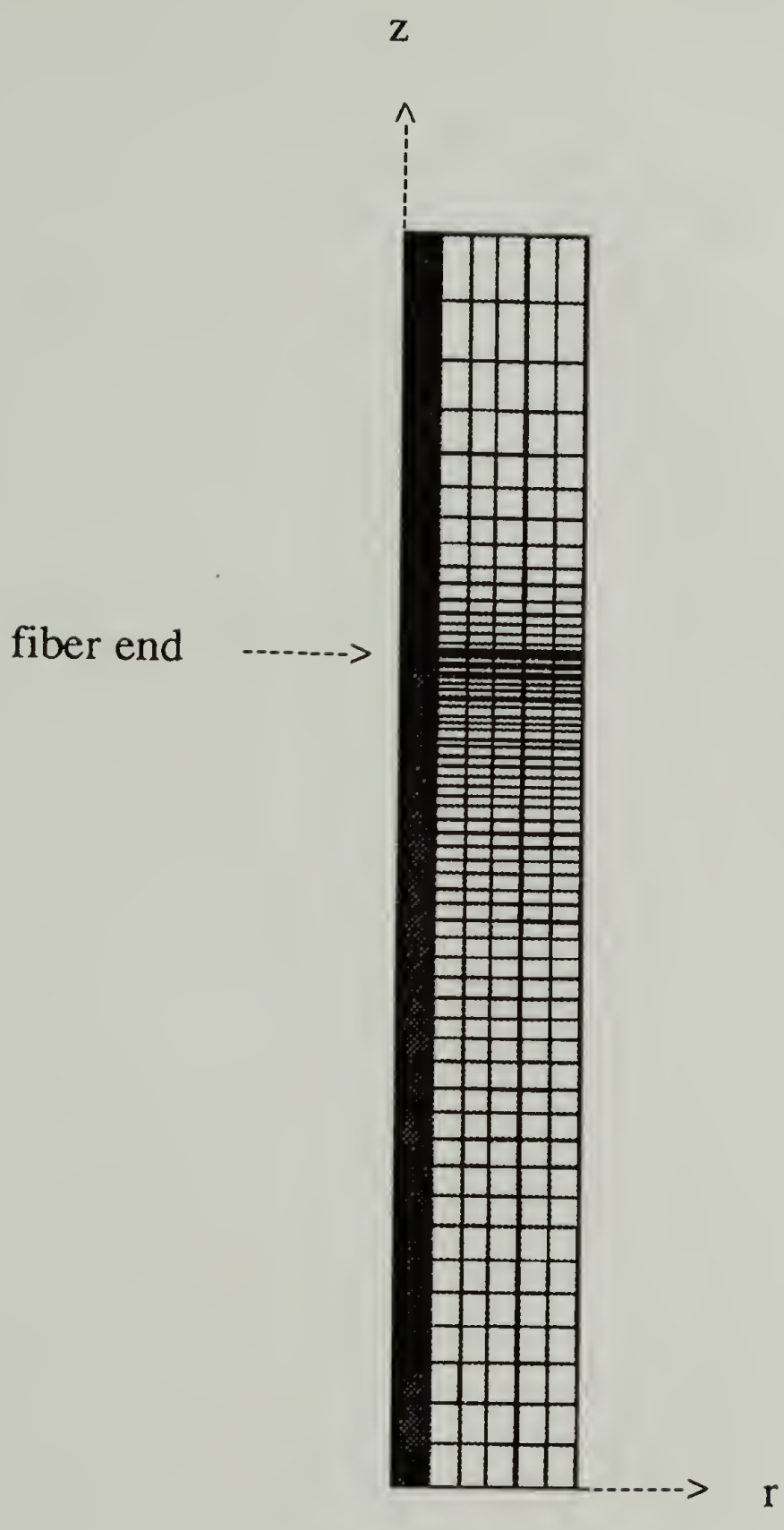

Figure 2.4. Finite element mesh. Complete model.

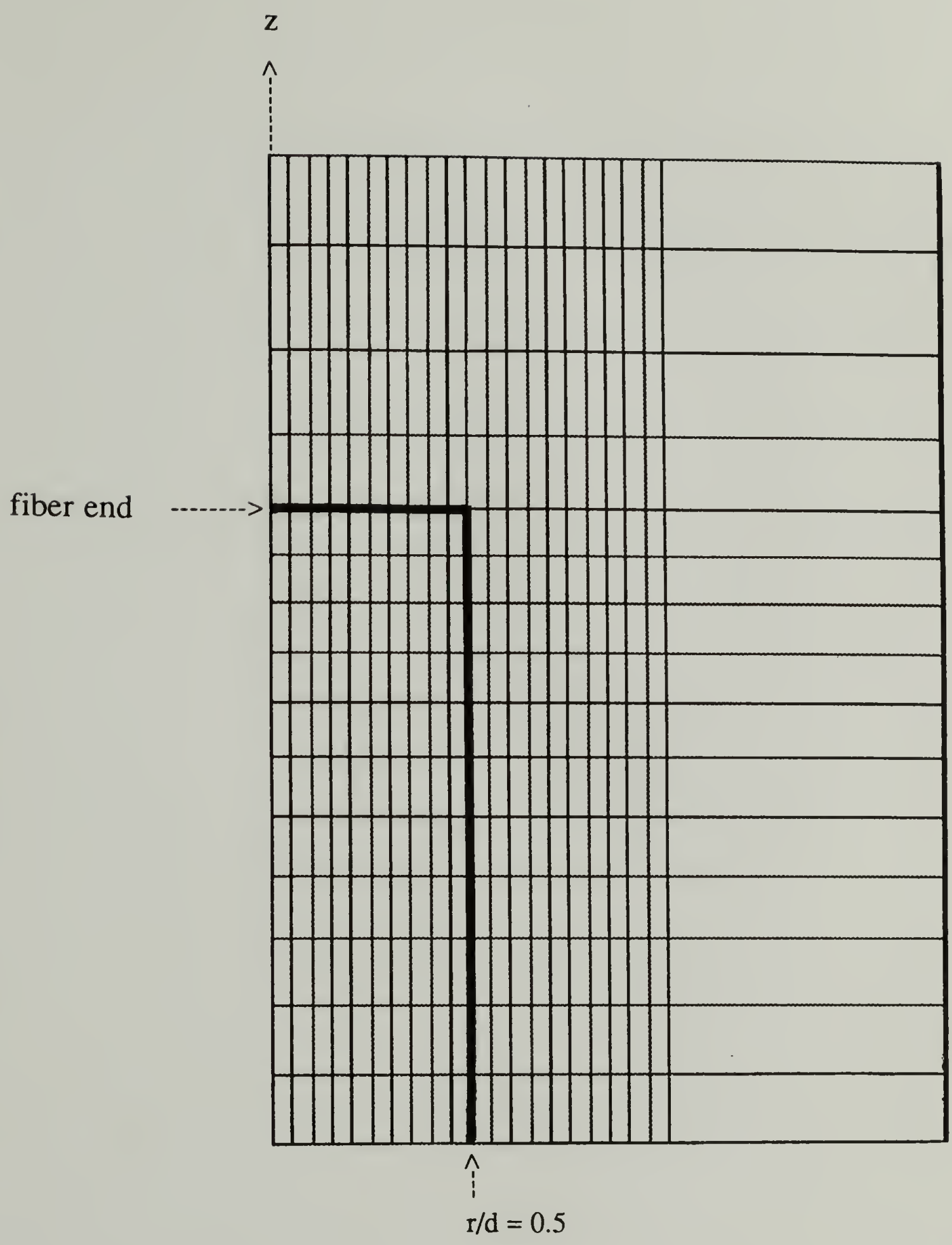

Figure 2.5. Finite element mesh. Detail.

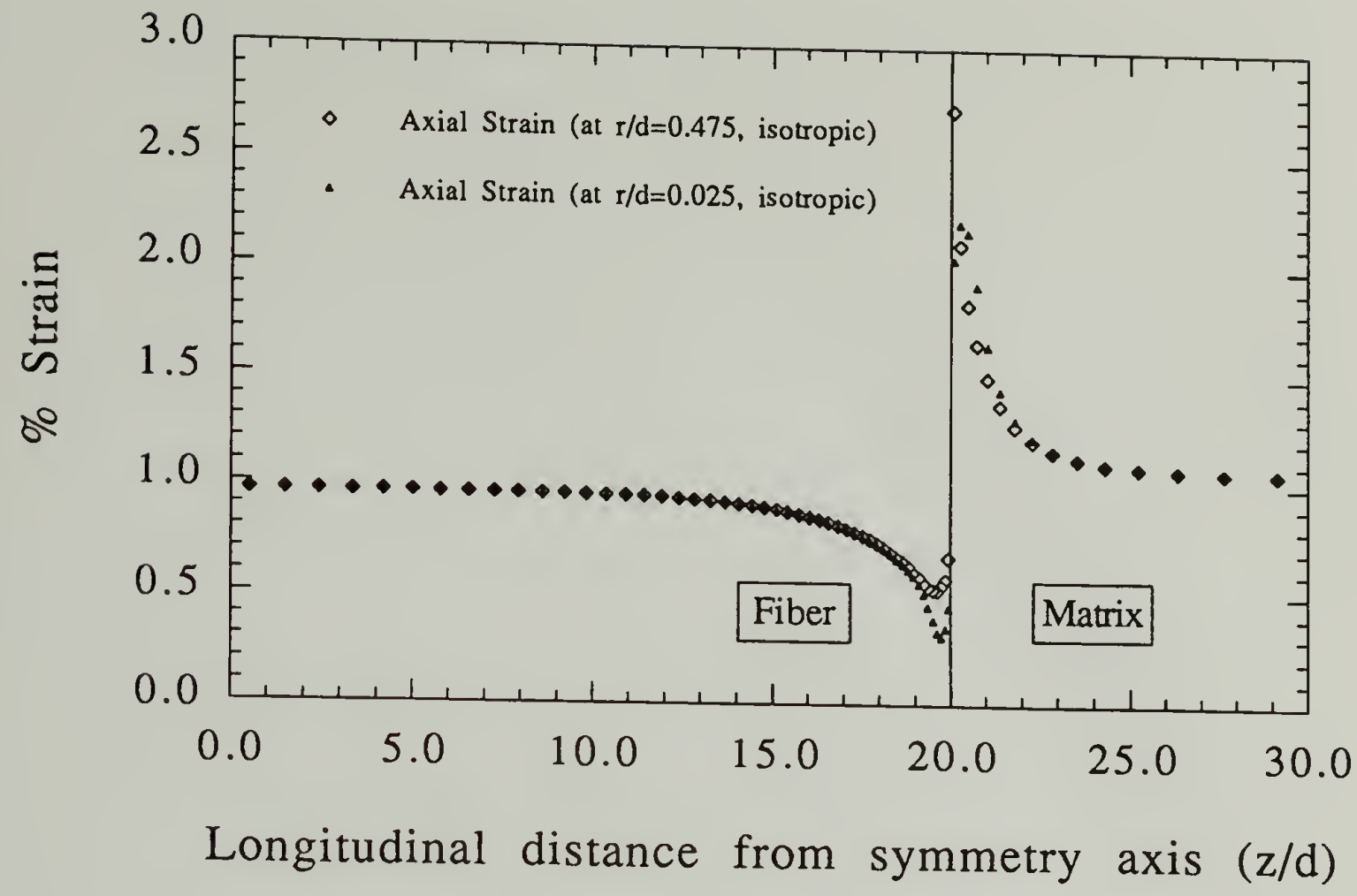

Figure 2.6. Axial strain distribution. PDA-matrix.

2.3.2 General Considerations

Even though most investigations deal with interfacial shear as the mode of failure for fibers, more attention was paid to transverse stresses which can develop when loading highly anisotropic fibers. Some studies do acknowledge the importance of these stresses on fiber performance.[11-16] Fiber failure may not be attributed to interfacial shear alone since the Poisson's effect in the matrix of some composite systems may be very close to that of the fiber (Kevlar 49/Shell Epoxy 828), resulting in low overall interfacial pressure.[12] It is well known that Kevlar goes through a longitudinal split when it fails in tension. Other examples of anisotropy induced failure may be found in highly oriented

superconducting YBa2Cu3Ox coatings and in boron nitride crucibles under a thermal load.[17]

As mentioned above, and depending on the fiber's morphology, its anisotropic characteristics can be classified into three categories: radial anisotropy, circumferential anisotropy and transverse isotropy. In any of these three cases the axial modulus and strength will always be higher than those in any transverse direction. Radial anisotropy is that where modulus and strength in the radial transverse direction are higher than in the tangential or hoop transverse direction. In circumferential anisotropy these properties are higher in the hoop than in the radial direction, this is sometimes referred to as an onion-skin anisotropy. A transversely isotropic fiber would then be one where the moduli and strength do not differ in either of the transverse directions. PPTA is an example of radial anisotropy where hydrogen bonded microfibrilar sheets propagate from the center outwards, refer to table 2.1. Circumferential anisotropy may be observed in the outer layers of Kevlar fibers due to the last steps in their manufacture. Radial and circumferential anisotropy is encountered in carbon and graphite fibers. The basal planes of graphite crystals for example are mostly aligned along the axial direction, giving rise to their high modulus. But they can observe any combination of orientations throughout the cross section depending on processing history. Van der Waals forces provide intermolecular interaction in polyethylene fibers, and transverse isotropy is produced. Fully isotropic properties can be encountered in glass fibers where there is no mechanical property distinction between the axial and the transverse directions.

2.3.3 Results

2.3.3.1 Axial Phenomena

A compressive transverse stress concentration at the fiber end was calculated for these fibers. The major contributor to the compressive nature of these stresses would be the reduced Poisson's effect of the fiber itself at this point (Figure 2.7). This reduction in the Poisson's effect is a consequence of the rate of change of axial stress as the fiber end is approached (Figure 2.8). This rate of change in the axial stress distribution at the loaded extreme is a direct consequence of the stress transfer efficiency process that takes place between the fiber and the surrounding matrix.

It is well known that the axial stress distribution increases to reach a plateau that starts after a critical length is reached, a critical length is unique for a particular system, fiber end geometry, and testing conditions. This critical length, which is measured from the fiber's end, is a way to assess the stress transfer efficiency of the composite. The critical length is reached when the axial stress is approximately 96-98% of its far-field value. Critical length values are commonly derived from shear stress data and statistical fittings to experimental data.[18] A direct way has been to compute this critical length value directly from strain distributions on a single fiber as provided by Raman spectroscopy. These studies confirmed axial stress distributions for polydiacetylene,[19-23] rigid-rods,[24,25] and high density polyethylene fibers.[26-28]

Most studies on stress transfer in fibrous composites utilize the shear-lag model of Cox as a means of theoretical comparison.[29] This model provides an enormous

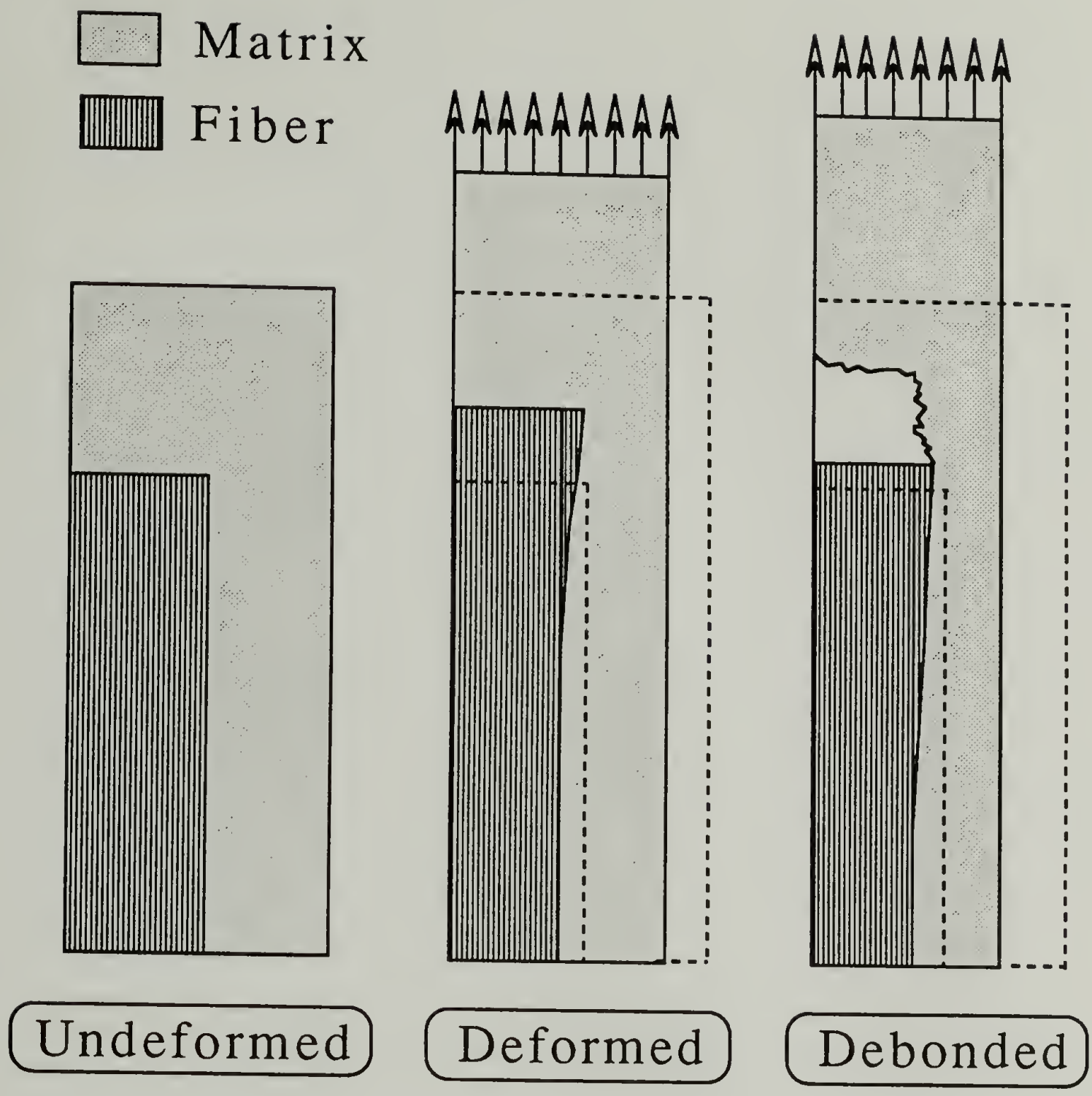

Figure 2.7. Consequences of Poisson's effect on model composites.

advantage due to its simplicity. It is a one-dimensional analysis for an isotropic system and therefore does not include the development of transverse stresses . Transverse stresses affect the stress transfer process and may be directly linked to interfacial failure.[16] Another drawback of the Cox-theory stems from the implication that a high

fiber volume fraction in the composite needs to be assumed to determine the shear interaction parameter. This assumption precludes its usage in single fiber model composites. The utilization of the Cox approximation is limited to applications where the fiber is not in the fragmented state even though one of its assumptions is that no stress is to be transferred through the fiber ends.

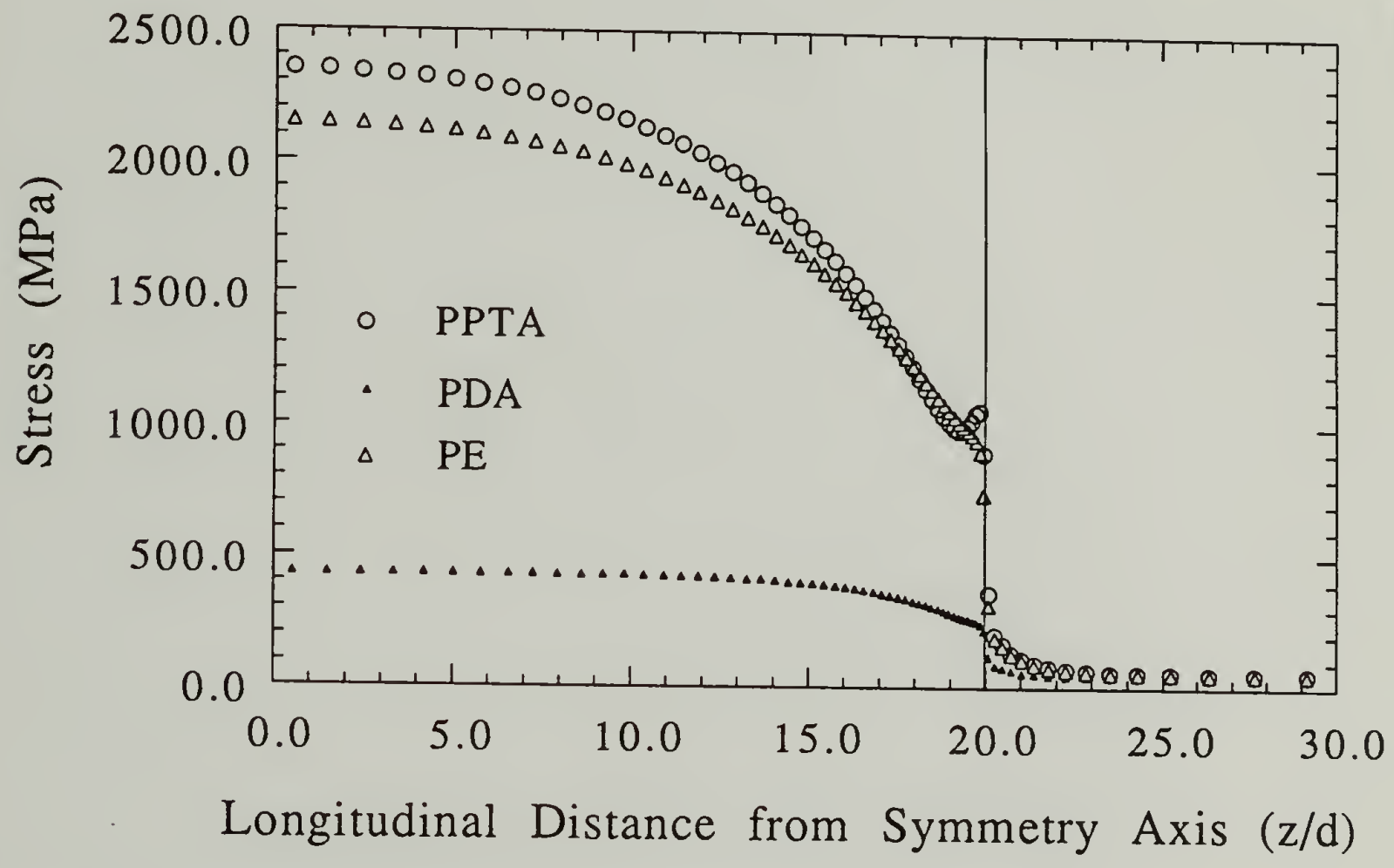

Figure 2.8. Axial stress distribution for PE, PPTA and PDA fibers. Fiber End.

Figures 2.9 and 2.10 show the magnitude of the compressive transverse stresses at the fiber end which reached values at least as high as those of interfacial shear (40 MPa), shown in Figure 2.11. These stresses correspond to the outermost layer of the fiber, their radial dependency towards the centerline is discussed in the next section. In Figure 2.9, the radial stresses along the fiber remain negative for all three sets of elastic constants. This provides an indication of the influence of the combined Poisson's effect of the fiber and its matrix.

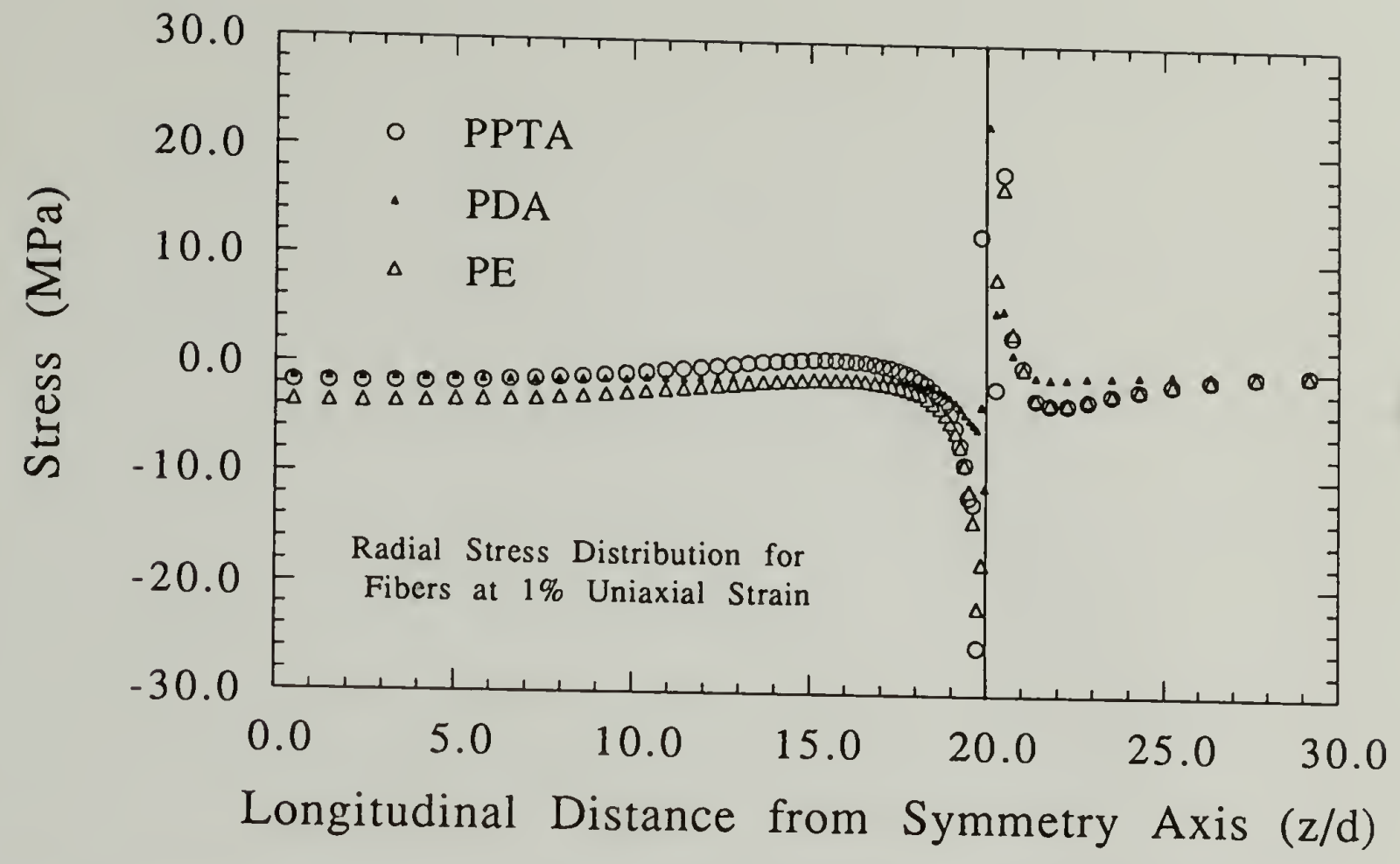

Figure 2.9. Radial stress distribution for PE, PPTA and PDA fibers. Fiber End.

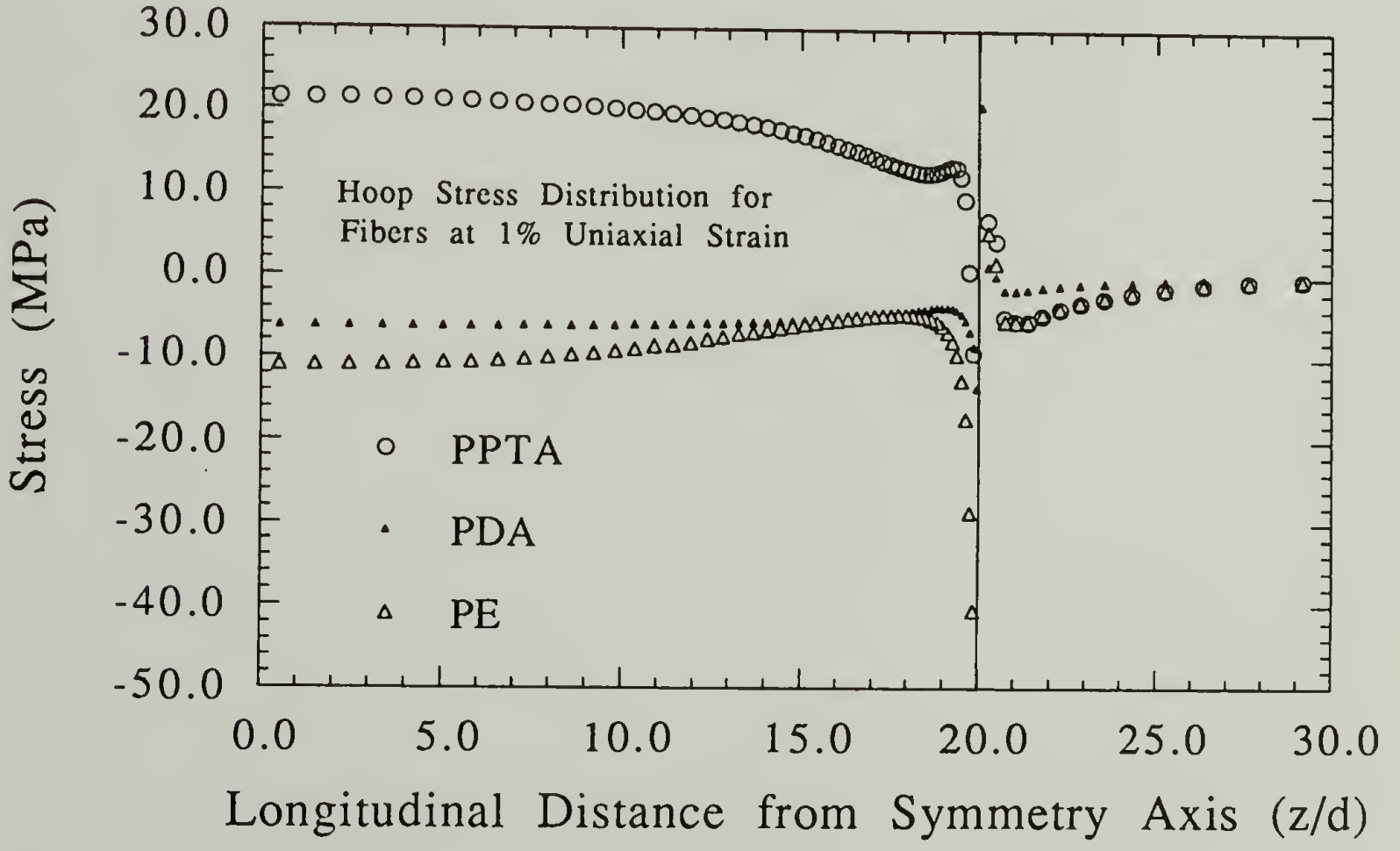

Figure 2.10. Hoop stress distribution for PE, PPTA and PDA fibers. Fiber End.

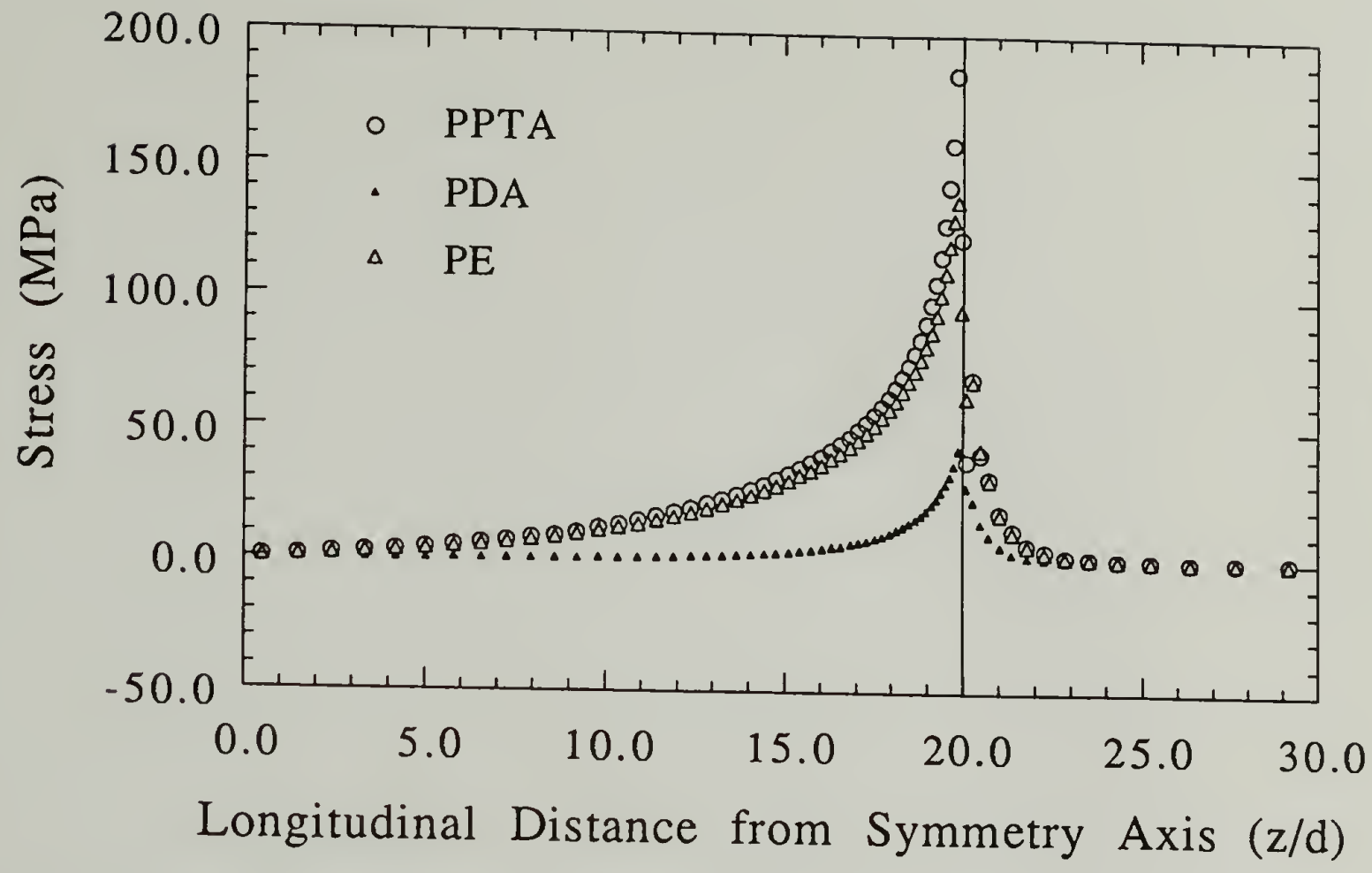

Figure 2.11. Shear stress distribution for PE, PPTA and PDA fibers. Fiber End.

For either one of the three cases, small radial stresses are indicative of the low magnitude of the pressure developed at the fiber's outer boundary. This is a necessary condition for some of the assumptions made in following sections for analytical far-field solutions to be feasible in the treatment of this problem. The compressive nature of hoop stress distributions at the fiber's blunt end are shown in Figure 2.10. A positive hoop stress developed for most of the PPTA fiber's length. This is due to difference in the set of elastic constants utilized for the analysis. This behavior is examined more thoroughly when the radial dependency of these transverse stresses is discussed in the next section.

From Figure 2.11, it can be observed that PPTA shows a high shear stress at the fiber end, this value of interfacial shear is at least three times as large as the interfacial shear values encountered in literature for untreated Kevlar embedded in epoxy.[18,30] It

has been pointed out that fiber failure, in this case (PPTA), is by fibrilar fracture with a propagation length of several diameters and that part of the fiber is still bonded to the matrix.[18] It is worth noting that some of these interfacial shear tests do not probe the fiber blunt end directly but merely the friction which exists at the periphery of the fiber end. The shear stress obtained here using the elastic constants from molecular simulation offers an upper limit that may never be experimentally reached due the nature of the interface, the shear strength of the matrix, its ductility, degree of interfacial pressure developed, or simply the finite size of the surface area available for contact.

Similarly, in composites where ultra-high modulus polyethylene fibers are used, the values for the interfacial strength are low in comparison to the stresses calculated in this work. One study attributed low values of shear stress to the poor adhesion of the polyethylene surfaces to the epoxy matrix.[31] The observation is made in the same study, that after a plasma treatment to improve adhesion, the failure mode switches to fiber splitting. Therefore, a true testing of the interface properties is not attained in neither of the cases cited here for these fibrilar materials.

Fibrilar failures and low apparent experimental values of the interfacial shear strength indicates that radial phenomena should be carefully considered when dealing with such morphologies.

Figures 2.12 and 2.13 show respectively, contour plots of shear stresses developed in a region near the end of isotropic and anisotropic fibers in single fiber model composites during axial loading (1%). The elastic constants used for the finite element calculations shown in figures 2.12 and 2.13 were those shown in table 2.1 for PDA single crystals. The isotropic case yielded a larger value of the maximum shear stress than the anisotropic case. The shear stress distribution for the anisotropic case exhibited a slower rate of decay than the isotropic case.

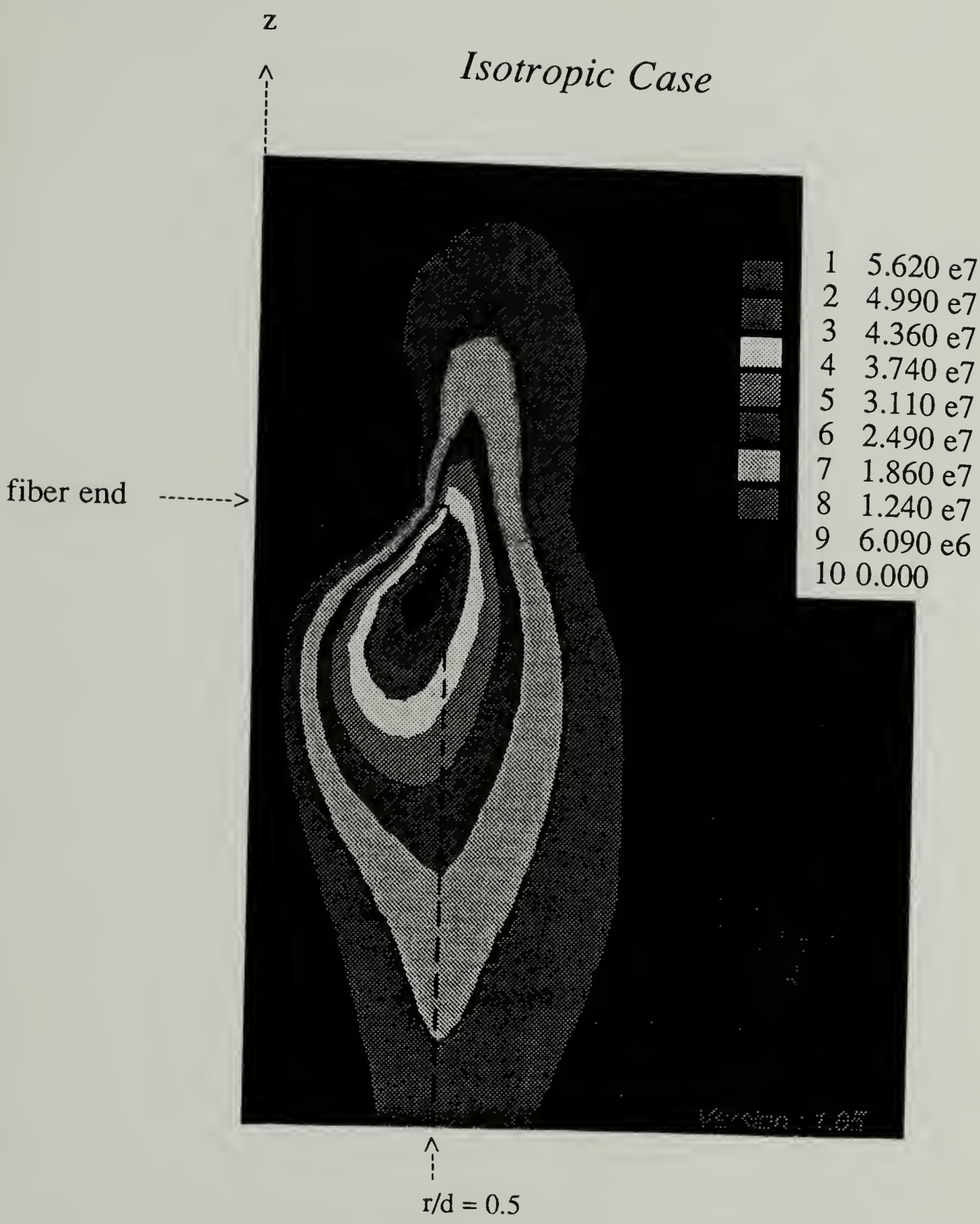

Figure 2.12. Shear stress contour plot for the isotropic case of a PDA-matrix system. Fiber end region.

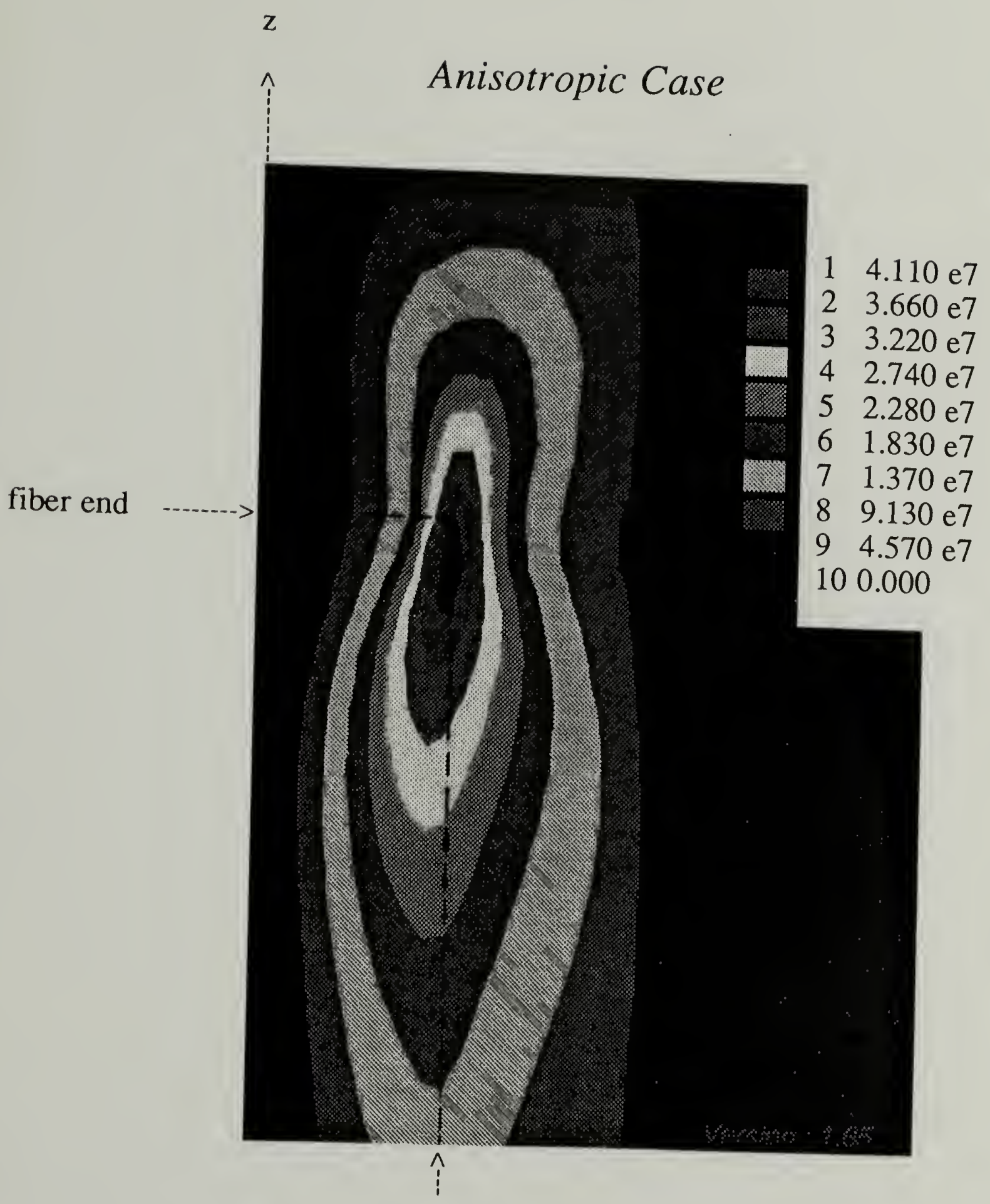

Figure 2.13. Shear stress contour plot for the anisotropic case of a PDA-matrix system. Fiber end region.

2.3.3.2 Radial Phenomena

Despite the loading mode, the effect of fiber anisotropy on overall composite performance manifested itself in a radial dependency of the three normal stresses. For example, due to low transverse strengths, fiber failure in uniaxial tension may be originated by transverse stresses.[13] The magnitude of transverse stresses observed at 1% strain approached the maximum transverse strength observed experimentally in radially orthotropic fibers. Kevlar® 49 has a transverse strength of approximately 15-30 MPa.[32,33]

The radial dependency of normal stresses was singular in nature as the fiber's center was approached. The distribution near the fiber's center, and away from the ends, can be tensile or compressive depending on the loading mode or the magnitude of the difference between the Poisson's ratio in the radial and hoop direction. The fiber is assumed isotropic in the limit of r=0, as is confirmed by the tendency of the radial and hoop stress plots to converge at this point. Figure 2.14, provides plots the dependency of far-field radial and hoop stress distributions on radial distance within the stressed anisotropic fiber. The stresses change significantly from the boundary to the fiber's center for the cases of PPTA and PDA, but these stresses were almost negligible for PE. This can be explained by the isotropic morphology of these PE fibers in the transverse direction. PPTA and PDA both exhibit radial anisotropy, that is $E_r > E_\theta$, Poisson's ratio in the radial direction is larger than that in the hoop direction for this latter material. The tensile or compressive nature of the resulting stress can then be explained by knowing that a larger shrinkage in the radial direction is bound to create a state of tension which grows larger towards the center due to the influence of the state of stress from all other points along that direction. Similarly if the shrinkage is larger in the hoop direction, a

state of compression would arise on an infinitesimal wedge of material. This wedge becomes larger with the influence of a similar stress state of other points in that direction as the center of the fiber is approached. However, it is to be noted that for the hoop stress distributions, a tensile stress at the fiber's center starts with a compressive value at its boundary and vice versa. For the specific case of a compressive hoop stress near the boundary of the fiber, its gradual progression into a tensile hoop stress towards the fiber's center is caused by a positive radial stress distribution.

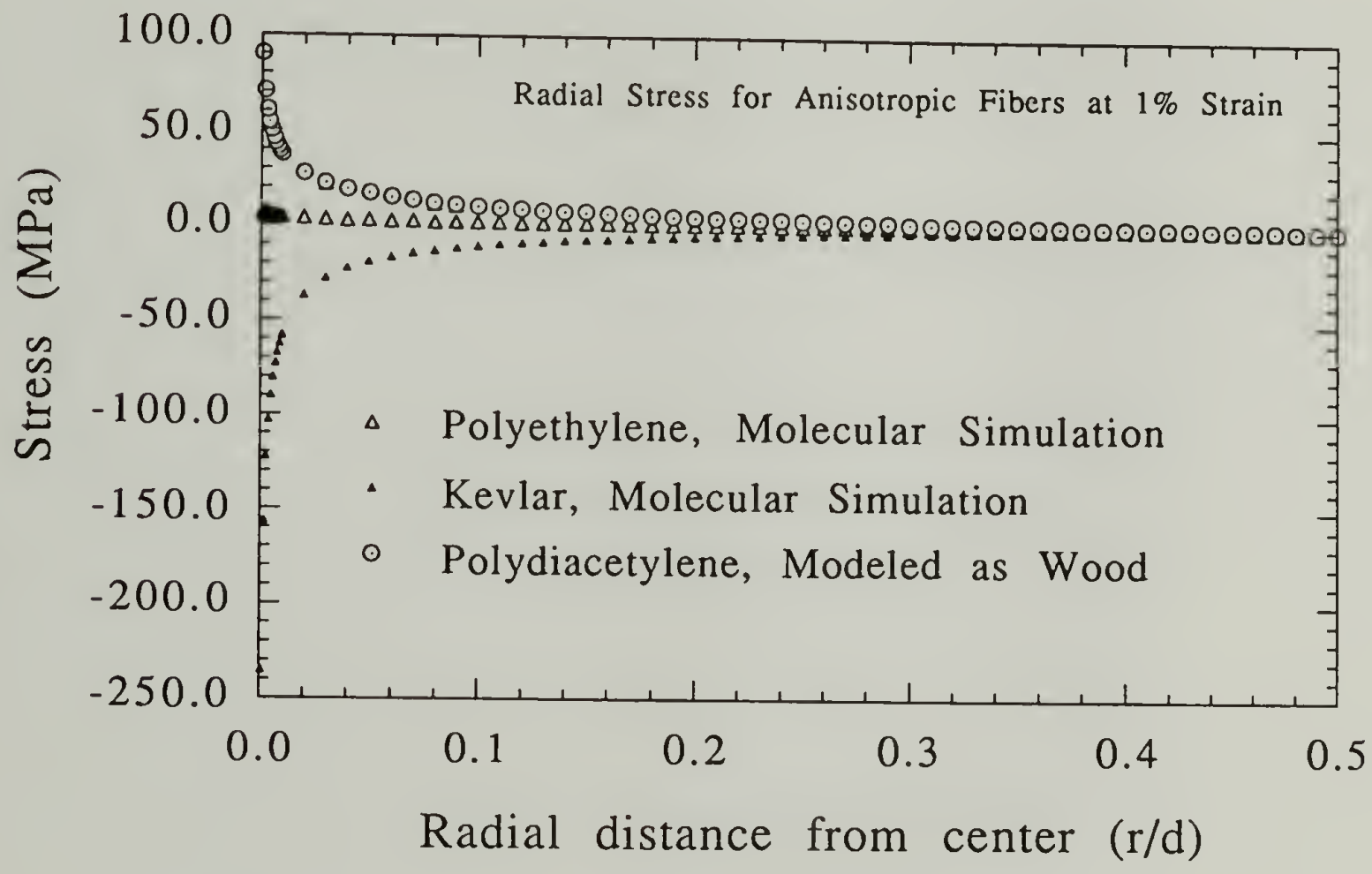

Figure 2.14. Analytical solution for far-field radial stress distribution of PE, PPTA and PDA films.

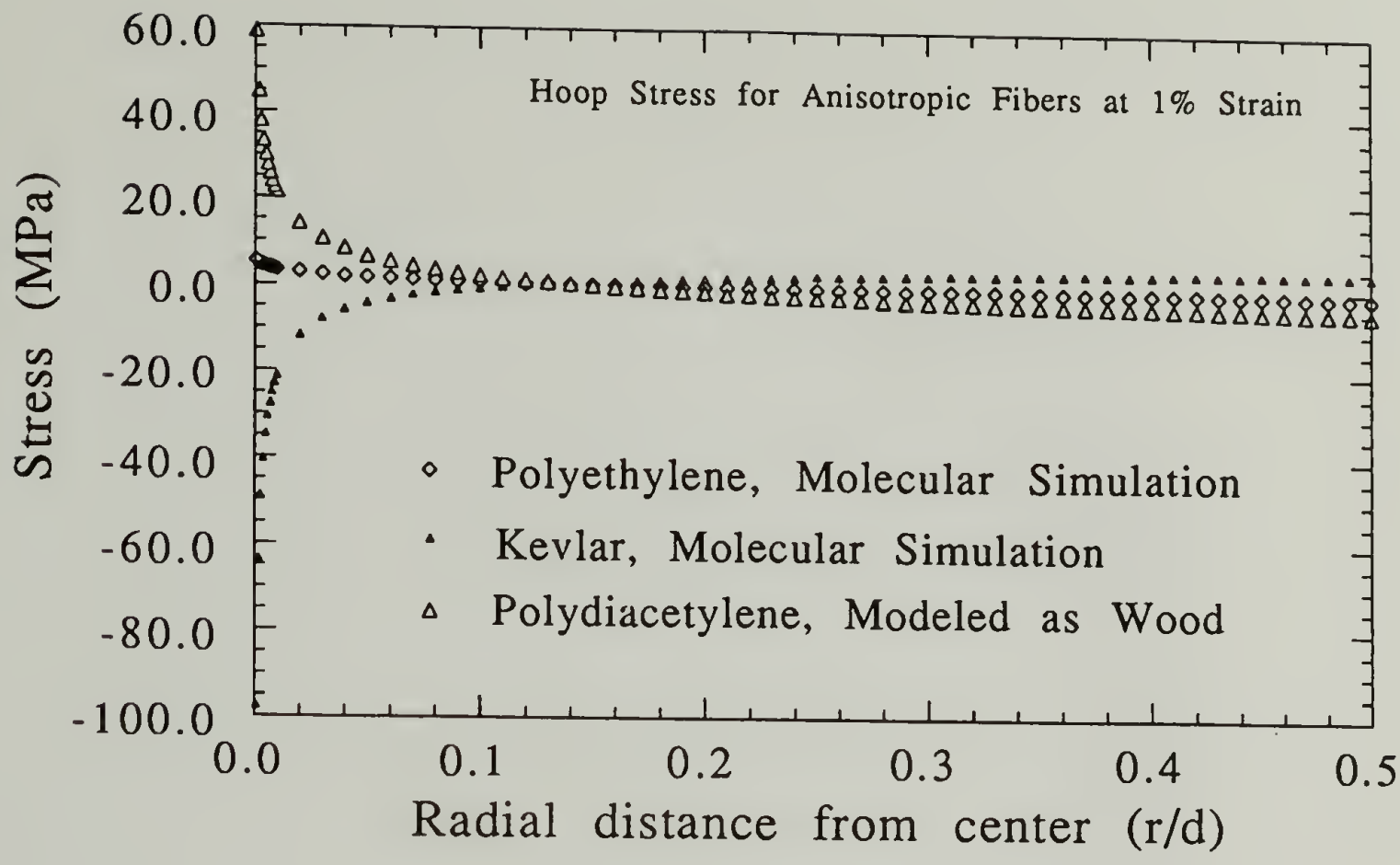

Figure 2.15. Analytical solution for far-field hoop stress distribution of PE, PPTA and PDA films.

2.4 Comparison of FEA Results with Analytical Solutions

Analytical solutions for a single anisotropic fiber provide a good agreement with finite element analysis. These solutions approximate those of the model composite only when the Poisson's ratios are similar in magnitude along the radial plane of the fiber and matrix. In previous sections, it was shown that radial stresses at the fiber's periphery are very close to zero along the z direction, with the exception being the fiber ends.

The analytical solutions for the far-field stress distributions in orthotropic cylinders from Lekhnitskii[34], and later Allen[13] have been utilized here. Equations 2.25-

2.27 provide the radial, hoop and axial stress distributions respectively. The shear stress, equation 2.28, is of course zero in the far-field. Only one stress is present for the case of an ideal transversely isotropic fiber. No other stresses besides the axial exist for this latter case. Highly oriented polyethylene fibers are examples of fibers that exhibit transverse isotropic behavior.

$$\sigma_r = \left(\frac{P\,h}{T_o}\right)\left[1 - \left(\frac{r}{b}\right)^{k-1}\right] \tag{2.25}$$

$$\sigma_\theta = \left(\frac{P\,h}{T_o}\right)\left[1 - k\left(\frac{r}{b}\right)^{k-1}\right] \tag{2.26}$$

$$\sigma_z = \left(\frac{P}{T_o}\right) - \left(\frac{P\,h}{T_o\,a_{33}}\right)\left[a_{13} + a_{23} - (a_{13} + k\,a_{23})\left(\frac{r}{b}\right)^{k-1}\right] \tag{2.27}$$

$$\tau_{rz} = \tau_{\theta z} = \tau_{r\theta} = 0 \tag{2.28}$$

where,

$$k = \sqrt{\frac{a_{11}\,a_{33} - a_{13}^2}{a_{22}\,a_{33} - a_{23}^2}} \tag{2.29}$$

$$h = \frac{a_{23} - a_{13}}{a_{11} - a_{22} + \dfrac{a_{23}^2 - a_{13}^2}{a_{33}}} \tag{2.30}$$

$$\frac{T_o}{\pi\,b^2} = \left(\frac{h}{a_{33}}\right)\left(\frac{k-1}{k+1}\right)(a_{23} - a_{13}) + 1 \tag{2.31}$$

where: b = radius, a_{ij} = compliance coefficients and P = load.

For transversely isotropic systems:

$$\sigma_{z\,(isotropic)} = \frac{P}{\pi\, b^2} \tag{2.32}$$

for this case,

$$\sigma_r = \sigma_\theta = \tau_{rz} = \tau_{\theta z} = \tau_{r\theta} = 0 \tag{2.33}$$

Compliance coefficients were calculated from the elastic constants provided in table 2.1. As an example, for polydiacetylene these coefficients were in Pa^{-1}: $a_{11} = 2.04x10^{-10}$, $a_{22} = 4.0x10^{-10}$, $a_{33} = 2.22x10^{-11}$, $a_{12} = -8.0x10^{-11}$, $a_{13} = -8.67x10^{-12}$, $a_{23} = -5.56x10^{-13}$.

A comparison of these solutions to finite element calculations is shown in Figure 2.16 . That figure illustrates that both techniques provide solutions for stress distributions which are mutually descriptive. The slight difference observed is a product of the influence of the interfacial pressure exerted by a matrix on the fiber's periphery.

Another comparison was made in Figure 2.17, where the analytical solution for the radial stress distribution was plotted using elastic constants from molecular simulation and a set of compliance coefficients obtained by Allen[13] from scaled experimental data on elastic constants for PPTA. The data matches well at larger radii values but they differ slightly as the centerline of the fiber is approached. This figure is proof of the accurate description of macroscopic behavior that can be provided by molecular simulation methods.

Figure 2.18 illustrates how the difference in the magnitude between the Poisson's ratio in the hoop and radial directions influence the nature of the radial dependency of the transverse stresses in the fiber. If ν_{zr} is larger then $\nu_{z\theta}$ the radial stress distribution is

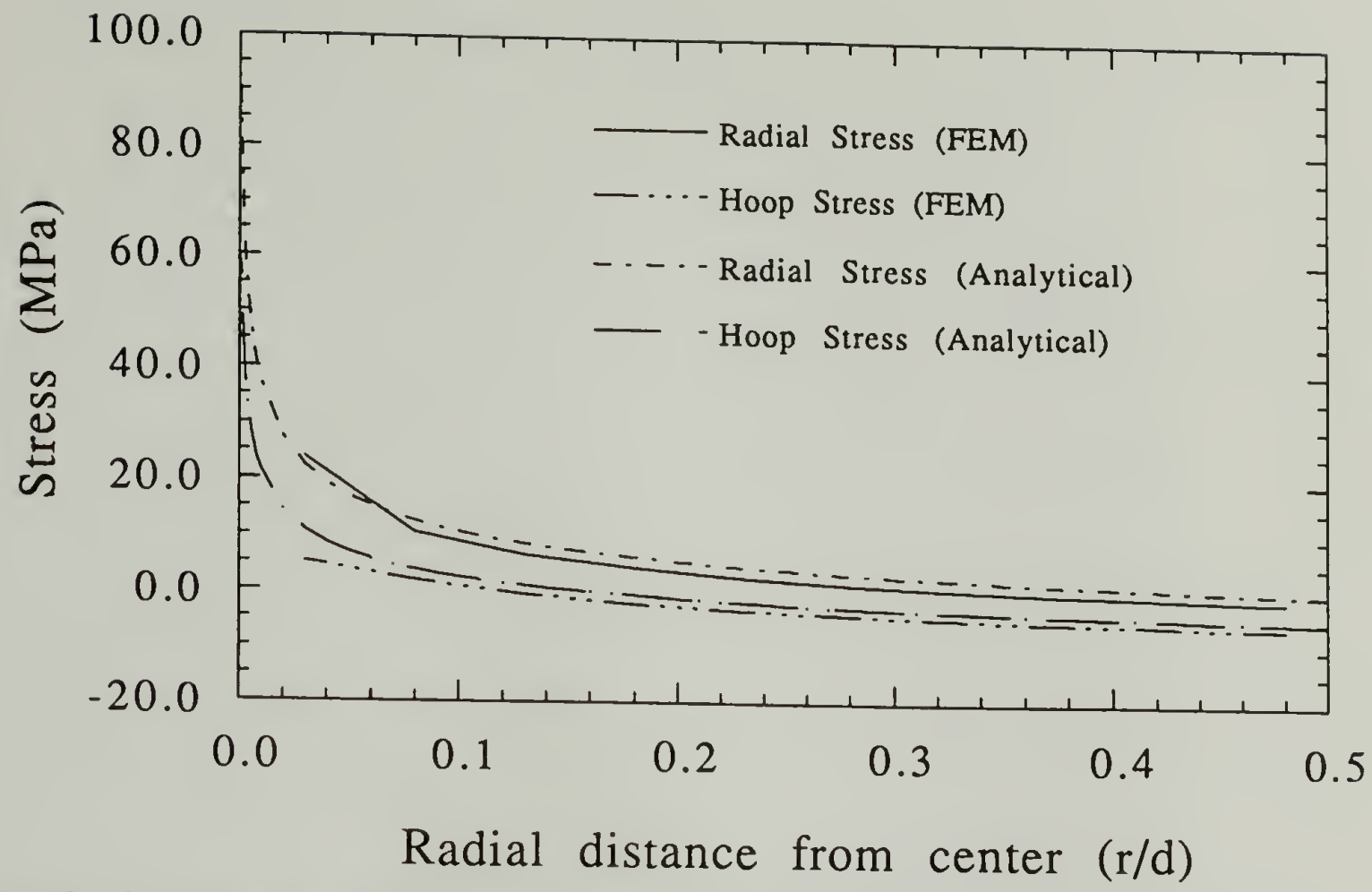

Figure 2.16. Comparison of finite element results and analytical solutions for far-field radial and hoop stress distributions.

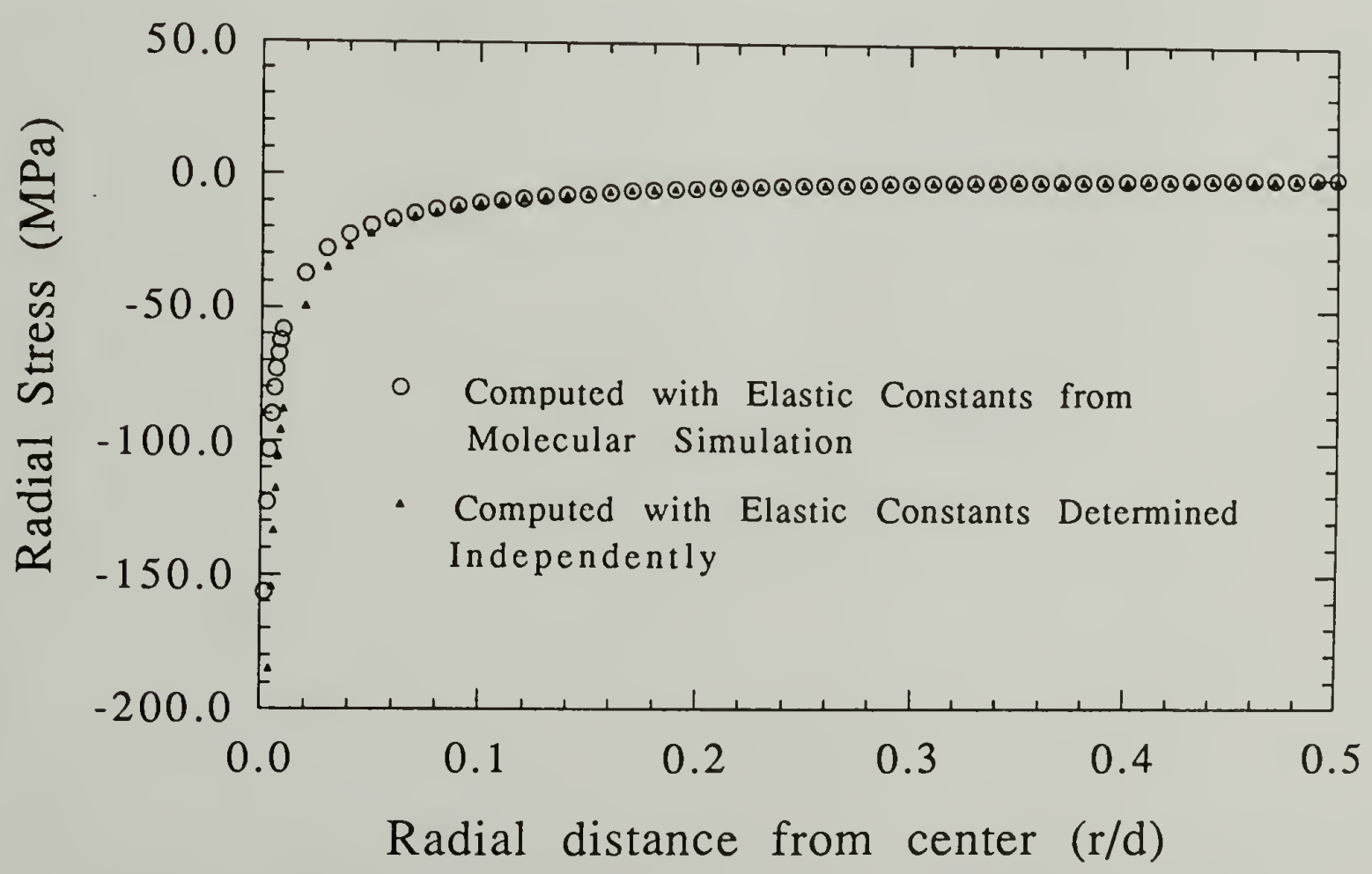

Figure 2.17. Comparison of analytical solutions for the radial stress distributions of PPTA with two sets of elastic constants.

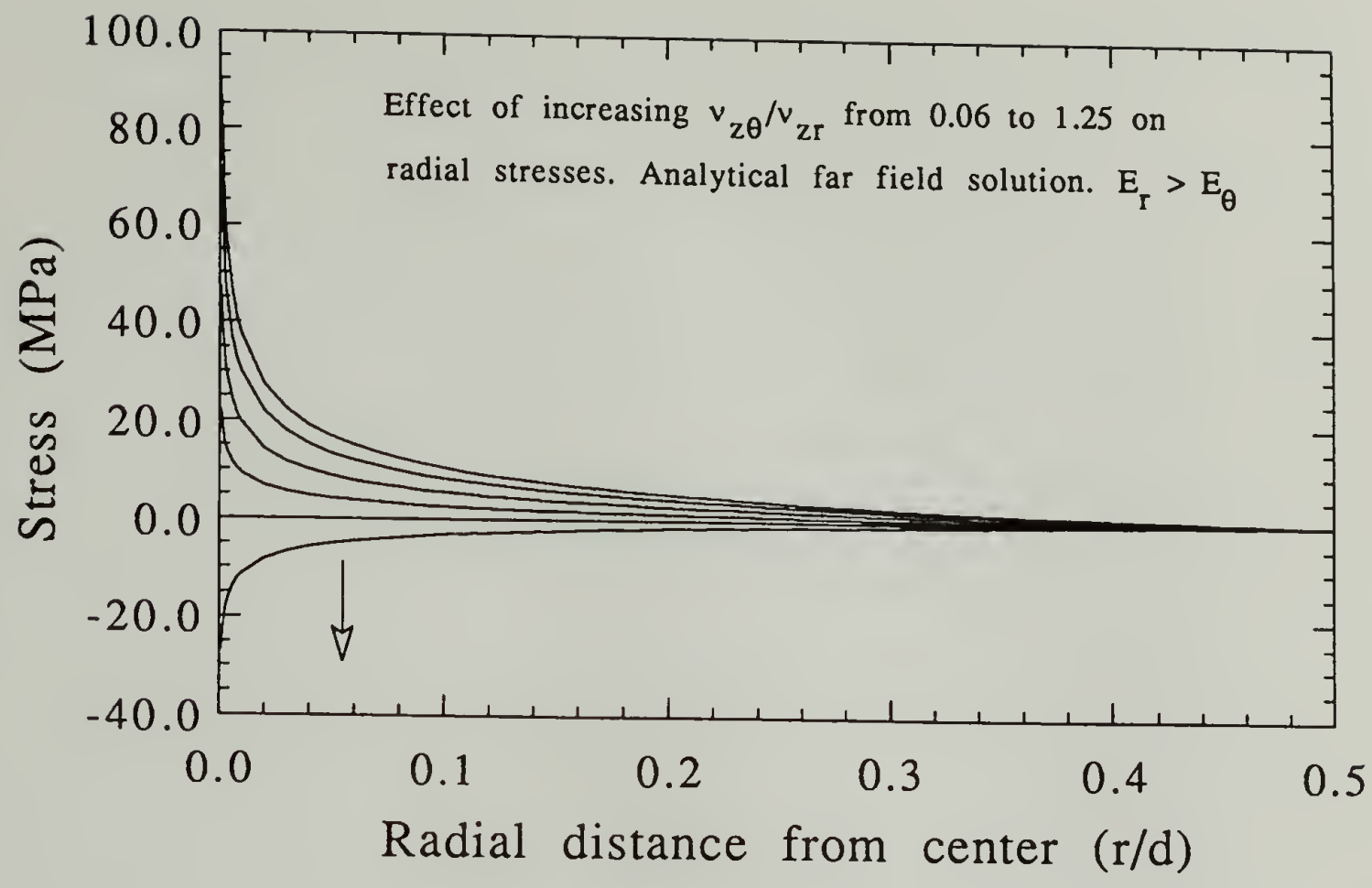

Figure 2.18. Effect of increasing $\nu_{z\theta}/\nu_{zr}$ from 0.06 to 1.25 on the radial stress distribution of radially anisotropic fibers. PDA case.

positive. Naturally, when there is no difference between the radial and hoop directions the condition of transverse isotropy is met and no radial dependency of any stress distribution is observed in the far-field.

Figure 2.19, describes the effect of the Poisson's ratio reversal on hoop stress distribution. A crossover point appears at an r/d of about 0.15. The crossover point marks the place at which the hoop stress changes sign. A radial shift of this point towards the fiber's boundary would occur if the ratio of the radial modulus to the hoop modulus was increased.

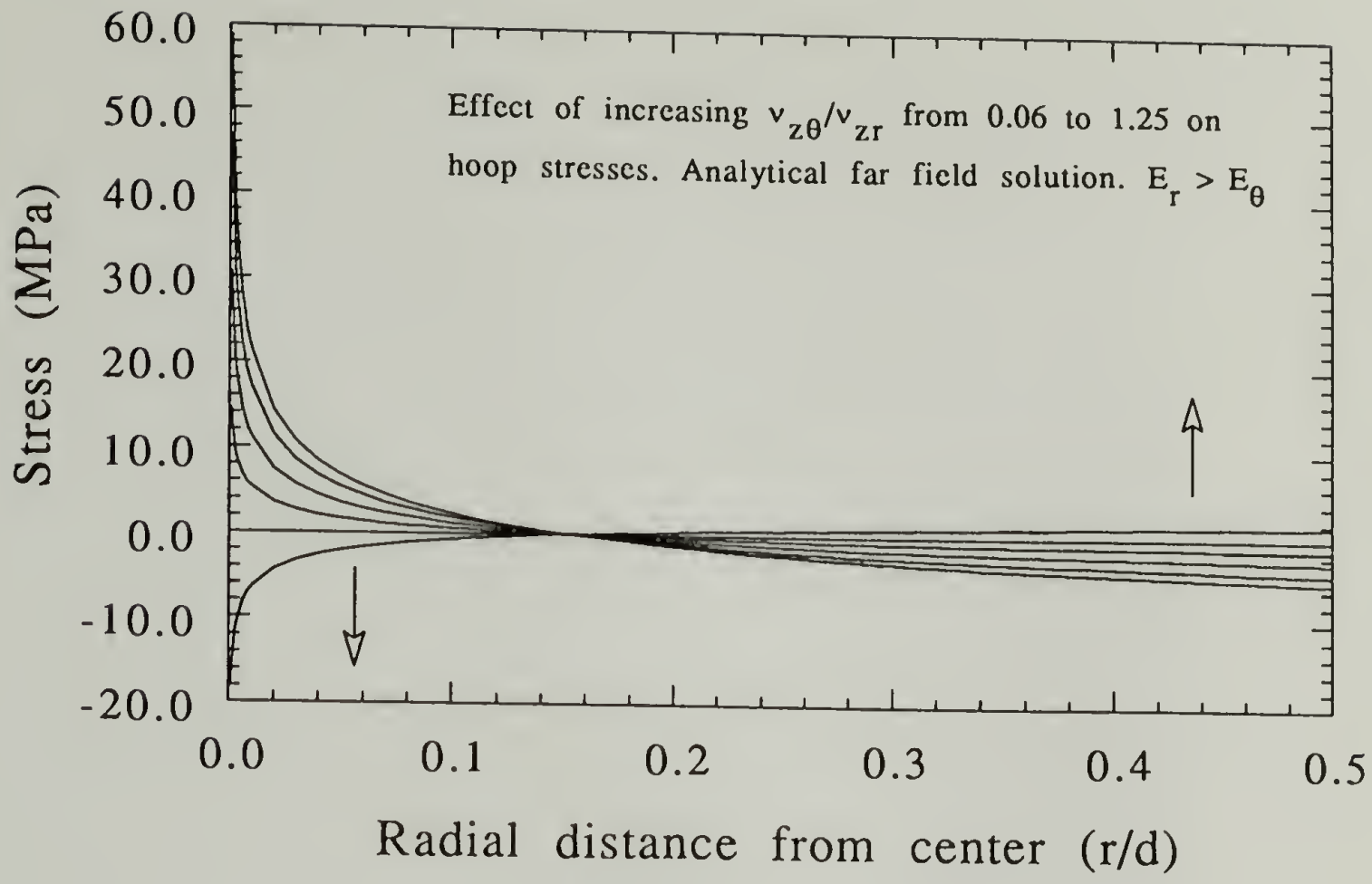

Figure 2.19. Effect of increasing $\nu_{z\theta}/\nu_{zr}$ from 0.06 to 1.25 on the hoop stress distribution of radially anisotropic fibers. PDA case.

A similar trend is observed from Figure 2.20 where the axial stress distribution is shown as a function of radial distance from the center of the fiber. A value of ~434 MPa can be computed using equation 2.32 for a transversely isotropic material, this corresponds to the straight line shown in this plot. All other curves correspond to deviations from equal Poisson's ratios in the radial and hoop directions.

The magnitude of the radial stress near the center of the fiber is noticeably decreased if the modulus in the hoop direction is greater than that in the radial direction. This result is shown in Figure 2.21. Implied by resulting equilibrium equations, equation 2.21, is the increased relief in radial tension caused by the appearance of a positive hoop

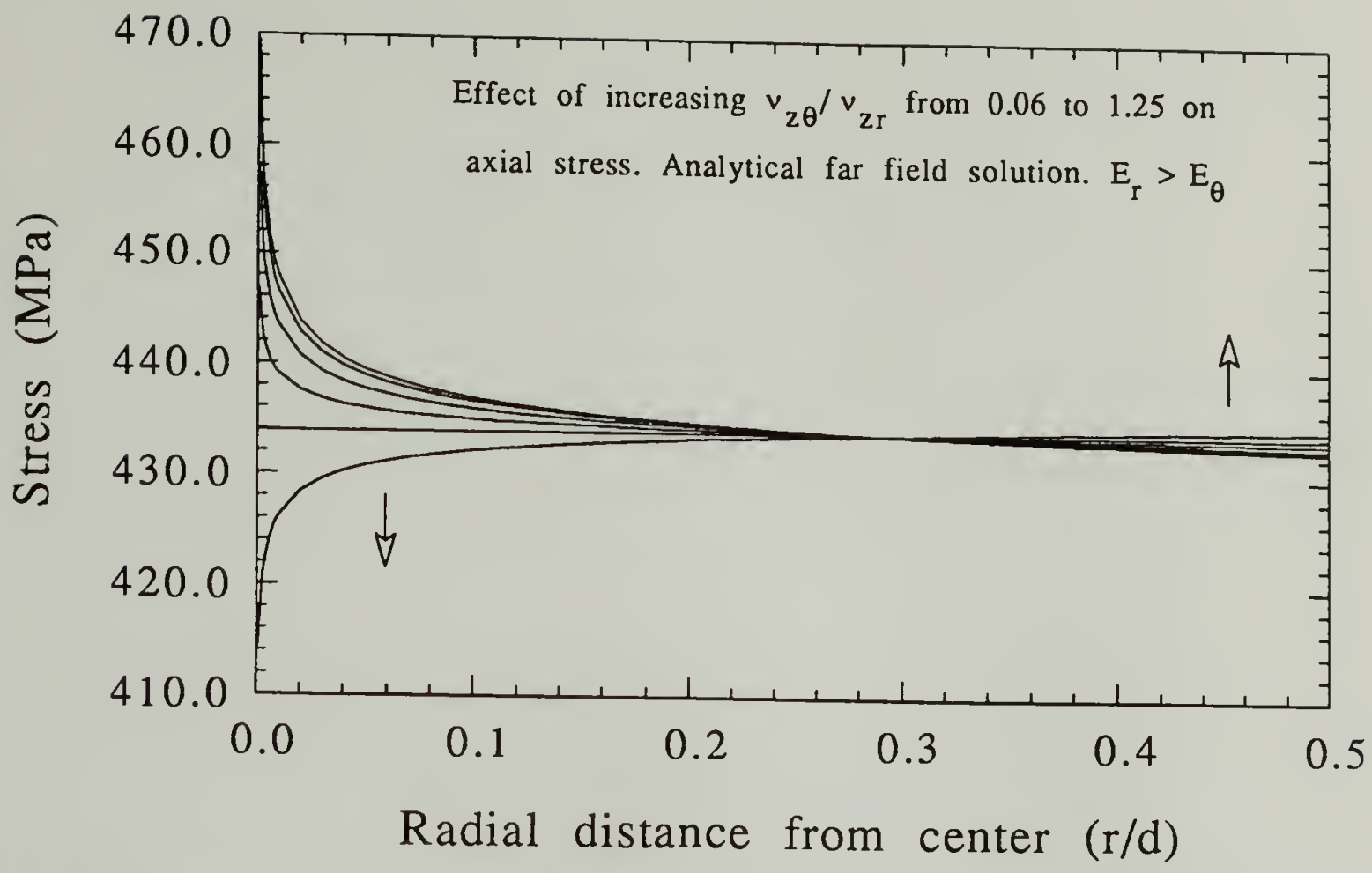

Figure 2.20. Effect of increasing $\nu_{z\theta}/\nu_{zr}$ from 0.06 to 1.25 on the axial stress distribution of radially anisotropic fibers. PDA case.

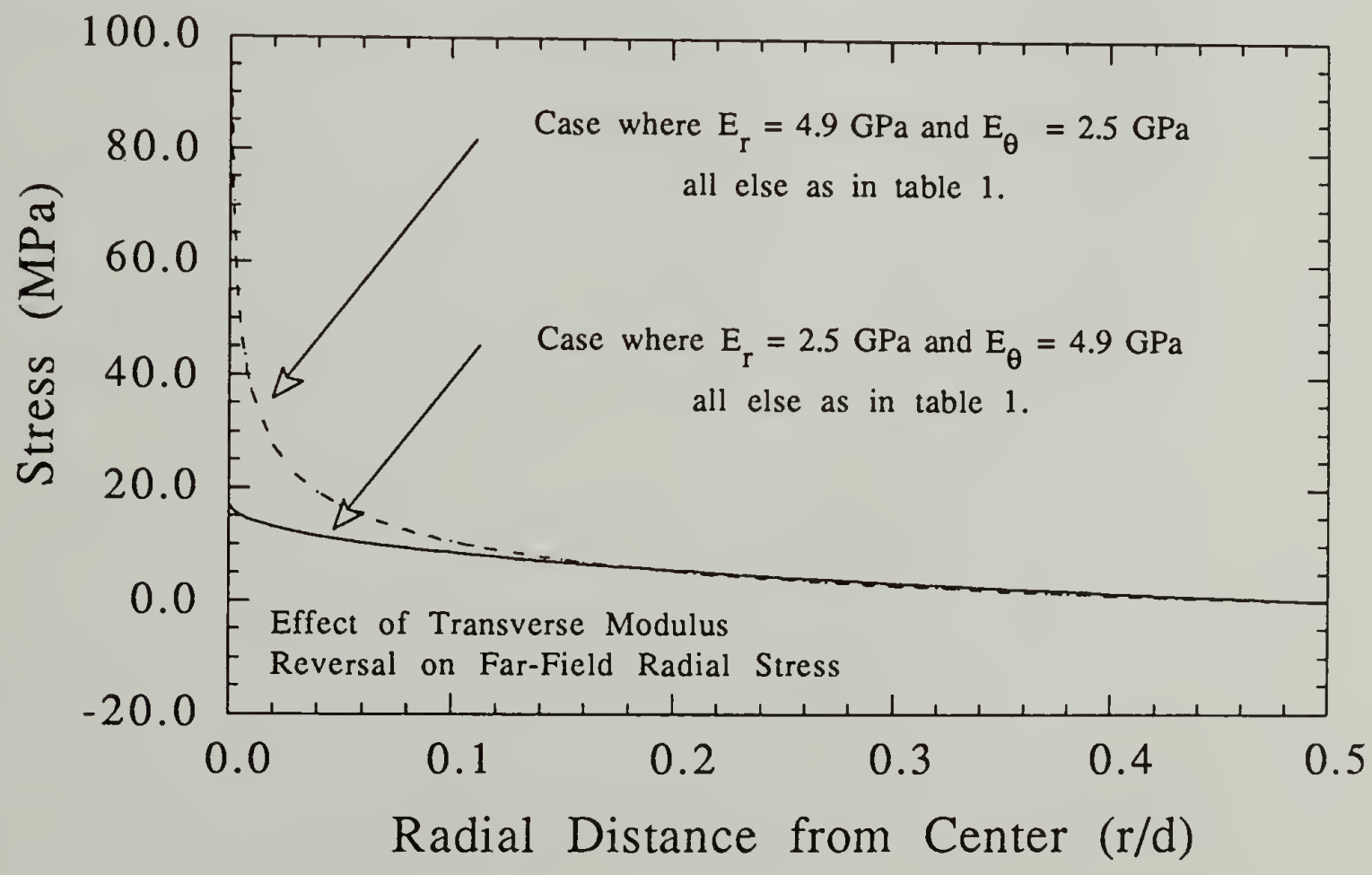

Figure 2.21. Effect of elastic modulus reversal on far-field radial stress. PDA-matrix case.

stress at a shorter distance from the fiber's outer surface. Figure 2.22 shows this earlier onset of a positive hoop stress in the fiber.

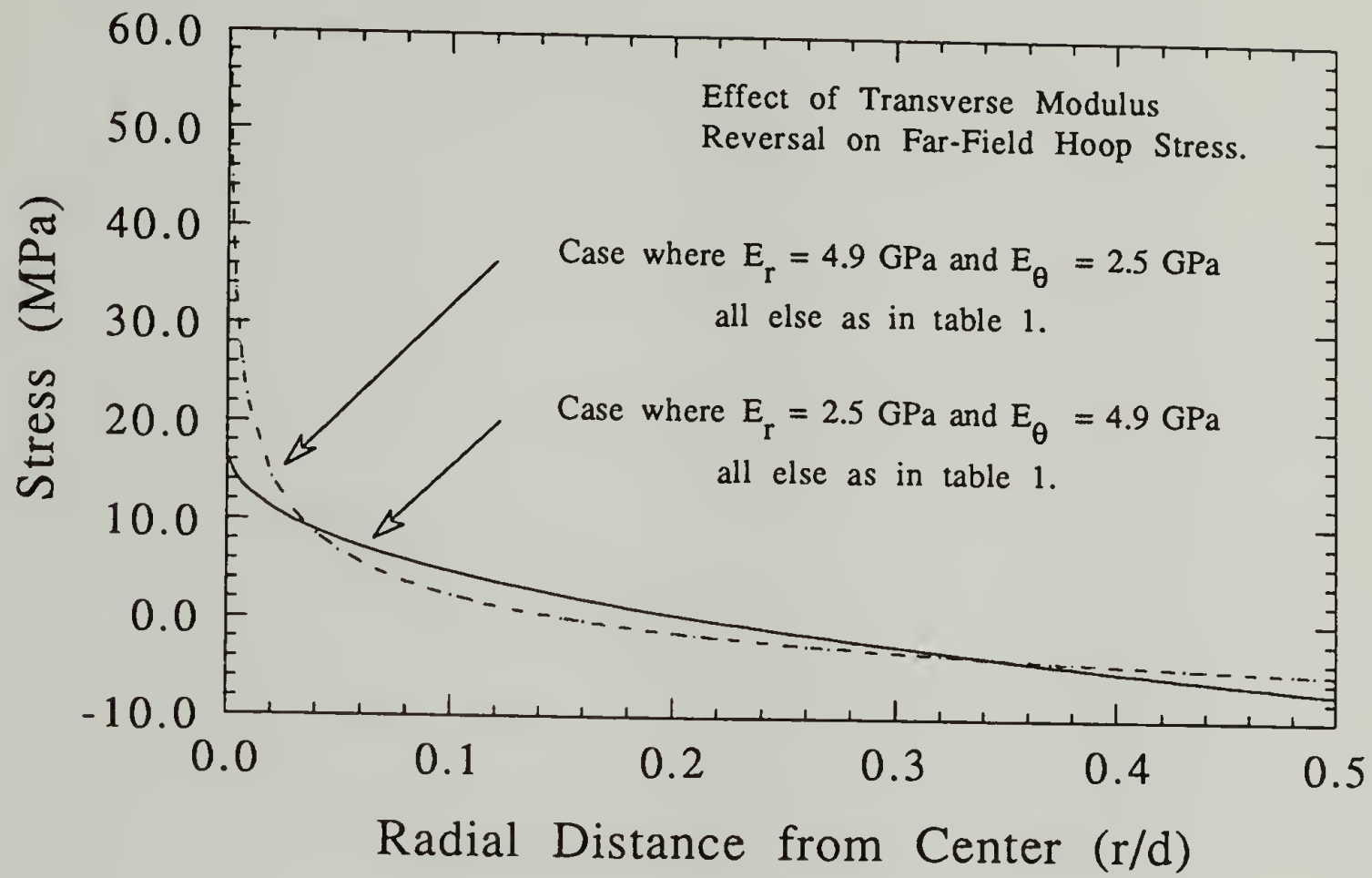

Figure 2.22. Effect of elastic modulus reversal on far-field hoop stress. PDA-matrix case.

Large incremental changes in transverse direction stresses are realized if the magnitude of the axial modulus of the fiber is changed. The effect of decreasing the magnitude of the axial modulus from 45 GPa to 4.9 GPa, $E_z = E_r$, is shown in Figure 2.23. A great increase in radial tension is observed due to this decrease.

This effect can be also explained in terms of the corresponding equilibrium equation. Assuming that the contribution of $\partial\tau_{rz}/\partial z$ is negligible in equation 2.21, the shear stress should be zero away from the edges anyway, and upon substitution of

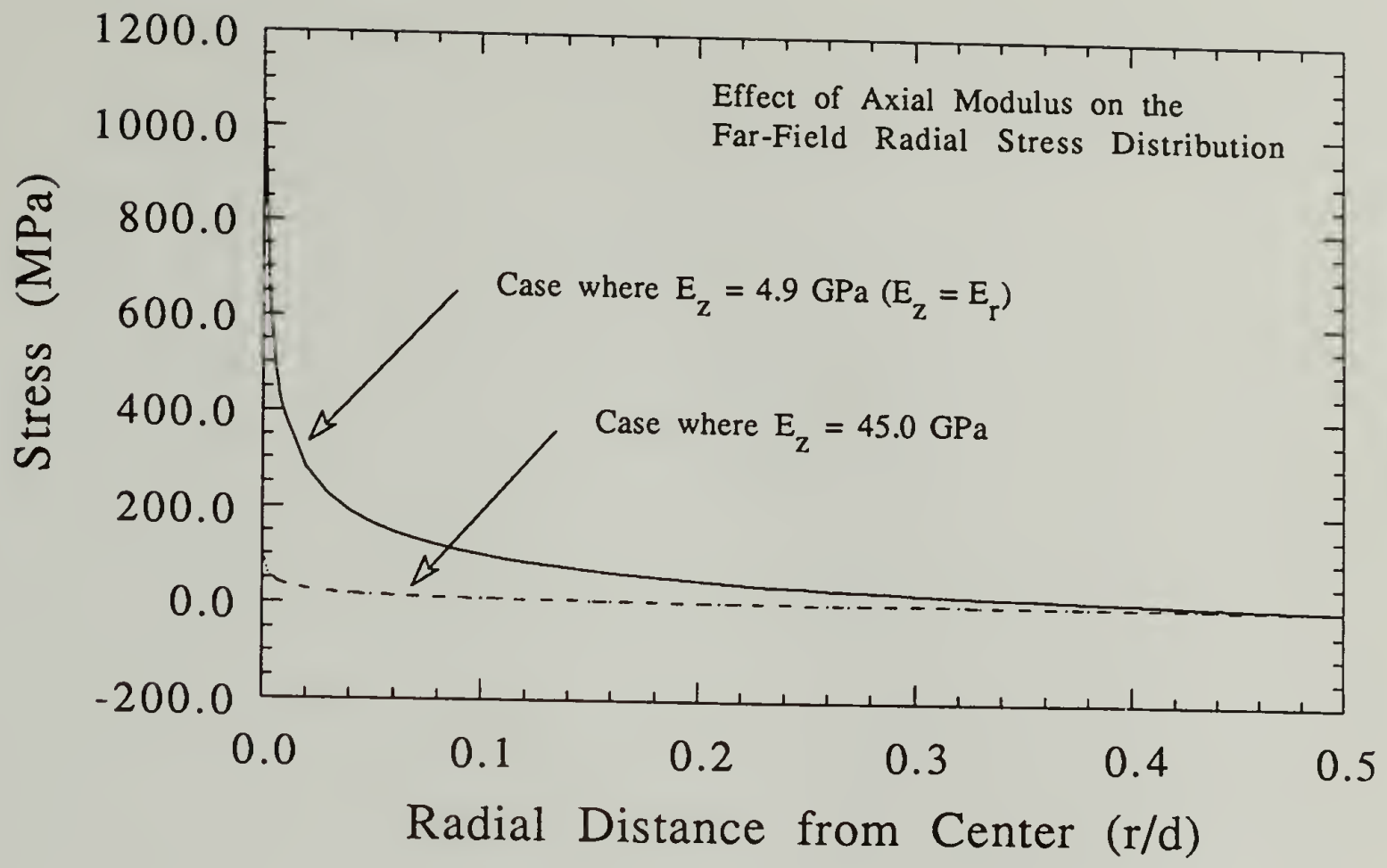

Figure 2.23. Effect of axial modulus increase on the far-field radial stress distribution. PDA-matrix case.

Hooke's law it becomes equation 2.34. From this equation, it can be noted that the third term is dominant when the axial modulus is small.

$$r\frac{\partial\sigma_r}{\partial r} = \sigma_\theta\left(1+\frac{E_r}{E_\theta}\nu_{\theta r}\right)-\sigma_r\left(1+\frac{E_\theta}{E_r}\nu_{r\theta}\right)+\frac{\sigma_z}{E_z}(E_r\nu_{zr}-E_\theta\nu_{z\theta}) \qquad (2.34)$$

The analytical solutions were also tested using data from reference 11 for a circumferentially anisotropic carbon fiber. As it can be observed from Figure 2.24, the consequences of deforming a composite with such fibers may not be as catastrophic as those with radially orthotropic counterparts.

The radial stress decreases from a finite value at the center to zero at the periphery in the absence of interfacial pressure. The hoop stress goes from tensile to compressive

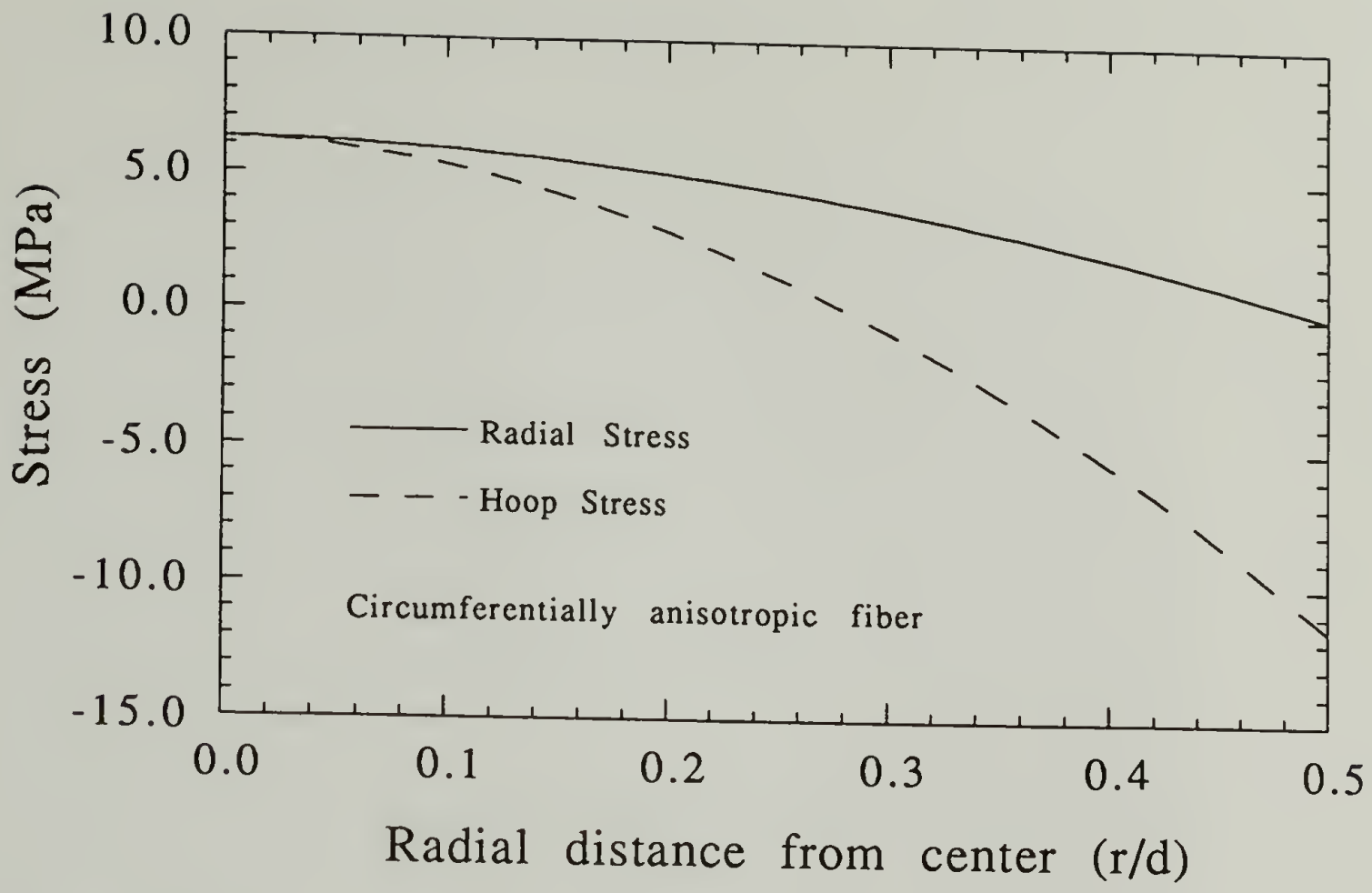

Figure 2.24. Radial and hoop stress distributions in a cylindrically orthotropic fiber.

at larger radii but no singular tendencies are observed neither at the boundary or at the center of the fiber.

The transverse stresses are equal at the fiber's center since it is yet a variation of an orthorhombic fiber in an axisymmetrical geometry with an isotropic core. Overall, a radially anisotropic fiber would be more likely to fail catastrophically. It should therefore be analyzed more carefully, than its circumferentially orthotropic counterpart.

Other analytical solutions for orthotropic bodies can be found in literature.[10] Some of these furnish analytical solutions for the description of the effect of fiber anisotropy on thermal stress development in fibrous composites. These solutions showed singular stress tendencies in radially orthotropic fibers. None was observed for circumferentially or transversely isotropic fibers. It was also observed by the same study

that fiber volume fraction only affects axial stresses and not hoop or radial stresses in either radial or circumferentially anisotropic fibers.

As mentioned in the previous paragraph, there is no distinction between the radial or hoop directions at the fiber axis and one can say that isotropy exists at this infinitesimal region. The singular nature of the stress distribution of radially orthotropic fibers when r=0 could not be removed by the introduction of a hole at the fiber axis.[10] The trend in stress distribution is not altered significantly by these modifications. In any case of radial orthotropy however, caution is to be exercised when examination of the stress distribution very near the fiber axis is required.

Experimental and theoretical knowledge of orthotropic rods has been developed to a great extent by wood scientists. Similar stress distributions as those provided here for the radially anisotropic PDA case have been reported for wood.[35] Complete sets of elastic constants for several wood species are provided in appendix A of this latter reference. Experimental verification of residual transverse stress distributions in trees and heat treated metal cylinders commonly involve the extraction of layers and subsequent conditioning to ensure that any other stresses introduced by this process are removed.[36] Despite the fact that these idealized situations may not account for fiber or morphology imperfections it is hoped that the work presented above has helped to elucidate on the behavior of strained cylindrically orthotropic materials. End imperfections such as those which would occur when trimming Kevlar to size are examples of these macroscopic flaws. It is also hoped that experimental non-destructive techniques, such as confocal Raman scattering, can provide direct confirmation of the strain distribution along the radial direction of these fibers.

2.5 Conclusions

Despite the aforementioned limitations, the elastic constants obtained by molecular simulation can provide a unique insight into the stress analysis of orthotropic materials. The assumption of complete fiber isotropy can yield very erroneous and misleading results for many of the known fiber morphologies. Shear stress distributions are slow varying functions at the fiber ends of highly anisotropic fibers.

Transverse stresses developed at fiber ends of radially orthotropic fibers embedded in model composites under tension are important design considerations. Transverse stresses observed at 1% strain are of the same order of magnitude as the maximum transverse strengths observed experimentally in radially orthotropic fibers. Axial, radial and hoop stress distributions in the far field can be tensile or compressive depending on the loading mode or the magnitude of the difference between the Poisson's ratio in the radial and hoop directions. A radial dependency of normal stresses becomes singular in nature as the fiber's center is approached. This was observed for different radially orthotropic materials. The fiber is isotropic in the limit of r=0, as is confirmed by the tendency of the finite element and analytical solution radial and hoop stress plots to converge at this point.

The analytical solutions for a single anisotropic fiber of Lekhnitskii provide a good approximation for the stress analysis in the far-field of single fiber model composites. It compared favorably with finite element analysis results. This analytical approximation is valid only for the case where Poisson's ratios in the fiber and matrix have a similar value.

2.6 References

(1) Maden, M. A.; Farris, R.J., *4th Int. Tech. Conf. on Polyimides. Sess. IV: Mechanical Aspects*; Ellenville, N.Y., **1991**, 1.

(2) Yang, X.; Hsu, S.L. *Macromol.* **1991**, *24*, 6680.

(3) Allen, S.R.; Farris, R.J. *Mat. Res. Soc. Symp.* **1989**, 34.

(4) Fan, F.C.; Hsu, S.L. *J. of Polym. Sci. Part B: Polym. Phys.* **1992**, *30*, 603.

(5) Fan, F.C.; Hsu, S.L. *J. of Polym. Sci. Part B: Polym. Phys.* **1992**, *30*, 619.

(6) Timoshenko, S.; Goodier, J.N., *Theory of Elasticity*; McGraw-Hill Book Co.: New York., 343, 1951.

(7) Burnett, D.S., *Finite Element Analysis: From Concepts to Applications*; Addisson-Wesley Publishing Co.:N.Y., 766, 1987.

(8) Rutledge, G.C.; Suter, G.C. *Polymer* **1991**, *32* , 2179.

(9) Leyrer, R.J.; Wegner, G.; Wettling, W. *Ber. Bunsenges. Phys. Chem.* **1978**, 82, 697.

(10) Lekhnitskii, S.G. *Theory of Elasticity of an Anisotropic Body*; MIR Publishers: Moscow, 70, 1981.

(11) Avery, W.B.; Herakovich, C.T. *J. of Appl. Mech.* **1986**, *53*, 751.

(12) Whitney, J.M.; Drzal, L.T.; *Axisymmetric Stress Distribution Around an Isolated Fiber Fragment. Toughened Composites, ASTM STP 937*, Norman J. Johnston, Ed., Am. Soc. for Test. and Mat., Philadelphia, 179, 1987.

(13) Allen, S.R.; Farris, R.J. *Polym.* **1990**, *31*, 1467.

(14) Knott, T. W.; Herakovich, C.T. *J. of Compos. Mater.* **1991**, *25*, 732.

(15) McGarry, F.J.; Moalli, J.E. *Polym.* **1991**, *32*, 1811.

(16) Nairn, J. A. *A Variational Mechanics Analysis of the Stresses Around Breaks in Embedded Fibers*. Submitted *Mech. of Mater.*

(17) Hsueh, C.H.; Becher, P.F. *J. of Mat. Sci. Lett.*, **1991**, *10*, 1165.

(18) Netravali, A.N.; Sachse, W. *Polym. Comp.* **1991**,*12*, 370.

(19) Fan, C.F.; Hsu, S.L. *J. Pol. Sci., Part B: Polym. Phys.* **1989**, *27*, 337.

(20) Fan, C.; Hsu, S.L., *Macromol.* **1989**, *22*, 1474.

(21) Galiotis, C.; Young, R.J.; Yeung, P.H.J.; Batchelder, D.N. *J. Mat. Sci.* **1984**, *19*, 3640.

(22) Robinson, I.M.; Young, R.J.; Galiotis, C.; Batchelder, D.N. *J. of Mat. Sci.* **1987**, *22*, 3642.

(23) Robinson, I.M.; Galiotis, C.;Batchelder, D.N.; Young, R.J. *J. of Mat. Sci.* **1991**, *26*, 2293.

(24) Young, R.J.; Day, R.J.; Zakikhani, M. *Mat. Res. Soc. Sym. Proc.* **1989**, *34*, 351.

(25) Jahankhani, H.; Galiotis, C. *J. of Comp.Mat.* **1991**, *25*, 609.

(26) Boogh, L.C.N.; Meier, R.J.; Kausch, H.H.; Kip, B.J. *J. Polym. Sci., Part B: Phys.* **1992**, *30*, 325.

(27) Moonen, J.A.H.M.; Roovers, W.A.C.; Meier, R.J. Kip, B.J. *J. Polym. Sci., Part B: Phys.* **1992**, *30*, 361

(28) Van Eijk, M.C.P.; Leblans, P.J.R.; Meier, R.J.; Kip, B.J. *J. Mat. Sci. Lett.* **1990**, *9*, 1263

(29) Cox, H.L. *British J. of Appl. Phys.* **1952**, *3*, 72.

(30) Rao, V.; Drzal, L.T. *Polym.Comp.* **1991**, *12*, 48.

(31) Tissington, B.; Pollard, G.; Ward, I. M. *J. of Mat. Sci.* **1991**, *26*, 82.

(32) Farris, R.J. Personnal Communication. Jan/1991.

(33) Dupont, Data Manual for Kevlar® 49 Aramid", E.I. Dupont de Nemours Co., 1986.

(34) Lekhnitskii, S.G. *Theory of Elasticity of an Anisotropic Elastic Body*; Holden-Day, Inc.: San Francisco., 1963.

(35) Archer, R.R., *Growth Stresses and Strains in Trees*; Springer Series in Wood Science. Springer-Verlag: N.Y., 73 and 209, 1986.

(36) Noyan, I.C.; and Cohen, J.B. *Residual Stress: Measurement by Diffraction and Interpretation;*. Springer-Verlag: N.Y., 218, 1987.

CHAPTER 3

PLANAR GEOMETRIES

3.1 What Produces Molecular Anisotropy in Polymeric Coatings?

Previous work has shown that chains in polymeric materials are preferentially aligned in a direction parallel to the plane of the substrate in a solvent-casting process.[1] Segmental alignment by solvent evaporation is originated by the combined effect of film shrinkage parallel to the substrate and gel-collapse in the direction perpendicular to the substrate. Furthermore, any type of ring moeities will tend to align in favor of solvent transport. In polymers where the optically anisotropic group is part of the backbone, a positive birefringence occurs in the plane of the film. Examples are solvent cast films of bisphenol-A-polycarbonate.[2] Conversely, a negative birefringence results in the case of polystyrene, where the anisotropic styrene ring is perpendicular to the chain direction and substrate plane.

Birefringence is only one way of providing information on chain conformations that are frozen-in during the solvent casting process. There are other methods to obtain more details on molecular anisotropy. Some of these techniques will be described in subsequent chapters.

3.2 Influence of Processing Conditions on The Anisotropic Development of PMDA-ODA Polyimides

In-plane molecular alignment of polymeric backbones is influenced by manufacturing processes. For example, birefringence in PMDA-ODA polyimides has been found to vary with processing conditions.[3] In-plane orientation of chains in films during cure is influenced by heating rate and final curing temperature. Other processing conditions that influence spin coating of these materials are spin speed and solvent evaporation method. Spin speed influences attained orientation indirectly by varying the thickness of the coating. Birefringence measurements on films ranging from 2-17 μm indicated that thinner polyimide coatings had a higher degree of in-plane orientation.[4,5] The decrease in birefringence, $\Delta n \sim 0.015$ in a 15 μm range, was attributed to a decrease in in-plane orientation. However, the possibility that a higher density layer at the air/polymer interface had a significant influence in the magnitude of the birefringence obtained for various film thicknesses was considered. It is not clear that this is the same type of process observed for very thin films where orientation changes are marked.

PMDA-ODA polyimide is made from its polyamic acid precursor. This precursor is provided by its manufacturers, E.I. Dupont de Nemours as a 10-20% solution in N-methyl-2-pyrrolidone. In the absence of a thermal gradient or chemical reaction, chain relaxation competes with film shrinkage by solvent loss. Relaxation times are increasingly longer as the solvent evaporation proceeds due to an increase number of entanglements and an overall reduction in chain mobility. This mobility reduction results in a lack of response of the molecule or inability to re-accommodate localized stresses thereby having in-plane orientation as the net result. In the case of PMDA-ODA, imidization by heating takes place during processing. The enhanced mobility of the

polymer chains obtained by rapid heating keeps the polymer ahead of its glass transition. A faster onset of film collapse due to a more rapid solvent evaporation leads to an earlier conformation freeze. Imidization is less likely to be complete at earlier onsets of this glassy phase.

The initial solvent evaporation has a great influence on the process. Most curing cycles allow ≈ 15-20 minutes at 85 °C for a 1-2 micron coating. Subsequent curing at 250-300 °C for an hour usually provides adequate cures. It is now known that faster curing rates after the initial solvent evaporation stage lead to increased crystalline ordering at the expense of less orientational order.[6] A more refined structure with rapid heating has also been documented with pre-stretched samples of this polymer.[7]

Anisotropy in coatings can be induced uniaxially by "doctor blading" the polymeric material onto the substrate and also by subsequently stretching the film at a point during or after its curing cycle. If the anisotropy was to be induced by doctor blading, the rate of heating during cure should be as slow as possible to preserve the orientation attained. Rapid heating can be utilized to increase the degree of order in the sample but the attained orientation would be lost due to the increased chain mobility. This would create a difference in film behavior between in-plane and out-of plane directions in a coating since the polyimide chains arrange themselves so that their axes are mostly parallel to the in-plane direction of the coating. If the anisotropy was to be induced by straining the film, then the stretched (thicker) film can be adhered to the substrate by means of a very thin layer of polyimide whose presence may be rendered negligible.

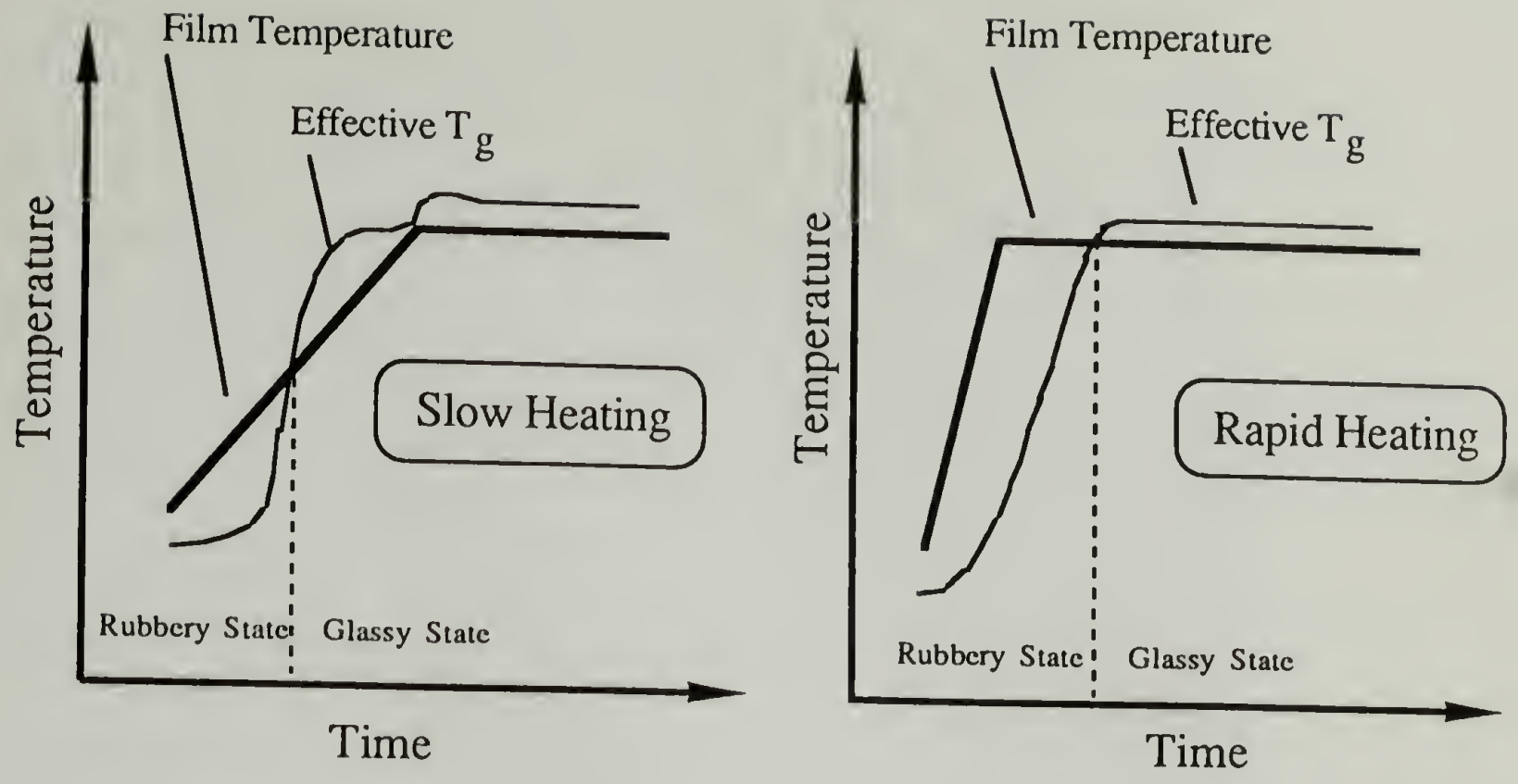

Figure 3.1 Effect of heating rate on effective glass transition temperature. Adapted from reference 8.

As mentioned above, anisotropy is also induced by the spin coating process. Anisotropy is amenable to useful comparisons with finite element calculations because axisymmetric simplifications can be employed for the analysis. Out of plane displacements could be calculated directly without using a three-dimensional structure or a subsequent calculation of the out -of-plane displacement based on data obtained for a plane stress situation. Anisotropy can be measured as a function of spin rate, spin time, heat treatment, or thickness. Larger mismatches in the thermal expansion coefficient between the coating and its substrates may also lead to higher out-of-plane displacements. The effect of polyimide shrinkage on residual stress development has been analyzed.[9] In general, the development of orientation in thin constrained polymeric films has already been considered.[10,11]

3.3 References

(1) Prest, Jr, W.M.; Luca, D.J. *J. of Appl. Phys.* **1980**, *51*, 5170.

(2) Prest, Jr., W.M.; Luca, D.J. *J. Appl. Phys.* **1979**, *50*, 6067.

(3) Coburn, J.C.; Pottiger, M.T., *Fourth Int. Tech. Conf. on Polyimides. Session VI. Applications,* **1991**, 3.

(4) Coburn, J.C.; Pottiger, M.T.; Noe, S.C.; Senturia, S.D., *Stress in Polyimide Coatings*, submitted to *J. Polym. Sci. B: Polym. Phys.*, 1994.

(5) Noe, S.C., PhD Dissertation. Dept. of Mat. Sci. Eng. Massachusetts Institute of Technology. Cambridge, Mass., 1992.

(6) Molis, S.E.; Saraf, R.; Hodgson, R.T.*Antec* **1991**, 1700.

(7) Strunnikov, A. Yu.; Mikhailova, N.V.; Sidorovich, A.V. *Polym. Sci. USSR* **1990**, *32*, 1.

(8) Coburn, J.C.; Pottiger, M.T., in *Advances in Polyimide Science and Technology*; Feger, C.; Kohjasteh, M.M.; Htoo, M.S., ed., Technomic Pub. Co. Inc.: Lancaster, 360, 1991.

(9) Jennings, R., PhD Dissertation. Dept. of Polym. Sci. and Eng. The University of Massachusetts at Amherst., 53, 1993.

(10) Collier, J.R., *Polymer Orientation Induced by Solvent Removal. J. of MRL at the Pennsylvania State University.* University Park, PA. ,1981.

(11) Jungnickel, B.J. *Polym. Eng.and Sci.* **1987**, *27*, 1021.

CHAPTER 4

CHARACTERIZATION OF CRYSTALLINE ORDER IN PMDA-ODA POLYIMIDES

4.1 Introduction

The principal objective of this chapter is to characterize the crystalline order in variously prepared PMDA-ODA polyimide powders, pyromellitic dianhydride-di-(4-aminophenyl)ether, and to expand on previous works involving characterization of films and fibers. It also serves as background preparation for the orientation and stress transfer analysis that is presented in subsequent chapters. As explained in earlier chapters, polyimide materials are principally employed in electrical and electronic industries in the form of liquid precursors or imidized films. They possess good dielectric properties and are stable, chemically and dimensionally, at high temperatures. Various processing parameters may introduce differences in microstructures, e.g. chain conformation, as well as macrostructures, e.g. segmental orientation.

The observation of the effect of different crystalline contents in polyimide films is of utmost importance, faster processing cycles for these materials may shorten their solvent evaporation stage. A fast rate cure after the initial solvent evaporation stage leads to increased crystalline ordering and less orientational order.[1,2] Higher crystalline order attained with rapid heating is accompanied by a reduction in the degree of in-plane orientation in PMDA-ODA polyimide films. A change in the degree of ordering of these films also implies that their moduli and thermal expansion coefficients will be different,

resulting in a different state of stress for the system.[3] The structures of these polyimides can only be slightly altered by thermal annealing.

The exact determination of the polyimide structure is difficult to obtain. Because of the difficulty in preparing highly ordered samples the crystalline structure of PMDA-ODA polyimide, including chain conformation and intermolecular packing, has not been established clearly. Most structural studies on PMDA-ODA polyimide have referred to the work of Kazaryan et al.,[4] who obtained the x-ray diffraction pattern with most reflections published to date. That effort revealed a possible orthorhombic unit cell with a 16 Å repeat along the chain direction. A 2_1 helix conformation was assumed due to the systematic absence of odd *00l* reflections. The rectangular equatorial lattice, with one chain per unit cell, has the following dimensions: a = 6.31 Å and b = 3.97 Å, and c = 32 Å. In addition, a diffuse reflection with d = 4.7-4.9 Å was attributed to ordering in amorphous regions. Their model does not provide twist angles between the aromatic units but it acknowledges a valence angle at the ether oxygen. Subsequently, X-ray diffraction and theoretical conformational analysis of PMDA-ODA monomers have shown the possibility of a quite different monoclinic unit cell.[5] The unit cell parameters they obtained were: a = 5.9 Å, b = 4.6 Å, c = 32.9 Å with $\gamma = 100°$. Their interplanar spacing, as obtained by X-ray diffraction were difficult to extract. Other studies on PMDA-ODA polyimide have adopted an orthorhombic unit cell as a basis for further structural analysis.[6,7] The exact structure of PMDA-ODA polyimide has yet to be determined.

Various processing procedures may introduce very different degrees of crystallinity, crystallite size, as well as segmental anisotropy in films. The usual starting material is a 10-20% solution in N-methyl 2-pyrrolidone. Recently, by extending the time that the solvent is in contact with the polyamic acid precursor during curing, highly crystalline polyimide powder has been obtained.[8] Conversely, by removing solvent

before full imidization has taken place, the films or fibers produced result in materials of lower degree of crystallinity. Because of the present availability of highly crystalline polymers, a new analysis of the structure of this polyimide seems to be promising.

Spectroscopic data discussed below, targets the study of conformational distributions in these materials. Conformational changes and probably the first set of complete tentative assignments for IR and Raman bands in model polyimide compounds was provided in the work of Ishida.[9] No complete normal coordinate analysis on this molecule has been performed to date. The study suggested that crystalline order increases the phenyl ether conjugation and structure coplanarity. In the work presented here, contributions from ordered and disordered phases are well defined for a specific vibration. These spectral changes allowed for the study of details characteristic of conformations belonging to crystalline regions. Two factors, one, the hybridization of the nitrogen atom, and two, the hybridization of the ether oxygen between the two phenyl rings, seemed to notably influence the chain conformation of PMDA-ODA polyimide. The participation of nitrogen in a conjugated structure leads to a planar pyrromellitimide unit and at the same time yielded a unit cell with smaller interplanar distance and a shorter projected chain repeat. A better understanding of these conformations and other structural features of PMDA-ODA polyimide was provided with molecular simulation.

The usefulness of molecular simulation techniques in the analysis of crystalline and amorphous polymers have been demonstrated extensively.[10-12] X-ray diffraction is perhaps the most definitive technique in assigning atomic placements within individual unit cells. With recent advances in simulation software, it is also possible to generate diffraction patterns from simulated crystalline structures.[14,15] Comparison between calculated and experimental patterns should reveal structural differences of various crystalline and amorphous sequences of this model polyimide. In this current study we have used vibrational spectroscopy, both infrared and Raman, and X-ray diffraction, in

conjunction with molecular simulation techniques to analyze the structure of unusually highly crystalline PMDA-ODA powders and to expand on previous investigations involving characterization of the films and fibers of this model polyimide.

4.2 Experimental

4.2.1 Sample Preparation

The starting material was provided by DuPont E.I. deNemours in the form of a polyamic acid precursor in a 20% solution with N-methyl-2-pyrrolidone. The polyamic acid precursor was employed to make the films and powders utilized for the spectroscopic methods. The polyamic solution was diluted to 15% with dimethylacetamide and then spin coated on a glass substrate at 2000 rpm for one minute. For thermal curing, these non-imidized samples were placed on a hot plate at 85°C for 15 minutes and then cured under vacuum at 225°C for one hour. Alternatively and as indicated below, some of the films utilized in the Raman spectroscopic experiments were chemically cured using an anhydride-amine system. PMDA-ODA powder has been prepared as described earlier, by the method of Jennings.[8] Using that preparation method, the polyamic acid was cured under a nitrogen blanket at 200 psi and 225°C in the presence of a water scavenger. The intention was to increase the amount of time that the solvent remained in contact with the polymer during curing. These powders allowed for probing an isotropic state of this polyimide and the characterization of a high level of crystalline order. All PMDA-ODA polyimide film or powder samples examined with the wide-angle X-ray photographic method were annealed for one hour at 300 °C, since their previous processing did not

include any temperatures above 225 °C. No annealing was performed on the powder samples utilized for the diffractometer scans.

4.2.2 X-ray Diffraction

Transmission X-ray experiments using the photographic technique were done in a vacuum with a Statton camera at the 50 mm position. Ni filtered CuKα radiation was employed with a 40 kv and 35 mA setting and a take-off angle of 6°. Distance calibration was done by using Calcite (d = 3.035 Å) for every exposure. The films were then scanned via microdensitometer. The diffractometer scans were done on a Siemens type F diffractometer set at 45 kv and 18 mA with a Cu target X-ray tube and a NiKβ filter. The instrument was equipped with a 1° divergence slit and a 0.4 mm receiving slit. The diffractometer scans were done at a step size of 0.05°; typical exposure times for the powder patterns were 2 hours.

The degree of crystallinity, x_c, in the powder was estimated from a diffractometer scan (see Appendix A). The crystalline component , $I_c(s)$ was simply separated from the total scatter, I(s), by drawing a smooth curve under the sharp peaks and taking the crystalline component to be the scatter above this curve; x_c was then calculated to a first approximation by:

$$x_c = \frac{\int_{s_1}^{s_2} s^2 I_c(s)\, ds}{\int_{s_1}^{s_2} s^2 I(s)\, ds} \qquad (4.1)$$

where s_1 and s_2 are the lower and upper limits of the integration respectively. Values of s_2 and s_1 corresponding to scattering angles (2θ) of 38° to 3° were used. Such an analysis gave a value of x_c of 61.4 %. The predicted value of crystal density of this predicted cell is 1.49 g/cm^3, which is slightly higher than the experimentally determined values for the partially crystalline powder and film of 1.46 and 1.42 g/cm^3 respectively.[8]

The crystallite size was estimated using the Scherrer equation on the diffractometer scan peaks corresponding to (002), (101) and (010). Crystallite dimensions were also estimated from simulation, where the intensities were carefully matched with the experimental data. Since the simulation is an absolute zero measurement, an anisotropic temperature factor of 0.3 in the b-dimension was utilized to decrease the intensity of higher angle reflections by about 10-15% and provide a better match with experimental intensities.

4.2.3 Spectroscopy

All infrared spectra was taken in a Bruker 98v FT-IR equipped with a globar source and an MCT detector. The resolution was maintained at 4 cm^{-1} unless otherwise indicated in the figures. Usually 128 scans were obtained with sufficient signal/noise ratio for analysis. A CTI-Cryogenics Cold Head Model 22 equipped with a model SC compressor unit were utilized to perform measurements below room temperature. A digital cryogenic thermometer/controller, model 4025, from RMC-Cryosystems was used. Also included with these items were: two different silicon sensors and three different heating systems to independently monitor and control below and above room temperature with an accuracy of ± 0.5 K in the range from 8-20 K and ± 1.0 K in the

range of 20-400 K. The first measurement was taken at 10 K after the sample had been at that temperature for 8 hours. All successive measurements were taken at 20 K intervals every hour after temperature stabilization. A high vacuum of $1x10^{-6}$ torrs was created in the sample chamber before cool-down. An Alcatel ZM2012A rotary vacuum pump was utilized for roughing and backing. A Diffstack MK2 diffusion pump manufactured by Edwards High Vacuum International created the high-vacuum. An Edwards 1005 digital display equipped with a Pirani vacuum gauge (Useful range: atmosphere to 1x10-3 torrs) and a Pennings gauge (Useful range: 1x10-3 to 1x10-8 torrs) was employed for monitoring the vacuum. Indium foil was utilized to ensure good contact between the sample and its holder and from the holder to the last stage of the cold finger. The Fourier transform Raman experiments were conducted in a Bruker FRA 106 instrument. The excitation wavelength is 1.06 μm from a Nd:YAG laser.

4.2.4 Simulation Methodology

The force field utilized is called *Dreiding* .[15] This field is included *Polygraf*™ 3.2. This software was used to assign and equilibrate charges added to the structure by the method of Gasteiger.[16] Molecular mechanics energy minimizations were carried out in accordance to methodology by Fletcher and Powell.[17] Structure minimizations were done when the energy change was smaller than 0.001 kcal/mol. Many trials were needed to ensure that a global minima was indeed reached. Simulation of the X-ray diffraction characteristics of the minimized PMDA-ODA conformation were done on*Cerius* ™. A triclinic unit cell was chosen for minimizations to ensure that all its parameters would be dictated by the choices of hybridization adopted in the model and not by the imposition of any symmetry restrictions. The same criteria was utilized for the simulated X-ray

diffraction. Dynamics and mechanics minimizations were utilized interchangeably in addition to stretching and compression runs to ensure that the cell's energy was indeed at its global minima. The drift along the axial direction persisted, although its magnitude became acceptable only after this latter procedure was applied.

4.3 Results and Discussion

4.3.1 X-ray Diffraction

Highly crystalline bulk forms of PMDA-ODA polyimide have not been observed previously. Although recently, a highly crystalline air/polyimide interface has been reported.[18] X-ray data for anisotropic polyimide powder samples could not be obtained. A high glass transition and melting point made it impossible to fuse and deform polyimide powders. Instead the unit cell was fitted using information from patterns from stretched films and powder patterns from highly crystalline polyimide powder. The results where then compared with simulated spacings and intensities.

Figure 4.1 provides a comparison of the simulated wide-angle X-ray 2θ scan, an experimental diffractometer scan of the powder and a microdensitometer scan of uniaxially drawn film. Apparent from this figure are the match between simulation and experimental diffractometer scans and their higher dimensional order over that of the film. Our experimental patterns from uniaxially oriented films and fibers, as it has been the case with many other studies, were far from providing detailed information on non-meridional reflections. Figure 4.2 and 4.3 show the pattern of a stretched polyimide film and that of

the highly crystalline powders respectively. Detailed fiber patterns can be simulated. These are shown in Figures 4.4 and 4.5.

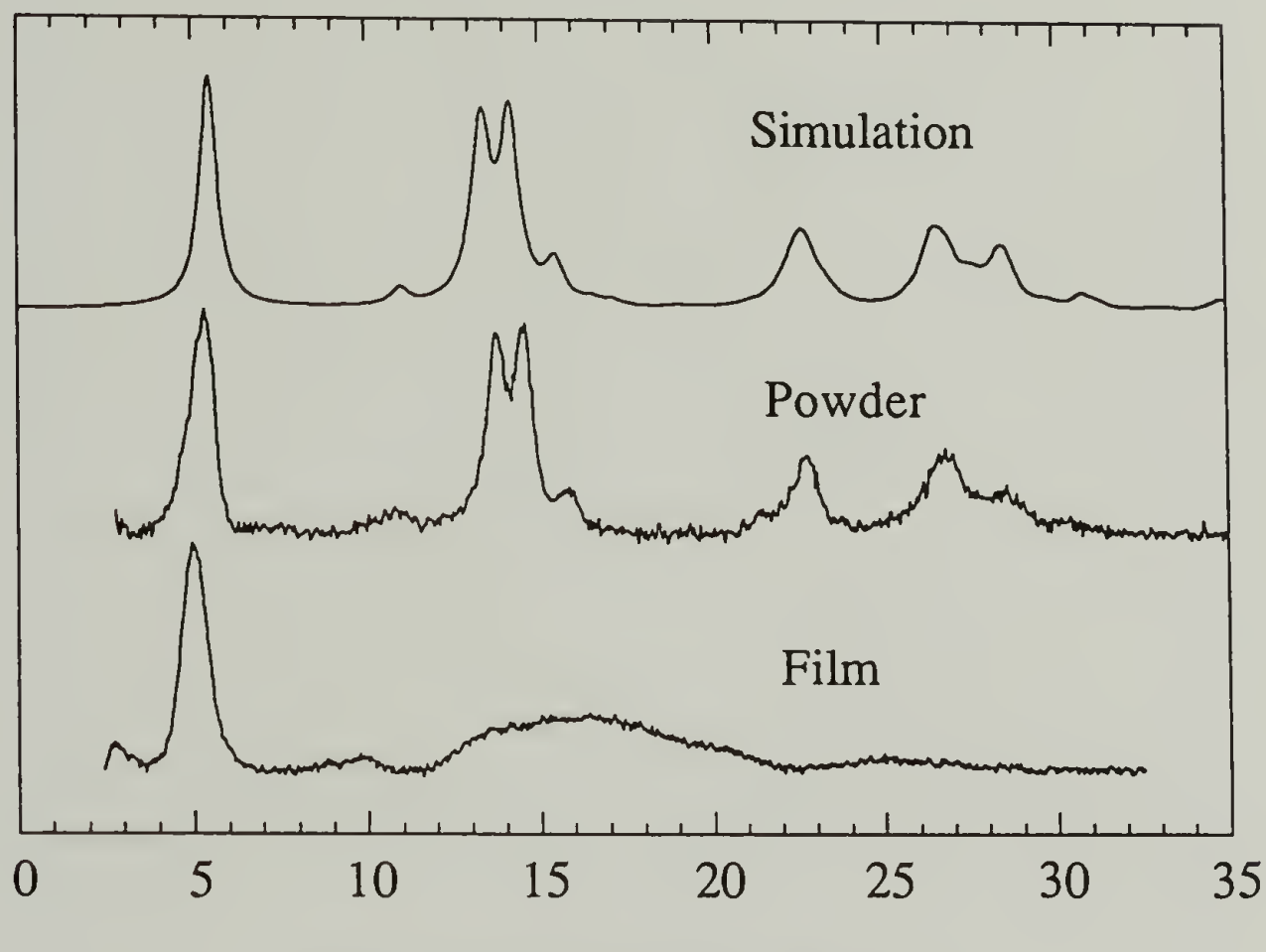

Figure 4.1. Experimental and simulated wide-angle X-ray diffractometer scans for PMDA-ODA polyimide.

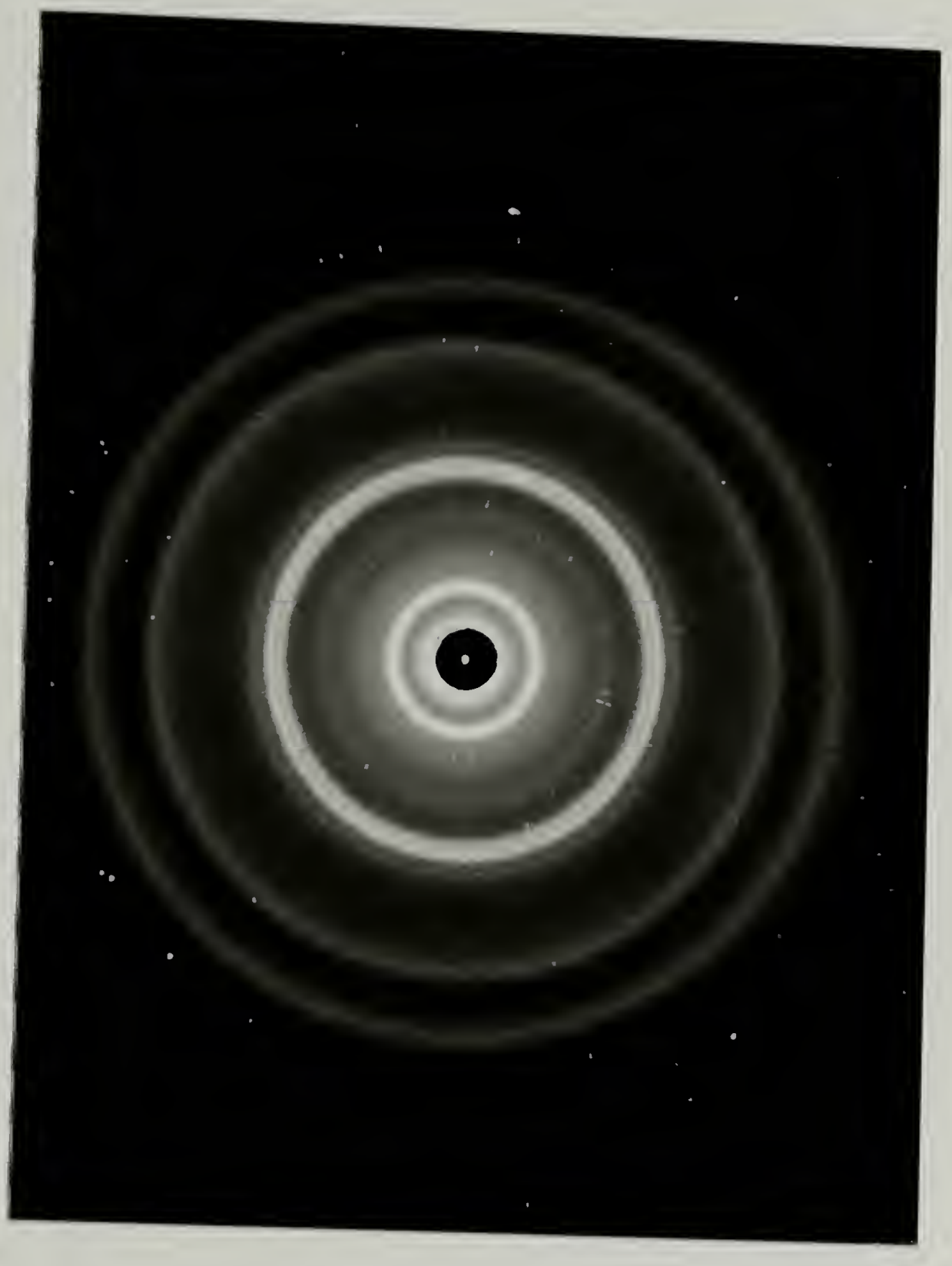

Figure 4.3. Wide angle X-ray pattern of a highly crystalline PMDA-ODA polyimide powder.

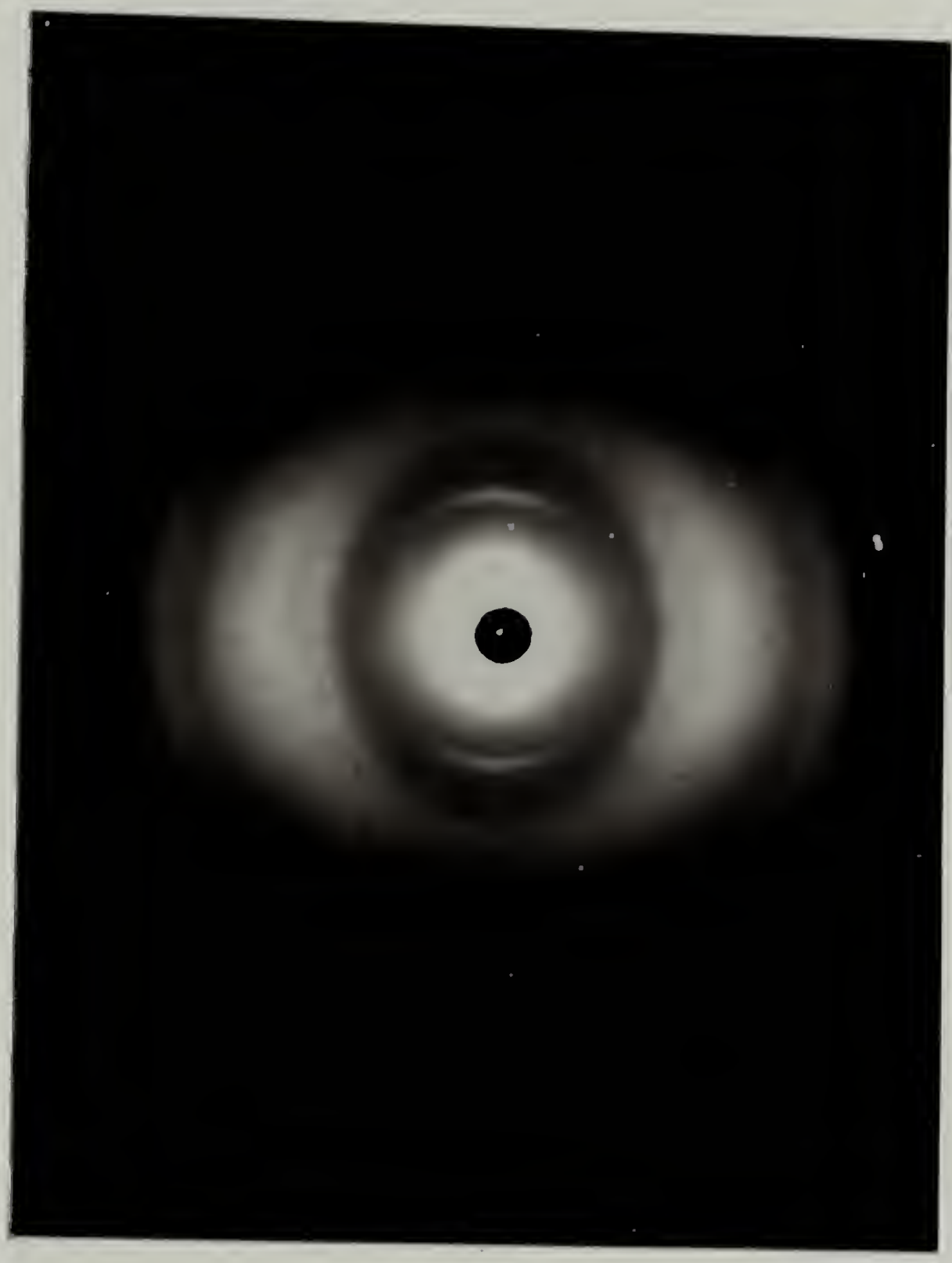

Figure 4.2. Wide angle X-ray pattern of an oriented polyimide film.

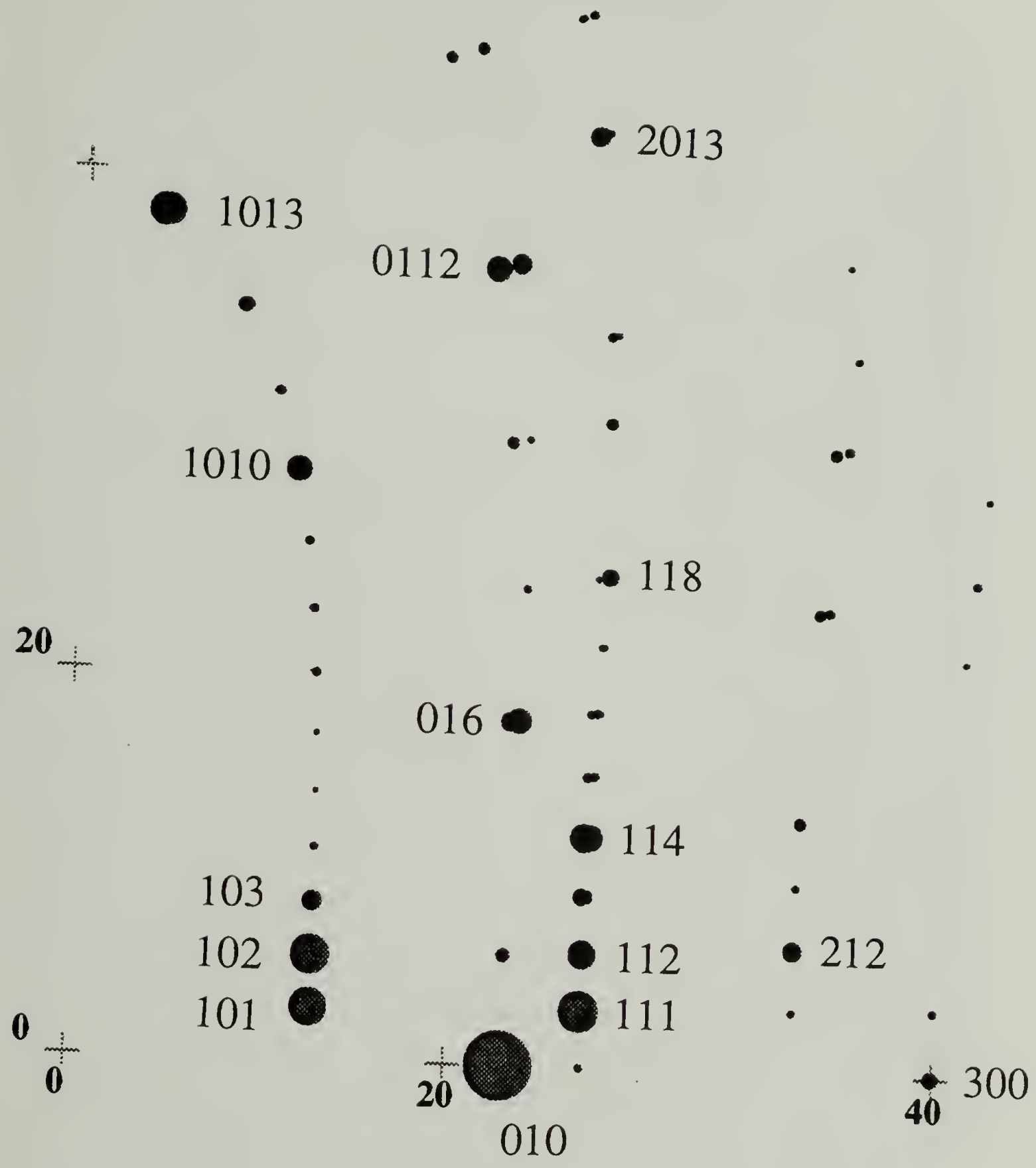

Figure 4.4. Predicted wide-angle X-ray diffraction pattern of PMDA-ODA polyimide.

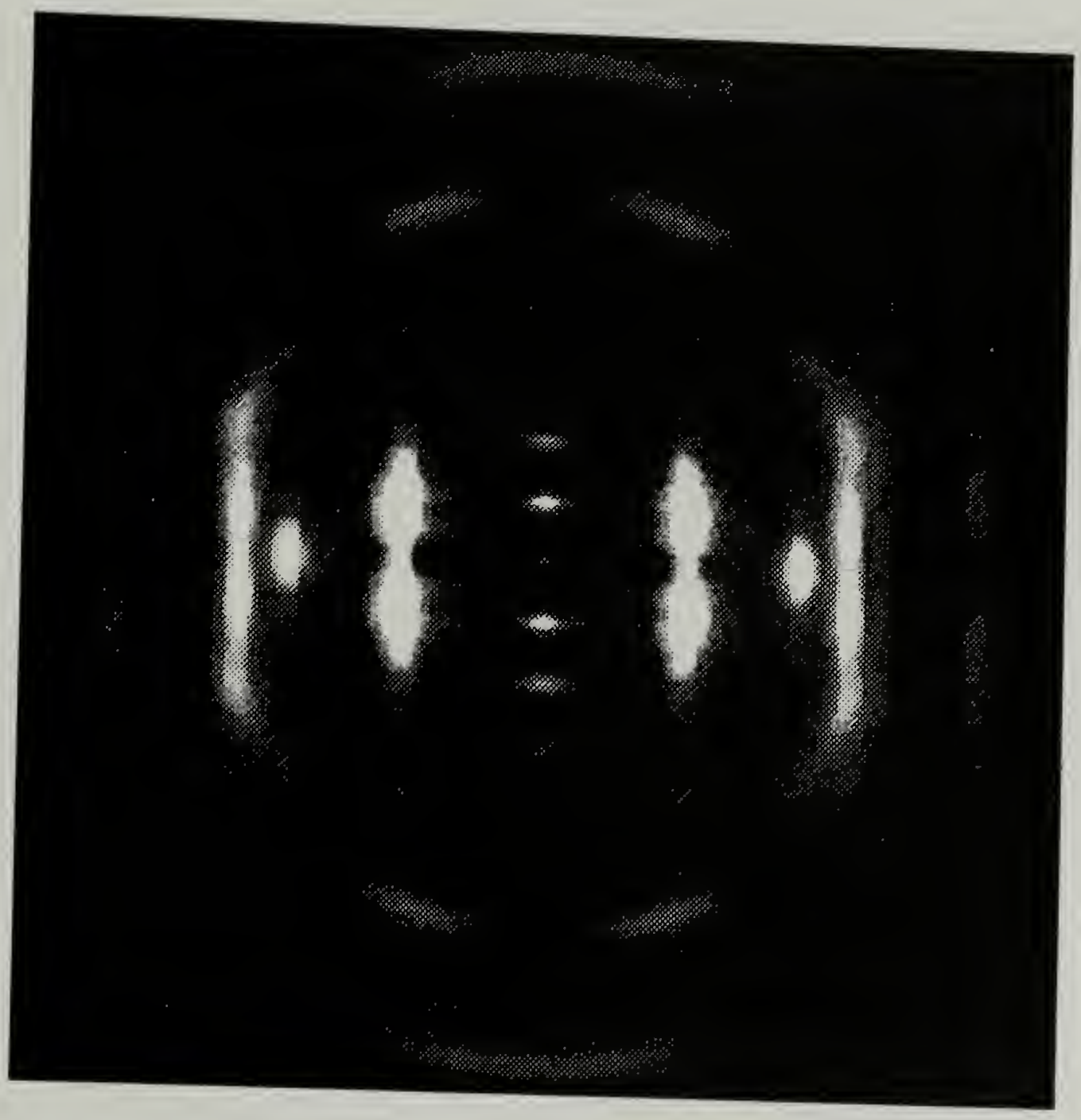

Figure 4.5. Simulated wide-angle X-ray diffraction pattern of a PMDA-ODA stretched film at 5 % orientation distribution half width.

From Figures 4.4 and 4.5 one can observe that meridional reflections do not appear unless there is chain axis disorientation. The strongest feature observed in these figures corresponded to the meridional intensity of the (002) plane. The d-spacings for this reflection were 16.07 Å and 16.52 Å as given by molecular simulation and diffractometer scans respectively. This reflection corresponds to the projected length of the PMDA-ODA polyimide repeat unit along the c-direction. All odd number meridional reflections would not be observable due to the space group symmetry of this 2_1 helix. With this symmetry, even number meridional reflections appear due to the regularity of the polymer chain and to the length of the repeat unit. No meridional reflections should appear under these conditions if ideal textures were being observed. But as it was mentioned above, axial disorientation makes these reflections visible even if no sample tilting was used to purposely observe them. Meridional reflections in PMDA-ODA films can also show the effect of imposed or residual deformation, as it has been shown by Russell.[19] This effect can be observed from Figure 4.1, where the (002) reflection of the stretched film is at a lower angle than the powder and simulation.

The next peak from the diffractometer scans was assigned to the (004) reflection. This modest peak was observed at a value of 2θ near eleven. In the 2θ scan there are no other contributions to the intensity of this peak either. The experimental d-spacing corresponding to this peak was 8.18 Å. The (006) reflection cannot be detected in the photographic powder pattern or diffractometer scans due to the presence of other very strong reflections at those scattering angles. The (008) is next to the (010) peak in the scan and its experimentally obtained spacing was 4.14 Å. No other meridional reflections can be readily observed from our experimental or simulated comparison to anisotropic sample patterns. However, there are some near meridional reflections such as the (1013) that may be mistaken by a (0012) meridional reflection in a fiber pattern when axial disorientation is observed.

Good chain registry is found in the axial direction, meridional reflections are strong and sharp but the blurred non-meridional reflections observed from the experimental fiber patterns imply lesser order in fibers and films. The diffractometer scans of the highly crystalline powder and simulations elucidate order in those dimensions other than the axial, with sharp and well defined features. The twin peak feature of the diffractometer scan corresponded to the (101) and (102) planes. A less intense higher angle peak corresponds to the (103) plane. The (104) peak can be observed from the simulated and powder pattern but it was lost amidst all the noise of the experimental scan. This family of planes corresponded to the spacing in the designated a-direction of the unit cell where the absent reflection corresponding to (100) provides the value of a = 6.76 Å. Fiber patterns of films cured at a slow rate show very diffuse non-meridional reflections.

Broad peaks from diffractometer scans of PMDA-ODA films show a broad hump that corresponds to a d-spacing of approximately 5 Å. This spacing which encompasses an average lateral coherence has been attributed to interchain interference.[20] These diffuse regions are attributed to the wide distribution of spacings among adjacent chains and to the distribution in transverse crystallite dimensions caused by asynchronous reductions in their cross sectional areas during cure. The non-crystalline hump representative of this disorder can be observed from Figure 4.1.

At higher angles, our diffractometer scans showed several strong reflections. The (010) reflection appeared at a 2θ of 22.68°. In relationship to the spacings at these diffraction angles, Figure 4.6, shows the geometry between phenyl rings from adjacent chains. The 30° angle shown in this figure is a consequence of the ether oxygen valence angle and the 60° stagger is likely to be the result of complementary interplanar π-system packing. Staggered stacking of planar ring units has been proposed.[21] This alternative

interaction among planar units was determined to be a result of overcoming mutually repulsive π-electron forces by attractive electronic forces between π-electrons and the σ-framework. For example, the interplanar separation of porphyrin-porphyrin systems is known to be between 3.4 and 3.6 Å. An intermolecular stagger between porphyrin-pyrromellitimide systems was also reported. Similar magnitudes of interplanar spacings, 3.39 Å on polyimide model compounds, has been previously observed.[22]

The last of the observed meridionals was the (008) reflection that appeared at a 2θ of 21.43°. Within the same region, the (012) and (107) reflections are observed in the vicinity of 23.6°. The broad peak at 26.7° has intense contributions from the (111) and (112) reflections. Its shoulder peak at 28.4 exhibited contributions from (016) and (114) at 28.6°. These reflections are tabulated in table 4.4 of the simulation section ahead.

A set of crystallite sizes was computed from simulated powder patterns. The intensities of the simulated pattern were adjusted by varying crystallite sizes until a match with intensities shown experimentally was found.

The crystallite size dimensions obtained from simulation were as follows: a = 110 Å, b = 85 Å and c = 150 Å. These dimensions were also computed experimentally using wide-angle X-rays. These crystal dimensions were: L_{002} = 107 Å, L_{101} = 92 Å, L_{010} = 117 Å, with an average reliability of ± 10 Å. Since the experimental diffractometer data was not corrected for instrumental peak broadening, the experimentally determined crystal dimensions should represent a lower size limit. And the sharper peaks obtained by simulation should yield the higher limit in the absence of any broadening induced by experimental measurements.

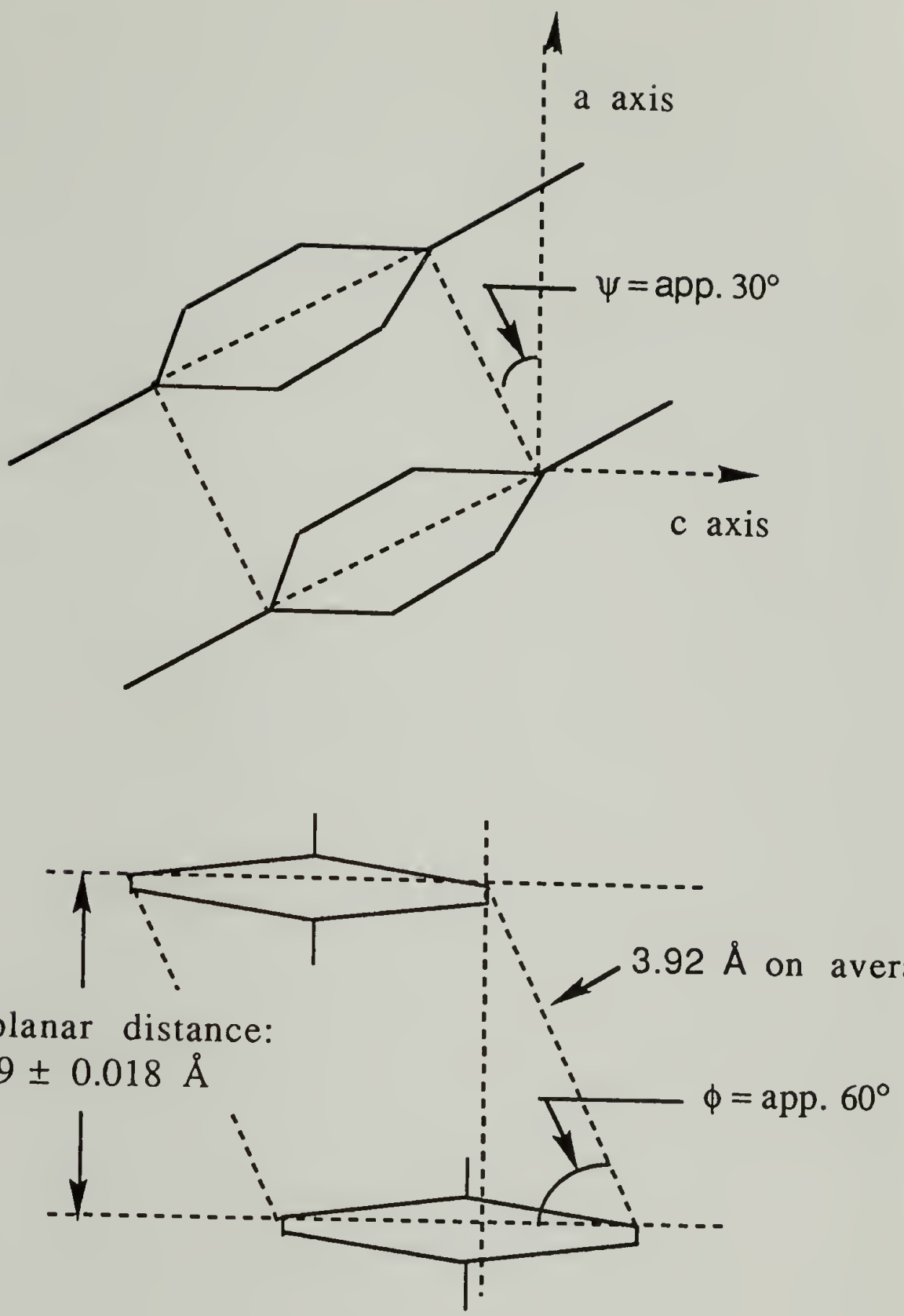

Figure 4.6. Geometry of phenyl rings between adjacent chains.

4.3.2 Infrared Spectroscopy

A higher crystalline order by vibrational spectroscopy is evidenced by the tendency of several bands to split into two components. The splitting in the carbonyl region for example, has been attributed to the coupling between nearing carbonyl dipoles, and frequency shift between its crystalline and non-crystalline components becomes greater with increasing degree of packing.[9] This tendency is more pronounced in the asymmetric carbonyl stretching regions and in the axial C-N-C stretch, but important changes also occur with other spectral features. As shown in Figure 4.7, the lower frequency component of the antisymmetric carbonyl stretch shifts to even lower frequencies upon ordering. This is due to the weakening of the carbonyl bond by the electron exchange of the oxygen and the increasingly conjugated ring carbon. This shift, from 1726 to 1718 cm^{-1}, exposes the higher frequency component which is thought to be representative of the disordered regions in the system.

The symmetric C=O stretch at 1778 cm^{-1} is only lowered by 2 cm^{-1}. It was reported by reference 9 that the frequency changed from 1717 to 1725 cm^{-1} for the crystalline and amorphous difference spectra respectively. Studies with meta and para tert-di-butyl pyromellitic acid revealed that upward shifts in frequency of the C=O antisymmetric stretch are due to a decreased intermolecular bonding, as it occurs when going from a crystalline to a solution state or from para to meta substituted compounds.[23]

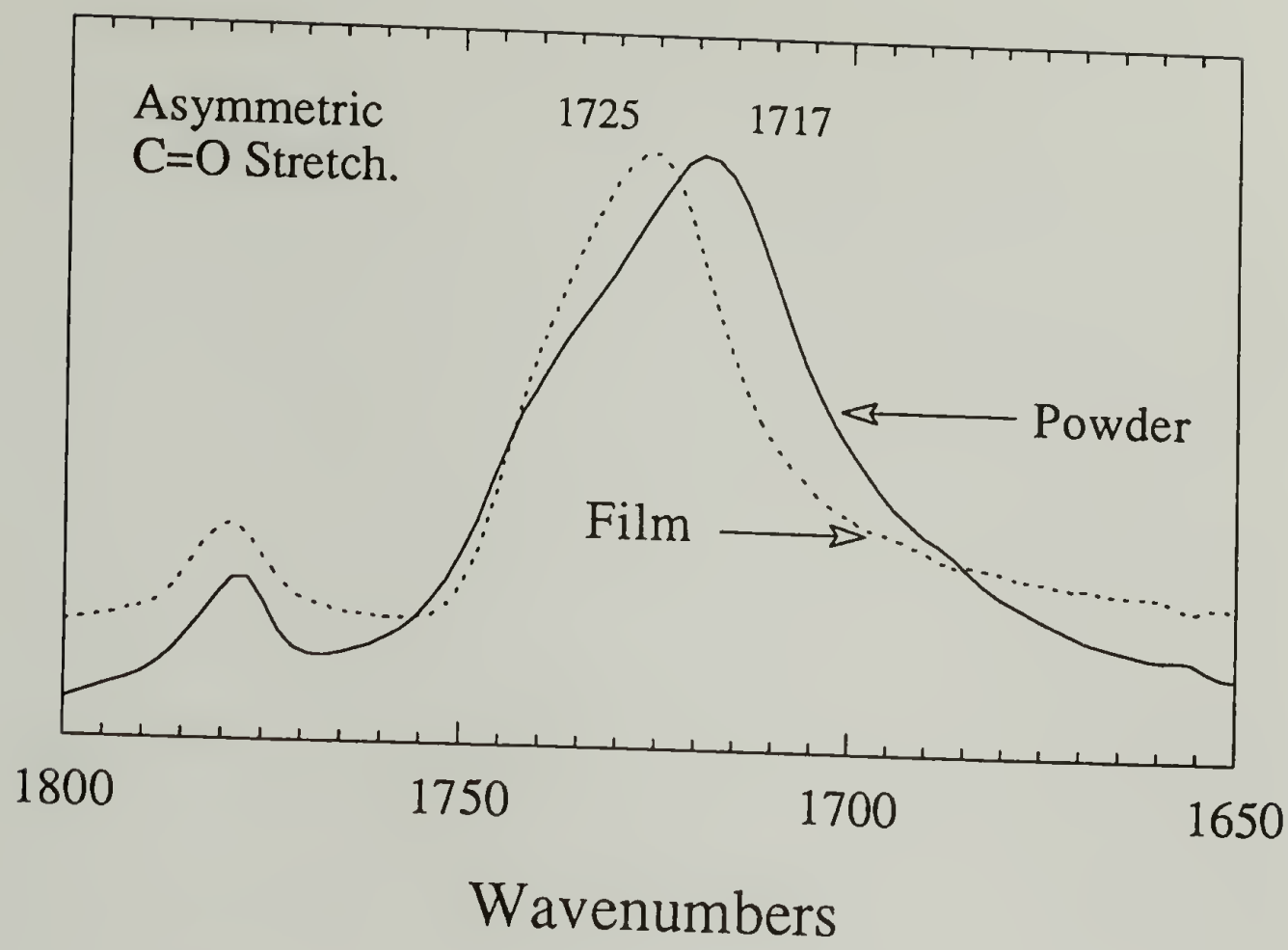

Figure 4.7. Infrared Spectra of the 1800-1650 region. PMDA-ODA polyimide.

Just as band assignments can be made for carbonyl stretches in ordered regions of polyimides, the assignment of the 1738 cm^{-1} shoulder to a carbonyl stretching in disordered regions can also be made. Results based on external reflection infrared spectroscopy of PMDA-ODA films have provided experimental evidence to support this assignment.[24] The observation has been made, based on simulated spectra, that the intensity of the high frequency shoulder (at 1738 cm^{-1}) of the asymmetric carbonyl stretch is not altered significantly when the angle of the incident radiation on polyimide films is deviated from normal.[25] This indicated that C=O dipoles belonging to disordered regions, band at 1738 cm^{-1}, have less affinity for orientational preferences. One study suggested that the 1738 cm^{-1} shoulder may be due to the presence of intermolecular linkages.[26] Our experimental evidence does not support this latter conclusion.

The emergence of another component in the axial CNC stretch region of Figure 4.8, shows an opposite trend to that of the above in the carbonyl stretching region. A higher frequency band emerges and its relative intensity is higher than its lower frequency counterpart. This lower frequency component must belong to vibrations of this type in a more disordered environment. The frequency difference in the powder spectra between the crystalline and non-crystalline components is 16 cm^{-1} (1395 -1379 cm^{-1}). A higher ring coplanarity, as it occurs in more ordered regions, will increase conjugation and therefore frequency.

The tangential phenyl ring stretch mode at 1504 cm^{-1} only showed a modest shift to higher frequency, this is shown in Figure 4.9. This peak and its shoulder are a product of the differences in the degree of order in different regions of the sample. A much higher relative intensity for this peak is observed in the films. This is due to the anisotropy which develops during spin casting and curing. The transition moment vector associated with this vibration can be utilized to approximate the degree of in-plane orientation. This anisotropy cannot be observed with the powder. A similar change in relative band intensity was also observed in a comparison of normal and rapidly cured imides.[1]

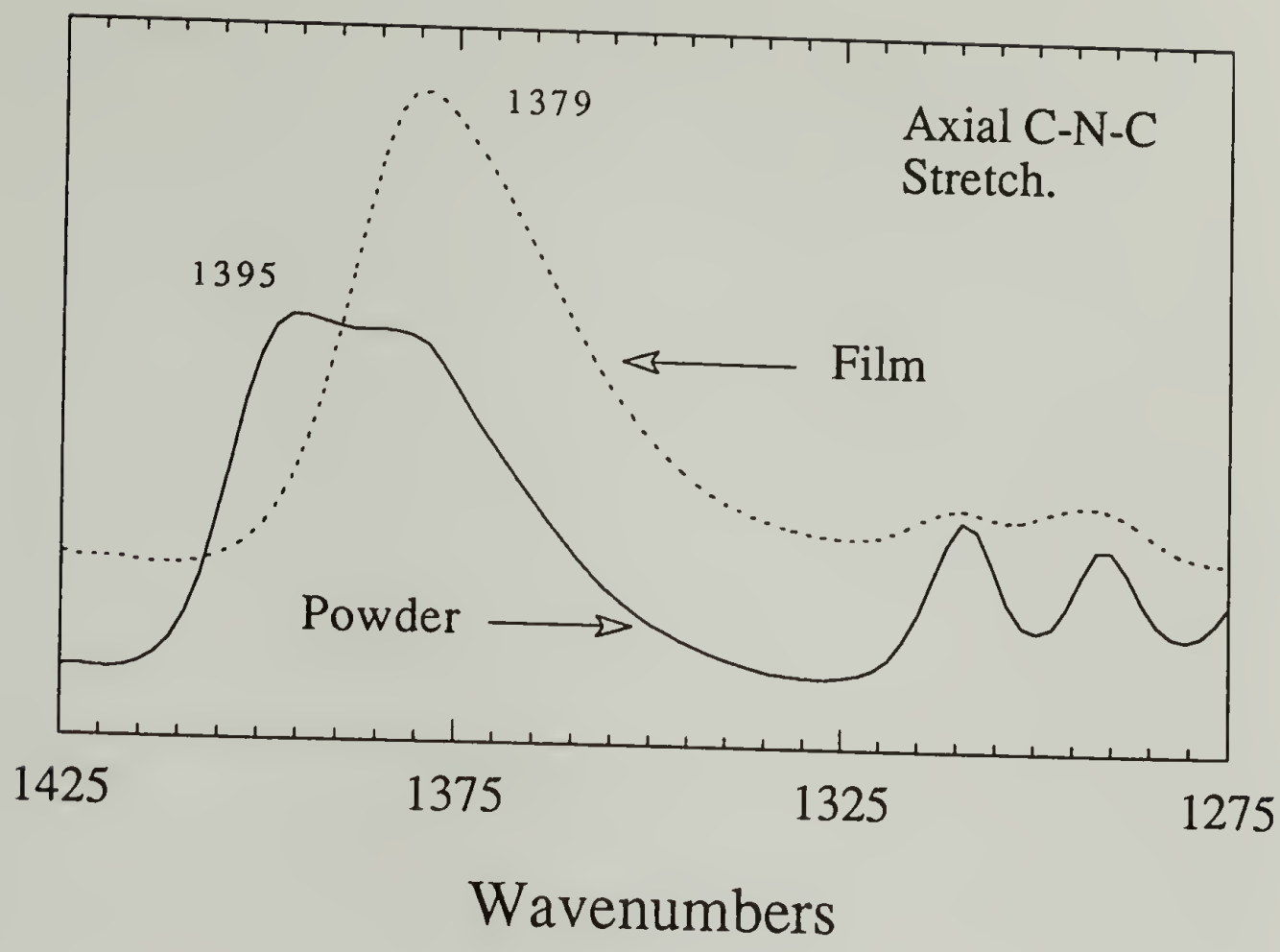

Figure 4.8. Infrared Spectra of the 1425-1275 region. PMDA-ODA polyimide.

The antisymmetric COC stretch, Figure 4.10, exhibited a significant frequency increase. It changed from 1245 cm^{-1} in the film to 1253 cm^{-1} in the powder. This is an expected change since the increase in conjugation brought about by the planarization of the structure should produce a shift towards higher frequencies. No significant width increase and therefore no apparent difference in order is detected from this peak. No distinguishable splitting can be noticed from this band. Although the influence of this oxygen linkage in the environment of other vibrations is certainly felt. Such is the case of large intensity changes in the band associated with the transverse CNC stretch at 1117 cm^{-1}, as it is seen from Figure 4.10. The band is intense for samples of high structural order. This vibration has been labeled as a combination of imide ring distortion and deformation of the carbon nitrogen bond.[27]

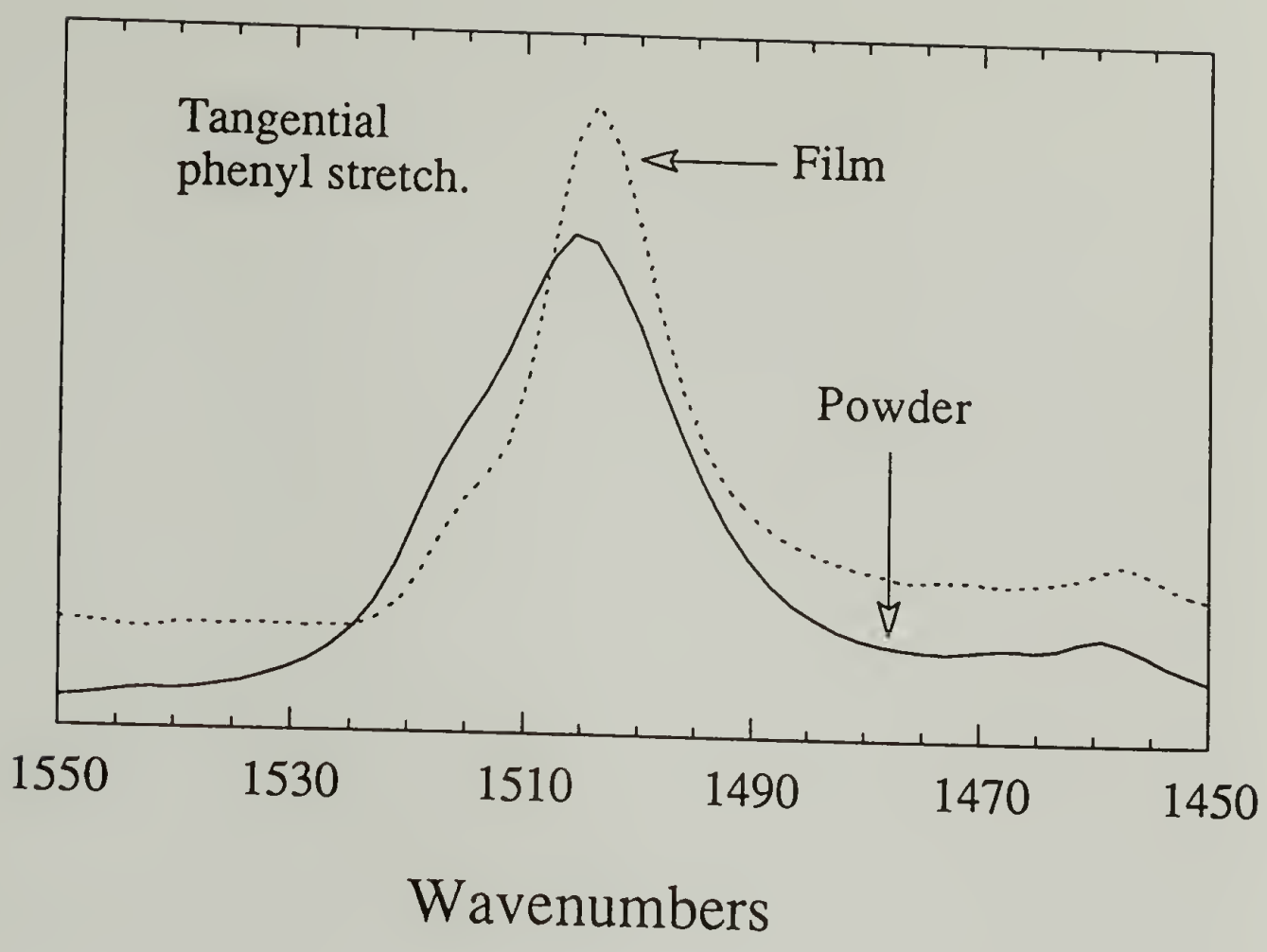

Figure 4.9. Infrared Spectra of the 1550-1450 region. PMDA-ODA polyimide.

Figure 4.11 Provides a comparison of this spectral region at 10 K and 280 K for a powder sample cured at 200 °C. An upward shift of 3 cm^{-1} is observed for the antisymmetric COC stretch and the CNC transverse stretch. As shown from Figure 4.10, the relative intensity of the CNC transverse stretch increased markedly in the absence of a frequency shift. Conjugation affected this vibration indirectly by coplanarizing the structure and providing for a more perfect stacking of the pyromellitimide ring units.

A related phenomenon is ring coplanarity. Out-of-plane CH bending and ring out-of-plane deformations, in Figure 4.12,[28] can be utilized to compare compare ring coplanarities in films and powder. Each of these bands tend to split into two components

that belong to different symmetry species. So, techniques to compute the twist angle analytically based on these bands have been proposed.[29]

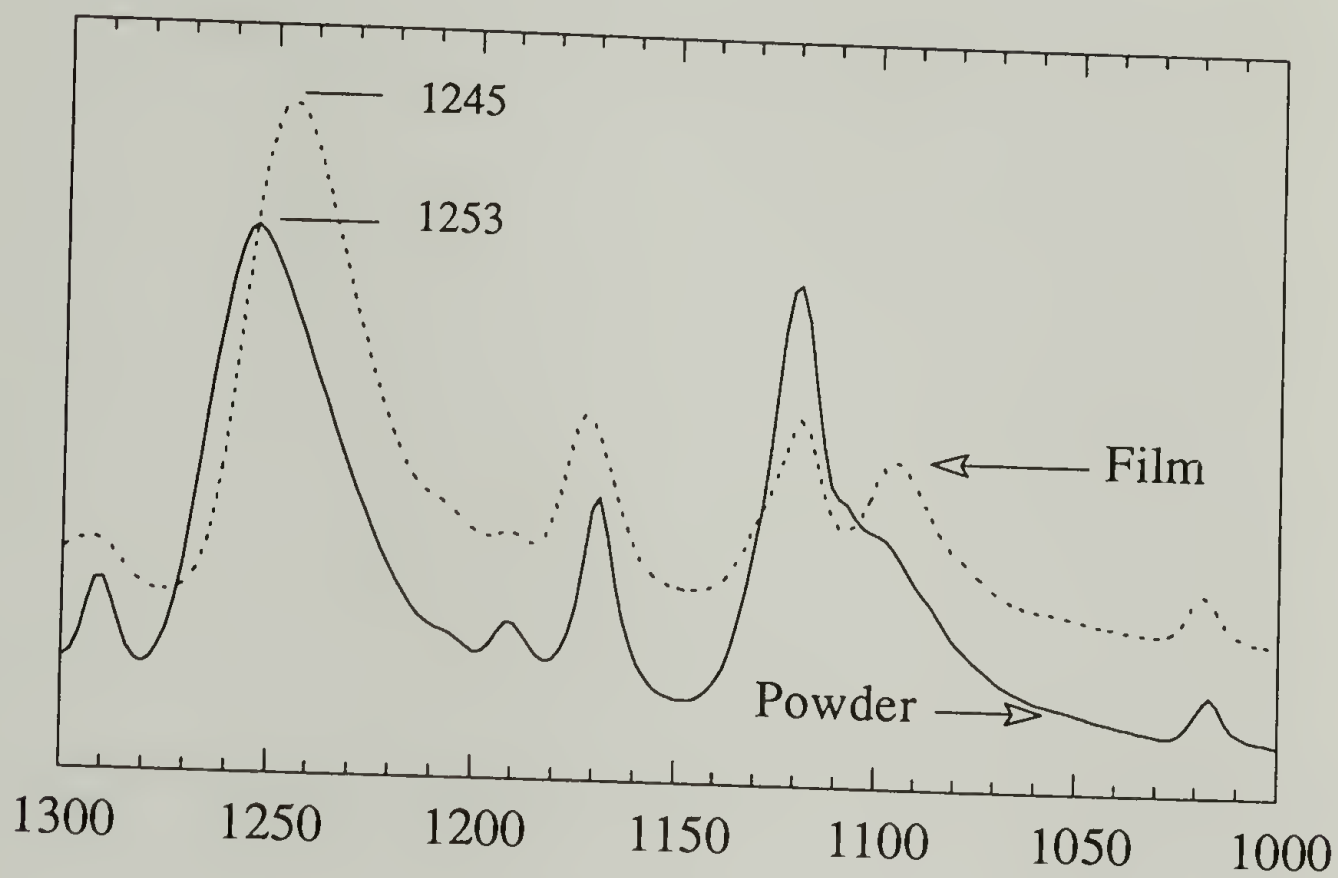

Figure 4.10. Infrared Spectra of the 1300-1000 region. PMDA-ODA polyimide.

Expressions for the intensity were derived based on the original work of Gribov.[30] The total intensity associated with n number of equivalent groups in the same molecule is given by the following semi-empirical expression

$$I_i(n) = I_o \frac{\nu_i^2(n)}{\sum_k^n \alpha_{ik}^2} \left(\sum_k^n \alpha_{ik}\, h_{ik} \right)^2 , \qquad (4.2)$$

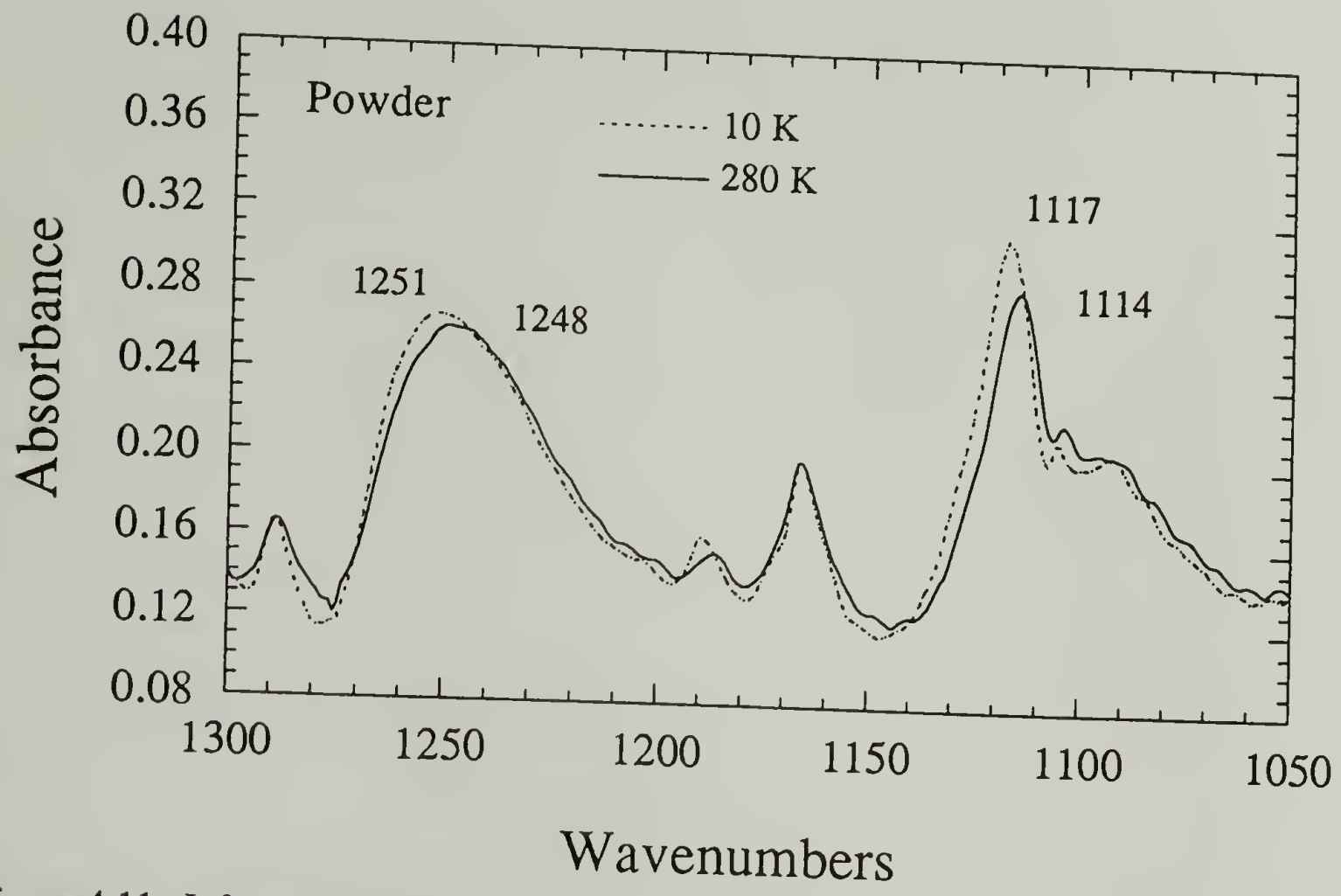

Figure 4.11. Infrared Spectra of the 1300-1050 region at a temperature of 10 K and 280 K. PMDA-ODA polyimide.

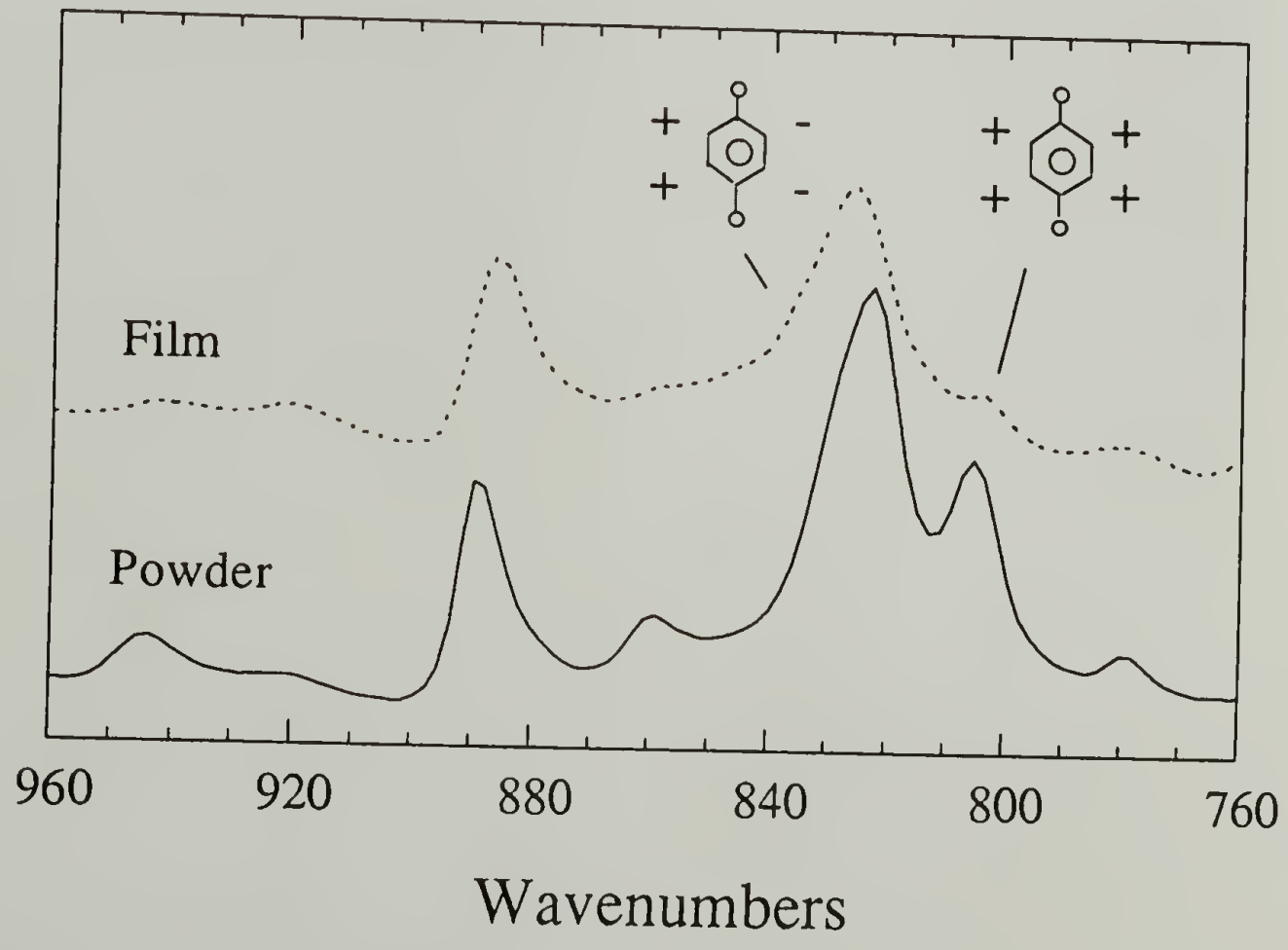

Figure 4.12. Infrared Spectra of the 960-760 region. PMDA-ODA polyimide.

where $I_i(n)$ is the intensity; $\nu_i(n)$ is the frequency; α_{ik} is a factor that accounts for the relative phases and amplitudes of a group vibration among groups; h_{ik} is the unit vector of the vibrational polarization;n is the number of the equivalent groups; I_0 is the undisturbed intensity of a single group. Application of the above expression to that of a Ph_2X molecule (X = ether oxygen in our case), as shown in Figure 4.13, can be written as

$$I_{sym} = I_o \left(\frac{\nu}{\nu_o}\right)^2 (1 - \cos\varphi) \cos^2\theta \quad , \tag{4.3}$$

$$I_{asym} = I_o \left(\frac{\nu}{\nu_o}\right)^2 [(1 + \cos\varphi) + (1 - \cos\varphi) \sin^2\theta)], \tag{4.4}$$

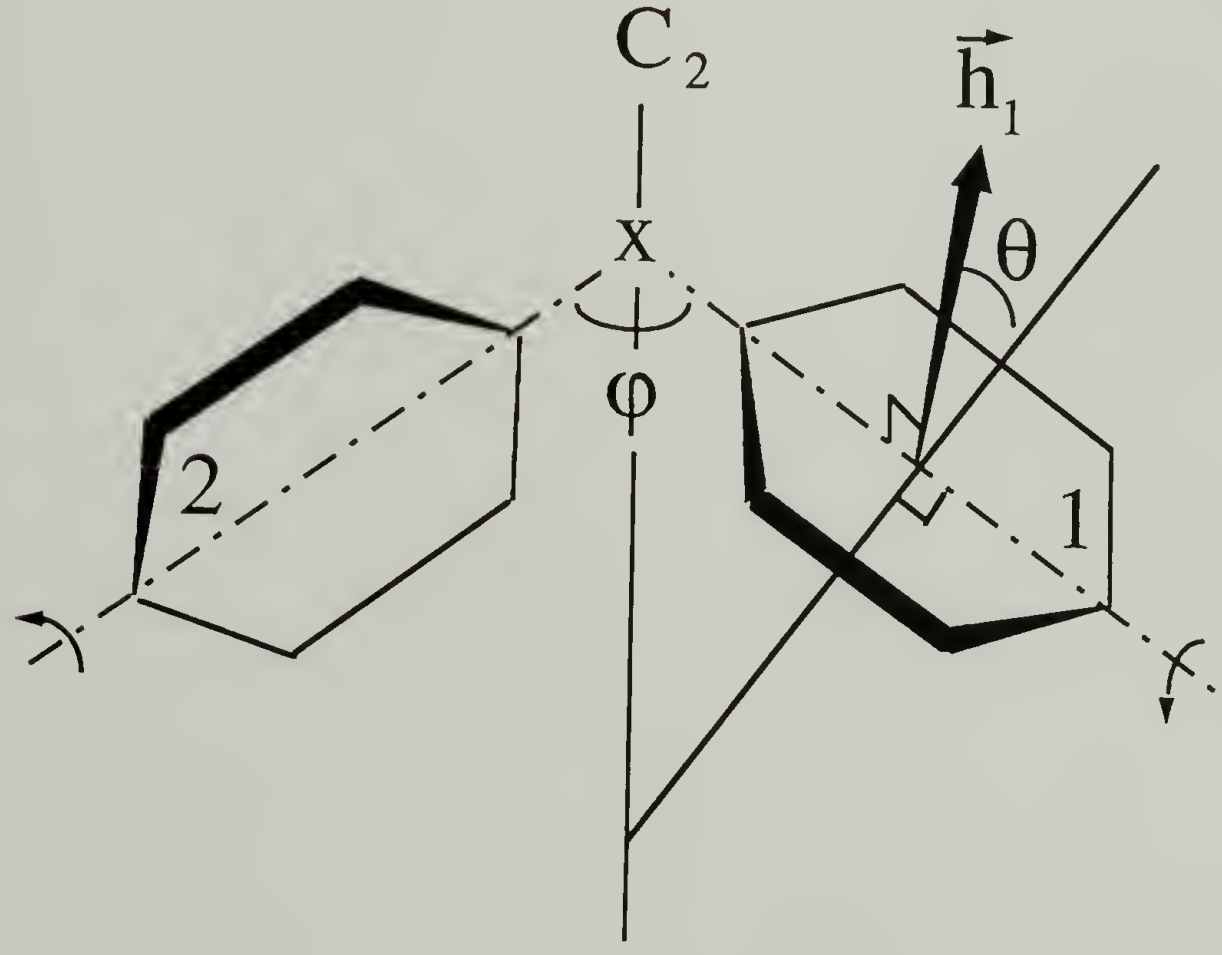

Figure 4.13. Schematic of the geometry utilized in the computation of the phenyl twist angles from infrared modes.

where ϕ is the valence angle; θ is the torsional angle; I_{sym} and I_{asym} are the intensities of the vibrations belonging to the symmetric and asymmetric species, ν_0 is the unperturbed frequency; ν is the observed frequency. The ratio $(\nu/\nu_0)^2$ can be taken as unity since the frequency difference due to the interaction between different symmetry species is small.

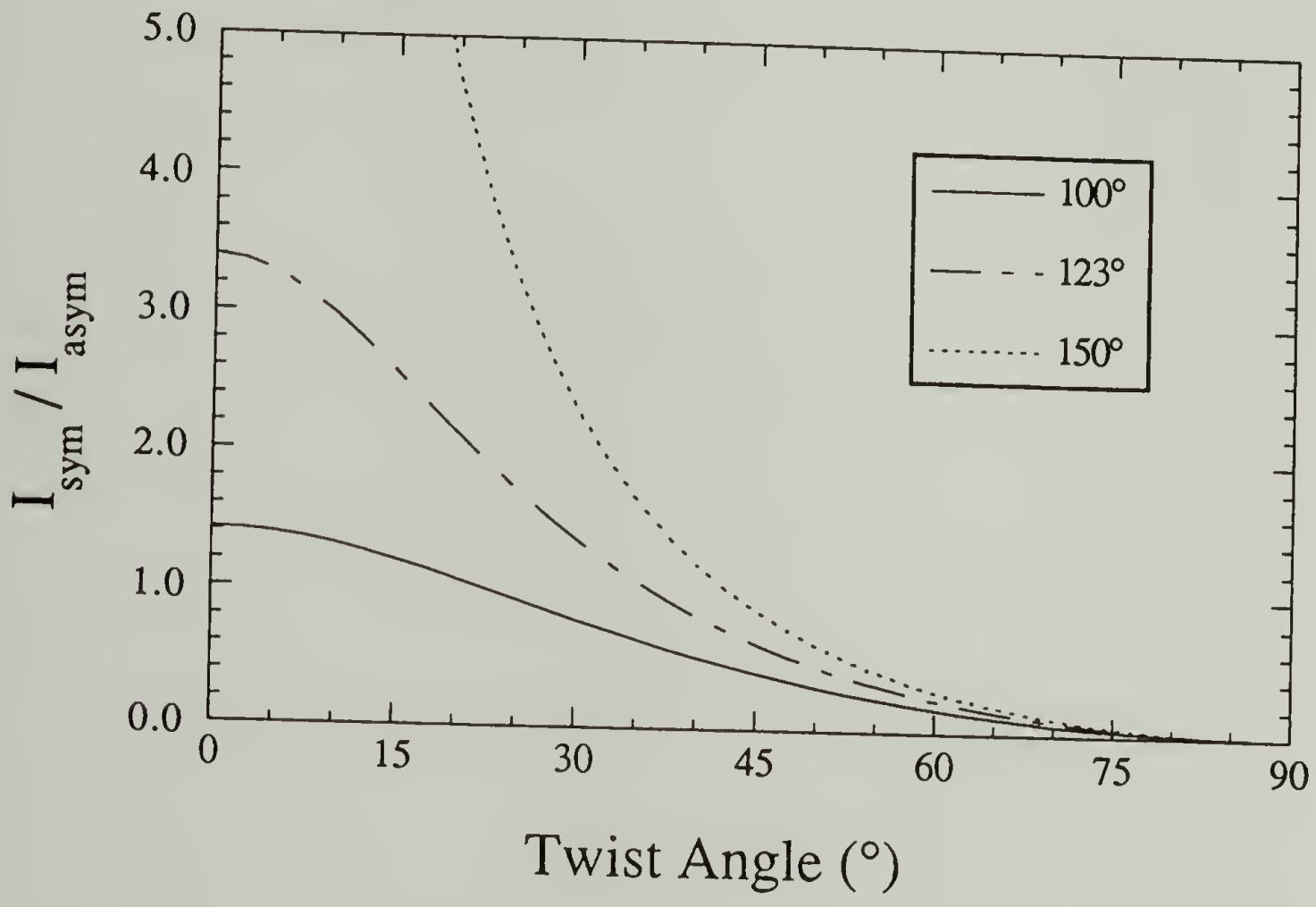

Figure 4.14. Ratio of symmetric to antisymmetric intensities of selected vibrations of Ph_2X type molecules versus ring twist angle.

These vibrations can be utilized to provide an estimation of the twist angle if the intensity ratio of species A to B is found. The ratio of the symmetric species to the antisymmetric species as a function of angle of twist angle has been plotted in Figure 4.14. From this plot, one can obtain estimations of ring twist angles for a Ph_2X type molecule. For a valence angle of 123° and if vibrations between 800 and 840 cm^{-1} are

utilized, the computed angle is 57° for the films and 46° for the powder. A decrease in twist angle was to be expected for the powder because of increase in packing and ring coplanarity. However, this value of 46° is far from the ideally predicted simulation value of 31°. A value of 40° was found for a solution of Ph_2O at low temperatures, using the methodology described above and a value of 53° was determined at room temperature by Kerr constant analysis measurements on Ph_2O.[31]

4.3.3 Raman Spectroscopy

Raman spectroscopy was needed to provide supplementary information on the conformational differences of PMDA-ODA polyimide. And also to discuss the validity and usefulness of tentative band assignments.

Distinct features from the crystalline polyimide samples can be extracted from Fourier transform Raman spectra at lower frequencies, while data for higher frequencies provides for an assessment of curing efficiency or film anisotropy. As it is expected the symmetric C=O stretch is strong in Raman and its antisymmetric mode is very weak. Various carbonyl stretching modes and tentative peak assignments are provided in Figure 4.15. These peaks are sharper in the spectra of the powder than that of the films. They appear at 1789 and 1727 cm^{-1} for the films and at 1783 and 1721 cm^{-1} for the powder respectively. Figure 4.16 shows the spectra of the powder and film in the range of 1000-1900 cm^{-1}. The shift of these vibrations to higher frequencies for the less crystalline samples is in accordance to that observed with the infrared measurements. The loss of C=O bond character due to the increased influence of the intermolecular environment in more crystalline samples results in the downward shift in frequency. Also, one can

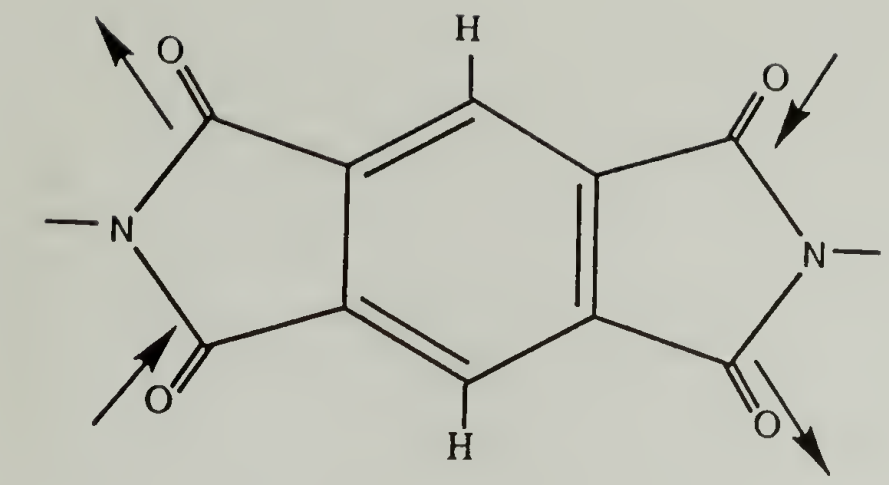

Raman Weak, B_{1g}

Ordered: 1722 cm^{-1}

Disordered: 1728 cm^{-1}

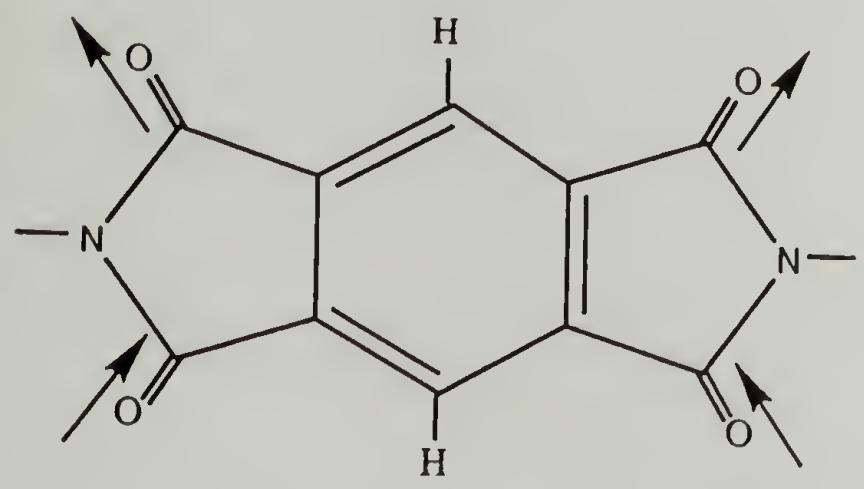

Infrared Strong, B_{2u}

Ordered: 1717 cm^{-1}

Disordered: 1725 cm^{-1}

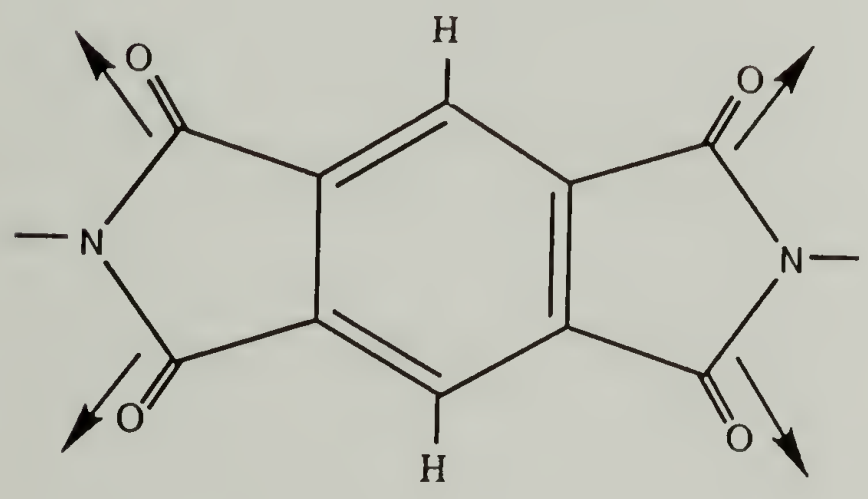

Raman Strong, A_g

Ordered: 1783 cm^{-1}

Disordered: 1789 cm^{-1}

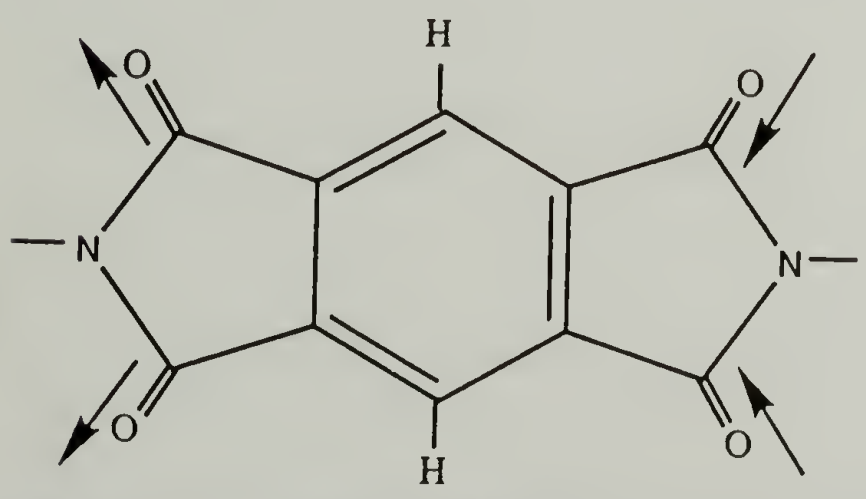

Infrared Weak, B_{3u}

Ordered: 1774 cm^{-1}

Disordered: 1776 cm^{-1}

Figure 4.15. Carbonyl stretching modes and frequency assignments for ordered and disordered regions in polyimides.

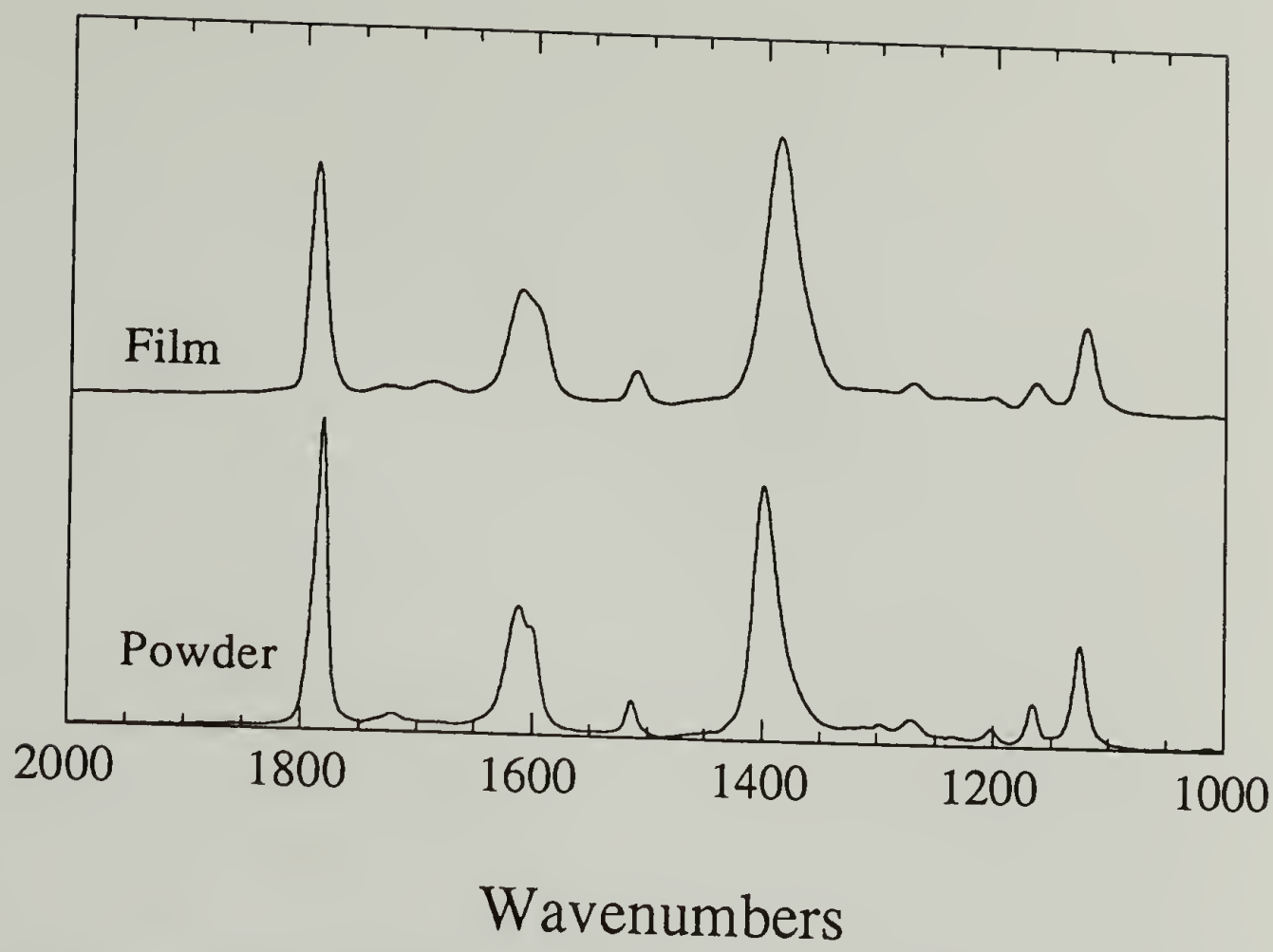

Figure 4.16. FT-Raman spectra of the high frequency region for polyimide powder and heat cured film.

observe relative intensity changes in this figure which are originated by increases in sample anisotropy. For example, the change in relative intensity observed for the vibrations near 1785 cm^{-1} and that at 1390 cm^{-1}.

Besides the powder, spin coated films with a final cure temperature of 200 °C and chemically cured films without any heat treatment were analyzed. Figure 4.17 shows the Raman spectra of this film without any heat treatment in the range between 1900 to 1000 cm^{-1}. Sample color changes brought about by annealing or curing beyond 200 ° C increased the background and distorted the neat baseline obtained for those samples shown here. At slightly lower frequency from the carbonyl stretching, appreciable changes can be observed between the films and the powder. A band which is non-existent in the powder appears in the films ranging from 1688 to 1690 cm^{-1}. This band

can be linked to pockets of material where imidization may be incomplete.[26] A key feature in the preparation of the powder polyimide is that the solvent is made to remain as a part of the system for a longer time, thus allowing a greater degree of molecular freedom to that of films in which solvents are evaporated more rapidly. Solidification during chemical curing was reached fast and the solvent exuded to the boundaries. For thermally cured films, the solvent was evaporated at 85 °C for 15 minutes and then baked under vacuum for an hour at 200 °C.

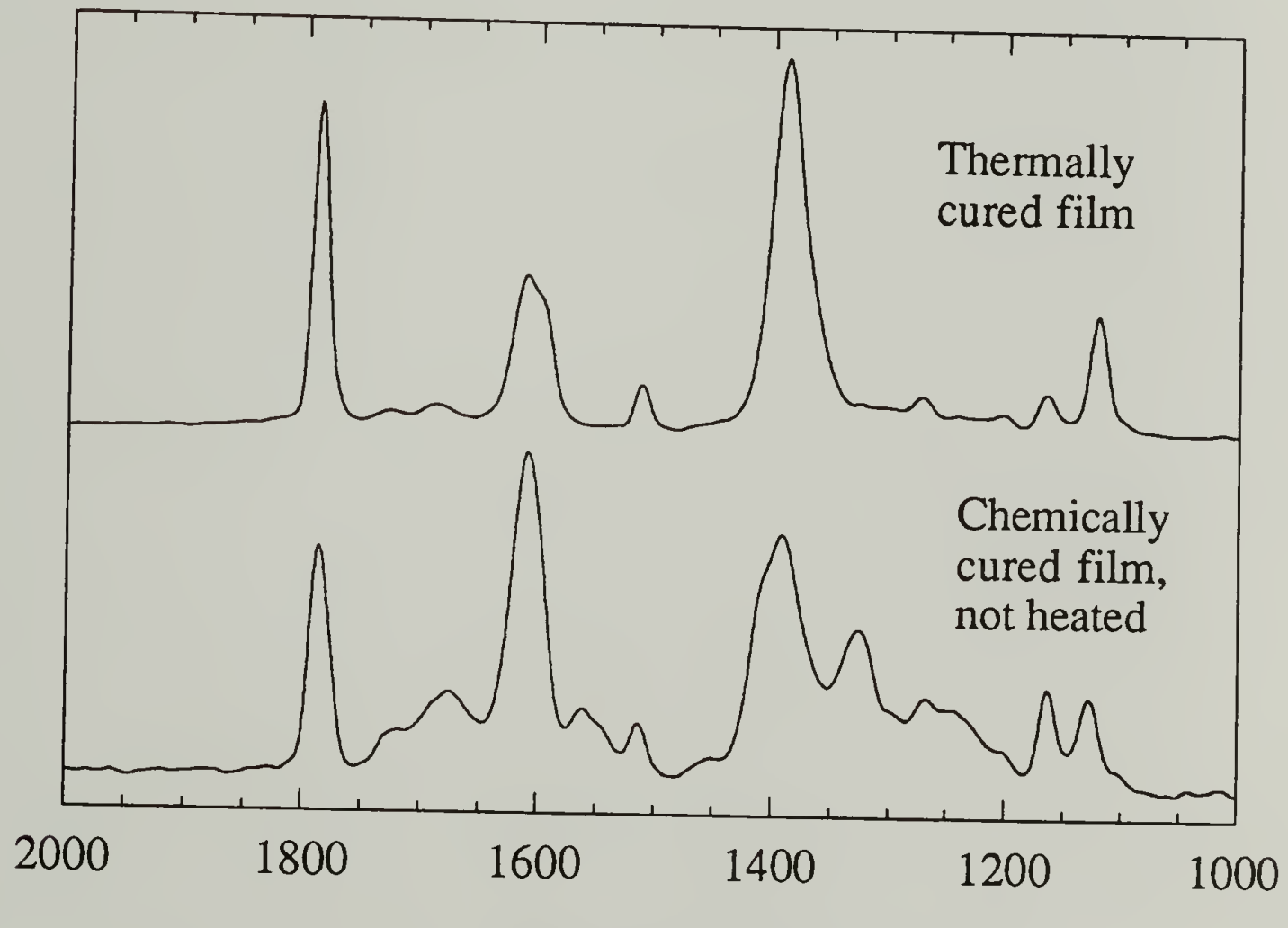

Figure 4.17. FT-Raman spectra of the high frequency region of heat cured and chemically cured film

In reference to Figure 4.16, a strong peak with a prominent shoulder can be observed at 1611 cm^{-1} and 1598 cm^{-1} (sh) for films and at 1614 cm^{-1} and 1602 cm^{-1} for the powder. These assignments correspond to the C=C stretch (8a and 8b according to Wilson's notation) of the central and phenylene rings respectively.[32] These bands usually lie very close to the original benzene vibration (1596 cm^{-1}) and therefore they cannot be utilized as good indicators of substituents. However, in this case the effect of pendant groups and conjugation are very marked as observed especially with the higher frequency mode or central ring vibration. A quantitative relationship for the determination of the twist angle of biphenyls can be derived from the intensity of this vibration.[33] In our particular case, this relationship is complicated by the influence of the ether oxygen on the phenyl rings. The intensity increases with ring coplanarity as a $\cos^2$ law, and it was shown that the largest value observed was for fluorene where the rings where very coplanar. Other studies have probed the validity of the analysis on trans and cis poly(p-phenylene benzobisoxazole) and poly(p-phenylene benzobisthiazole) model compounds.[34] This band in c-PBO (where rings are near planar) was found to be the most intense, and that for t-PBT showed the smallest intensity since it corresponded to an angle of 23° attributed mostly to steric interactions.

The aromatic CH vibration, not shown here, is a single peak at 3073-3074 cm^{-1} for the films but it splits into a strong and sharp peak at 3067 cm^{-1} with two higher frequency shoulders (3078 cm^{-1} and 3090 cm^{-1}) for the powder.

A minor change was observed for the phenylene ring stretch at 1512 cm^{-1}, but a large frequency shift was seen for the intense CN stretching mode. This mode was observed at 1389 cm^{-1} for films and at 1398 cm^{-1} for the highly crystalline powder. Here a stiffer CN bond is obtained through the increased conjugation. The relative intensity of

this band is higher than that of the symmetric C=O vibration in the films. The opposite effect is observed in the powder where in-plane anisotropic effects are not observed.

The next set of strong vibrations occur in the range between 1120 and 1165 cm^{-1}. The relative intensity of both increase with crystalline order. A peak intensity reversal is observed for the chemically cured film. These bands are attributed to the CH in-plane bending of the phenylene ring or central aromatic ring in the imide unit and to the CNC transverse stretch. Other vibrations in this region are a small peak for the antisymmetric COC vibration at 1202 cm^{-1} and CH in plane bending (type v9b) for para-tetrasubstituted rings at 1298 cm^{-1}, and that of the para-disubstituted phenyls (v9a) at 1270 cm^{-1}. A combined mode of ring breathing (v1) for the tetrasubstituted ring can be observed at 1013 cm^{-1}. This mode only appears on Raman spectra, while a ring bending mode (v12) of approximately same relative intensity appears in the same region of the infrared spectra.

Tentative assignments for bands observed below 1000 cm^{-1} have been made but are not discussed here for brevity. Some features found below below 200 cm^{-1} are indicative of the crystallinity of the powder samples and are shown in Figure 4.18. The region below 200 cm^{-1} is dominated by torsional vibrations. As a means of comparison, the C=O torsional frequencies for benzaldehyde and para-hydroxybenzaldehyde have been reported to be 130 cm^{-1} and 110 cm^{-1} respectively.[32] Peaks at 164 cm^{-1} and 130 cm^{-1} were only observed for powder polyimide samples and not for films.

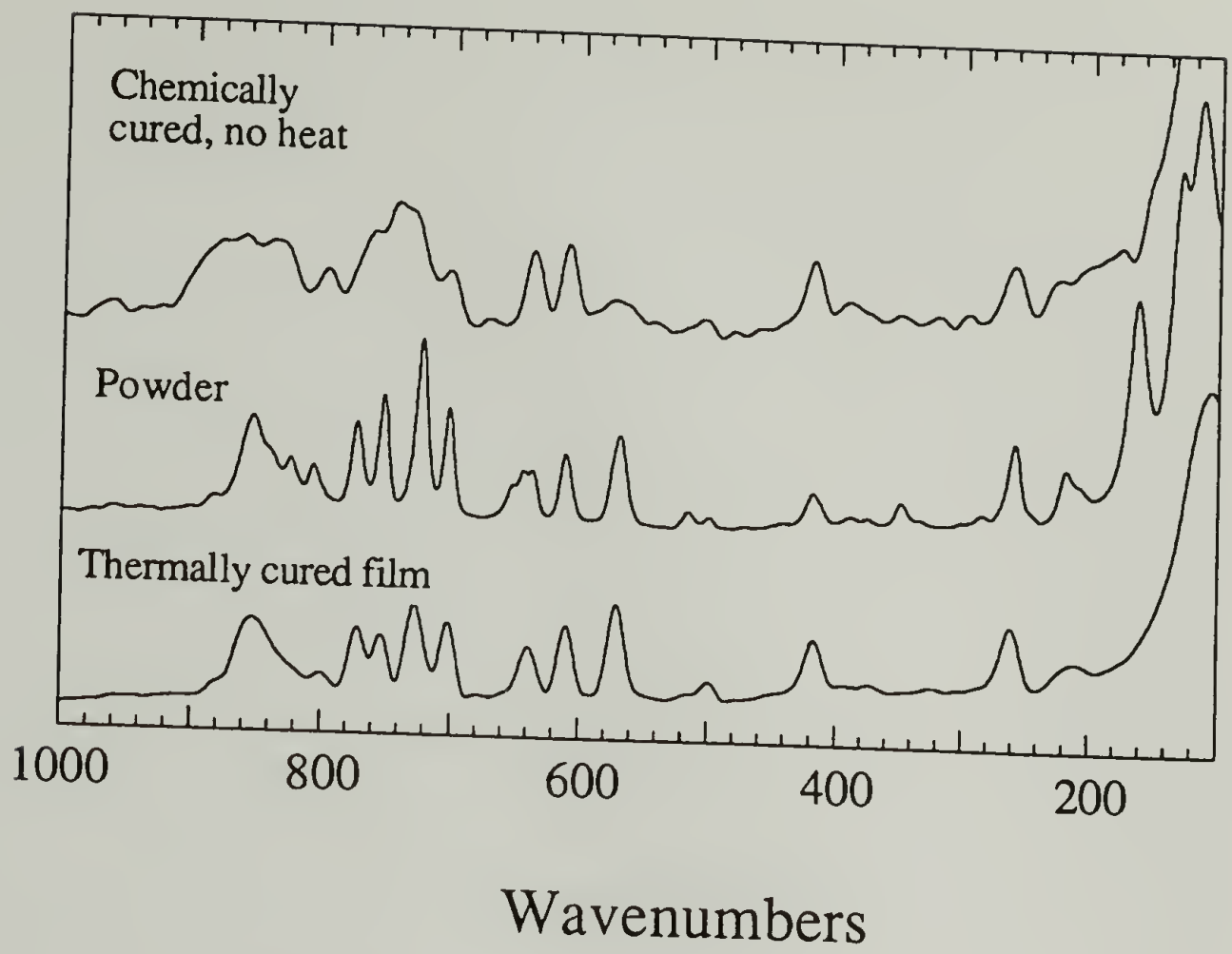

Figure 4.18. FT-Raman spectra of PMDA-ODA polyimides in the low frequency region.

Peaks below 120 cm^{-1} in our FT-Raman are considered suspect due to proximity of Raleigh line filter cutoff. Although the intensity and frequency of a strong peak at 115 cm^{-1} persisted in the films. Molecular dynamics studies using dipole autocorrelation function studies have been done for PMDA-ODA polyimide chains of 197 and 392 segments in length.[35] Two notable frequencies were obtained by this method, one at ≈ 20 cm^{-1} and the other at ≈ 110 cm^{-1}. The first was attributed longitudinal skeletal motion and it was found to be dependent on chain length. Its description fitted that of a longitudinal acoustic mode vibration. And based on snapshots of the filtered motion, the peak at 110 cm^{-1} was suggested to originate from a complex effect which included contributions from torsions about the ether linkage and out-of-plane deformations of the CN bond among PMDA units and phenyl rings. This work also points out that a strong

coupling between the aforementioned torsion and the flexing motion of single repeat units exists, and resembled that of the twisting of a loosely held string.

4.3.4 Molecular Simulation

An initial set of simulations was tailored to reflect the influence of nitrogen hybridization on the angle that an N-Ph bond vector would form with the plane of the pyromellitimide moiety and the influence of this state on the unit cell dimensions. The assumption of sp^3 hybridization enhanced the influence of the lone pair of electrons in the minimized structure of PMDA-ODA polyimide, which deviated from planarity a great deal. The sp^2 hybridization of the ether oxygen atom provided the closest match to experimental data and the most geometric resemblance to that of similar molecular structures. The sp^2 character of the nitrogen heteroatom in a pentacyclic compound can be illustrated with pyrrole,[36] where its aromatic character is furnished by six π electrons filling the bonding orbitals. It has been pointed out by other researchers that the hybridization state of the nitrogen atom will change from sp^2 to sp^3 if there is enough energy available to disrupt conjugation in the imide ring, for instance when uniaxial deformation is imposed.[37] The conformations and unit cell measurements discussed here are ones for which the deviation from 180 ° of the angle between the N-Ph bond and the pyromellitimide plane was negligible. The energetic contributions of the different conformations obtained due to changes in hybridization are shown in table 4.1 below.

Table 4.1. Energetic contributions of PMDA-ODA polyimide conformations obtained with different hybridizations in molecular simulation.

Atom type utilized in minimization†	1	2	3	4	5	6*	7
Interplanar Angle PMDA-ODA Rings (°)	53.8	56.4	51.2	47.2	51.3	54	40.3
Interplanar Angle ODA-ODA Rings (°)	29.6	31.6	25.7	24.1	26.2	31	68.9
Ph-O-Ph Valence Angle (°)	123	123	131.7	132.3	134.3	123.2	115.6
a-unit cell dimension (Å)	6.85	6.76	6.79	6.91	6.75	6.82	4.32
b-unit cell dimension (Å)	3.88	3.92	3.81	3.76	3.82	3.86	5.99
c-unit cell dimension (Å)	32.21	32.13	32.63	33.07	32.63	32.33	32.34
Unit cell angle alpha (degrees)	90.64	90.74	89.92	89.78	90.28	90.71	94.99
Unit cell angle beta (degress)	89.9	89.94	89.98	89.98	89.96	89.98	89.98
Unit cell angle gamma (degrees)	89.9	89.96	90.01	90	90.02	90	90.03
Total Energy (Kcal/mol)	61	70	63.3	42.4	81.2	144	38.9
Bonds contribution (Kcal/mol)	10.4	11.8	11.6	9.4	12.2	12.6	12.8
Angles contribution (Kcal/mol)	89.5	92	84.7	81.2	87	92.5	68.3
Torsion contribution (Kcal/mol)	29	30	32.1	29	32	28.6	13
vdW contribution (Kcal/mol)	2.5	8.5	6.38	-3.62	10	10.1	1
Electrostatic contribution (Kcal/mol)	-71	-72	-71.6	-73.6	-60.7	0	-57.2
Computed density (g/cc)	1.483	1.489	1.504	1.479	1.507	1.492	1.523

† Legend: 1: N_R,O_3; 2: N_2,O_3; 3: N_2,O_R; 4: N_R,O_R; 5: N_2,O_2; 6: N_2,O_3; 7: N_3,O_3

* Calculated without electrostatic charge interactions.

Density, unit cell dimensions, and the magnitude of energy contributions from table 4.1 were considered when choosing structure 2 as the one which more closely resembles available experimental data.

PMDA-ODA polyimide was minimized using full periodic boundary conditions. The resulting structure was a simple orthorhombic unit cell. The cell parameters are shown in Table 4.2. A triclinic symmetry was assumed for the simulations, this provided the opportunity to know if these values deviated from the suspected orthorhombic dimensions. As indicated in table 4.2, all these angles were so close to 90° that an orthorhombic unit cell was undisputable. This fact was confirmed experimentally. However, it was also recently reported that high resolution transmission microscopy on single crystals of PMDA-ODA polyimide indicated that one angle, γ oscillates $\pm$ 5° from 90°.[38] These fluctuations are averaged in our bulk powder samples, therefore providing perfect orthorhombic dimensions. Recent attempts have also been made to elucidate the superstructure of PMDA-ODA polyimides with alternative molecular simulation techniques.[39]

Table 4.2. Unit cell parameters of PMDA-ODA polyimide.

	Results from Simulation	Results from Experiment	Difference from Simulation (%)	Literature Results *	Difference from Simulation (%)
a (Å)	6.76	6.76	0.0	6.31	7.1
b (Å)	3.92	3.91	0.0	3.97	1.3
c (Å)	32.13	31.99	0.0	32.00	0.0
α (degrees)	89.94	90.00	0.1	90.00	0.1
β (degrees)	90.74	90.00	0.8	90.00	0.8
γ (degrees)	89.96	90.00	0.0	90.00	0.0
Cell Volume (Å^3)	852.76	845.55	1.2	801.62	6.6

* Kazaryan,[5] most widely accepted published cell parameters for PMDA-ODA.

Several conformations have been proposed for PMDA-ODA polyimide. Two of those possible conformations are shown in Figure 4.19. The *propeller* conformation emerged from the energy minimizations, irrespective of the initial atomic coordinate input. This conformation is more likely to form due to the stronger effect of intramolecular hindrance over intermolecular interactions. The strain in bond angles contribute almost 70% to the total conformational energy. This is a reflection of the inherent constraints posed by the aromatic nature of the chain structure. Torsional effects accounted for 23% of this energy and the rest was attributed to bonding constraints.

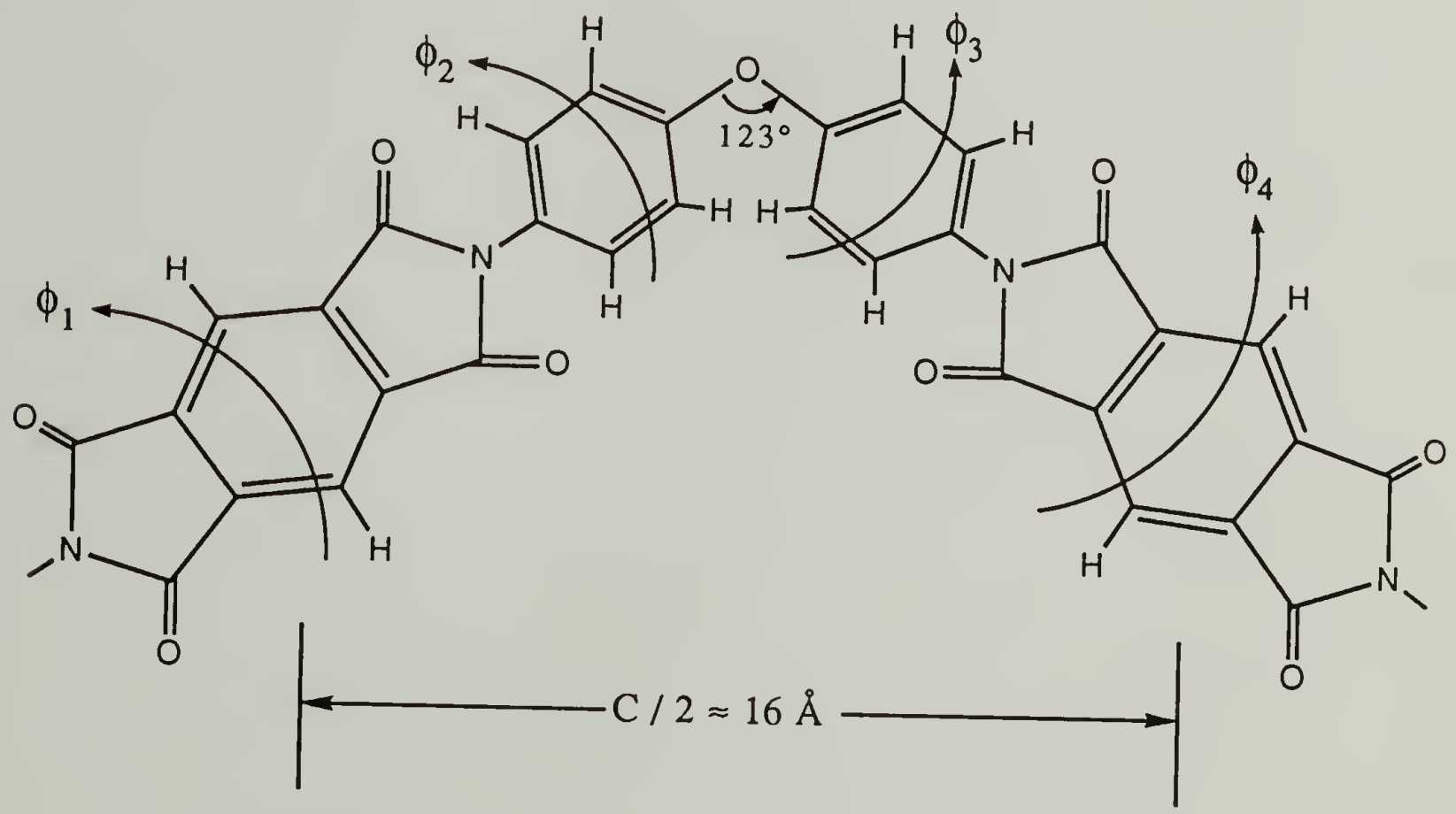

Chair Conformation: $\phi_1 = \phi_4, \phi_2 = \phi_3$

Propeller Conformation: $\phi_1 = -\phi_4, \phi_2 = -\phi_3$

Figure 4.19. PMDA-ODA conformational model as proposed by Lukasheva, et al.[6]

Table 4.3 shows the estimated bond lengths, twist and valence angles for PMDA-ODA. Most of the geometrical parameters presented in this table are similar to values from previous estimations in PMDA-ODA polyimide,[40] from 4,4'-bis (phthalimide) diphenyl ether,[41] and from N-(a-Glutarimido)-4-bromophthalimide.[42]

Table 4.3. Geometrical attributes of the minimized structure 2 of PMDA-ODA polyimide.

Bond Distances (Å) :

CPh-N	1.33	CPh-O	1.38	(CH-CH)Ph	1.41
CPh-H	1.22	CO-N	1.29	C=O	1.22
CO-C	1.36	(C-C)imide	1.39	(C-H)imide	1.02
(CH-C)imide	1.41	(CH-CO)Ph	1.41	(CH-CN)Ph	1.41

Length of a repeat unit:	17.63 Å
Length of a Imide unit (N-N):	6.51 Å
Length of an Phenyl unit (CN-O):	4.23 Å

Valence Angles (degrees) :

Ph-O-Ph	122.91	N-C=O	127.05	CO-N-Ph	125.68
(C-C-H)imide	121.83	(CH-C-H)Ph	118.66	CO-CH_CH	120.85
CN-CH-CH	120.96	N-CO-C	109.81	CO-C-C	105.26
CH-C-C	122.02	C-CH-C	116.26	Ph-C-N	120.95
C-C=O	122.87				

Dihedral angles (degrees) :

Phenyl-Phenyl:	31.64	Ph-Imide:	56.31

As can be observed from Table 4.2, a comparison of the unit cell measurements with those obtained experimentally by X-ray diffraction show errors smaller than 1% in any given direction. Since molecular mechanics minimization routines were done at absolute zero, differences between simulation and experiment were expected to arise.

Other errors which may not show in Table 4.2 can be attributed to the lesser accuracy in measuring the less intense higher angle reflections. The a-unit cell dimension fitted only with the strongest reflections yields 6.45 Å instead of the 6.76 Å obtained with all others taken into account. Larger anomalies were encountered when the data for the a-dimension was compared with a literature value. The degrees of freedom or instability of the ether linkage will assist in the development of less energetically favorable packings, that is, those deviating from the ideal planar zigzag with $P2_1$ symmetry. This is true especially when chain mobility is hindered, as it would occur as more solvent is evaporated and as the glass transition rises during cure.

It is important to note that the simulated diffraction patterns come directly from the minimized unit cell in periodic boundary conditions, no refinement was carried out. As mentioned above, a triclinic unit cell was assumed in order to avoid geometrical restrictions on the computation of unit cell parameters. The same assumption was applied for the simulation of X-ray diffraction patterns, all possible reflections for a triclinic unit cell were obtained. The resulting unit cell angles were all 90°±1°. The initial guesses on crystallite size were made based on the experimentally obtained values from an experimental diffractometer scan using the width at half height of the (002), (101) and (010) reflections. The crystallite size was then modified until a match was obtained between experimentally obtained intensities and simulated intensities. In order to compare with simulation, the intensities of the experimentally obtained scans had to be corrected for polarization and temperature factors and its background had to be carefully removed.

The minimized conformation showed twist angles of ~ 31° between the zigzag plane and the phenyl ring unit. A twist angle of ~ 26° between the zigzag plane and the imide ring plane was observed. That is, the angles between the phenyl-phenyl planes of is 62°, the angle between the phenyl-imide planes is 57°and the angles between the imide

ring plane and that of its adjacent repeat units is then 52°. The valence angle of the ether linkage between phenyl rings was calculated to be 123°. Values of this angle from the works quoted in previous sections are: Kazaryan [4]: 123°, Conte [5]: 130°, and Lukasheva [6,7]: 124°. Recently, a value of 126° has been optimized for a thermoplastic polyimide.[43]

Table 4.4. Comparison of PMDA-ODA polyimide reflections observed by X-ray diffraction and simulation techniques.

	Diffractometer Scan		Photographic method		Simulated Cerius™	
hkl	d (Å)	2θ	d (Å)	2θ	d (Å)	2θ
002	16.50	5.35	15.95	5.53	16.07	5.50
004	8.18	10.81	7.96	11.11	8.03	11.01
006			5.37	16.50	5.36	16.55
008			4.00	22.21	4.02	22.13
101	6.43	13.75	6.36	13.92	6.62	13.37
102	6.10	14.52	5.99	14.78	6.23	14.21
103	5.61	15.79	5.49	16.14	5.72	15.49
010	3.91	22.75	3.91	22.73	3.92	22.66
111,112	3.33	26.80	3.33	26.76	3.37	26.43
					3.31	26.90
016			3.20	27.87	3.15	28.37
114	3.13	28.51	3.11	28.69	3.12	28.67
1010			2.92	30.60	2.90	30.80
118			2.60	34.48	2.58	34.78
212			2.48	36.20	2.53	35.52
1013			2.33	38.45	2.32	38.78
300,0112			2.19	41.20	2.25	39.99
					2.20	41.06

The conformational analysis of diphenyl linkages have been summarized previously.[44] The study predicted *twist* conformations for the -CO- linkage by the usage of energy maps which showed minima near (38°, 38° and 142°,142°). These rotation minima as well as their listed values for the valence angle are within reasonable agreement of our results.

Utilization of periodic boundary conditions, as it was done in our case, will lead to a more realistic value of these angles. A *twist* conformation for the C_{ph}-O-C_{ph} system can be attributed to a balance between the steric interaction of of the hydrogens and the planarization tendency due an electron delocalization induced by the lone pair of electrons in the oxygen molecule. A "Morino" structure is expected in the absence of conjugation, where steric interaction of the hydrogens in the phenyl rings is dominant (0°,90°). The planar conformation (0°,0°) is only approximated when the conjugation is so strong that the π-electron overlap is predominant against any other opposing force. A butterfly conformation would be possible only when the steric interaction coming from the central group, oxygen in our case, predominates. Figure 4.20 illustrates these conformations.

Planar (0°,0°)

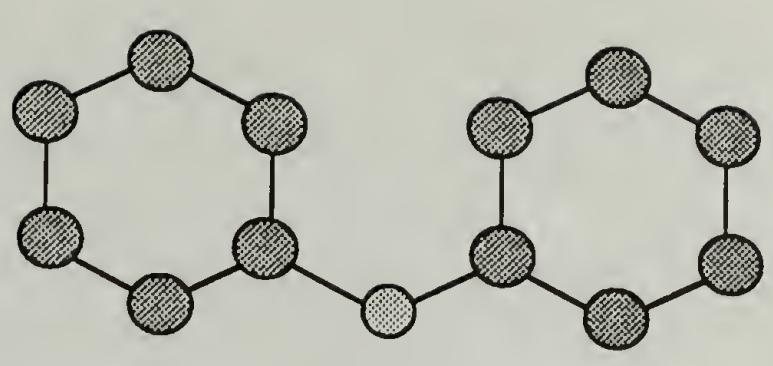

Butterfly (90°,90°)

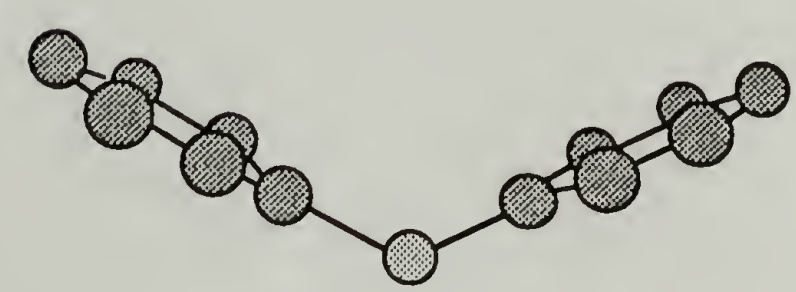

Twist ($\psi = -\psi$)

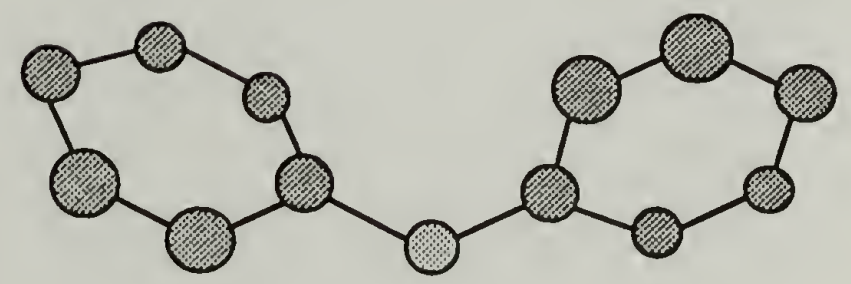

Morino (0°,90°)

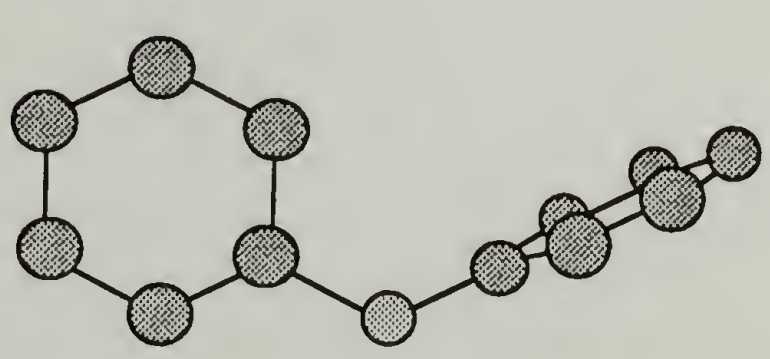

Figure 4.20. Possible conformations provided by the nature of the diphenyl linkage.

4.4 Conclusions

Usually polyimides are extremely difficult to characterize because so much of the data obtained are associated with samples of low degree of crystallinity. Because of the increasingly availability of highly crystalline samples the structure of pyromellitic dianhydride-di-(4-aminophenyl)ether (PMDA-ODA), a commercially important polyimide, was examined again. An energetically feasible conformation of highly ordered PMDA-ODA polyimide and associated unit cell as determined by molecular simulation are consistent with all of our experimental the X-ray and spectroscopic measurements. An orthorhombic unit cell with dimensions of a = 6.76 Å, b = 3.91, and c = 32.13 Å has been proposed. The structural parameters of the chain have been calculated. The "propeller" planar zigzag conformation is determined to be the favorable one in crystalline domains. The relative orientation of the phenyl rings of the C_{ph}-O-C_{ph} linkages have also been calculated. The twist angles of the phenyl rings and the imide rings with respect to the idealized planar zigzag conformation are 31 and 26° respectively. These angles were determined using molecular simulation techniques. These values are consistent with infrared measurements. The crystallite size estimations, the dimensions obtained from simulation were as follows: a = 110 Å, b = 85 Å and c = 150 Å. The experimentally determined crystal dimensions were: L_{002} = 107 Å, L_{101} = 92 Å, L_{010} = 117 Å, with an average reliability of ± 10 Å. It is clear that a higher degree of crystallinity was obtained with the powder in contrast to the polyimide films usually obtained. X-ray diffraction patterns obtained exhibit significant differences for the two types of samples. Differences in the infrared spectra are more subtle, but they do demonstrate the existence of various environments. It can be shown that the change in the intensity of some bands is linked to the degree of order in the polymer.

4.5 References

(1) Molis, S.E.; Saraf, R.; Hodgson, R.T.*Antec* **1991**, 1700.

(2) Coburn, J. C.; Pottiger, M. T. *Antec* **1993**, 656.

(3) Ree, M.; Nunes, T.L.; Czornyj, G.; Volksen, W. *Polymer* **1992**, *33*, 1228.

(4) Kazaryan, I.G.; Tsvankin, D. Y.; Ginzburg, B.M.; Tuichiev, S.; Korzahvin,L.N.; Frenkel, S. Y. *Polym. Sci. USSR* **1972**, *14*, 1344.

(5) Conte, G.; D'Ilario, L.; and Pavel, N.V. *Journal of Polym. Sci. Polym. Phys. Ed.* **1976**, *14*, 1553.

(6) Lukasheva, N.V.; Zubkov, V.A.; Milevskaya, I.S.; Baklagina, Y.G.; Strunnikov, A.Y. *Polym. Sci. USSR* **1987**, *29*, 1453.

(7) Lukasheva, N.V.; Milevskaya, I.S.; and Baklagina, Y. G. *Polym. Sci. USSR* **1989**, *31*, 471.

(8) Jennings, B.; Farris, R.J. *J. of Polym. Sci.: Part B: Polym. Phys.* **1994**, *32*, 1457.

(9) Ishida, H.; Wellinghoff, S.T.; Baer, E.; Koenig, J.L. *Macromol.* **1980**, *13*, 826

(10) Yang, X.; Hsu, S.L. *Macromol.* **1991**, *24*, 6680.

(11) Bicerano, J. *Computational Modeling of Polymers*; Marcel Dekker, Co.: N.Y., 1992.

(12) Roe, R.J. *Computer Simulation of Polymers*; Prentice Hall. Englewood Cliffs: N.J., 1991.

(13) Hobson, R.J.; Windle, A.H. *Polym.* **1993**, *34*, 3582.

(14) Blundell, D.J. *Polym.* **1992**, *33*, 3773.

(15) Mayo, S. L.; Olafson, B.D.; Goddard III, W.A. *J.Phys.Chem.* **1990**, *94*, 8897.

(16) Gasteiger, J.; Marsili, M. *Tetrahedron* **1980**, *36*, 3219.

(17) Fletcher, R.; Powell, M.J.D. *The Computer Journal* **1963**, *6*, 163.

(18) Factor, B.J.; Russell, T.P.; Toney, M.F. *Macromol.*, **1993**, *26*, 2847.

(19) Russell, T. P.; Brown, H.R. *J. of Polym. Sci. Phys., Part B: Phys.* **1987**, *25*, 1129.

(20) Boehme, R.F.; Cargill III, G.S. into *Polyimides: Synthesis, Characterization and Applications*; Ed. K.L.Mittal. Plenum Press: N.Y., 1, 461, 1984.

(21) Hunter, C. A.; Sanders, J. K. M. *J. Am. Chem. Soc.* **1990**, *112*, 5525.

(22) O'Mahoney, C. A.; Williams, D. J.; Colquhoun, H. M.; Mayo, R.; Young, S. M.; Askari, A.; Kendrick, J.; Robson, E. *Macromol.* **1991**, *24*, 6527.

(23) Johnson, C.; Xu, H.; Wunder, S.L.; Houlihan, F.M.; Chin, E. *J. of Polym. Sci., Part B: Polym. Phys.* **1992**, *30*, 1409.

(24) Perez, M. A.; Ren, Y.; Farris, R. J.; Hsu, S. L. *Submitted for publication.* **1994**.

(25) Boese, D.; Lee, H.; Yoon, D.Y.; Swalen, J.D.; Rabolt, J.F. *J. of Polym. Sci., Part B: Polym. Phys.* **1992**, *30*, 1321.

(26) Snyder, R.W.; Thomson, B.; Bartges, B.; Czerniawski, D.; Painter, P.C. *Macromol.* **1989**, *22*, 4166.

(27) Silverman, B. D. *Macromol.* **1989**, *22*, 3768.

(28) Colthup, N. B.; Daly, L. H.; Wiberley, S. E. *Introduction to Infrared and Raman Spectroscopy;* Third edition ed.; Academic Press: N.Y., 1990.

(29) Higuchi, S.; Tsuyama, H.; Tanaka, S.; Kamada, H. *Spectrochim. Acta* **1974**, *30A*, 463.

(30) Gribov, L. A. *Intensity Theory for Infrared Spectra of Polyatomic Molecules*; Academy of Sciences of USSR Press: Moscow. 79, 1963.

(31) LeFévre, R. J.; Sundaram, A.; Sundaram, K. M. *Bull. Chem. Soc. Japan* **1962**, *35*, 690.

(32) Varsanyi, G. *Vibrational Spectra of Benzene Derivatives*; Academic Press: New York, 1974.

(33) Schmid, E.D.; Brosa, B. *The J. of Chem. Phys.* **1972**, *56*, 6267.

(34) Venkatesh, G.M.; Shen, D.Y.; S.L.Hsu *J. of Polym. Sci.: Polym. Phys. Ed.* **1981**, *19*, 1475.

(35) Tiller, A.R. *Macromol.* **1992**, *25*, 4605.

(36) Streitwieser, Jr.; Heathcock, C.H. *Introduction to Organic Chemistry*; Macmillan Publishing Co, Inc.: N.Y.,1073, 1976.

(37) Wellinghoff, S.T.; Ishida, H.; Koenig, J.L.; Baer, E. *Macromol.* **1980**, *13*, 834.

(38) Ojeda, J. R.; Martin, D. C. *Macromol.* **1993**, *26*, 6557.

(39) Poon, T. W.; Saraf, R. F.; Silverman, B. D. *Macromol.* **1993**, *26*, 3369.

(40) Takahashi, N.; Yoon, D.Y.; Parrish, W. *Macromol.* **1984**, *17*, 2583.

(41) Matzat, Von E. *Acta Cryst.* **1972**, *B28*, 415.

(42) Petersen, C.S. *Acta Chem Scand.* **1969**, *23*, 2389.

(43) Okuyama, K.; Sakaitani, H.; Arikawa, H. *Macromol.* **1992**, *25*, 7261.

(44) Anwer, A.; Lovell, R.; Windle, A.H. in *Computer Simulation of Polymers*; edited by R.J. Roe. Prentice Hall. Englewood Cliffs: N.J., 41, 1991.

CHAPTER 5

CHARACTERIZATION OF THE ORIENTATIONAL ORDER OF PMDA-ODA POLYIMIDE FILMS

5.1 Introduction

Crystallinity and orientation represent important structural parameters in consideration of mechanical, thermal, and electrical properties of polyimide coatings. Coating performance is critical in demanding applications such as inter-layer dielectrics in semiconductor integrated circuitry and other packaging applications.[1] Studies were aimed at a better understanding of the solidification process of this polyimide in restricted geometries, such as in very thin coatings, as well as the interfacial layer between the polyimide and substrate. In these cases, polyimides are confined geometrically so that individual chains are unable to adopt the full range of conformations available in a bulk material. Studies of thin polyimide films are important as both rigid and semi-flexible polyimides are known to develop a significant degree of anisotropy when utilized as coatings. The anisotropy of these films in terms of their elasticity coefficients has been previously measured.[2] In addition, the nature of the interfacial layer is important and relevant as bonding of polyimide with substrate may significantly influence the occurrence of cohesive failure of coatings.

PMDA-ODA is provided by E.I. Dupont deNemours as a 10-20% solution of polyamic acid precursor in N-methyl 2-pyrrolidone (NMP). The in-plane isotropy

observed in virtually all polyimide films probably occurs as a result of film shrinkage under the constraining influence of a substrate. In the absence of a thermal gradient or chemical reaction when spin-cast onto substrates, the orientation process represents a competition between chain relaxation and film shrinkage during solvent loss, resulting in the inability to relieve local stresses and formation of in-plane orientation. Imidization in PMDA-ODA is achieved by heating. Anisotropy is known to be induced during the spin coating process of the polyamic acid. It is, however, uncertain whether the degree of anisotropy is maintained during curing.

The anisotropic nature of polyimide films has been observed by numerous techniques such as wide-angle X-ray diffraction, birefringence, conoscopy, optical wave guide spectroscopy, dielectric loss measurements, and attenuated-reflectance Fourier transform infrared spectroscopy.[3-8] Quantitative information on the degree of anisotropy and the related micro-structures as a function of film thickness for thermally cured polyimide films has yet to be reported. The microstructures and degree of anisotropy in polyimide films can be characterized by orientation of the pyromellitimide groups with respect to the plane of the substrate. This orientation is most conveniently measured utilizing grazing angle infrared techniques. Vibrational spectroscopy is a localized technique capable of measuring changes in chain conformation and packing, especially when accurate band assignments and polarization characteristics, i. e. transition moments, are defined. PMDA-ODA polyimide band assignments and characterization of transition moment directions have been provided by prior studies.[9,10]

Gold was chosen as substrate because of its limited chemical reactivity with polyamic acid. Extensive studies have been performed on reflectivity of electromagnetic waves for multi-layered systems, including both dielectric and metallic substrates.[11-17] The boundary conditions are such that at grazing angles external reflection infrared spectroscopy of adlayers on metallic substrates measures only the transition moments

which have components perpendicular to the substrate surface (p-polarization). Although significant anomalies and spectral distortions exist with utilization of grazing angle infrared spectroscopy,[18,19] application of this technique in studies of polyimides adsorbed onto metals has proven extremely useful.[20,21] Films thicknesses in the range of 75 Å to 750 Å were examined in this study. Although this technique is applicable for films thicker than 1000 Å, the computational complexity is greatly increased to account for decreases in the mean square electric field intensity as a function of distance from the substrate. Isotropic infrared reflectance theory and its applications [22-24] have recently been modified and applied to optically anisotropic monolayers on an isotropic low-absorbing substrates.[25] Utilizing these methods, information on lateral and axial orientations is obtained by a quantitative analysis of spectroscopic data. Spectroscopic analysis of PMDA-ODA polyimide films on a metallic substrate is reported in this study. Results on dielectric substrates shall be reported shortly.

5.2 Experimental

The precursor, polyamic acid, was obtained from E.I. Dupont deNemours and received as 20% of solids by weight in N-methyl-2-pyrrolidone (NMP). The solution was diluted with di-methyl acetamide (DMAc) to the appropriate concentrations. The solutions were spin cast onto gold coated glass slides, obtained from Brysen Optical Corporation, at 4000 rpm. The gold layer on these glass slides had an average thickness of ~2000 Å. The samples were then placed on a hot plate for 15 minutes at 85 °C and cured at 225 °C in nitrogen atmosphere for 1 hr. Thickness was determined with a Rudolph Research Ellipsometer AUTOEL®-II using the 6328 Å line (0.2 mW) reflected at a 70° angle with respect to surface normal. A series of nine measurements were

performed for gold surfaces with and without the adsorbed polyimide. More details on the measurement of film thickness are provided in Appendix B. Film continuity and roughness in the substrate and adsorbed polymer were measured with a Zygo optical phase interference microscope Maxim3D 5800. Average surface roughness was found to be in the range of 8-10 Å. A 20X, 40X and 100X Mirau lens was utilized in these measurements. The smaller magnification lens, 20X, provides a vertical resolution of ~1 Å and a lateral resolution of ~1 μm. If supported on a substrate and with removal of a portion of the film, thickness can also be measured directly by the profilometer.

Electron diffraction studies were performed with a JEOL 100CX TEM. For these experiments, the polyimide films were removed from the gold coated slides by first shearing the outermost portion of the gold layer partially under water. The films were then picked up with a carbon coated grid. Samples obtained utilizing this technique were relatively undamaged and unwrinkled. These features are required for acquisition of reliable film tilting data. Gold still adhered to some sections of the film which facilitated determination of interplanar spacings in the polymer by providing a direct calibration using spacings known for gold.

Infrared spectra were obtained using a Nicolet 60SXB Fourier transform infrared spectrometer equipped with a Specac external reflectance attachment. 1024 scans at a resolution of 2 cm^{-1} were collected. The incident angle of the p-polarized radiation on the sample was maintained at 84° for all measurements. Transmission measurements for the polyimide powder in KBr pellets were obtained in a Bruker 113 FTIR. In this case, 256 scans were signal averaged and the spectral resolution was maintained at 2 cm^{-1}. Highly crystalline polyimide powder samples were created by a one step cure at 200°C under 200 psi of nitrogen pressure. Details associated with the structure of these powders were previously provided.[26,27] As shown in Figure 5.1, X-ray diffraction analysis in

conjunction with density measurements reveal that this polyimide powder has a much higher degree of crystallinity and larger crystalline domains than thin films.[28]

Transmission wide-angle X-ray experiments were performed in vacuum with a Statton camera. Ni filtered CuKα radiation was employed. All film or powder samples were annealed for 1 hr at 300 °C.

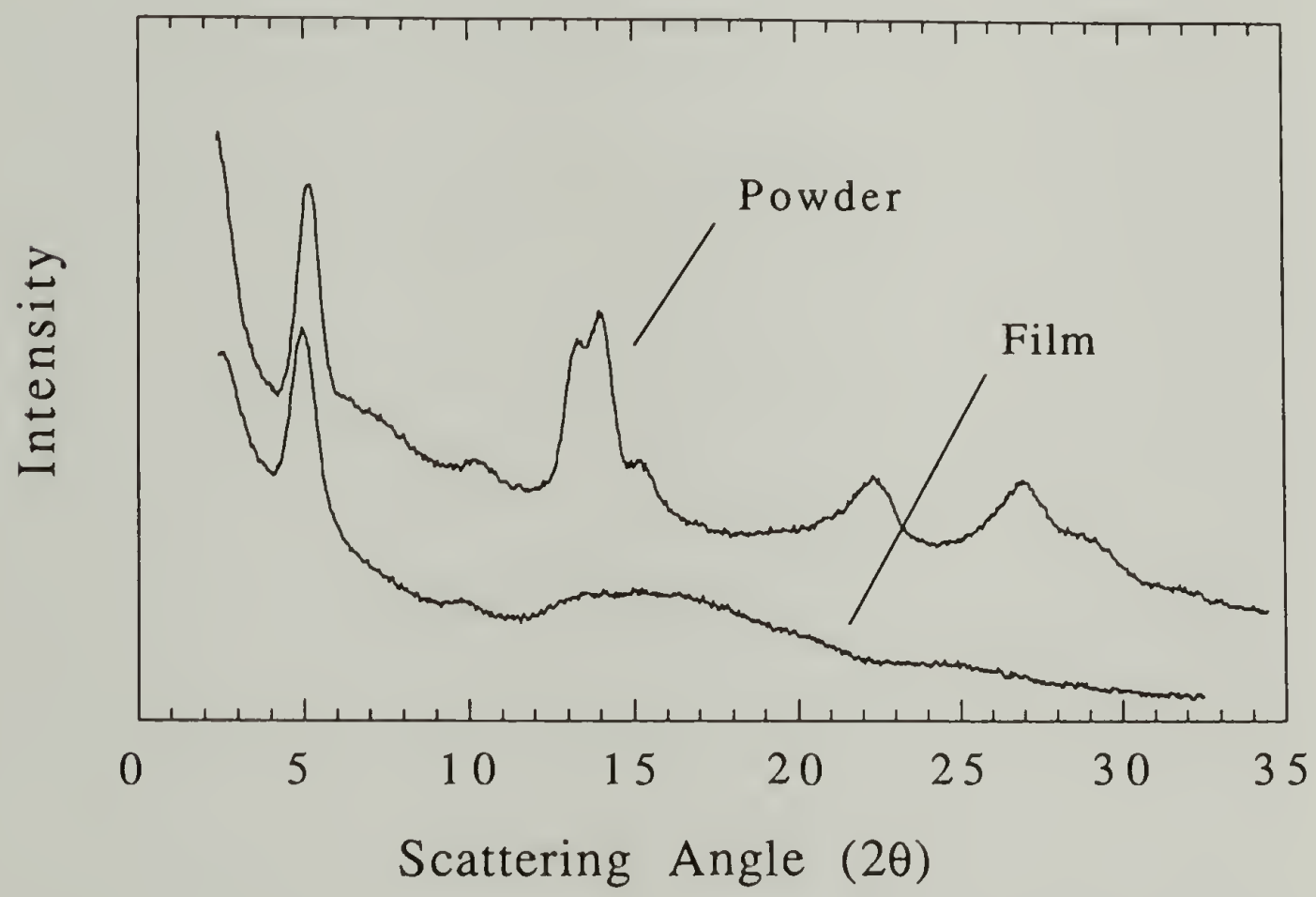

Figure 5.1. Comparison of wide-angle X-ray diffraction microdensitometer scans obtained for PMDA-ODA polyimide samples.

5.3. Review and Consequences of Reflectivity at Grazing Incidence. Infrared Range

The reflectivity theory for layered planar systems was formulated by Heavens,[11] Hansen,[12,13] and McIntyre.[14] Practical aspects of infrared reflectivity for monolayers adsorbed into metals were explored by Greenler,[29] who found experimentally that infrared absorption had a maxima for radiation incident at ≈ 88° from the plane normal. This grazing incidence condition provided an absorption enhancement that enabled the acquisition of spectra for a thin layer that may not have been observable otherwise. A great part of the experimental work in thin films and monolayers adsorbed on metals has been carried out by Allara, et. al., [18] who has pointed out anomalies and spectral distortions that arise when dealing with these systems. In addition, they have also studied the molecular orientation of these adsorbates. Dluhy, calculated optimal angles of incidence for infrared external reflection of monolayers deposited on water and metals.[22] Ishino and Ishida, utilized external reflection FTIR at Brewster's angle to obtain spectra for thick layers of hard and dark materials.[23] Yen and Wong have developed and experimentally verified approximate expressions for the characterization of longitudinal optical and transverse optical modes in the infrared reflectance spectra of polymeric films adhered to metal and dielectric substrates. [16] A different approach to orientation studies through the external reflection FTIR of molecules adsorbed in dielectric and metal substrates has been carried out by Buontempo and Rice, [17] who developed simplified formulations from classical electrodynamic theories.

In the infrared range, a metal such as gold will have nearly perfect reflectance at all angles of incidence. As McIntyre, [14] points out the electrical conductivity of a metal approaches its dc value at low optical frequencies. Whether in transmission or reflection, a phase change will take place at each boundary crossing. Phase changes in reflection are

given by the argument of the reflectivity coefficient for each polarization. The phase shift for the parallel component goes up abruptly near grazing incident angles, which implies a enhancement of the electric field intensity. A standing-wave electric field in the incident phase is produced under these conditions. The computation of phase changes is necessary for the obtainment of the reflectance and transmittance for the three phase systems. The calculated reflectance and transmittance are then occupied to obtain the mean square of the electric field amplitude. The electric field strength of the incident phase is minimally attenuated by a very thin polymeric film because of its low energy dissipation in this instance. It follows that the nature of the electric field near the substrate dictates the system's properties in the thin coating limit, that is when $k_2 \ll k_3$. The absorbance of an adlayer is obtained by comparing the reflectance obtained for a system with an adlayer to that obtained without it (k=0).

Application of the exact classical theories by Hansen and McIntyre to our three layer system follows. The general form of the Fresnel coefficients of reflection and transmission in stratified media, as derived from the Maxwellian equations of the propagation of electromagnetic disturbances for a linear isotropic substance, are given by equations 5.1-5.4 below:

$$r_{\perp jk} = \frac{\xi_j - \xi_k}{\xi_j + \xi_k} \tag{5.1}$$

$$r_{\parallel jk} = \frac{\hat{n}_k^2\ \xi_j - \hat{n}_j^2\ \xi_k}{\hat{n}_k^2\ \xi_j + \hat{n}_j^2\ \xi_k} \tag{5.2}$$

$$t_{\perp jk} = \frac{2\ \xi_j}{\xi_j + \xi_k} \tag{5.3}$$

$$t_{\parallel jk} = \frac{2\ \hat{n}_j\ \hat{n}_k\ \xi_j}{\hat{n}_k^2\ \xi_j + \hat{n}_j^2\ \xi_k} \tag{5.4}$$

r and t represent the reflection and transmission coefficients for the parallel and perpendicular polarizations. t and r represents the ratio of the transmitted or reflected complex electric field amplitude to that of the incident wave at a boundary between phases j and k. ξ is the angle dependent refractive index defined as:

$$\xi_j = (\hat{n}_j^2 - n_1^2 \sin^2\theta_j)^{1/2} \tag{5.5}$$

this expression is derived from the expression for the complex refractive index of the material, $\hat{n}_j = n_j - ik_j$, and Snell's law:

$$\hat{n}_j \sin\theta_j = n_1 \sin\theta_1 \tag{5.6}$$

where n_1 is the real refractive index of the transparent incident phase and θ_1 is the angle of incidence that infrared beam makes with the surface normal. Although, the position of ξ in the complex plane is uncertain. Hansen states, with reference to the physics involved, that in order to insure that phase jumps on reflection are positive and be between 0 and 2π the real part of ξ be always equal or greater than zero and its imaginary part be always equal or smaller than zero.

Now, consider the system described by Figure 5.2, where the incident medium is air, the substrate is an absorbing metal and the adlayer is a dielectric.

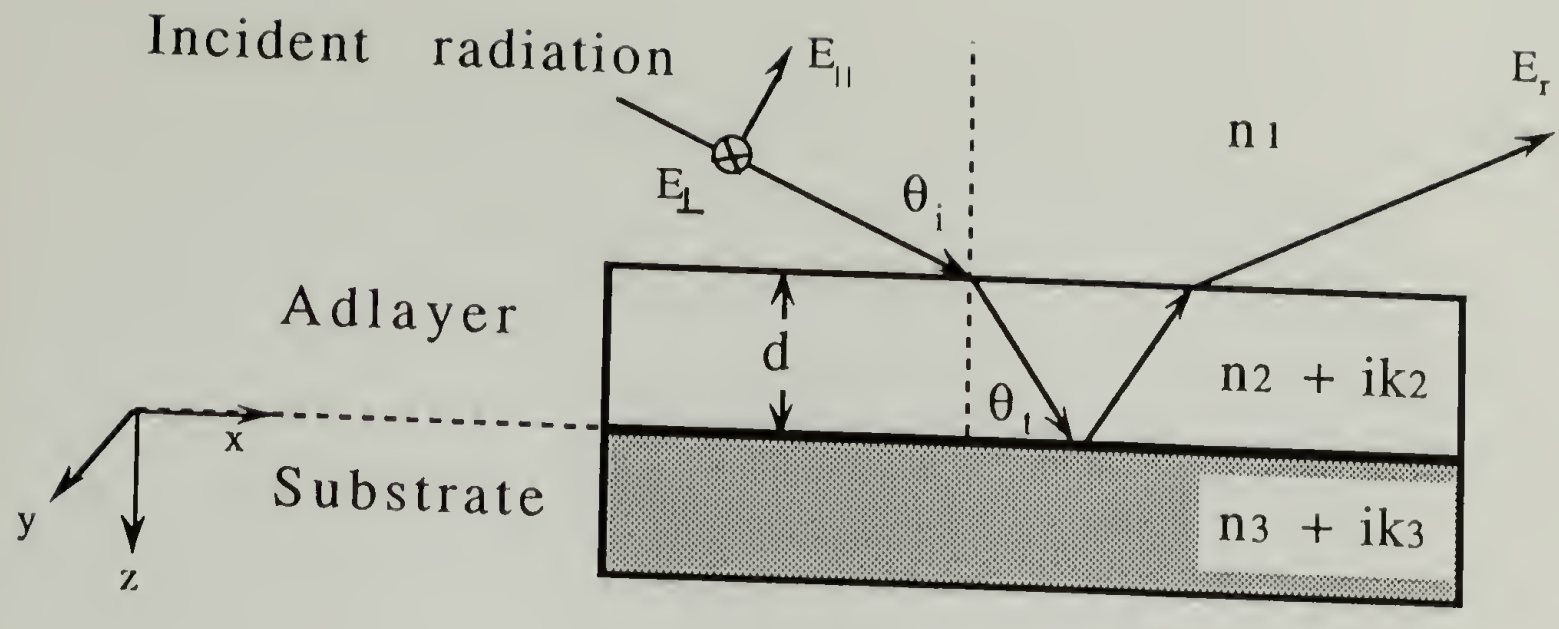

Figure 5.2 Coordinate frame used to define interaction of radiation with adsorbed polyimide film on metallic substrate.

The specific Fresnel formulas for this three-phase system are given by equations 5.7-5.10:

$$r_{\perp} = \frac{r_{\perp 12} + r_{\perp 23} e^{-2i\beta}}{1 + r_{\perp 12}\, r_{\perp 23} e^{-2i\beta}} \tag{5.7}$$

$$r_{\parallel} = \frac{r_{\parallel 12} + r_{\parallel 23} e^{-2i\beta}}{1 + r_{\parallel 12}\, r_{\parallel 23} e^{-2i\beta}} \tag{5.8}$$

$$t_{\perp} = \frac{t_{\perp 12}\, t_{\perp 23} e^{-i\beta}}{1 + r_{\perp 12}\, r_{\perp 23} e^{-2i\beta}} \tag{5.9}$$

$$t_{\parallel} = \frac{t_{\parallel 12}\, t_{\parallel 23} e^{-i\beta}}{1 + r_{\parallel 12}\, r_{\parallel 23} e^{-2i\beta}} \tag{5.10}$$

$$\beta = 2\pi \left(\frac{d_2}{\lambda}\right) \xi_{2} \tag{5.11}$$

here, d_2/λ_2 is the thickness of the second phase (adlayer) in wavelengths.

Once r and t have been computed, reflectance and transmittance can be obtained. Transmittance, 'T', is defined here as "the fraction of energy incident in the first phase that crosses the final interface into the semi-infinite final phase", 'f'. Reflectance is measured in the first (incident) phase. Equations 5.12-5.15 give the reflectance and transmittance equations for parallel and perpendicular polarizations:

$$R_{\parallel} = |r_{\parallel}|^2 \tag{5.12}$$

$$R_{\perp} = |r_{\perp}|^2 \tag{5.13}$$

$$T_{\perp} = \frac{\mathrm{Re}\,\xi_f}{\xi_1} |t_{\perp}|^2 \tag{5.14}$$

$$T_{\parallel} = \frac{\mathrm{Re}\,(\xi_f/\hat{n}_f^2)}{\xi_1} |\hat{n}_f t_{\parallel}|^2 \tag{5.15}$$

As mentioned above, a phase change will take place at each boundary crossing. For example, phase changes in reflection are given by the argument of the reflectivity coefficient for each polarization:

$$\delta_{\perp}^{r} = \tan^{-1}\left[\frac{\mathrm{Im}\, r_{\perp}}{\mathrm{Re}\, r_{\perp}}\right] \tag{5.16}$$

$$\delta_{\parallel}^{r} = \tan^{-1}\left[\frac{\mathrm{Im}\, r_{\parallel}}{\mathrm{Re}\, r_{\parallel}}\right] \tag{5.17}$$

Figure 5.3 illustrates the phase change which takes place at the air-gold boundary. It can be observed the phase shift for the parallel component goes up abruptly near grazing incident angles, which implies a enhancement of the electric field intensity. A standing-wave electric field in the incident phase is produced under these conditions. The computation of phase changes is necessary for the obtainment of the reflectance and transmittance for the three phase systems, which is described by equations 5.18 and 5.19:

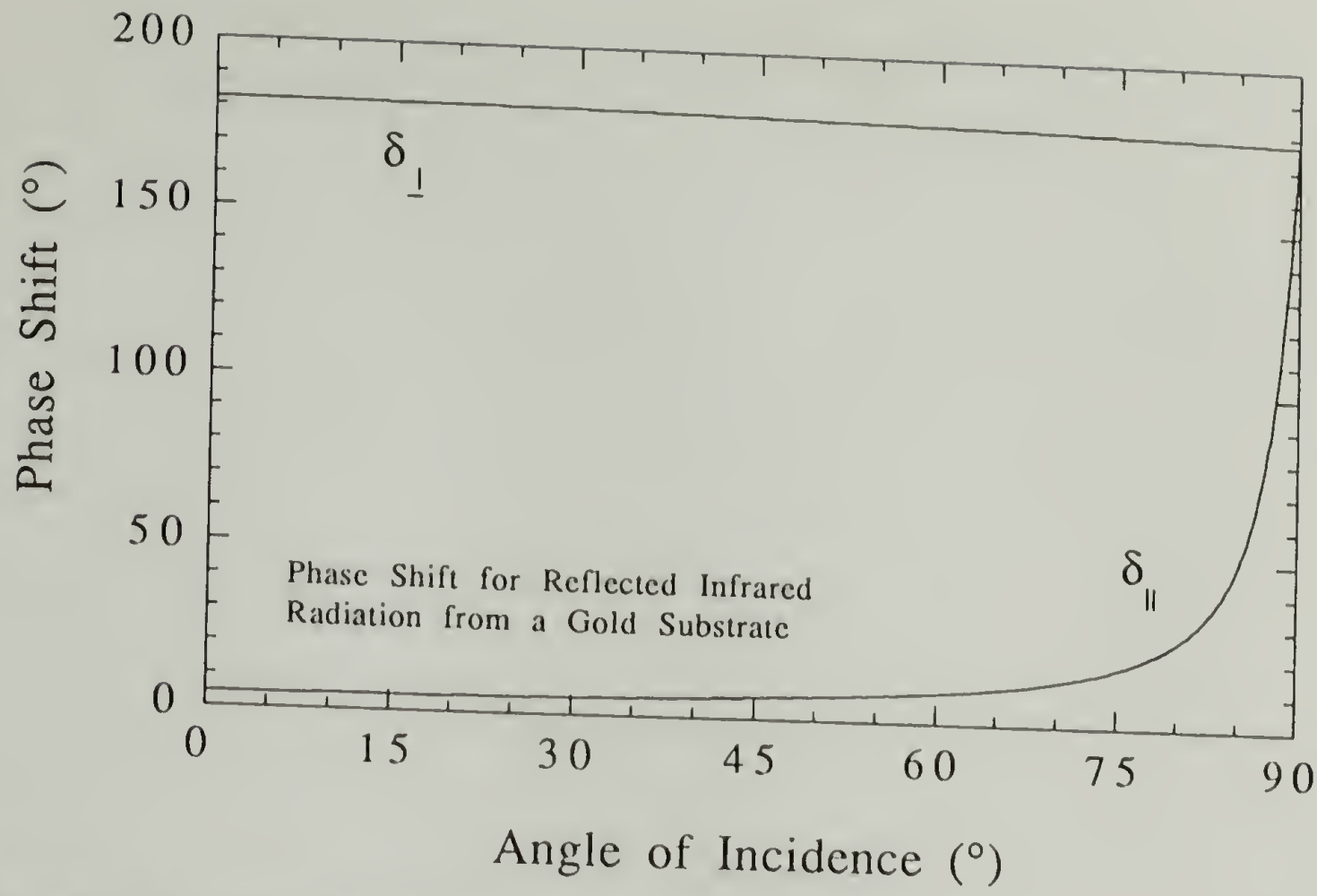

Figure 5.3. Phase shift at the interface of a metallic substrate as a function of angle of incidence.

$$R = \frac{R_{12} + R_{23} e^{4 \mathrm{Im}\beta} + 2 R_{12}^{1/2} R_{23}^{1/2} e^{2 \mathrm{Im}\beta} \cos(\delta_{23}^{r} - \delta_{12}^{r} - 2 \mathrm{Re}\,\beta)}{1 + R_{12} R_{23} e^{4 \mathrm{Im}\beta} + 2 R_{12}^{1/2} R_{23}^{1/2} e^{2 \mathrm{Im}\beta} \cos(\delta_{12}^{r} + \delta_{23}^{r} - 2 \mathrm{Re}\,\beta)} \tag{5.18}$$

$$T = Q \frac{|t_{12}|^2 \, |t_{23}|^2 \, e^{2 \mathrm{Im}\beta}}{1 + R_{12} R_{23} e^{4 \mathrm{Im}\beta} + 2 R_{12}^{1/2} R_{23}^{1/2} e^{2 \mathrm{Im}\beta} \cos(\delta_{12}^{r} + \delta_{23}^{r} - 2 \mathrm{Re}\,\beta)} \tag{5.19}$$

where,

$$Q_{\perp} = \left(\frac{\mathrm{Re}\,\xi_3}{\xi_1} \right) \tag{5.20}$$

and

$$Q_{\parallel} = \left\{ \left| \frac{\hat{n}_3}{n_1} \right|^2 \mathrm{Re} \left[\frac{(\xi_3 / \hat{n}_3^2)}{(\xi_1 / n_1^2)} \right] \right\} \tag{5.21}$$

The calculated reflectance and transmittance are then occupied to obtain the mean square of the electric field amplitude. The electric field strength of the incident phase is minimally attenuated by a very thin polymeric film because of its low energy dissipation in this instance. It follows that the nature of the electric field near the substrate dictates the system's properties in the thin coating limit, that is when $k_2 \ll k_3$. Figure 5.4 shows the intensity enhancement of the z parallel component which can then be obtained if electric field components plotted as a function of incident angle.

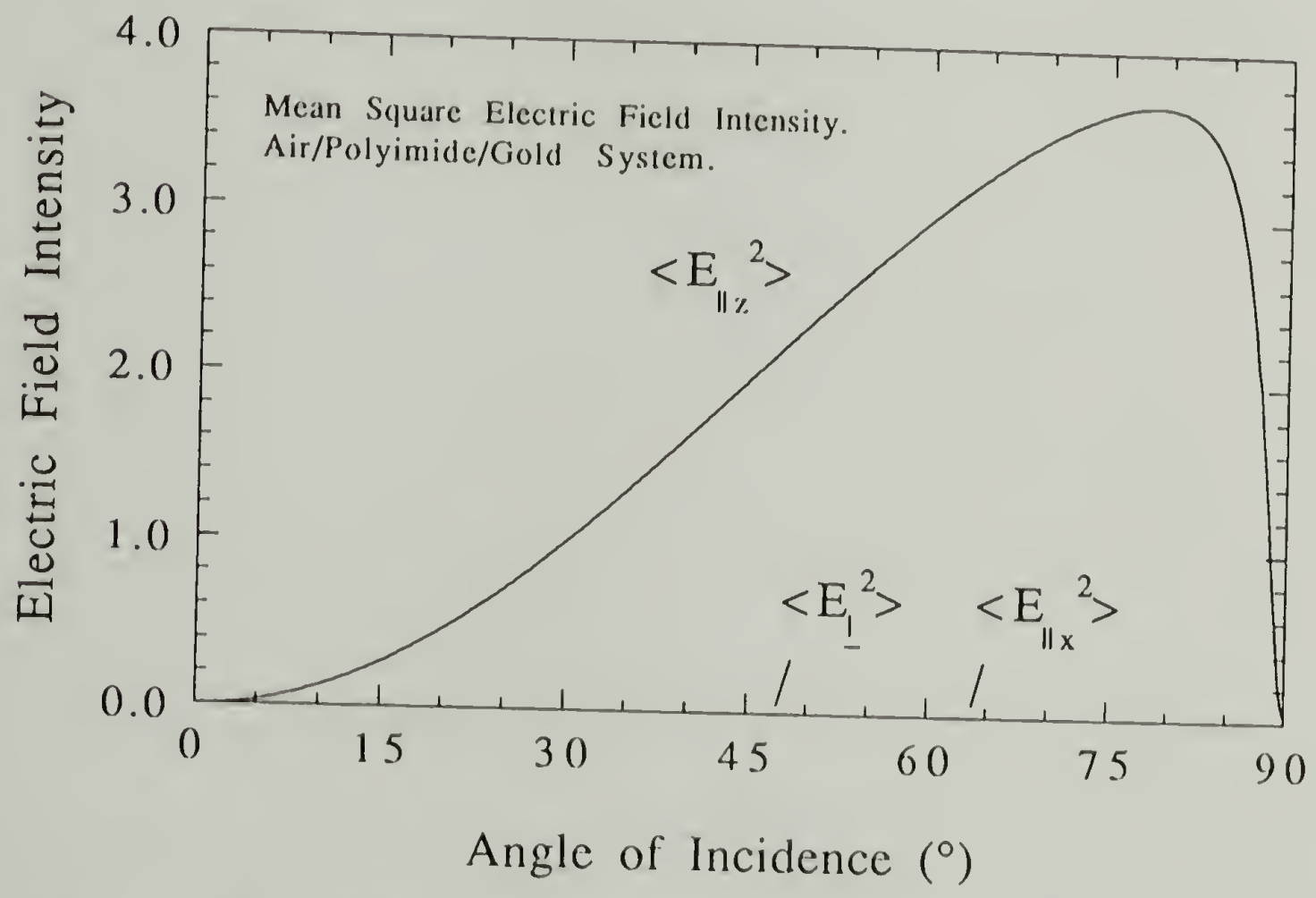

Figure 5.4. Mean square electric field intensity as a function of angle of incidence for IR radiation incident on a metallic substrate.

The mean square of the electric field amplitudes, as ratioed to that of the incident beam, for the first phase are given by equations 5.21-5.23:

$$\langle E_{\perp 1}^2 \rangle = [(1 + R_\perp) + 2\, R_\perp^{1/2} \cos(\delta_\perp^r + 4\pi(z/\lambda)\, \xi_1)] \tag{5.21}$$

$$\langle E_{\parallel 1x}^2 \rangle = \cos^2\theta\, [(1 + R_\parallel) - 2\, R_\parallel^{1/2} \cos(\delta_\parallel^r + 4\pi(z/\lambda)\xi_1)] \tag{5.22}$$

$$\langle E_{\parallel 1z}^2 \rangle = \sin^2\theta\, [(1+ R_\parallel) + 2\, R_\parallel^{1/2} \cos(\delta_\parallel^r + 4\pi(z/\lambda)\xi_1)] \tag{5.23}$$

where, θ is the angle of incidence or refraction for each layer. Equations 5.21-5.23 imply that, as z decreases, moving away from the metal's surface, the influence of the two components rendered insignificant in Figure 5.4 will increase. This would complicate the orientation analysis shown above for the case of very thick films, those of similar magnitude to that of the incident wavelength. An analysis of this sort will necessitate the mean square electric field intensity equations in the second medium where the wave would be evanescent. Equations 5.24-5.26 show these equations:

$$\langle E_{\perp 2}^2 \rangle = |t_\perp|^2 \exp(4\pi\, (z/\lambda)\, \mathrm{Im}\, \xi_2) \tag{5.24}$$

$$\langle E_{\parallel 2x}^2 \rangle = \left| \frac{\xi_2}{\hat{n}_2}\, t_\parallel \right|^2 \exp(4\pi\, (z/\lambda)\, \mathrm{Im}\, \xi_2) \tag{5.25}$$

$$\langle E_{\parallel 2z}^2 \rangle = \left| \frac{n_1 \sin\theta_1}{\hat{n}_2}\, t_\parallel \right|^2 \exp(4\pi\, (z/\lambda)\, \mathrm{Im}\, \xi_2) \tag{5.26}$$

The absorbance of an adlayer is obtained by comparing the reflectance obtained for a system with an adlayer to that obtained without it (k=0). Figure 5.5 shows a plot of absorbance versus angle of incidence for a 100 Å polyimide film on a gold substrate. In this figure the angle at which the maxima occurs is higher than that of Figure 5.4, this is due to a factor of $1/\cos\theta_1$ which arises due to the reflectivity change introduced by the adlayer in that component of the mean square electric field intensity.

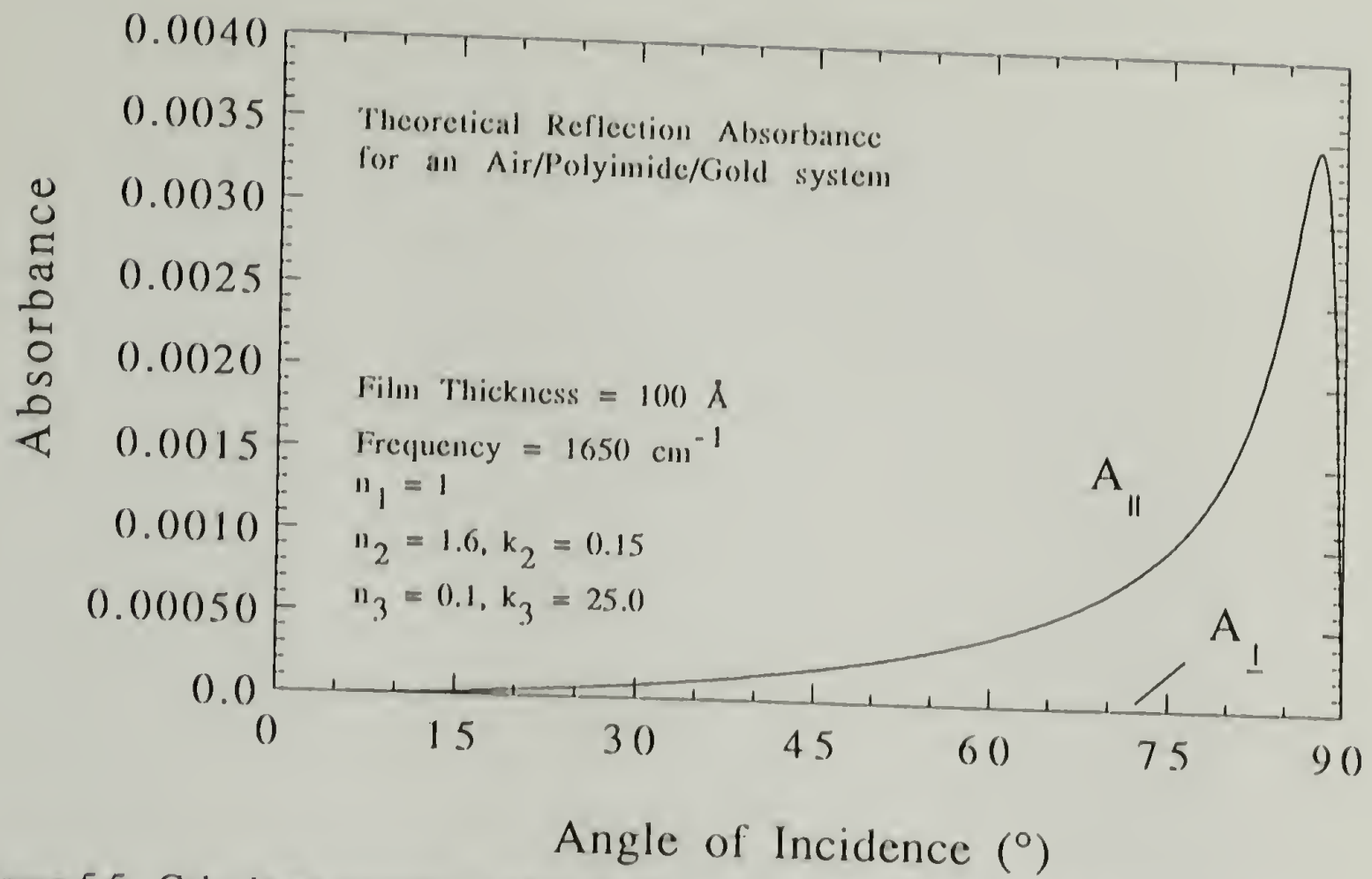

Figure 5.5. Calculated absorbance for an adlayer on a metallic substrate as a function of angle of incidence.

5.4 Method for Interpreting Film Anisotropy

The use of vibrational spectroscopy as an analytical tool to measure anisotropy is based on the measurement and analysis of relative band intensity and width. To derive structural information from reflection infrared experiments, care must be exercised in analysis to separate structural features from optical anomalies. This section provides analytical expressions from which reflected spectra can be computed for planar electromagnetic waves incident on optically anisotropic and absorbing thin films adsorbed on a metallic isotropic substrate. Several variations have been presented in the literature.[11-15] Because of the metallic substrate, only the p-polarized waves are present

in the adsorbed film. A quantitative analysis is sought for the absorption coefficient and transition moment direction of vibrational modes relative to the surface normal. With determination of the absorption coefficient and transition moment direction, structural information in terms of changing chain conformation and orientation may be derived.

The anisotropy of the polyimide film can be obtained by comparing the reflected spectrum to that obtained for an isotropic sample of the same thickness. Equation 5.27 relates the observed band intensity in the reflected spectrum to the expected value.[30]

$$\theta = \cos^{-1}\left(\sqrt{\frac{R_{obs}}{3\,A_{calc}}}\right) \tag{5.27}$$

Here, θ is the angle that a particular transition moment makes relative to the surface normal (z axis), R_{obs} is the experimentally obtained absorbance from reflection experiment, and A_{calc} is the calculated absorbance for film of the same film thickness. A direct analysis utilizing relative band intensity cannot be meaningful as reflected data are distorted due to dispersion effects. Transmission data from an isotropic polyimide sample were utilized to compute the frequency dispersion of the real part of the complex refractive index. The optical coefficients are necessary for generation of *isotropic* spectra of different film thickness. Molecular orientation in coatings can then be computed by comparison of peak absorbances of the experimental and calculated spectra of the same thickness. The intensity of a given mode is related to the transition moment by:

$$I \propto \left|\frac{\partial \mu}{\partial q} \cdot E\right|^2, \tag{5.28}$$

where E is the electric field vector, μ is the dipole moment, and q is the normal coordinate direction. If z is to be the direction parallel to the surface normal, the transition moment for a thin film geometry where only the parallel component of the electric field is a significant contributor to the intensity is dependent on θ at the surface by

$$\cos^2\theta \propto \left|\frac{\partial\mu}{\partial q} \cdot z\right|^2 . \tag{5.29}$$

As mentioned earlier, many variations for derivation of Fresnel's law for complex refractive indices exist. It is not the intent of this section to derive another variation but rather to show how the present analysis is applied in determining the absorption coefficient and transition moment direction of various vibrations for molecules at the interface. Transmission data at normal incidence from the material in isotropic form is necessary as an initial estimate in calculation of the optical constants n and k. This can be expressed by

$$\frac{I}{I_o} = \exp(-4\pi\nu k d) . \tag{5.30}$$

where I_o is the incident intensity, I is the transmitted intensity with the absorbing material present, ν is the frequency, d is the linear optical path through the pellet, and k is the absorption coefficient when sample concentration in the pellet is considered. The complex refractive index of the jth layer of an absorbing material is defined as:

$$\hat{n}_j(\nu) = n_j(\nu) + i\, k_j(\nu). \tag{5.31}$$

The fundamental relationship between n and k is given by the Kramers-Kronig relationship

$$n(\nu_j) = n_\infty + \frac{2}{\pi}\int_0^\infty \frac{k(\nu)\,\nu}{\nu^2 - \nu_j^2}\, d\nu, \tag{5.32}$$

where $n(\nu)$ and $k(\nu)$ are the frequency dependent real and imaginary components of the complex refractive index, respectively . n_∞ is the refractive index at infinite frequency (1.65). These optical coefficients are then utilized to simulate reflection data for the geometry used in the experiment. In this study, equation 5.32 can only be approximated

due to the finite frequency range of measurement. The transmission data of an isotropic sample serves as the initial *estimate* to compute the refraction index. A new spectra is then calculated and compared with experiments. This process is reiterated until a match is obtained for calculation and experiment. Upon refinement of the refraction index, both real and imaginary, an isotropic spectra at any angle of incidence can be calculated. The coordinate frame used for this calculation is shown in Figure 5.2 and the flow chart of the routine is described in Figure 5.6.

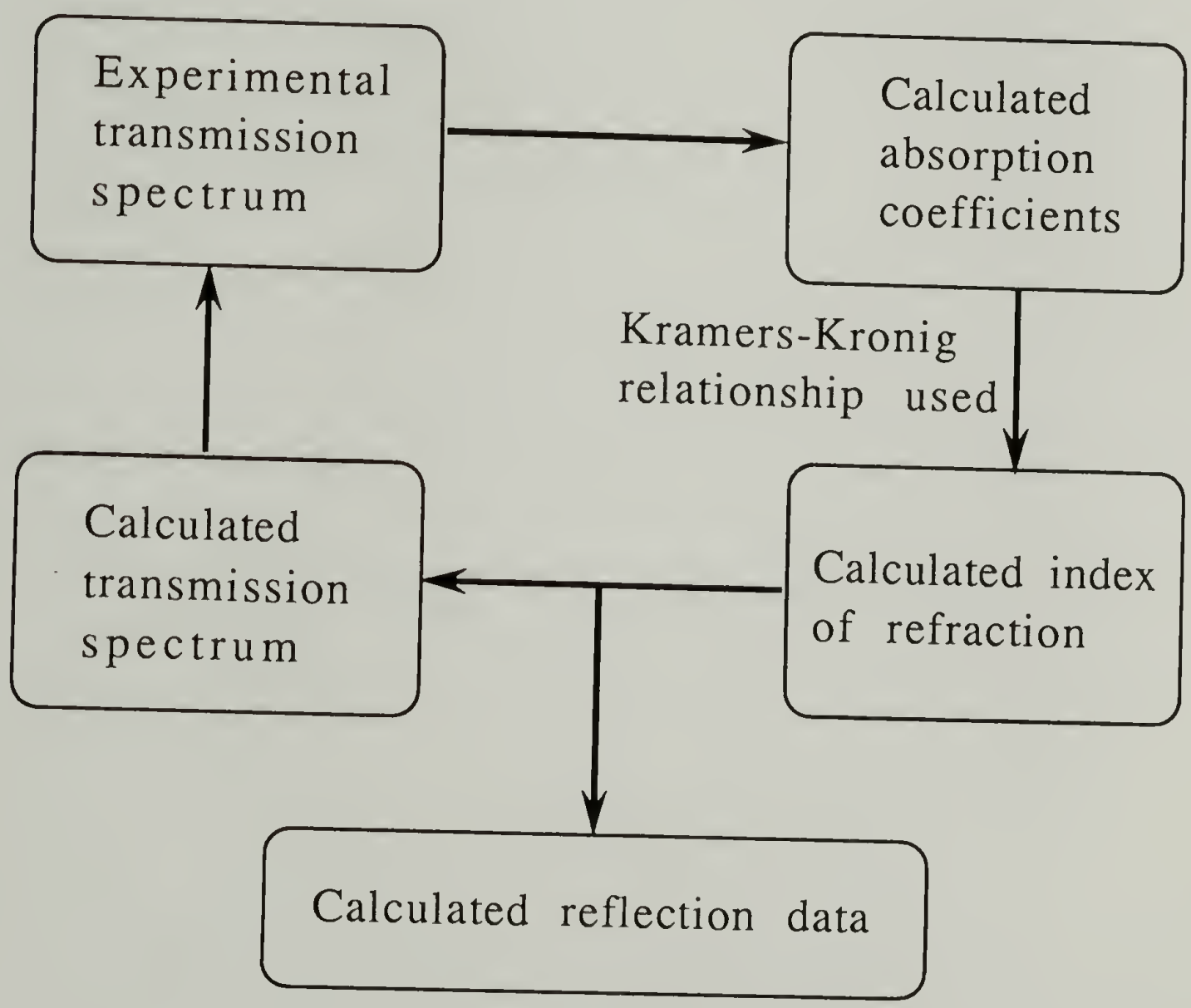

Figure 5.6. Flow chart of the routine employed in the calculation of the isotropic reflection spectra for different film thicknesses.

The optical coefficients obtained as a function of frequency for the in-plane region are shown in Figure 5.7.

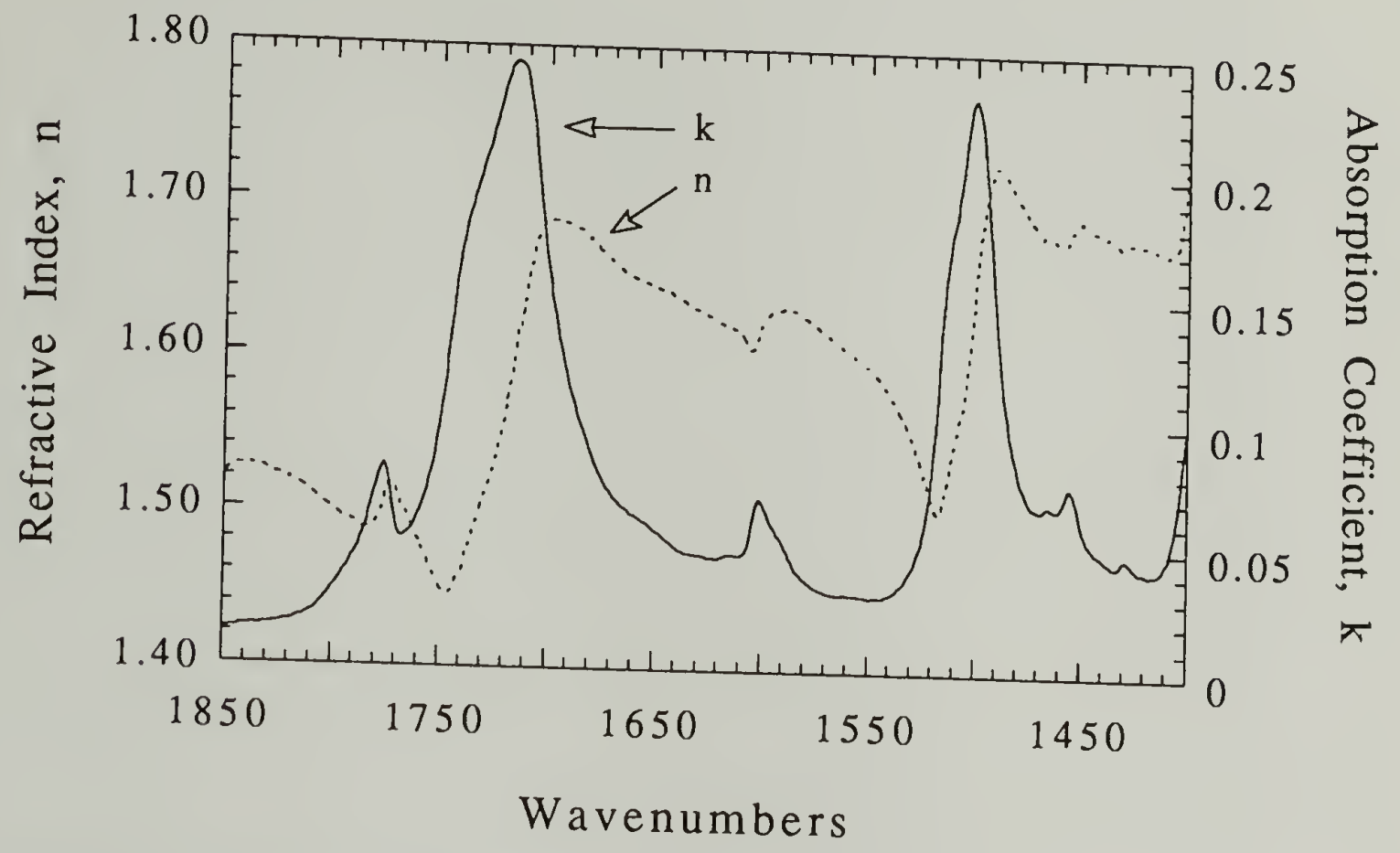

Figure 5.7. Calculated n(ν) and k(ν) for PMDA-ODA polyimide.

Computation of dispersion in the optical coefficients for the metallic substrate has been performed using the Drude model as described earlier.[31] The complex refractive index in the metal is given by:

$$\hat{n}_3 = n_3 + ik_3 \tag{5.33}$$

Here, the real component of the complex refractive index and the absorption coefficient are given as

$$n_3 = \sqrt{\frac{1}{2}\sqrt{\varepsilon'^2 + \varepsilon''^2} + \varepsilon'} \tag{5.34}$$

$$k_3 = \sqrt{\frac{1}{2}\sqrt{\varepsilon'^2 + \varepsilon''^2} - \varepsilon'}$$

(5.35)

constant respectively. Frequency dependencies are shown in equations 5.36 and 5.37:

$$\varepsilon' = \varepsilon_\infty - \frac{\omega_p^2}{\omega^2 + \omega_\tau^2}$$

(5.36)

$$\varepsilon'' = \frac{\omega_p^2\,\omega_\tau}{\omega^3 + \omega_\tau^2\,\omega}$$

(5.37)

where ω_τ is the damping frequency, ω_p is the plasma frequency of the substrate, and ε_∞ is the dielectric constant at infinite frequency. For gold, these constants are: $\omega_\tau = 216\ cm^{-1}$, $\omega_p = 72{,}500\ cm^{-1}$, and $\varepsilon_\infty = 1.0$.

5.5 Results

The infrared spectra obtained for 2 differently prepared polyimides shown in Figure 5.8 exhibit significant differences in band frequency, width, and relative intensity. Particular attention has been given to previously assigned localized vibrations associated with symmetric and asymmetric C=O stretching vibrations or skeletal bending (tangential stretching) such as the band near 1500 cm^{-1}. This tangential stretching vibration is designated as mode 19a using Wilson's classification.[32] These spectroscopic features can be attributed to different structures or orientation.

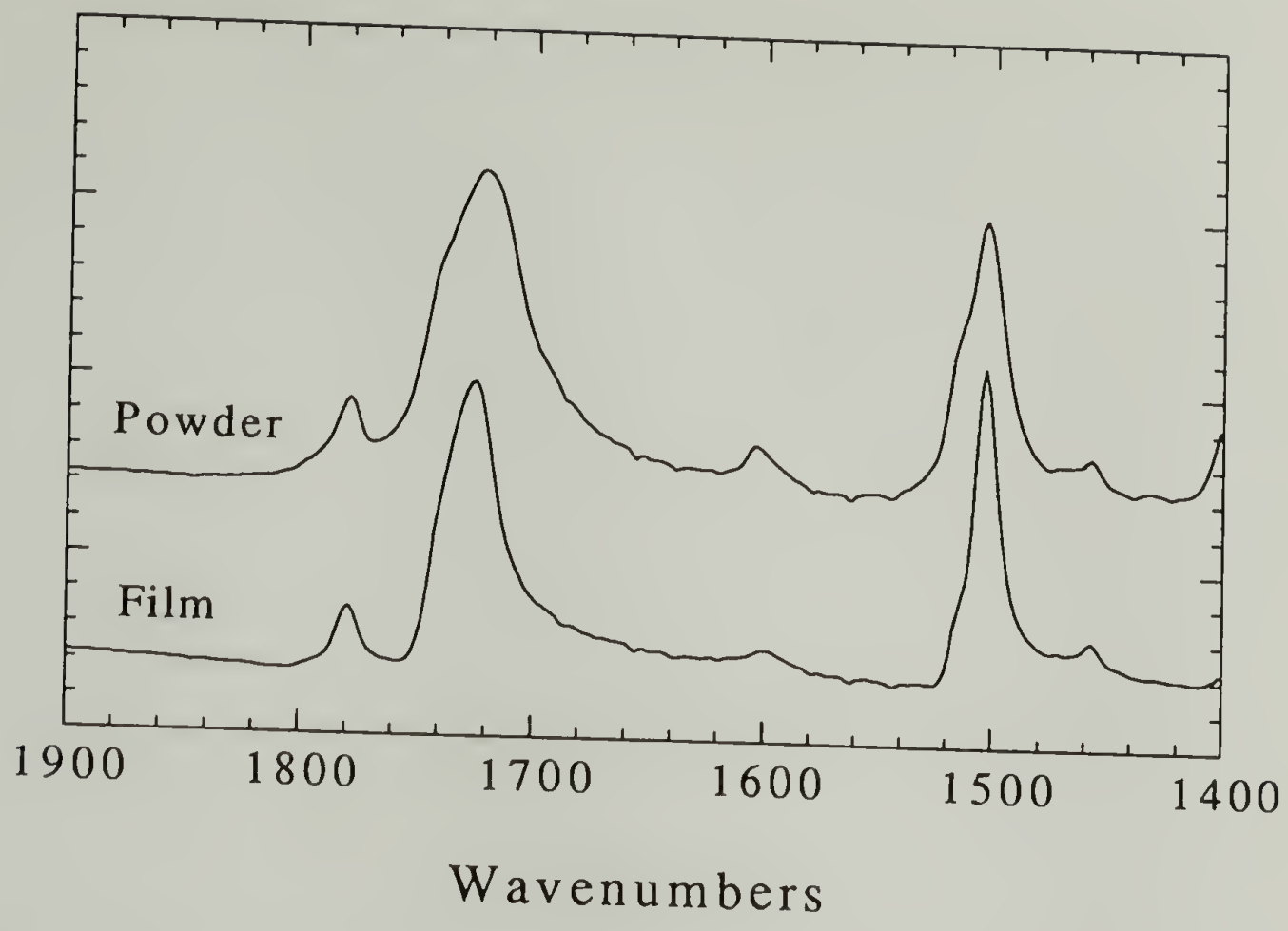

Figure 5.8. Comparison of the infrared spectra obtained for PMDA-ODA polyimide powder and film.

Curing history which provides for a longer solvent residence time will produce samples of higher degrees of crystallinity as well as reduce in-plane orientation for PMDA-ODA polyimides. Spectroscopic and wide-angle X-ray diffraction studies of PMDA-ODA polyimide produced with rapid curing exhibit spectroscopic features similar to those shown above.[33,34]

Due to the impossibility of obtaining thin isotropic polyimide films, the transmission spectrum obtained for the polyimide powder mixed with KBr was chosen to simulate the reflection spectrum for specific thicknesses on gold. It is emphasized that the simulated reflection spectrum used for comparison, i.e. that based on polyimide powder, represents a sample of higher degree of crystallinity than expected for a thin film. Thin films possess non-crystalline domains as high as 85 %. These regions are not designated

as amorphous as a "smectic-like" liquid crystalline order is present due to the rigid nature of these chains.[35] Thermal annealing is known to remove conformational defects while increasing the degree of crystallinity and crystallite size. The obvious differences observed for the simulated and experimental spectra can then be used for analysis of degree of order in thin polyimide films prepared on gold substrate.

To provide greater accuracy in the calculation of the orientation angle from these spectra, it is important to utilize the non-crystalline or higher frequency component of the asymmetric C=O stretching vibration. Correction of peak intensities is necessary to account for population differences arising from changes in crystalline content between powder and film samples. Utilizing X-ray diffraction methods, a 65% crystalline content was computed for the powder and 10% assumed for the films.

5.5.1 Orientation Analysis

The symmetric and asymmetric stretching and out of plane bending vibrations of the C=O's are those most convenient for use in characterization of segmental orientational distribution, Figure 5.9. Deviations from an idealized planar zigzag conformation will occur due to flexibility of the ether linkage. M_1 and M_2 represent transition moments associated with the symmetric and asymmetric stretching vibrations, respectively. M_1 has been determined to be mainly along the chain axis and M_2 in the plane of the imide ring.[9,10] Chain orientation with respect to the substrate's surface normal can be computed using the polarization measured for M_1. Similarly, the PMDA ring tilt can be obtained by analyzing the average direction of M_2 in the film. The transition dipole moment designated as M_3 is the C-N-C out-of-plane bending which appears at 725 cm^{-1}.

The other mode which can be analyzed is the para-substituted phenyl ring CH out-of-plane vibration at 825 cm^{-1}. An alternative method for samples with higher dimensional anisotropy is provided in Appendix C.

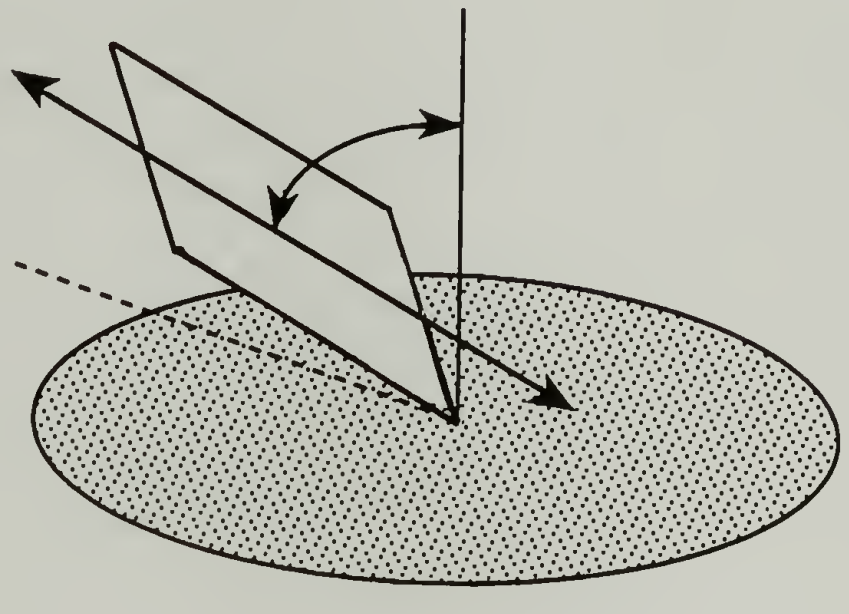

Figure 5.9. Sketch representing the PMDA unit and its location in terms of tilt and axial orientation with respect to the surface normal.

The experimental and calculated infrared spectra of PMDA-ODA polyimide films of various thicknesses are shown in Figures 5.10 and 5.11. Differences observed in the 2 sets of spectra result from the effects of orientation and crystallinity. The lower frequency component of the C=O stretching vibration has considerable intensity in the simulated spectra. In contrast, the higher frequency component at 1738 cm^{-1} is more prominent in the measured spectra. The C=O stretching vibrations in polyimide consistently exhibit multiple components which are less obvious in the adsorbed film but quite clear in the highly crystalline samples. The high frequency component is assigned to the disordered phase.[34,36] Changes in chain conformation affect chain conjugation and thus the intensity and frequency of various observed vibrations. For example, when crystallization occurs, the C=O stretching mode decreases by as much as 8 cm^{-1} from

1725 cm^{-1} to 1717 cm^{-1} . This frequency change is assigned to the increase in chain conjugation in the ordered state. Polyimide chains exist in a planar form,[27,28,37] in the highly ordered state.

In reflection spectra obtained for an adlayer on metal, the components of vibrations aligned parallel to the substrate surface have a lower intensity than those perpendicular to the substrate. As stated previously, the boundary conditions are such that for this system only those vibrations having a component parallel to the plane normal will be observed. Due to the high in-plane orientation of the polyimide chains, bands such as the tangential phenyl stretching at 1505 cm^{-1} possess a much lower intensity than that of the asymmetric carbonyl stretch.

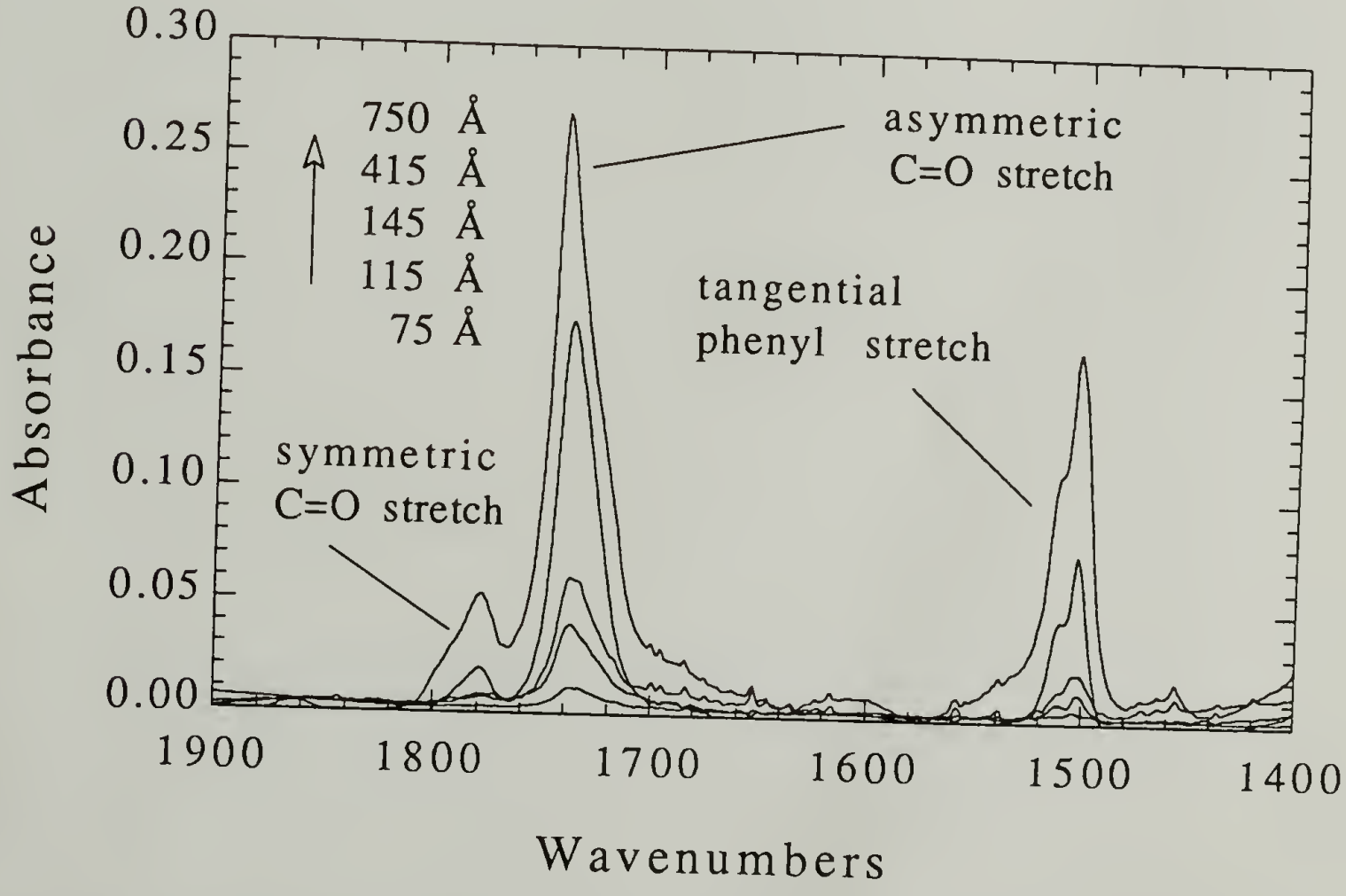

Figure 5.10 Experimentally observed reflection spectra of PMDA-ODA polyimide films of various thicknesses.

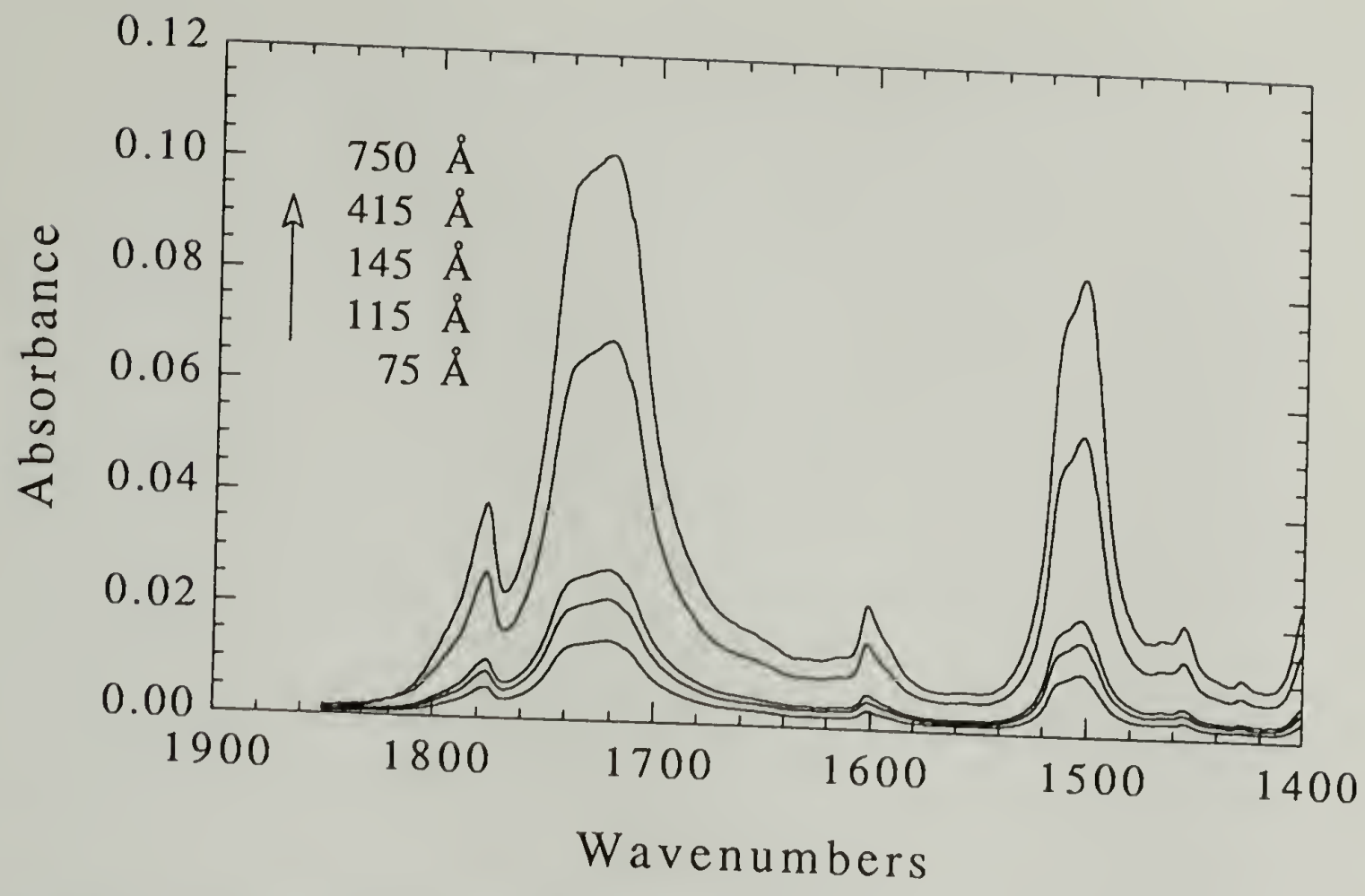

Figure 5.11. Calculated isotropic reflection spectra for polyimide films of various thicknesses.

The second moment of the orientation distribution function of the chain and imide rings are plotted in Figure 5.12. Data in this figure suggest that imide rings orient preferentially flat on the substrate. The average angle measured for the transition moment, M_2, is approximately 76° (measured relative to surface normal) for extremely thin films. It is clear that these rings disorient as a function of film thickness. This angle decreases to a value of 56° for thicker films. Values of f = 1.0 and f = -0.5 correspond to perfect parallel and perpendicular alignment with the surface normal. A value of f = 0 is indicative of random orientation of the transition moment direction with respect to the surface normal. For thin films, orientation of chain segments is very high with a value near -0.45. The degree of segmental orientation also decreases as a function of film thickness. A constant value of f = -0.28 was obtained for the chain axis direction for

film thickness greater than 150 Å. For these films, imide rings no longer maintain any orientation. These observations agree well with values derived from out of plane bending vibrations (M_3). A value of f = -0.24 was calculated with wide angle X-ray diffraction for thermally cured spin coated PMDA-ODA films.[3] Studies on films with thickness >25 μm suggest that structural anisotropy is present even at values which approach bulk. Optical anisotropy has been shown to be nearly independent of film thickness for PMDA-PDA films in the range of 0.5 to 4 μm.[6] Importantly, our measurements are averaged values for each film. Features observed for thick films contain features observed for thin films.

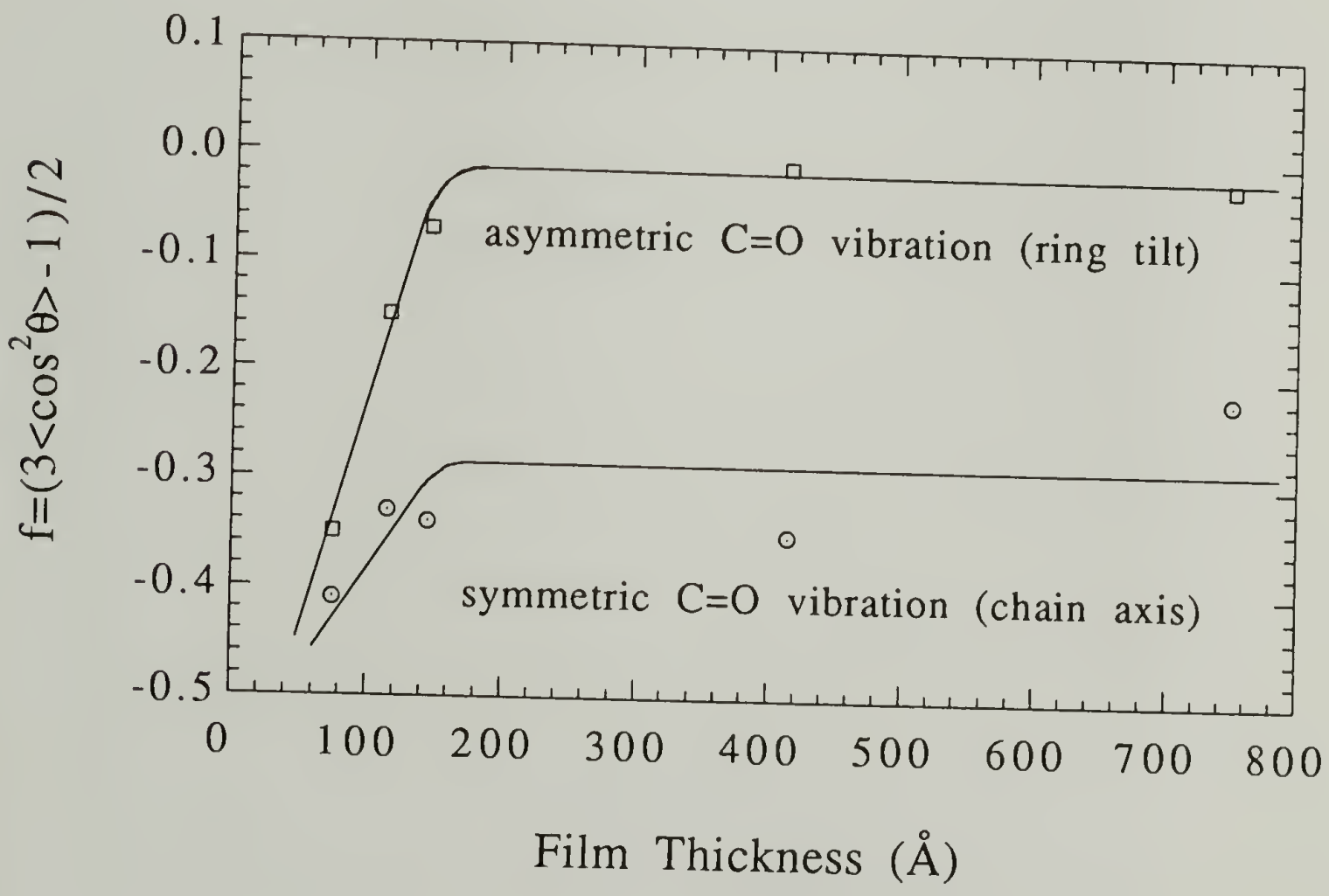

Figure 5.12. Orientational distribution function calculated for the imide ring and the chain.

Electron diffraction patterns of polyimide films at different tilt angles were obtained to confirm the anisotropy observed using vibrational spectroscopy. At normal incidence, the diffracted intensity is a ring, Figure 5.13. As the film is tilted with respect to the incident radiation propagation direction, a pattern (Figure 5.14) characteristic of molecular anisotropy emerges. The intensity of interplanar spacing (d = 4.3 Å) are concentrated along the equator as shown in Figure 5.14.[38] In addition to the anisotropic features observed, diffraction patterns of the film also indicate a lower dimensional order when compared to that found in the powder samples. Figures 5.15 and 5.16 show some of these polyimide films.

It has previously been suggested that for polyamic acid on unreactive metals such as gold, titanium and aluminum, the aryl ether rings are oriented nearly parallel to the metal surface with interconnecting amic acid or ester rings perpendicular to the surface.[39] In the vicinity of the substrate, this arrangement does not change with thermal imidization. Our results are consistent with the suggestion that an interfacial region with a thickness of 150 Å exists between the bulk polyimide and an weakly interacting substrate. This disordered interface can be considerably thicker if strong chemical interaction occurs between coating and substrate. This has been observed for polyimides on reactive substrates such as copper where its precipitates diffuse as far as 500 Å into the PMDA-ODA coating.[40]

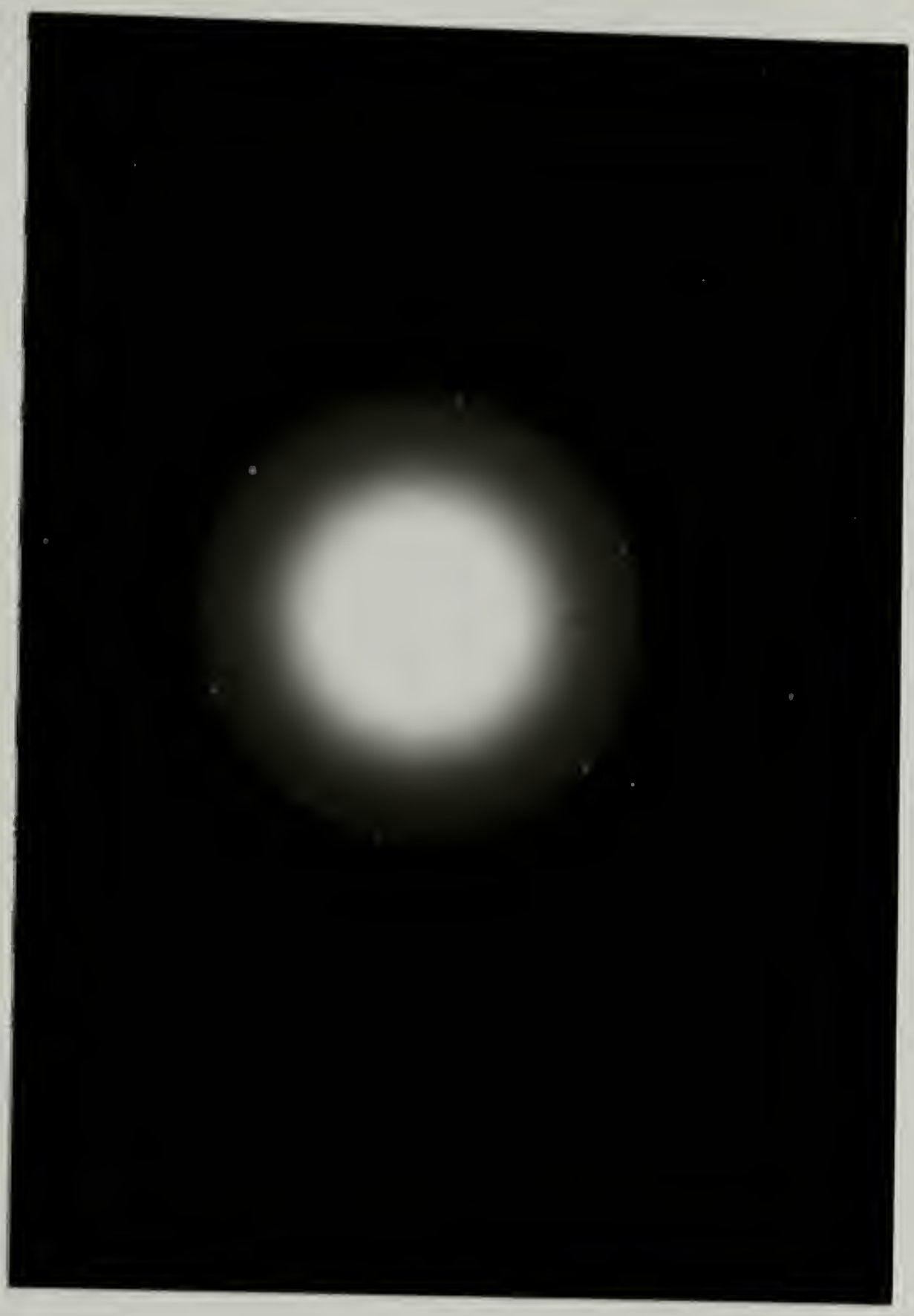

Figure 5.13. Electron diffraction patterns obtained for the 115 Å thick PMDA-ODA film. Incident beam at right angles.

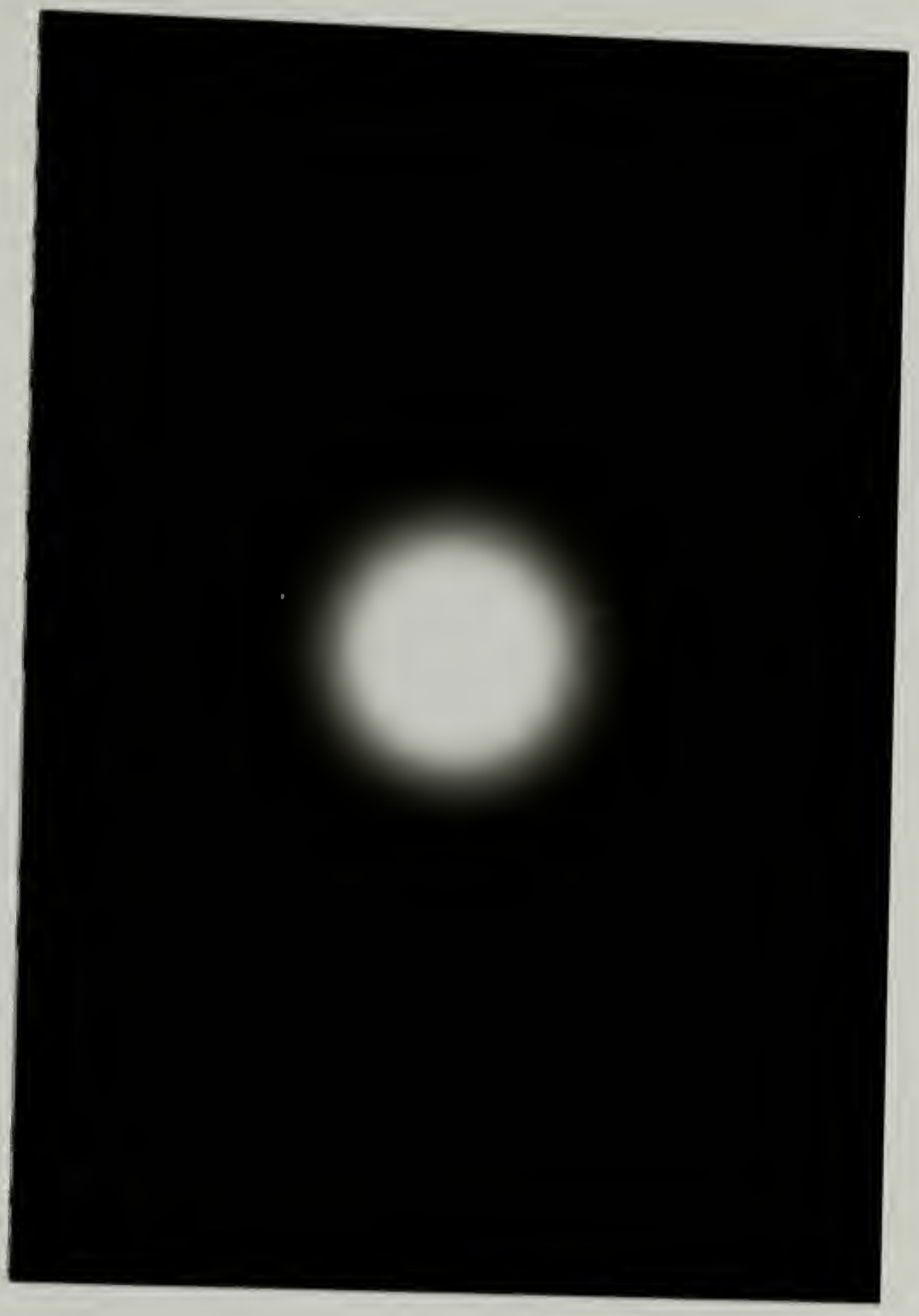

Figure 5.14. Electron diffraction patterns obtained for the 115 Å thick PMDA-ODA film. Tilted film.

Figure 5.15. Transmission electron micrographs of PMDA-ODA polyimide films as floated from gold substrates. Curled pieces next to grid.

Figure 5.16. Transmission electron micrographs of PMDA-ODA polyimide films as floated from gold substrates. Wrinkled film.

5.5.2 Packing Order in Thin Polyimide Films

As mentioned above, in the observed spectra the lower frequency out-of-phase component (1717 cm^{-1}) assignable to ordered regions is seen only as a shoulder of the higher frequency band. It is to be noted that for the transmission and therefore the simulated spectrum, the lower frequency band has a higher intensity than the component located at 1737 cm^{-1}. The relatively strong intensity of this disorder band observed for thin films suggests perturbative effects of the substrate on packing efficiency. There is little question that structures of low order exist for thin films. Evidence of decrease in order can also be found in the 1200-1000 cm^{-1} region (Figures 5.17 and 5.18). The intensity of the 1117 cm^{-1} vibration decreases with a decrease in film thickness. The intensity of this band increases for samples of increasing order. With the combination of infrared and X-ray diffraction analysis, one can conclude that the intensity of this vibration is extremely sensitive to the degree of order in polyimides. The mode observed at 1117 cm^{-1} involves imide ring distortion and deformation of the carbon-nitrogen bond.[10] For annealed samples with little structural disorder, the 1117 cm^{-1} band is very intense.

Grazing angle X-ray scattering of PMDA-ODA polyimide reveals that the degree of crystalline order is higher within 70 Å from the air/polymer interface.[41,42] For a 400 Å film, this crystalline-like layer was present at the free surface of the film but undetected near the polymer/substrate interface. The development of a crystalline-like structure is sensitive to curing conditions.

In this study, more densely packed or more ordered packing can also be revealed by frequency shifts observed for the 1117, 1240, 1374, 1735, and 1775 cm^{-1} vibrations. These changes are summarized in Figure 5.19. As mentioned earlier, a number of spectroscopic studies suggest that vibrational frequency is sensitive to changes in chain conformation. Frequency shifts in PMDA-ODA polyimides have been discussed

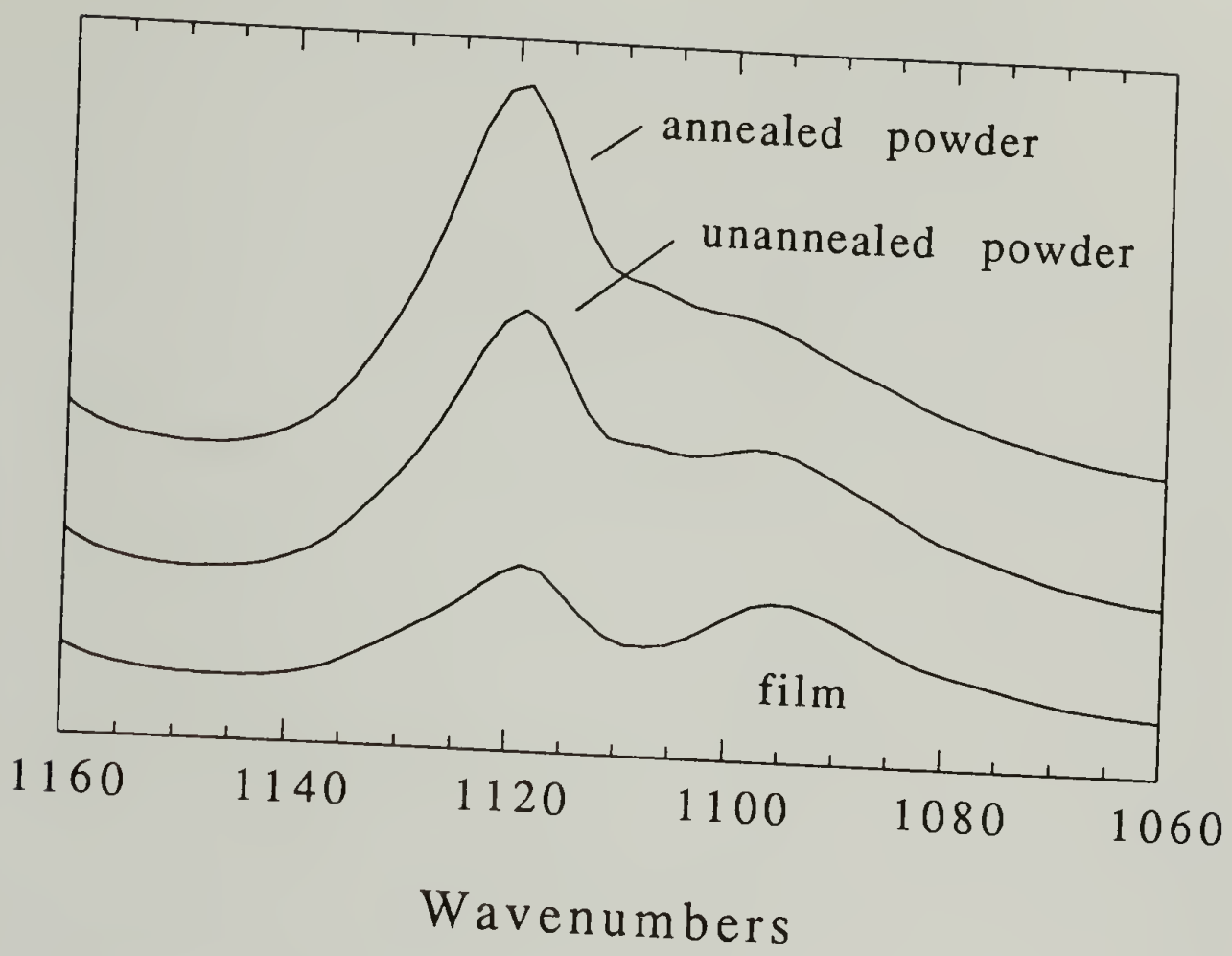

Figure 5.17. Infrared spectra in the 1160-1060 cm^{-1} region obtained for highly crystalline powders and films.

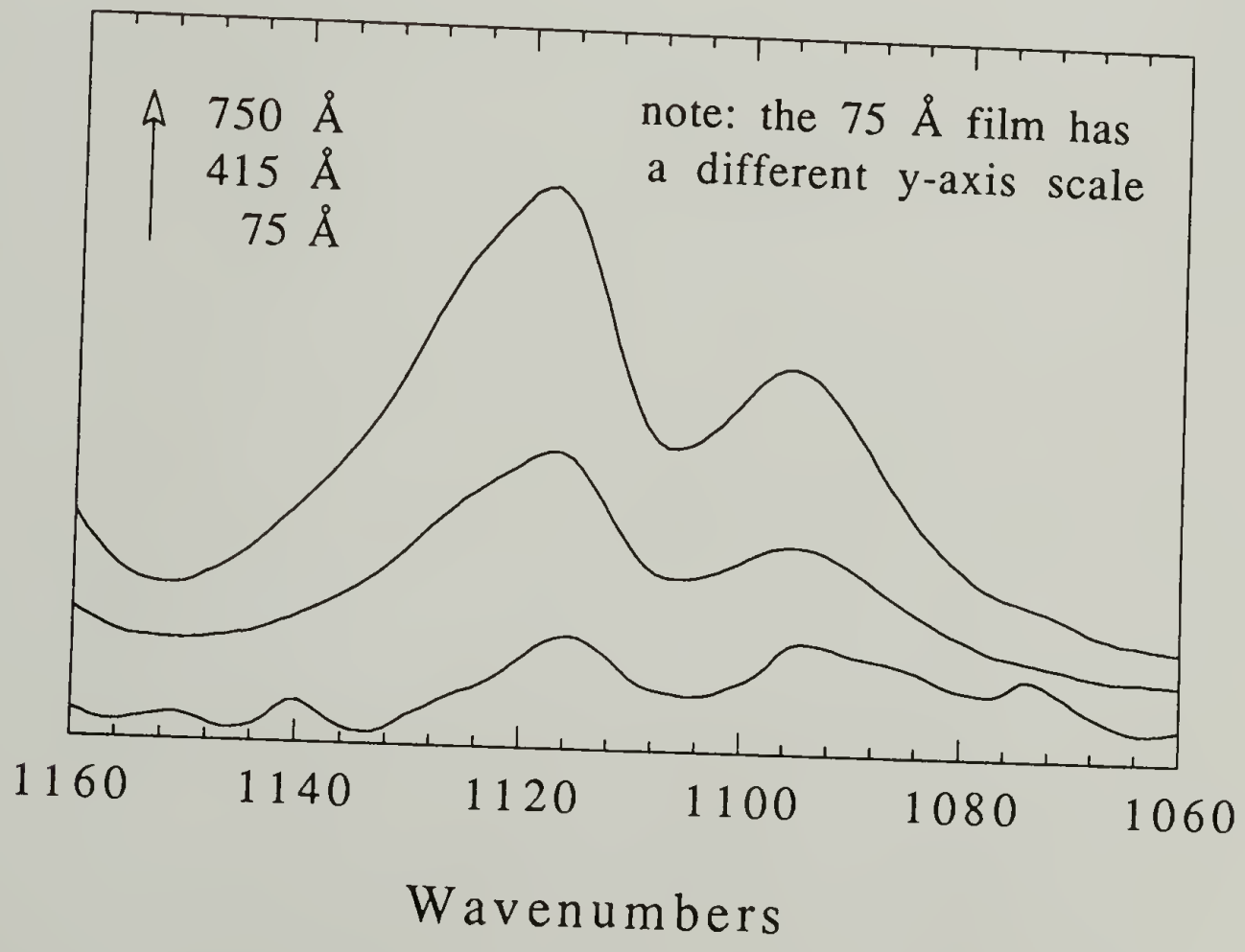

Figure 5.18. Infrared spectra in the 1060-1160 cm^{-1} region obtained for films of various thicknesses.

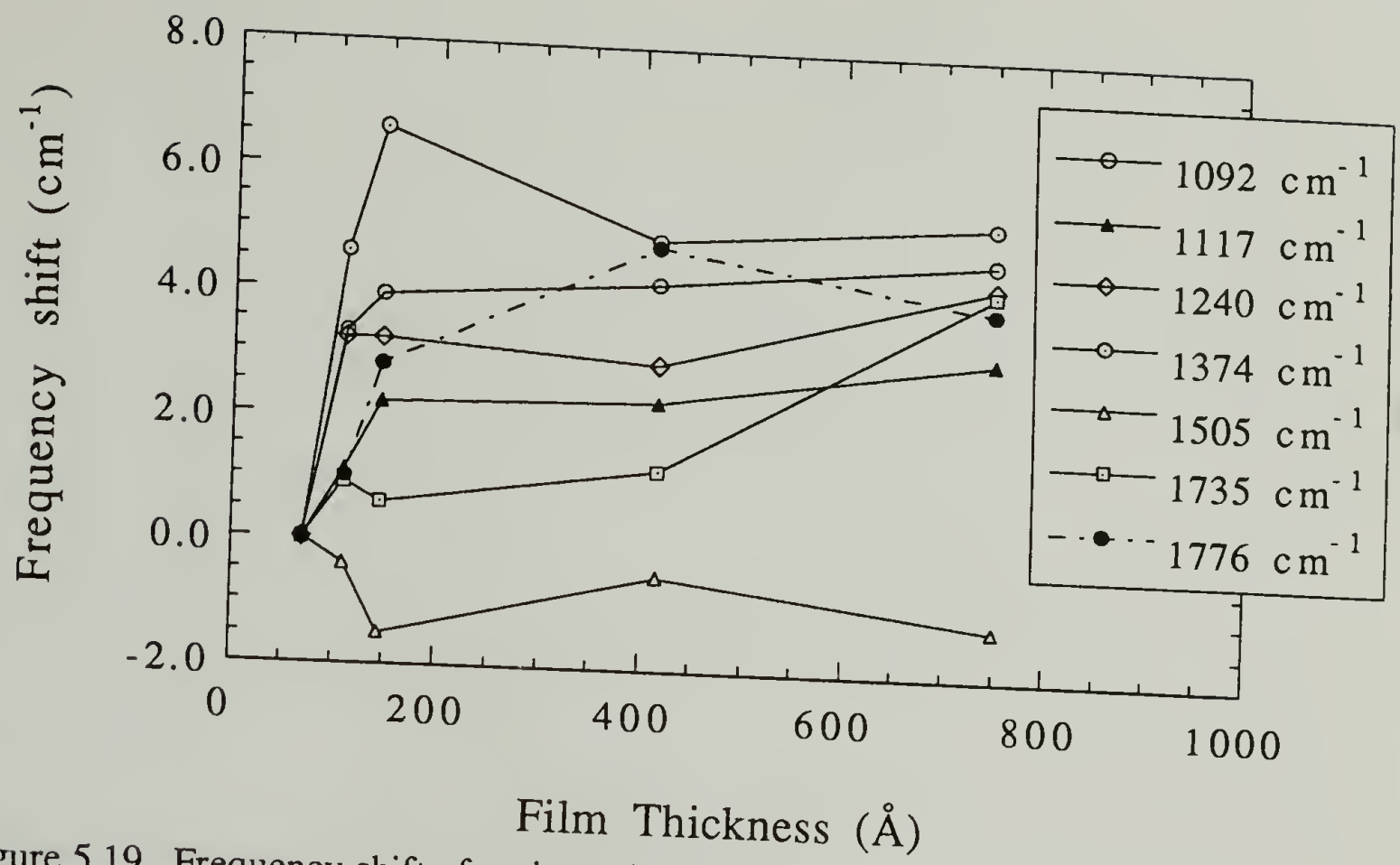

Figure 5.19. Frequency shift of various vibrations observed for polyimide films as a function of thickness.

previously.[34] The frequency shifts can be as large as 13 cm^{-1} between the CN modes of crystalline and non-crystalline samples. Similarly, the asymmetric COC stretching showed increases of 5 cm^{-1}. Frequency shifts usually accompany crystallization or changes in chain conjugation. Data suggest that increases in chain conjugation occur in thicker films. Chain packing order can be concluded to be lower in thinner films. This effect should not be confused with frequency shifts due to optical effects which may arise in going from transmission to reflection modes.

In any event, abrupt transitions from an interface layer to the bulk may lead to increases in the likelihood of cohesive failure. As shown here, films thicker than 150 Å exhibit more efficient average packing but random imide-ring plane orientation. In our particular case, adhesive weakness may arise not only from less efficient packing and different ring unit tilt but also from weaker chemical interaction with substrate.

5.6 Conclusions

Calculations based on the intensity of simulated and experimental out-of-phase and in-phase C=O stretching have provided results describing orientation of the imide ring plane with respect to the surface normal respectively. These results show that the tilt of PMDA ring units and the chain axis exhibit preferential orientation for films thinner than 150 Å. This structural anisotropy decreases rapidly as a function of increasing film thickness. However, the chain axis direction maintains a constant value of f = -0.28, even for thick films, indicating that a good degree of anisotropy exists at all times. Electron diffraction film tilting experiments have confirmed the molecular orientation observed by spectroscopy.

Films thinner than 150 Å were found to exhibit lower packing efficiency, evidenced by the decrease in the transverse CNC stretch (1117 cm^{-1}) for thinner films. Better packing would induce a higher degree of ring coplanarity, which, in turn, would increase conjugation. Frequency shifts would then be observed as a function of coating thickness for differing packing efficiencies. Indeed, frequency shifts were observed below 150 Å but constant frequency values were attained for thicker films. The work described here presents the possibility that different chain conformations and/or various degrees of packing exist near the polymer/hard wall interface for PMDA-ODA polyimides.

5.7 References

(1) Feger, C., Khojasteh, M.M., Htoo, M.S. *Advances in Polyimide Science and Technology;* Technomic Pub. Co. Inc.: Lanc.Basel, 1993.

(2) Farris, R.J.; Madden, M.A. in *Advances in Polyimide Science and Technology;* ed. by Feger, C., Khojasteh, M.M., Htoo, M.S. Technomic Pub. Co. Inc. Lanc.Basel, 1993, 644.

(3) Russell, T.P.; Gugger, H.; Swalen, J.D. *J. of Polym. Sci.: Polym. Phys. Ed.* **1983**, *21*, 1745.

(4) Cha, C.Y.; Samuels, R.J. *Antec* **1993**, 2896.

(5) Nakagawa, K. *J. of Appl. Polym. Sci.* **1990**, *41*, 2049.

(6) Herminghaus, S.; Boese, D.; Yoon, D.Y.; Smith, B.A. *Appl. Phys. Lett.* **1991**, *59*, 1043.

(7) Aboelfotoh, M.O.;Feger, C.;Castellano, A.; Kaufman, R.; Molis, S. *Appl.Phys.Lett.* **1993**, *62*, 2286.

(8) Walls, D.J. *Antec* **1993**, 1919.

(9) Laius, L.A. *Polym. Sci. USSR* **1974**, *16*, 2435.

(10) Silverman, B. D. *Macromol.* **1989**, *22*, 3768.

(11) Heavens, O.S. *Optical Properties of Thin Solid Films* ; Dover Publ.: New York, 1965.

(12) Hansen, W.N. *J. of the Opt. Soc. of Am.* **1968**, *58*, 380.

(13) Hansen, W.N. *Advances in Electrochemistry and Electrochemical Engineering*; Ed. R.H. Muller; John Wiley & Sons: New York. Vol. 9, Ch 1, 1973.

(14) McIntyre, J. D.E.*Advances in Electrochemistry and Electrochemical Engineering*; Ed. R.H. Muller; John Wiley & Sons: New York. Vol. 9, Ch 2, 1973.

(15) Fina, L.J.; Tung, Y. *Appl. Spect.* **1991**, *45*, 986.

(16) Yen, Y.; Wong, J.S. *J. of Phys. Chem.* **1989**, *93*, 7208.

(17) Buontempo, J.T.; Rice, S.A. *J. of Chem. Phys.* **1993**, *98*, 5825.

(18) Allara, D.L.; Baca, A.; Pryde, C.A. *Macromol.* **1978**, *11*, 1215.

(19) Allara, D.L.; Nuzzo, R.G. *Langmuir* **1985**, *1*, 50.

(20) Young, J.T.; Tsai, W.H.; Boerio, F.J. *Macromol.* **1992**, *25*, 887.

(21) Young, J.T.; Boerio, F.J. *J. of Surf.and Interf. Anal.* **1993**, *20*, 341.

(22) Dluhy, R.A. *J. Phys. Chem.* **1986**, *90*, 1373.

(23) Ishino, Y.; Ishida, H. Langmuir **1988**, *4*, 1341.

(24) Ishino, Y.; Ishida, H. *Appl. Spect.* **1992**, *46*, 504.

(25) Gericke, A.; Michailov, A.V.; Hühnerfuss, H. *Vib. Spect.* **1993**, *4*, 335.

(26) Jennings, R.; PhD Dissertation, Dept. of Polym. Sci. and Eng. The University of Massachusetts at Amherst, 1993.

(27) Perez, M.A.; Hsu, S.L.; Farris, R.J. *Polymer Prepr., Am. Chem. Soc.***1993**, *69*, 22.

(28) Perez, M.A.; Hsu, S.L.; Farris, R.J. submitted for publication.

(29) Greenler, R.G. *J. of Chem. Phys.* **1966**, *44*, 310.

(30) Parikh, A.N.; Allara, D.L. *J. Chem. Phys.* **1992**, *96*, 927.

(31) Pacansky, J.; England, C.; Waltman, R.J. *J. Polym. Sci. Part B:Phys.* **1987**, *25*, 901.

(32) Varsanyi, G. *Vibrational Spectra of Benzene Derivatives*; Academic Press: New York, 1974.

(33) Molis, S.E.; Saraf, R.; Hodgson, R.T. *Antec* **1991**, 1700.

(34) Ishida, H.; Wellinghoff, S.T.; Baer, E.; Koenig, J.L. *Macromol.* **1980**, *13*, 826

(35) Takahashi, N.; Yoon, D.Y.; Parrish, W. *Macromol.* **1984**, *17*, 2583.

(36) Boese, D.; Lee, H.; Yoon, D.Y.; Swalen, J.D.; Rabolt, J.F. *J. of Polym.Sci., Part B: Polym. Phys.* **1992**, *30*, 1321.

(37) Kazaryan, I.G.; Tsvankin, D. Y.; Ginzburg, B.M.; Tuichiev, S.; Korzahvin, L.N.; Frenkel, S. Y. *Polym. Sci. USSR* **1972**, *14*, 1344.

(38) Lebedev, G.A. *Polym. Sci. USSR* **1975**, *17*, 1338.

(39) Linde, H.G. *J. of Appl. Polym. Sci.* **1990**, *40*, 2049.

(40) Stewart, W.C.; Leu, J.; Jensen, K.F. *Mat. Res. Soc. Symp. Proc.* **1989**, *153*, 285.

(41) Factor, B.J.; Russell, R.P.; Toney, M.F. *Macromol.* **1993**, *26*, 2847.

(42) Factor, B.J.; Russell, T.P.; Toney, M.F. *Phys. Rev. Lett.* **1991**, *66*, 1181.

CHAPTER 6

CALCULATION OF ANISOTROPIC ELASTIC CONSTANTS AND THERMAL EXPANSION COEFFICIENTS OF PMDA-ODA POLYIMIDE BY MOLECULAR SIMULATION

6.1 Introduction

This chapter describes the calculation of anisotropic elastic constants for PMDA-ODA polyimide and its thermal expansion coefficients. Molecular mechanics was mainly utilized to minimize the energy of structures and unit cells for the subsequent calculation of elastic constants. Molecular dynamics was used to determine thermal expansion coefficients. The force field utilized for the minimizations is described below. The usage of these elastic constants and expansion coefficients in finite element methods are the subject of chapter 7.

6.2 Description of Methodologies Utilized in The Computation of Constants

6.2.1 Principal Distinctions Among Simulation Methodologies and Their Applications

Molecular Mechanics: An initial molecular geometry is needed as an input. The atomic coordinates are displaced in the direction required for energy minimization. Energy minimization procedures such as Fletcher-Powell or the conjugate gradient

methods were alternatively utilized. Molecular Dynamics: this enables the investigation of properties at non-zero temperatures. A set of initial positions and velocities is needed as input. At each stage, intermolecular energy functions are employed to calculate the force exerted on the molecule by its neighbors and the evolution of the configuration of the system then proceeds by stepwise numerical integration of the Newtonian equations of motion. Monte Carlo Simulations: these are particularly useful for the simulation of amorphous system configurations. Here a sequence of configurations is constructed by successive random displacements which derive, in a roulette-wheel fashion, from a random-number generator. But in order to simulate an actual thermodynamic system it is algorithmically arranged so that the probability of configurations appearing in the sequence is weighed by the Boltzmann factor.

6.2.2 Force Field Description

A Force Field is a set of expressions which allows for an evaluation of the forces in all particles of an n-body system by superposition of terms which can describe the energy of a molecule set into a particular geometry. It is an approximation, an exact description of the system can be obtained by "ab-initio" calculations which involve solving Schrödinger's equation for the electronic wave functions for each geometry. The contributions to the total potential energy of the system are then:

$$\Theta_{total} = \Theta_{bonded} + \Theta_{non\text{-}bonded}, \tag{6.1}$$

$$\Theta_{bonded} = \Theta_{b} + \Theta_{\theta} + \Theta_{\phi} + \Theta_{i}, \tag{6.2}$$

$$\Theta_{non\text{-}bonded} = \Theta_{vdW} + \Theta_{el} + \Theta_{hb}, \tag{6.3}$$

where, contributions to the bonded energy are, respectively: stretching, bending, torsion, and inversion. The terms in the non-bonded energy expression correspond to contributions from van der Waals forces, electrostatic forces and hydrogen bonding.

The molecular simulation technique has been generalized through computer codes with force fields capable of calculating the energy and force requirement for many molecular systems. One of these force fields is called *Dreiding* [1] which can be utilized by *Polygraf*™ 2.2 and 3.0, the molecular simulation package that was employed to predict the geometrical parameters and possible conformations of macromolecules.

In *Dreiding* hybridization considerations dominate force constants and geometrical parameters. This is contrary to other force-fields where a particular combination of atoms prescribes them. The Dreiding force field utilizes a superposition of the bonded and non-bonded interactions in minimizing the potential energy of an arbitrary molecular geometry. The bonded interactions can be of the two-body type, which is the case for bond stretching; three-body type, for bond angle bending; four-body type, in the case of dihedral angle torsion and inversion terms. The non-bonded interactions are partitioned into: van der Waals or dispersion, electrostatic, and hydrogen bonding. The system also has the capability of fitting charges to the structure by the method of Gasteiger [2], where the charges can be equilibrated and distributed at ease. But, the creators of the potential do acknowledge that a better method for charge assignment in large molecules is needed.

The molecular interaction of bond stretching in *Dreiding* can be described using a simple harmonic oscillator,

$$U = 0.5\, k_e\, (R - R_e)^2 \qquad (6.4)$$

or as a Morse Function, which includes anharmonicity, if a more refined geometry calculation is required. It can be utilized after the harmonic oscillator option has provided its approximation.

$$U = D_e \left[e^{-(\alpha R - Re)} - 1\right]^2 \tag{6.5}$$

where, U is energy and D_e is the finite bond rupture energy near R_e which is the equilibrium bond radius. The force constant and the Morse scale parameters are defined below,

$$k_e = \left(\frac{\delta^2 P}{\delta R^2}\right)_{R=R_e} \tag{6.6}$$

$$\alpha = \left[\frac{k_e}{2D_e}\right]^{1/2} \tag{6.7}$$

The contribution from three-body angle bends is of the harmonic cosine form:

$$U_{IJK} = 0.5\, C_{IJK} \left[\cos\theta_{IJK} - \cos\theta_J^0\right]^2 \tag{6.8}$$

where θ_{IJK} is the angle between bonds IJ and JK, θ_J^0 is an equilibrium angle obtained from standard reference structures and C_{IJK} is defined below,

$$C_{IJK} = \frac{K_{IJK}}{(\sin\theta_j^0)} \tag{6.9}$$

Torsion is the contribution from the four body interaction as follows:

$$U_{IJKL} = 0.5\, V_{JK} \left\{1 - \cos\left[n_{JK} (\phi - \phi_{JK}^0)\right]\right\} \tag{6.10}$$

where ϕ is the dihedral angle between the IJK and JKL planes, n_{JK} is the periodicity, ϕ_{JK}^0 is the equilibrium angle (the torsion energy is zero at the equilibrium angle) and V_{JK} is the barrier to rotation.

Van der Waals interactions are described by the Leonard-Jones 12-6 potential and a three parameter version that provides a better approximation for short-range interactions.

$$U_{vdw}\,(LJ) = A\,R^{-12} - B\,R^{-6} \qquad (6.11)$$

$$U_{vdw}\,(X6) = A\,e^{-CR} - B\,R^{-6} \qquad (6.12)$$

Hydrogen bonding is given by the Leonard-Jones 12-10 potential:

$$U_{hb} = D_{hb}\,[5\,(R_{hb}/R_{DA})^{12} - 6\,(R_{hb}/R_{DA})^{10}]\,\cos^4(\psi_{DHA}) \qquad (6.13)$$

where ψ_{DHA} is the bond angle between hydrogen donor (D) and the hydrogen (H), and the hydrogen acceptor (A), D_{hb} and R_{hb} are values which depend on the convention for charge assignment. Electrostatic interactions are given by:

$$U_Q = (322.0637)\,Q_i\,Q_j/\varepsilon\,R_{ij} \qquad (6.14)$$

here Q_i and Q_j are the charges, ε is the dielectric constant (usually equal to one) and the front factor converts units into kcal/mol. More options, besides the ones cited above are provided now by *Polygraf*™ and the force field can also be chosen among *Dreiding, AMBER, MM2, MMP2 and CHARMM* to suit a particular case.

The energy minimizations were carried out with the molecular mechanics methodology of Fletcher and Powell. [3] The system provides other options such as versions of a conjugate-gradient method and the method of steepest descents. The direction of the energy surface descent as prescribed by the force field should be followed

by the shift of atomic coordinates if energy minimization is to be carried out efficiently. The Fletcher-Powell method provides rapid convergence near a possible equilibrium state but care needs to be taken to ensure that a global minimum has indeed been reached. By contrast, the steepest descent method is best where local minima are not anticipated since it converges very slowly in these regions. The conjugate gradient methodology may also trap the molecule in a local minima. Besides the information provided by the first and second derivatives as to whether or not a minimum has been reached, the F matrix should be positive-definite. This implies that the eigenvalues of this matrix should all be real and positive. A structure may be at a saddle point if one eigenvalue is negative but it may also be at a hilltop if more than one eigenvalue is negative.[4]

Verification of the minimized unit cell structure of PMDA-ODA polyimide was presented in chapter 4.

6.2.3 Elastic Constants, Calculation Methods

6.2.3.1 Stress-Strain Method

Elastic constants are obtained by the application of either a strain or stress to an equilibrium structure, then carry out the energy minimization with stress on. How individual bonds, valence angles and torsional angles deform when the sample experiences a strain, Δl, is indicated by equation 6.15.[5]

$$\Delta l = \sum_i \frac{\partial l}{\partial r_i} \Delta r_i + \sum_j \frac{\partial l}{\partial \varphi_j} \Delta \varphi_j + \sum_k \frac{\partial l}{\partial \tau_k} \Delta \tau_k \qquad (6.15)$$

where l is the original dimension of the structure along the axis, r_i is the valence bond length, ϕ_i is the valence angle, and τ_i is the angle of rotation about the bonds.

The necessary to deform these parameters can then expressed in terms of the potential energy , U,

$$F = \frac{\partial U}{\partial r}\frac{\partial r}{\partial l} + \frac{\partial U}{\partial \varphi}\frac{\partial \varphi}{\partial l} + \frac{\partial U}{\partial \tau}\frac{\partial \tau}{\partial l} \tag{6.16}$$

and finally the modulus of elasticity can be computed by,

$$E = \frac{\left(\frac{F}{A}\right)}{\left(\frac{\Delta l}{l}\right)} \tag{6.17}$$

where A is the cross-sectional area of a single chain.

6.2.3.2 Calculation of Elastic Modulus by the Second Derivative Method

This method can be found as one of the optional modules provided by *Polygraf*™ 3.0 or higher. The name of the module is *Elastica*. Using a minimized unit cell, this module computes its energy based on equation 6.18, where U_o is the equilibrium energy and ε is the strain. The program then uses the second derivative term , $\partial U^2/\partial\varepsilon_i\partial\varepsilon_j$, which is utilized to calculate the components of the stiffness and compliance matrices (equations 6.19 and 6.20, respectively).

$$U = U_0 + \sum_i \frac{\partial U}{\partial \varepsilon}\varepsilon_i + \frac{1}{2}\sum_{ij}\frac{\partial^2 U}{\partial\varepsilon_i\partial\varepsilon_j}\varepsilon_i\varepsilon_j + \ldots \tag{6.18}$$

$$C_{ij} = \frac{\partial^2 U}{\partial \varepsilon_i \partial \varepsilon_j} \tag{6.19}$$

and

$$S = C^{-1} \tag{6.20}$$

in the z direction for example, the relationship of the modulus with its corresponding compliance coefficient is given in equation 6.21 below. Other relationships were described in chapter 2.

$$E_z = 1/S_{3,3} \tag{6.21}$$

6.3 Calculated Constants

Table 6.1 presents a summary of the constants. As mentioned above, two different methods were utilized for calculation of these constants, the stress-strain method and the second derivative method. The first was based on stress-strain data generated by deforming the unit cell in a given direction followed by subsequent energy minimization. The other was based on the second derivative of the potential energy of the minimized periodically bound structure. The bulk modulus was calculated by minimizations of hydrostatic pressure increments on the unit cell.

Table 6.1. Simulated elastic constants.

Calculated by method #1:		Calculated by method #2:	
E_z = 41.53 GPa	G_{xy} = 2.01 GPa	E_z = 39.50 GPa	G_{xy} = 1.58 GPa
E_y = 6.36 GPa	G_{yz} = 4.19 GPa	E_y = 8.22 GPa	G_{yz} = 4.39 GPa
E_x = 13.55 GPa	G_{xz} = 2.86 GPa	E_x = 14.90 GPa	G_{xz} = 2.63 GPa
K= 13.60 GPa		K= 11.50 GPa	
ν_{yx} = 0.25	ν_{xy} = 0.39	ν_{yx} = 0.26	ν_{xy} = 0.47
ν_{yz} = 0.26	ν_{zy} = 0.69	ν_{yz} = 0.18	ν_{zy} = 0.85
ν_{xz} = 0.22	ν_{zx} = 0.62	ν_{xz} = 0.17	ν_{zx} = 0.45

In table 6.1, x corresponds to the a-direction of the unit cell and y to the b-direction. The Cartesian directions are shown in Figure 6.1. The Poisson's ratios obtained by the second method should follow the equation 6.22. This relationship must be followed for proper representation of orthotropic properties. This equation may not hold exactly for the results of method one due to the presence of error arising from individual deformation measurements.

$$\frac{\nu_{ij}}{E_i} = \frac{\nu_{ji}}{E_j} \tag{6.22}$$

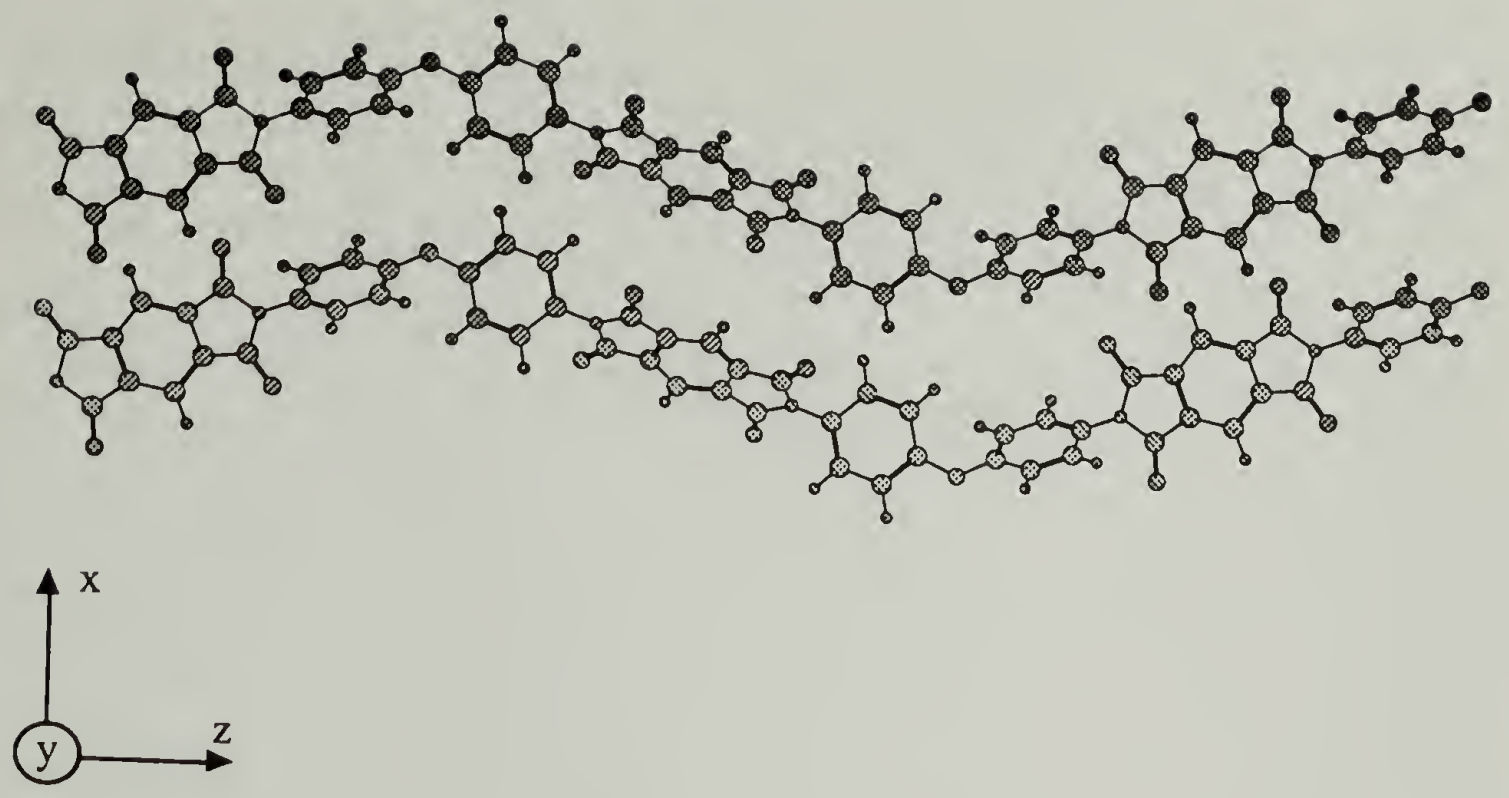

Figure 6.1. Cartesian coordinate system for unit cell directions in PMDA-ODA polyimide.

Due to the inhomogeneity of real polymer specimens, it is difficult to measure these ideal elastic constants directly. Even in the best case, amorphous regions still exist. Presumably chains in these regions will deform more readily when stress is applied. Methodologies to obtain these elastic constants in film geometries has been suggested by Maden.[6] In-plane and out of plane elastic properties of Kapton films have been measured recently by Brillouin scattering and mechanical techniques.[7] The values reported in this reference are listed below:

Bulk Modulus (GPa):	5.8 ± 0.1
In-plane Elastic Modulus (GPa):	3.5 ± 1.0
Out-of-plane Elastic Modulus (GPa):	1.6 ± 0.8
In-plane Shear Modulus (GPa):	1.57 ± 0.03

Out-of-Plane Shear Modulus (GPa):	1.2 ± 0.2
Biaxial Elastic Modulus (GPa):	4.0 ± 2.0

Low frequency Raman spectroscopy measurements can yield the modulus of the crystal in the axial direction. Problems with fluorescence made this measurement impossible with current set-up at the laboratory site. Our calculations indicated that the longitudinal acoustic mode frequency could have been observed near 7 cm^{-1}.

As shown in table 6.1, the modulus in the chain direction was computed to be 41.5 GPa with the stress-strain method and 39.5 GPa with the second derivative method. PMDA/4,4'-ODA polyimide molecules pack into a planar zigzag. The lower value of its theoretical axial modulus is believed to be due largely to the influence of the valence angle of the ether oxygen. The value calculated with the method of Treloar was 18 GPa.[8,9] Treloar's method illustrates the influence of valence angles in the calculation of crystal modulus based on force constants. Values of 23 GPa have been reported for hot drawn PMDA/3,4'-ODA.[10] This isomer develops more crystallinity in films; consequently its modulus in the undrawn state differs from that of the para-isomer.

As mentioned earlier, in-plane molecular orientation develops in polyimide films during processing. This implies that in order to obtain a better estimation of the modulus in the plane of the film from simulation results, one has to average the modulus in the axial direction with one or the average of the two transverse moduli.

Figure 6.2 shows the stress-strain plot generated with molecular simulations of tension and compression of a PMDA-ODA polyimide unit cell. These measurements were made by assuming a new value of the unit cell (c-direction in this case) to provide a given increase in strain; the unit cell was then minimized.

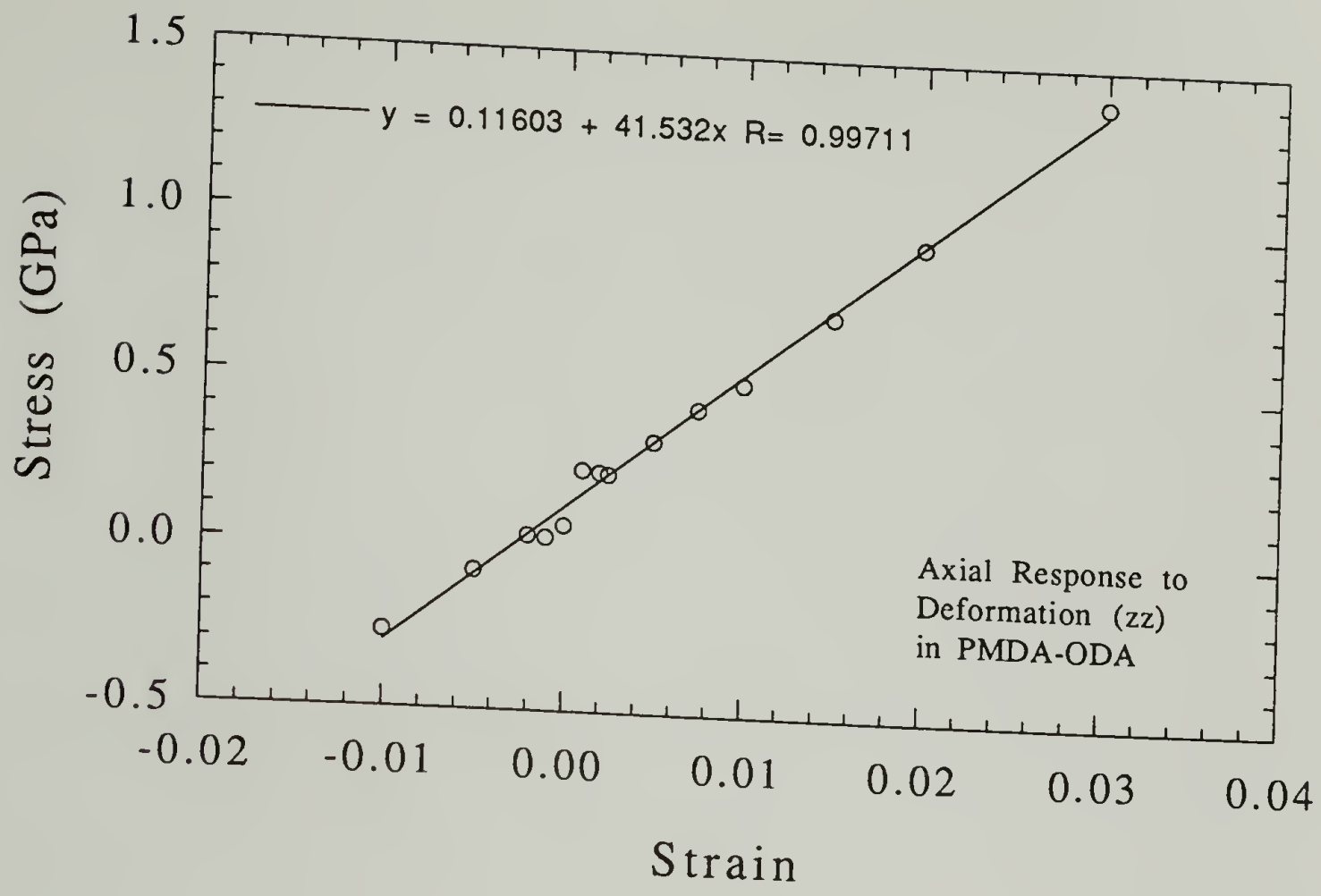

Figure 6.2. Data utilized for the calculation of the elastic modulus in the z-direction.

Figure 6.3 shows the data utilized in the computation of the modulus for the non-axial directions. The modulus in the a-direction, 13.55 Gpa, was larger than that for the b-direction of the unit cell, 6.36 GPa. A higher van der Waals energy contribution (3.1% higher) was noted for the a-direction as compared to the b-direction at the same level of strain in each direction (1%). The nature of these interactions was explored in chapter 4.

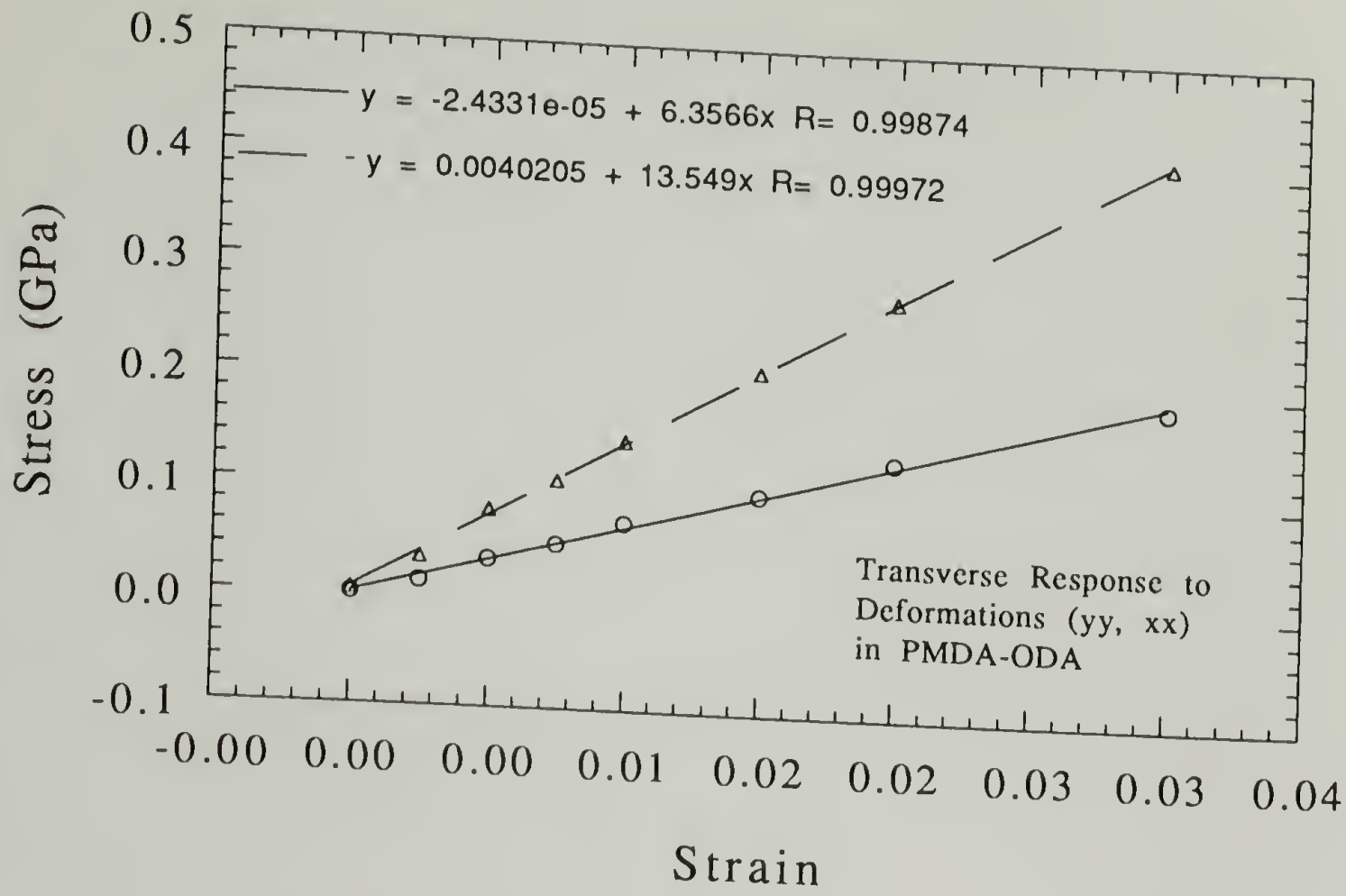

Figure 6.3. Transverse response to deformations (yy,xx) in PMDA-ODA polyimides.

6.4 Thermal Expansion Coefficients

Thermal expansion behavior of PMDA-ODA polyimides was investigated by constant-temperature constant-pressure canonical dynamics. The time step for the calculations was 0.001 picoseconds and the number of steps chosen was 16,400. A well minimized unit cell was utilized for the start of every calculation. Periodic boundary conditions were not removed for dynamics runs. Fluctuations on the unit cell dimensions are shown for 16.4 picoseconds in Figures 6.4-6.6. It was decided that the last 10,000 steps would be used in the computation of the expansion of the unit cell as a function of temperature.

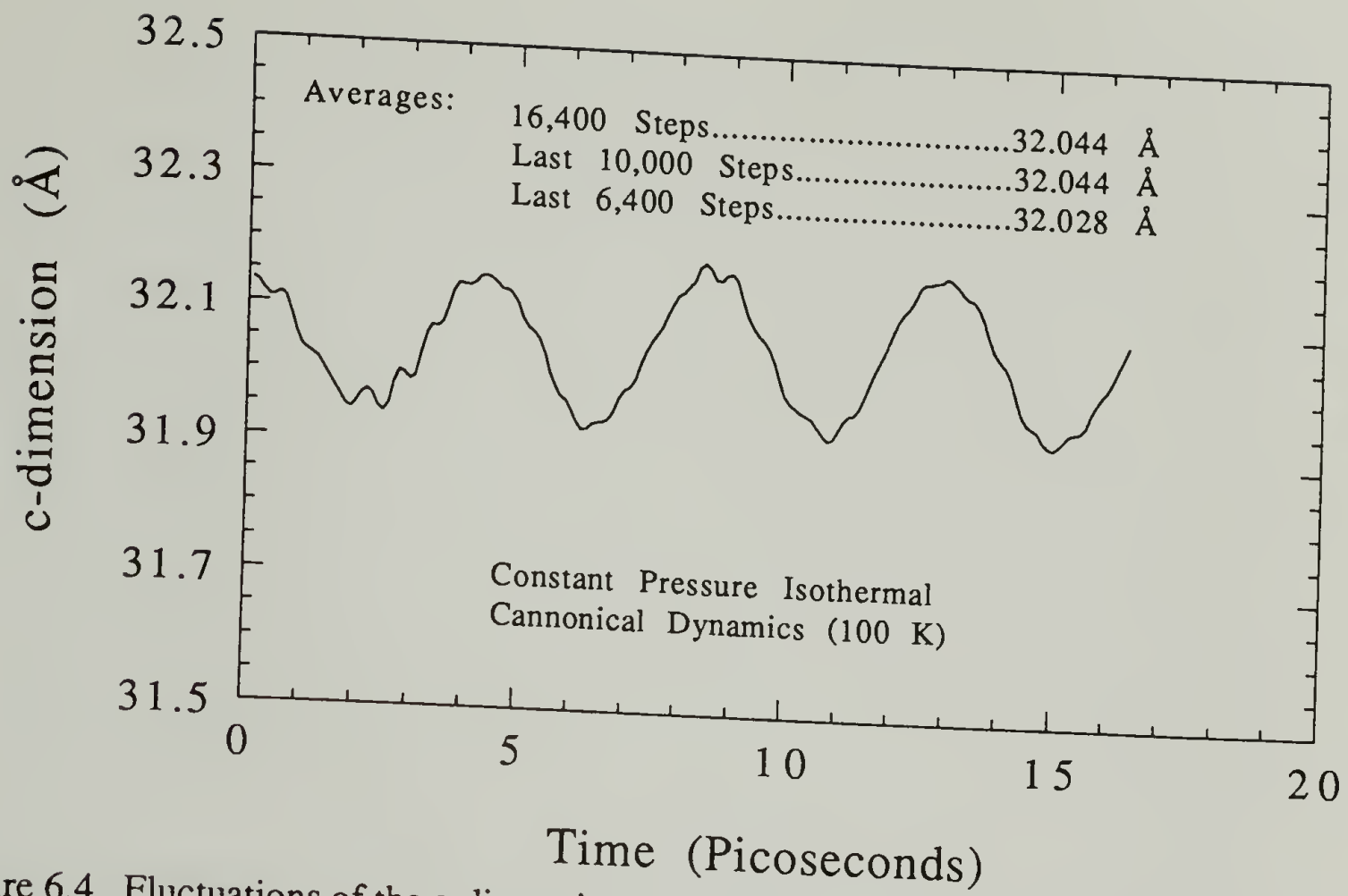

Figure 6.4. Fluctuations of the c-dimension of a PMDA-ODA unit cell shown for 16.4 picoseconds.

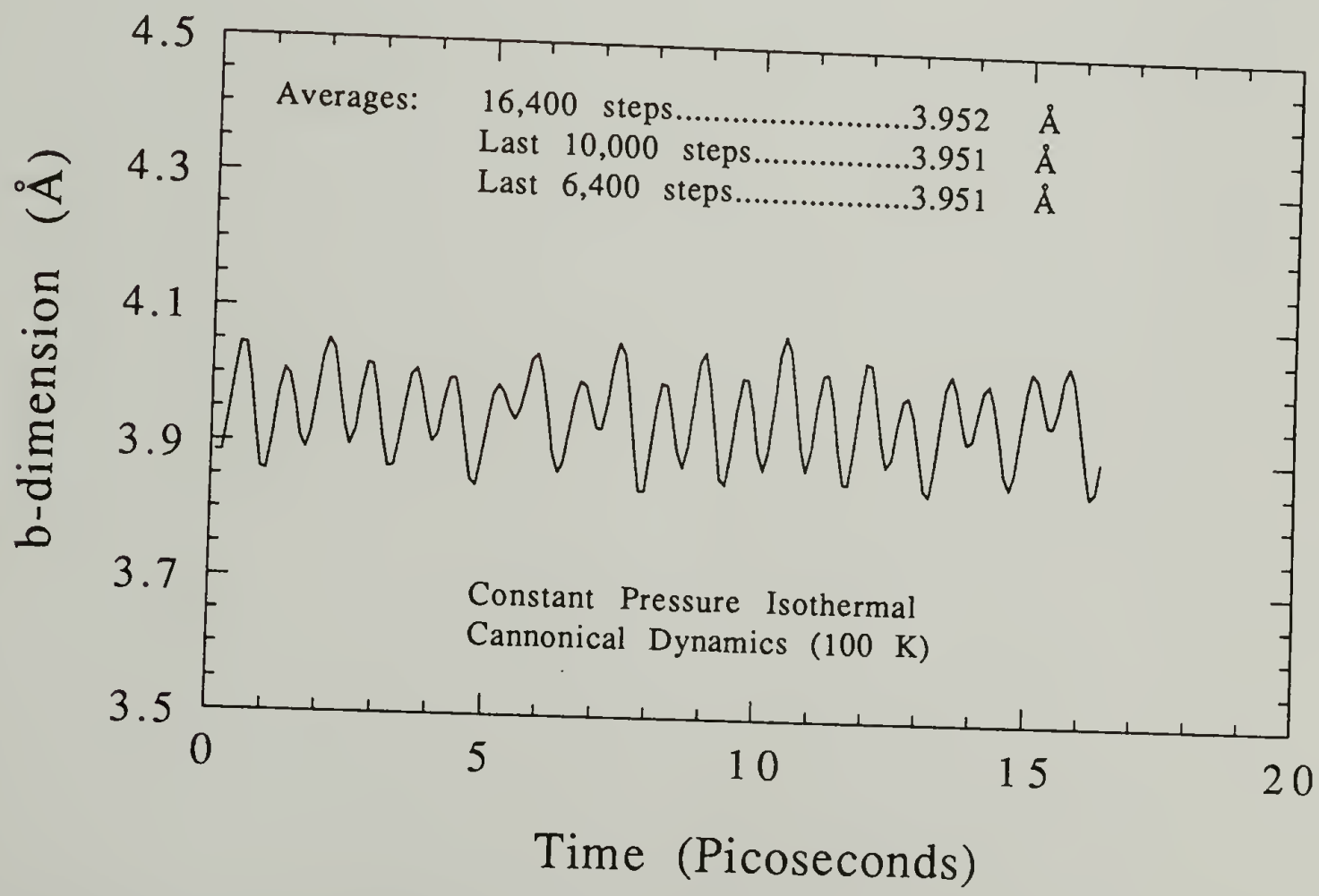

Figure 6.5. Fluctuations of the b-dimension of a PMDA-ODA unit cell shown 16.4 picoseconds.

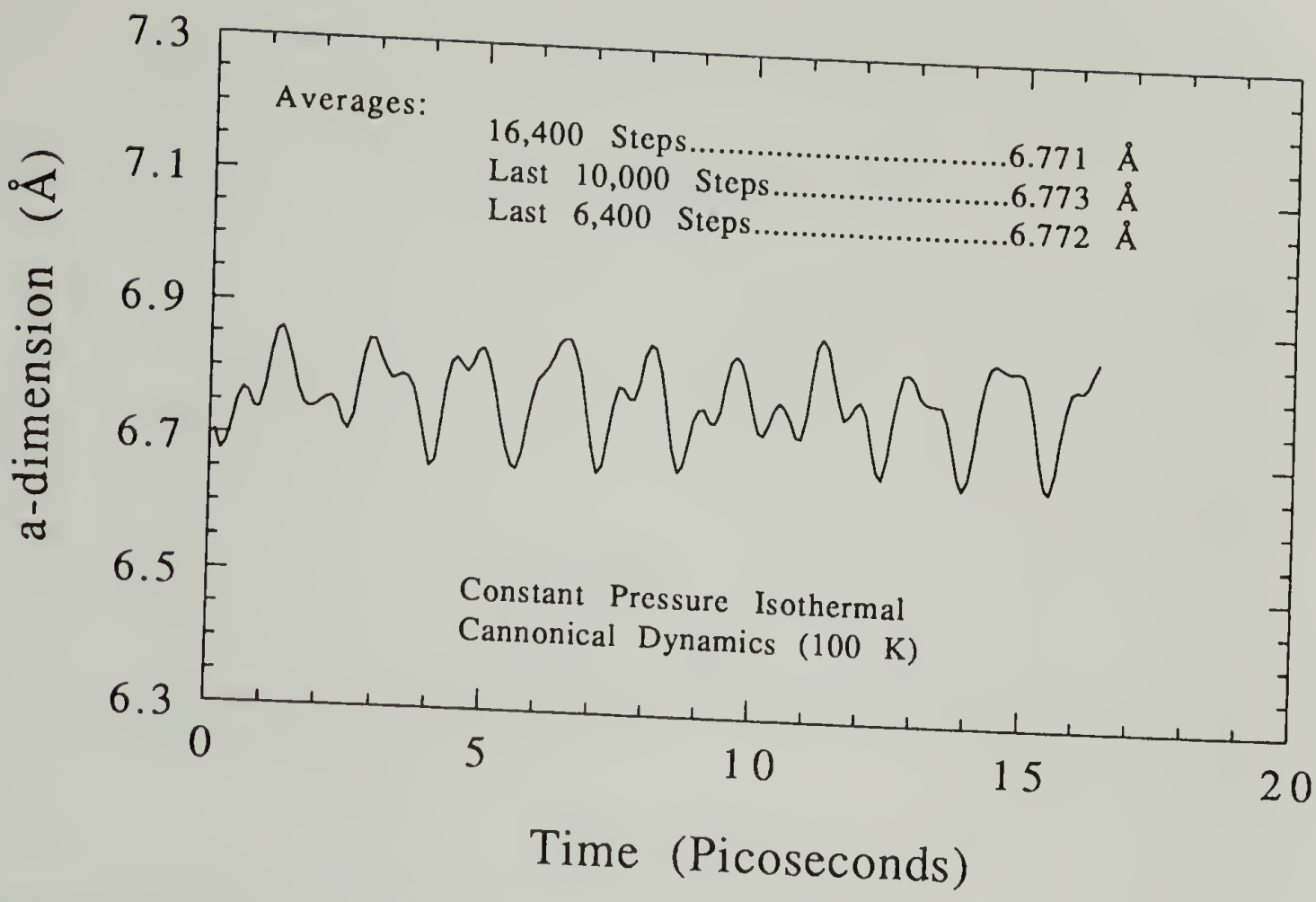

Figure 6.6. Fluctuations of the a-dimension of a PMDA-ODA unit cell shown for 16.4 picoseconds.

Thermal expansion coefficients were calculated by assuming linearity over a range of 0-500 K. As shown above, data for the fittings was obtained with isothermal constant-pressure canonical dynamics. Linearity over such a large range of temperatures may not be realistic for a polymeric material. The raw data is shown in Figure 6.7 in which one can indeed observe that the data is not linear. But if the assumption of linearity is made, the following expansion coefficients are calculated:

108.5 PPM/K in the y-direction (b direction of unit cell) R = 0.95

-17.60 PPM/K in the x-direction (a direction of unit cell) R = 0.97

18.56 PPM/K along the z-direction (Chain axis direction) R = 0.99

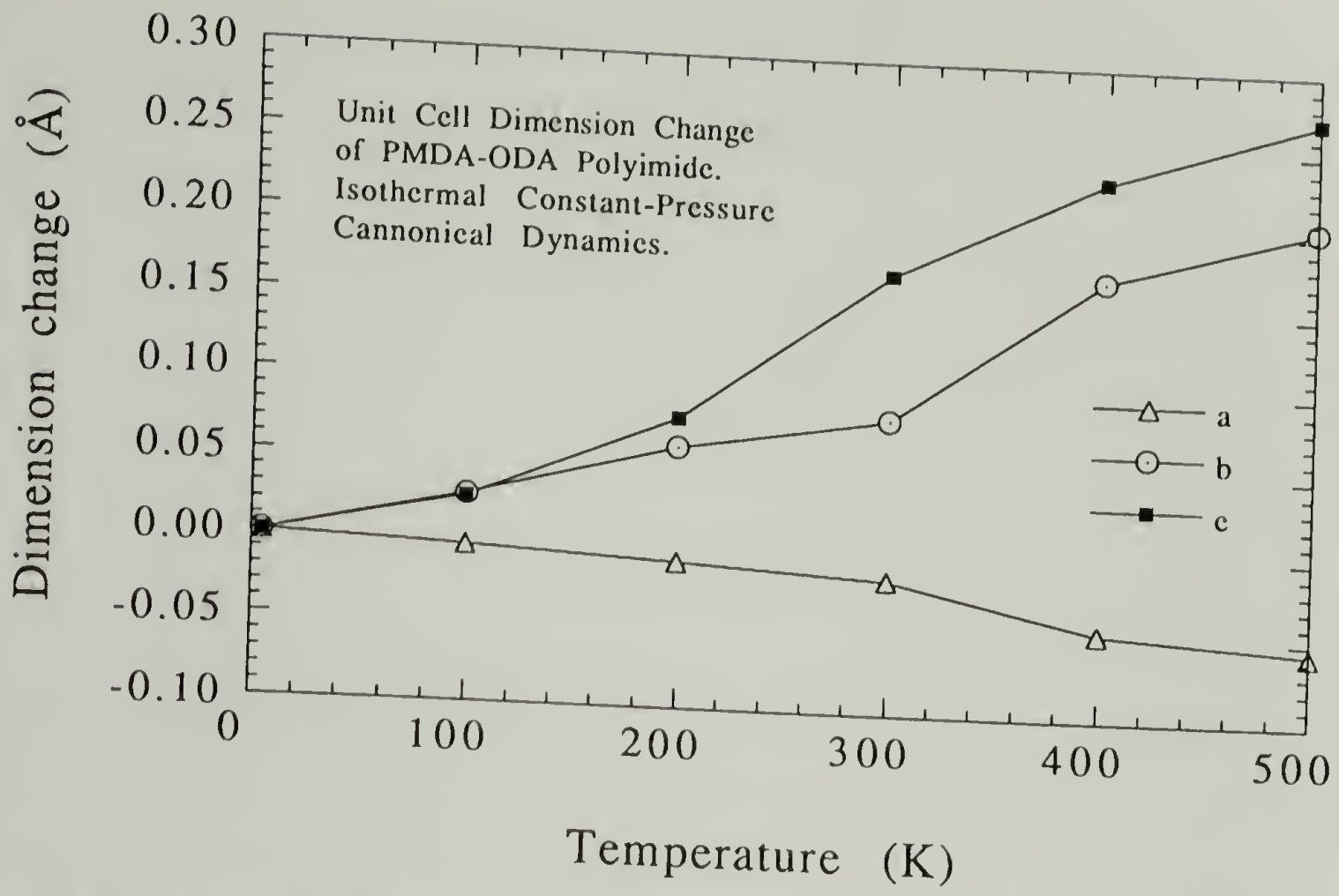

Figure 6.7. Thermal expansion of the unit cell dimensions of PMDA-ODA polyimide.

As is well known, these values should be considerably smaller along the chain axis than in lateral directions. This is especially true when dealing with trans-configurations or rigid rod molecules. In a film where the molecules are in-plane oriented, a larger expansion should be realized in the direction with weaker intermolecular forces as opposed to that given by covalent bonding in the axial direction. It is uncertain as to whether or not the negative sign in the expansion coefficient in the x-direction comes from the error involved in the method of calculation or energy minimization. It is likely be a product of an increase in the valence angle of the ether oxygen , expansion in the c-direction, and the relaxation of steric hindrance due to ring motion and re-stacking produced by the large increase in the expansion in the y-direction. The low elastic modulus and high expansion coefficient in the y-direction or b axis of the unit cell implied less intermolecular interaction.

Most experimental data shown in the literature has been obtained as in-plane and out-of-plane thermal expansion of films. The out-of-plane thermal expansion coefficient for BPDA-PDA was found to be ~100 ppm/K at room temperature and ~175 ppm/K at 550 K.[13] Coefficients of thermal expansion for the out-of-plane (83 PPM/K) and the in-plane (20 PPM/K) directions have been computed for PMDA-ODA by monitoring the capacitance of the film as a function of temperature.[14] PVT measurements have yielded values of 113 PPM/K for the out-of-plane thermal expansion coefficient of PMDA-ODA polyimide.[15] Data on polyethylene single crystals yielded values of 9.4 PPM/K and 111 PPM/K for the directions parallel and perpendicular to the chain axis respectively in the range of 100 to 300 K.[16] These results are summarized in table 6.2 below. Data from Ree and co-workers,[17] gives an average of 40.2 PPM/K for PMDA/4,4'-ODA polyimide in the range between 80 and 400 K. Similar values, 42 PPM/K, were obtained by Jennings,[18] for thermally cured PMDA/4,4'-ODA in the range between 300 and 600 K. Chemical cure brought these value down to 35 PPM/K. Thermal expansion decreased even further for the special cases where the solvent was forced to remain in the films for a longer time to obtain a higher degree of crystalline order. The thermal expansion coefficients for these films averaged from 5 to 10 PPM/K.

Therefore, an increase in the degree of crystallinity in these films decreases the thermal expansion coefficient in the plane. It is uncertain how does it affect the out-of-plane expansion coefficient. Nevertheless, if one assumes that the out-of-plane direction is the y-direction in our unit cell, one can then average the expansion coefficients in the other two directions. The average value is 1 PPM/K, which is as expected even below those of high degree of crystallinity. As reported in chapter 4, the degree of crystallinity obtained with the polyimide powder samples was ~65%. This is probably as high as one could ever attain in the bulk with these type of materials. Due to solvent evaporation effects it may be reasonable to expect that a conformation resembling the y-direction

would be pointing outwards from the plane of the film. The straightening of the rings in the direction of solvent evaporation has been experimentally corroborated in polymers with large aromatic units.[19] Good correlation with literature values, shown in table 6.2, is also a good reason to believe that the assumptions made above hold.

Figure 6.8 shows a plot of the cell volume expansion as a function of temperature. The origin of the abrupt increase in expansion denoted by the data points at 600 K and 700 K is not readily apparent at this juncture. Although, an abrupt increase in the out-of-plane thermal expansion was reported at the same range of temperatures for BPDA-PDA polyimide film.[13] This study attributed the increase to the glass transition temperature which occurred at ~ 595 K.

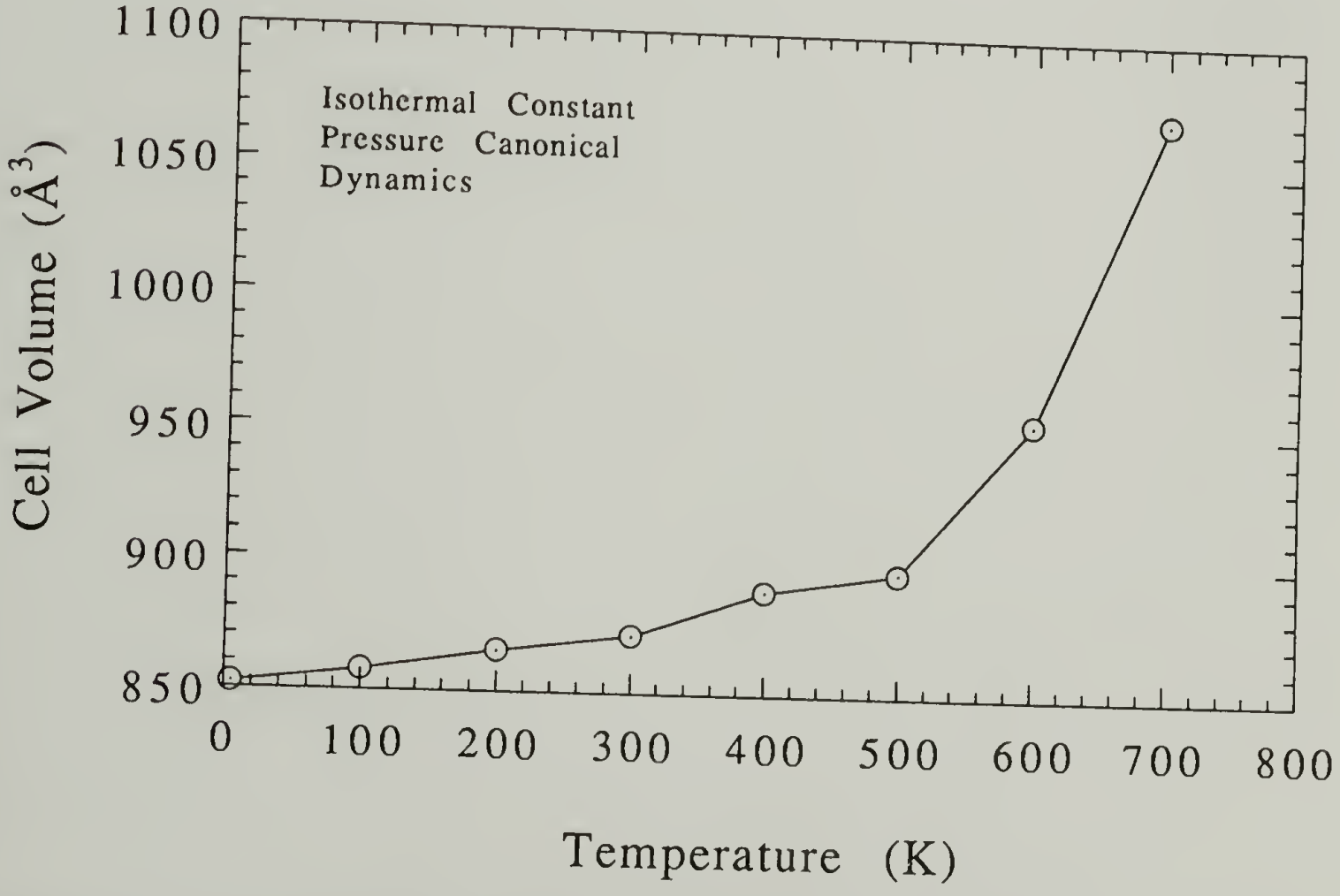

Figure 6.8. Volume expansion of the unit cell in PMDA-ODA polyimide as a function of temperature.

Table 6.2. Comparison with reported values for thermal expansion coefficients.

In-Plane (PPM/K)	Out-of-Plane (PPM/K)	Material	Temp. Range K	Method	Reference
1	109	PMDA-ODA	0-500	Simulation	This study
28	113	PMDA-ODA	300-700	PVT	1
20	83	PMDA-ODA	300-400	Capacitance	2
9	110	BTDA/DAPI	300-600	Interferometry	3
9	111	PE crystals	100-300	X-ray	4

1: reference 15.
2: reference 14.
3: reference 20.
4: reference 16.

6.5 Conclusions

A full set of elastic constants suitable for usage in mechanical modeling of these materials has been provided. The magnitude of the axial modulus of PMDA/4,4'-ODA polyimide appears to be closely related to the influence of its ether oxygen linkage. Anisotropic thermal expansion data can be generated with constant-pressure isothermal canonical dynamics. The average thermal expansion behavior correlates well with experimental data over similar temperature ranges.

6.6 References

(1) Mayo, S. L.; Olafson, B.D.; Goddard III, W.A. *J.Phys.Chem.***1990**, *94*, 8897.

(2) Gasteiger, J.; Marsili, M. *Tetrahedron* **1980**, *36*, 3219.

(3) Fletcher, R.; Powell, M.J.D. *The Computer Journal* **1963**, *6*, 163.

(4) Burkert, U.; Allinger, N. L., *Molecular Mechanics; ACS Monographs*: Washington D.C., 74, 1982.

(5) *Polygraf*™, Reference Manual, 1993.

(6) Farris, R.J.; Madden, M.A. in *Advances in Polyimide Science and Technology* ed. by Feger, C., Khojasteh, M.M., and Htoo, M.S.; Technomic Pub. Co. Inc.: Lanc.Basel, 1993, 644.

(7) Kurmar, S.S.; Fartash, A.; Grimsditch, M.; Schuller, I.K.; Kumar, R.S. *Macromol.* **1993**, *26*, 6184.

(8) Treloar, L.R.G., *Polym.* **1960**, *1*, 95.

(9) Treloar, L.R.G., *Polym.* **1960**, *1*, 279.

(10) Kochi, M.; Yonezawa, T.; Yokota, R.; Mita, I., *Advances in Polyimide Science and Technology;* ed. by Feger, C., Khojasteh, M.M., and Htoo, M.S. Technomic Pub. Co. Inc.: Lanc.Basel, **1993**, 375.

(11) Bessonov, M.I.; Koton, M.M.; Kudryavtsev, V.V.; Laius, L.A., *Polyimides: Thermally Stable Polymers;* Consultants Bureau: New York., 177, 1987.

(12) Sakurada, I.; Kaji, K. *J. Polym. Sci.: Part C* **1970**, *31*,57.

(13) Chen, S.T.; Wagner, H.H. *J. of Elect.Mat.* **1993**, *22*, 797.

(14) Saraf, R.F.; Tong, H.; Poon, T.W.;Silverman, B.D.; Ho, P.S.; Rossi, A.R. *J. of Appl. Polym. Sci.* **1992**, *46*, 1329.

(15) Pottiger, M.T.; Coburn, J.C., *Ann. Tech. Conf. of the Soc. of Plast. Eng. Antec* **1993**, 1925.

(16) Choy, C.L.;Wong, S.P.;Young, K. *J. Polym. Sci.: Polym. Phys. Ed.* **1984**, *22*, 979.

(17) Ree, M.; Nunes, T.L.; Czornyj, G.; Volksen, W. *Polymer* **1992**, *33*, 1228.

(18) Jennings, R.; PhD Dissertation, Dept. of Polym. Sci. and Eng. The University of Massachusetts at Amherst, 1993.

(19) Prest, Jr., W.M.; Luca, D.J. *J. Appl. Phys.* **1979**, *50*, 6067.

(20) Elsner, G.; Kempf, J.; Bartha, J.W.; Wagner, H.H. *Thin Solid Films* **1990**, *185*, 189.

CHAPTER 7

STRESS ANALYSIS OF PLANAR GEOMETRIES

7.1 Introduction

As explained in Chapter 2, stress transfer takes place mostly near fiber ends or near the edges of coatings. Finite element analysis was utilized to study the phenomena at the constrained edge of a polymeric coating in a manner similar to one used in the fiber case. Axisymmetric plane-2D elements were used for this analysis. Coating anisotropy is considered here by using an appropriate set of elastic constants. These elastic constants are a scaled subset of those obtained with computer simulation methods. Preferential molecular orientation in these films was taken into account when scaling these constants. As explained previously, preferential orientation in PMDA-ODA arises during the manufacturing of films.

Away from the edges, a constrained coating can be assessed only in terms of two dimensions. In this case, state-of-plane stress holds for a stress analysis of the most common case of a thin film adhered to a much thicker substrate. Effect of constraints on stress development in coatings can be simplified by observing plane stress conditions. These simplifications yield the stress-strain relations shown below for constrained films in Cartesian coordinates.

One dimensional constraint:

$$d\sigma_{xx} = -E\alpha dT \tag{7.1}$$

Biaxial constraint:

$$d\sigma_{xx} = d\sigma_{yy} = -E\alpha dT/(1-\nu) \tag{7.2}$$

Specifically for a coating:

$$d\sigma^c_{xx} = d\sigma^c_{yy} = E^c(\alpha^s-\alpha^c)dT/(1-\nu^c) \tag{7.3}$$

where $E^s\ t^s >> t^c\ E^c$

For equations 7.1-7.3, σ_{xx} and σ_{yy} are in-plane stresses that have the same magnitude due to the assumption of isotropy in the plane. $\sigma_{xy} = 0$ for the cases given above.

It can be readily seen from Equation 7.3 that the residual or in-plane stress will be strongly influenced by the resulting film moduli as well as the mismatch in the thermal expansion coefficients between the coating and its substrate.[1]

Stress level depends on the nature of the constraints in these films.[2] For example, the stress can increase from 9 to 14 MPa by increasing the dimensionality to a biaxial level, and further beyond these levels if the sample was volumetrically constrained. These numbers are for a PMDA-ODA polyimide film with a tensile modulus of 3 GPa, a Poisson's ratio of 0.34, a temperature change of -100 °C, and thermal expansion coefficients of 30 and 5 ppm/K for coating and substrate, respectively.

The equations shown above do not describe edge effects. Thus, they only describe the state of stress of the film away from edges. These far-field stresses do not

act to debond the coating. Out-of-plane stresses and in-plane shear stresses are only significant at the edges.

The tendency for coatings to peel spontaneously has always been a concern of scientists and engineers.[2,3] The problem of tension in metallic films deposited by electrolysis was considered by Stoney at the start of this century.[4] For Stoney's study and most subsequent work on the stresses developed by coatings or bilayer strips, isotropic properties were always assumed.[5-10] Due to their industrial importance, residual stresses developed in polymeric coatings have also been studied.[11-15] The stresses in polyimide coatings specifically have already been the subject of several works.

When isotropy is assumed, St. Venant's principle is fully applicable. The portion of the principle applicable to this situation pertains to the homogeneity of the body and has been stated as follows:[16] "A self-balanced system of forces applied to a small region of a homogeneous elastic body is ordinarily resisted principally by the material in the neighborhood of the region, the resulting stresses falling off rapidly away from the region and becoming negligible at distances large compared to the dimensions of the region". The rate of stress decay for an anisotropic material is expected to be different than that predicted by assuming isotropic conditions.

This chapter presents the evaluation of the effects of anisotropy on the stress transfer process that occurs at the edges of the coating. Elastic constants from molecular simulation are utilized to supplement those constants already known for anisotropic polyimide films.

7.2 Calculation of Thermally Induced Stresses Near The Coating's Edge

7.2.1 Explanation of The Finite Element Model and Boundary Conditions

The calculations shown below are for a temperature change of -100 K. Results from finite element analysis are compared with those obtained by analytical solutions. For either case, isotropic or not, it was observed that out-of-plane stresses and shear stresses were significant at the edges of the coating. These stresses, which are on the order of a few megapascals, decay within a few film thicknesses away from the edge of the film.

The finite element procedure is very similar to that utilized in chapter 2. Axisymmetric plane-2D elements were utilized to probe the stresses generated in the coating. The analyzed geometry, the boundary conditions and the loading are shown in Figure 7.1 below.

The ratio of the radius of the substrate with respect to its thickness was 100. The ratio of the thickness of the substrate to the coating, which covered the top surface of the substrate, was also 100. The total number of elements utilized in the model was 1500 and the total number of nodal points was 1581. A perfect bond between the coating and its substrate was assumed. The boundary conditions, as shown in Figure 7.1, indicate a zero shear and normal stress at the top surface and the free edge. The origin was pinned to avoid rigid body displacement.

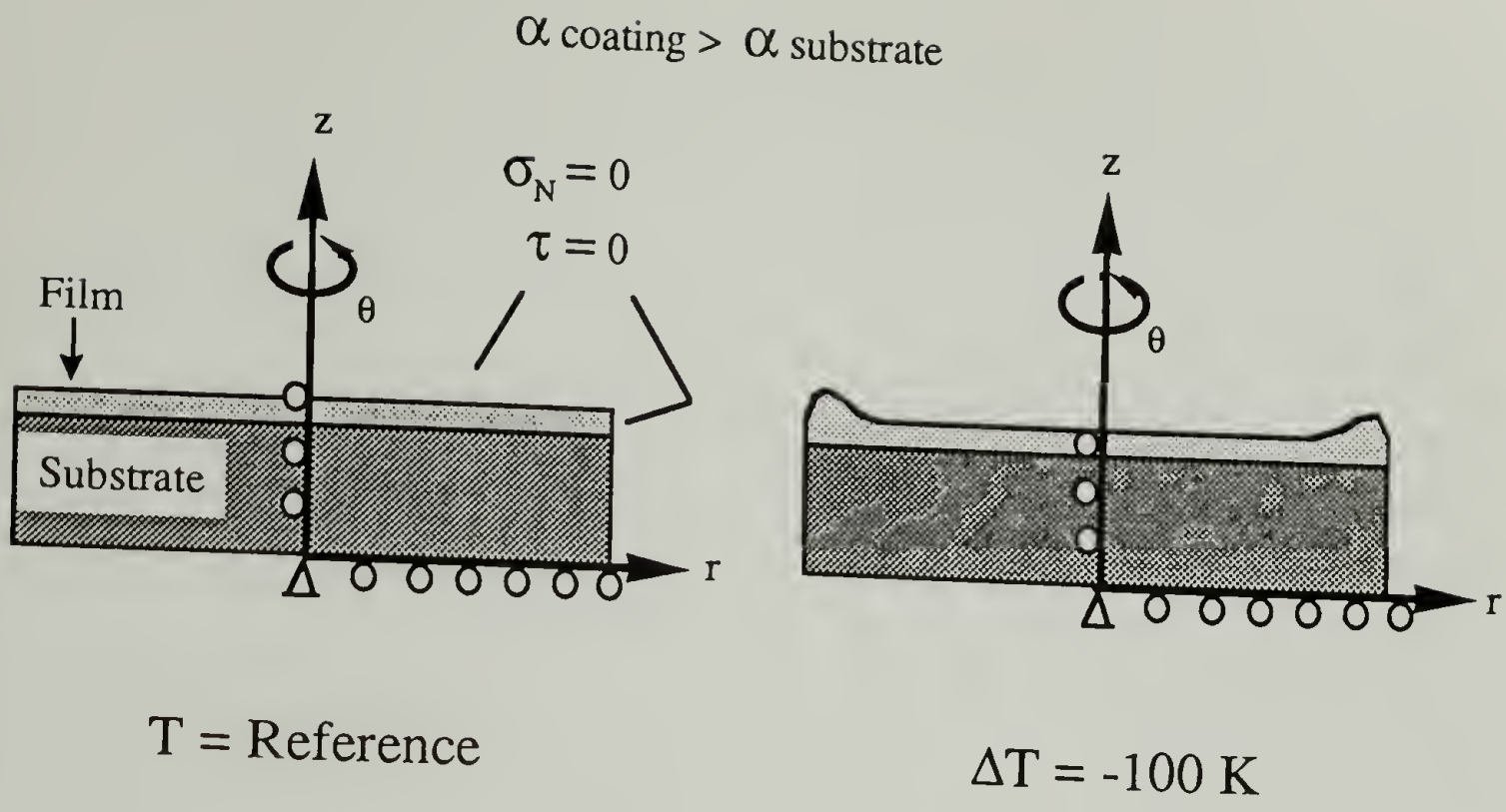

Figure 7.1. Deformation of a thin polymeric coating mounted on a hard substrate when the coefficient of thermal expansion is larger in the coating than the substrate.

The boundary conditions shown in 7.1 were checked on the top surface and edge of the coating. The isotropic finite element analysis for these regions are shown in Figures 7.2 and 7.3, respectively. In the first of these figures it is clear that there are no significant contributions of shear or out-of-plane stresses. The in-plane stress remains constant throughout the entire radius of the coating, except of course at the edges, and yields approximately the same far-field value as equation 7.3, 11.5-11.8 MPa. Figure 7.3 shows the stresses across the thickness of the substrate at the very edge of the coating. Shear and out-of-plane stresses decay rapidly from the coating/substrate interface.

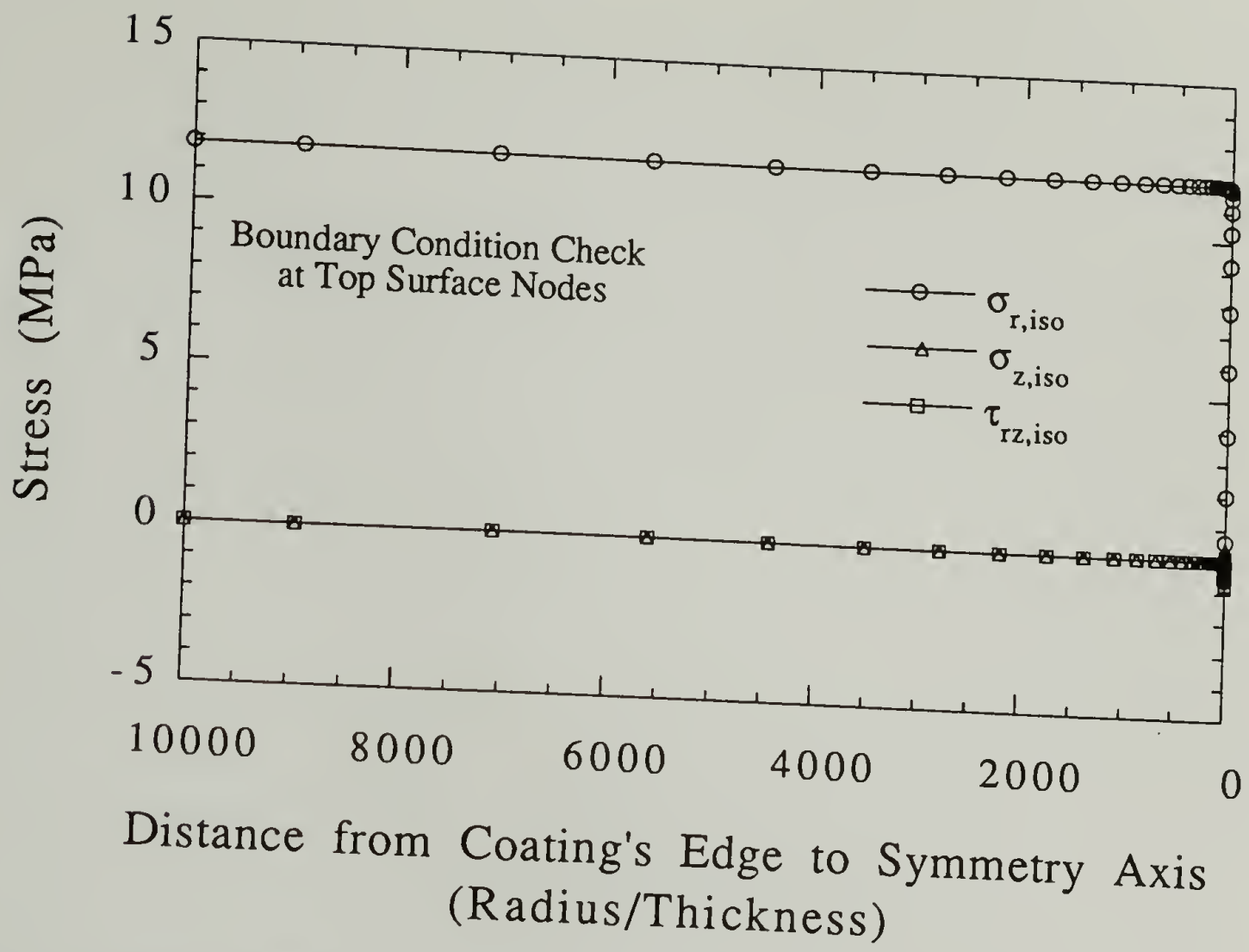

Figure 7.2. Nodal stresses at the top surface of a PMDA-ODA polyimide coating on a glass substrate. Thermally loaded.

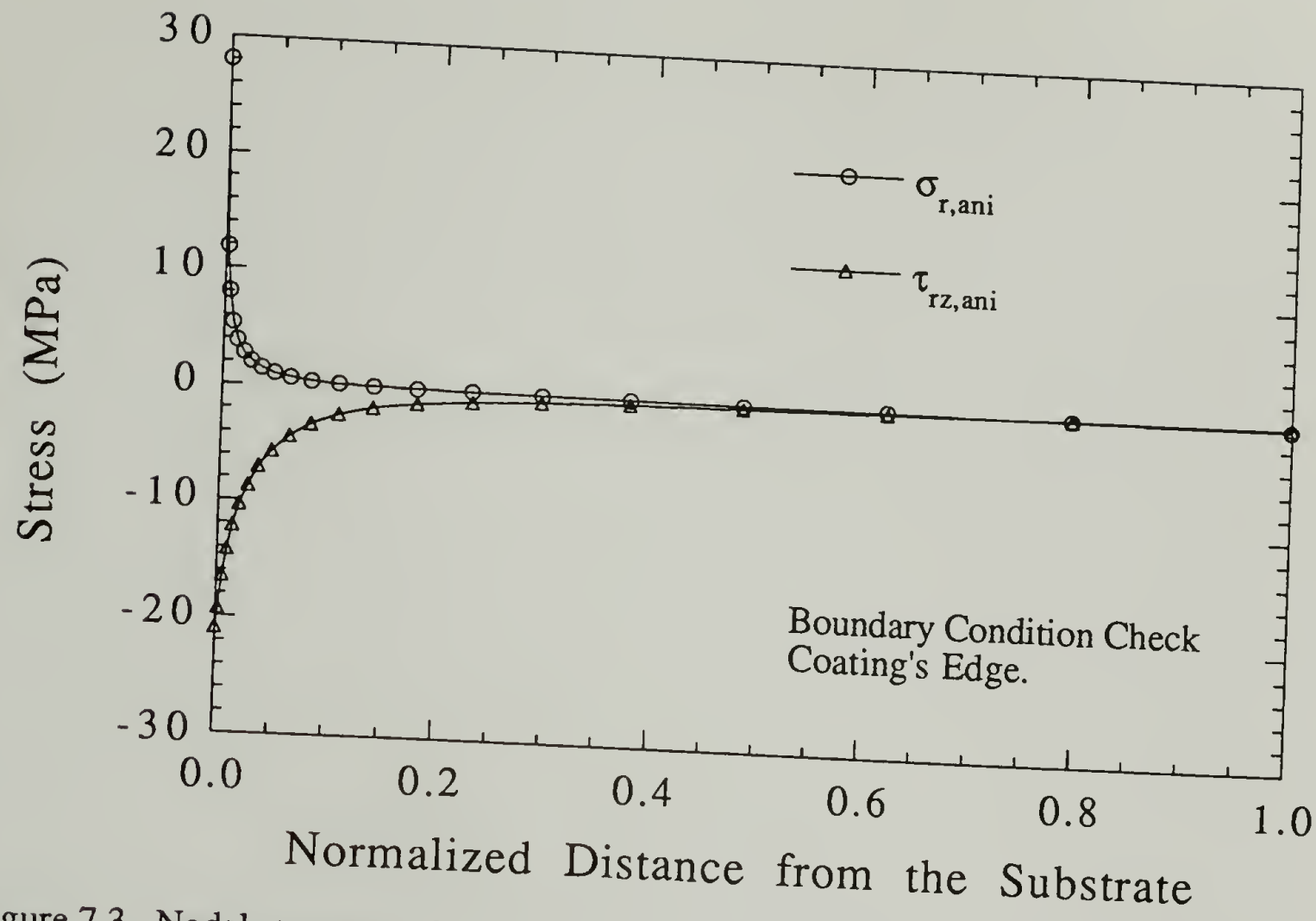

Figure 7.3. Nodal stresses at the edge of a PMDA-ODA polyimide coating on a glass substrate. Thermally loaded.

The side corresponding to the center of symmetry of the body of revolution was also checked, and this is shown in Figure 7.4. It can be observed from this latter figure that there are no anomalies at the center of symmetry. Shear and out-of-plane stresses are virtually non-existent and the in-plane stress displays its far-field value.

The Hooke's law equations for this special case of an orthotropic body, planar anisotropic material with axially symmetric geometry, are shown below.[17] The z-direction is the out-of-plane direction and the r and θ directions are those denoting the plane of the coating :

$$\varepsilon_r = \frac{1}{E} (\sigma_r - \nu \sigma_\theta) - \frac{\nu'}{E'} \sigma_z \qquad (7.4)$$

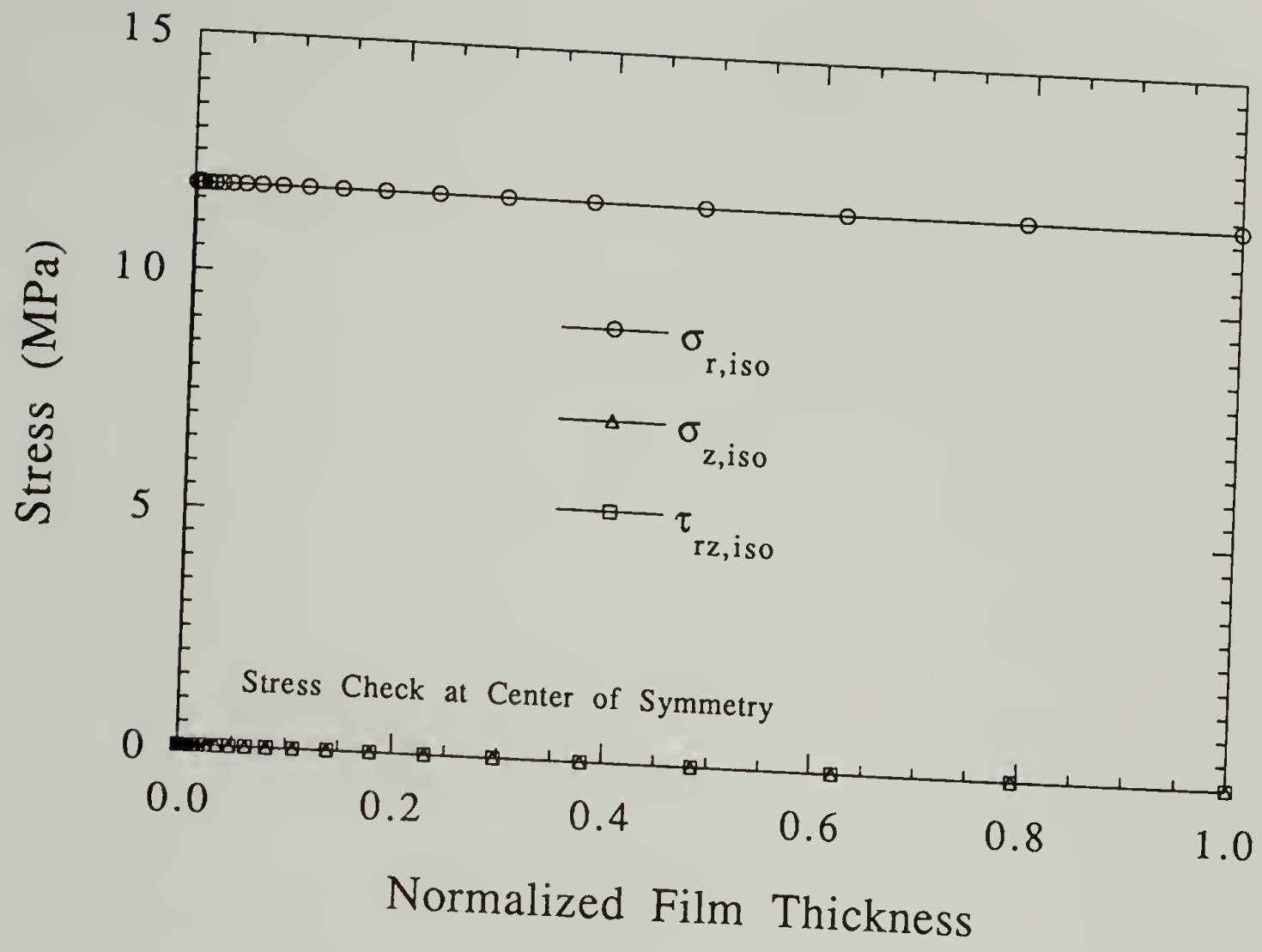

Figure 7.4. State of stress at the center of symmetry of a PMDA-ODA polyimide coating on glass substrate. Thermally loaded.

$$\varepsilon_\theta = \frac{1}{E}\,(\sigma_\theta - \nu\,\sigma_r) - \frac{\nu'}{E'}\,\sigma_z \tag{7.5}$$

$$\varepsilon_z = -\frac{\nu}{E}\,(\sigma_r - \sigma_\theta) + \frac{1}{E'}\,\sigma_z \tag{7.6}$$

$$\gamma_{\theta z} = \frac{1}{G'}\,\tau_{\theta z} \tag{7.7}$$

$$\gamma_{rz} = \frac{1}{G'}\,\tau_{rz} \tag{7.8}$$

$$\gamma_{r\theta} = \frac{1}{G}\,\tau_{r\theta} = \frac{2\,(1+\nu)}{E}\,\tau_{r\theta} \tag{7.9}$$

where E, G, and ν are the in-plane constants and E', G', and ν' are out-of-plane constants for the symmetry specified above.

The set of elastic and thermo-physical constants utilized for the fully isotropic and anisotropic cases are listed below.

Polyimide coating:

$E_r = 3$ GPa $\quad \nu_{rz} = 0.24 \quad G_{rz} = 0.15$ GPa $\quad \alpha_r = 30$ ppm/K

$E_\theta = 3$ GPa $\quad \nu_{r\theta} = 0.44 \quad G_{r\theta} = 0.26$ GPa $\quad \alpha_\theta = 30$ ppm/K

$E_z = 0.72$ GPa $\quad \nu_{z\theta} = 0.24 \quad G_{z\theta} = 0.15$ GPa $\quad \alpha_z = 110$ ppm/K

Glass substrate:

$E = 120$ GPa $\quad \nu = 0.25 \quad \alpha = 4$ ppm/K

For the isotropic case, the constants for the polyimide coating were:

$E = 3$ GPa $\quad \nu = 0.34 \quad \alpha = 30$ ppm/K

The anisotropic elastic constants for PMDA-ODA obtained with simulation were scaled according to the magnitude of those that could be determined experimentally. For example, 3 GPa was the experimentally determined modulus in the plane, and the ratio of the axial to transverse moduli from simulation was 4.17 (41.53/{[6.36+13.55]/2}). So, a value of 0.72 GPa was obtained for the out-of-plane direction. If the molecules preferentially point upwards, as suggested in chapter six, an alternative way of scaling in-plane anisotropy can be carried out. However, the ratio of in-plane to out-of-plane moduli has a similar magnitude as before 4.33 ({[41.53+13.55]/2}/6.36). In a similar manner, an experimentally obtained value of 0.44 was adopted for the highest Poisson

ratio.[18] Higher contrast in Poisson ratios would increase sensitivity in the detection of any anisotropic effect. Poisson ratios of 0.34 are frequently observed in the literature for film made from PMDA-ODA polyimide. This latter value was utilized for the Poisson ratio in the isotropic case.

At the edges of the coating, it was expected that there would be significant contributions from the out-of-plane and shear stresses. This is observed from Figure 7.5, which shows results obtained with finite element analysis at the coating/substrate interface. Out-of-plane and shear stresses are shown to have a significant magnitude at the edges in this figure. It can also be observed from the same figure that these stresses decayed to almost their full far-field value within 5 coating thicknesses away from the edge. However, the rate of decay is initially faster for the out-of-plane stress. The edge is then the only place where the coating is actually being pushed or sheared away from the substrate. The only stress present that is away from the edges is the in-plane stress and it also reaches its full value within 5 film thicknesses.

The results shown in Figure 7.5 were obtained with the constants listed above. It was surprising to observe so little change in the stress distributions between isotropic and anisotropic cases. A less subtle change can be observed when stresses at the edge of the coating are plotted as a function of film thickness. Anisotropy provides a more gradual stress decay and a longer stress transfer length. Figure 7.6 shows the isotropic and anisotropic shear stress distributions at the edge of the coating plotted versus distance from the coating/substrate interface.

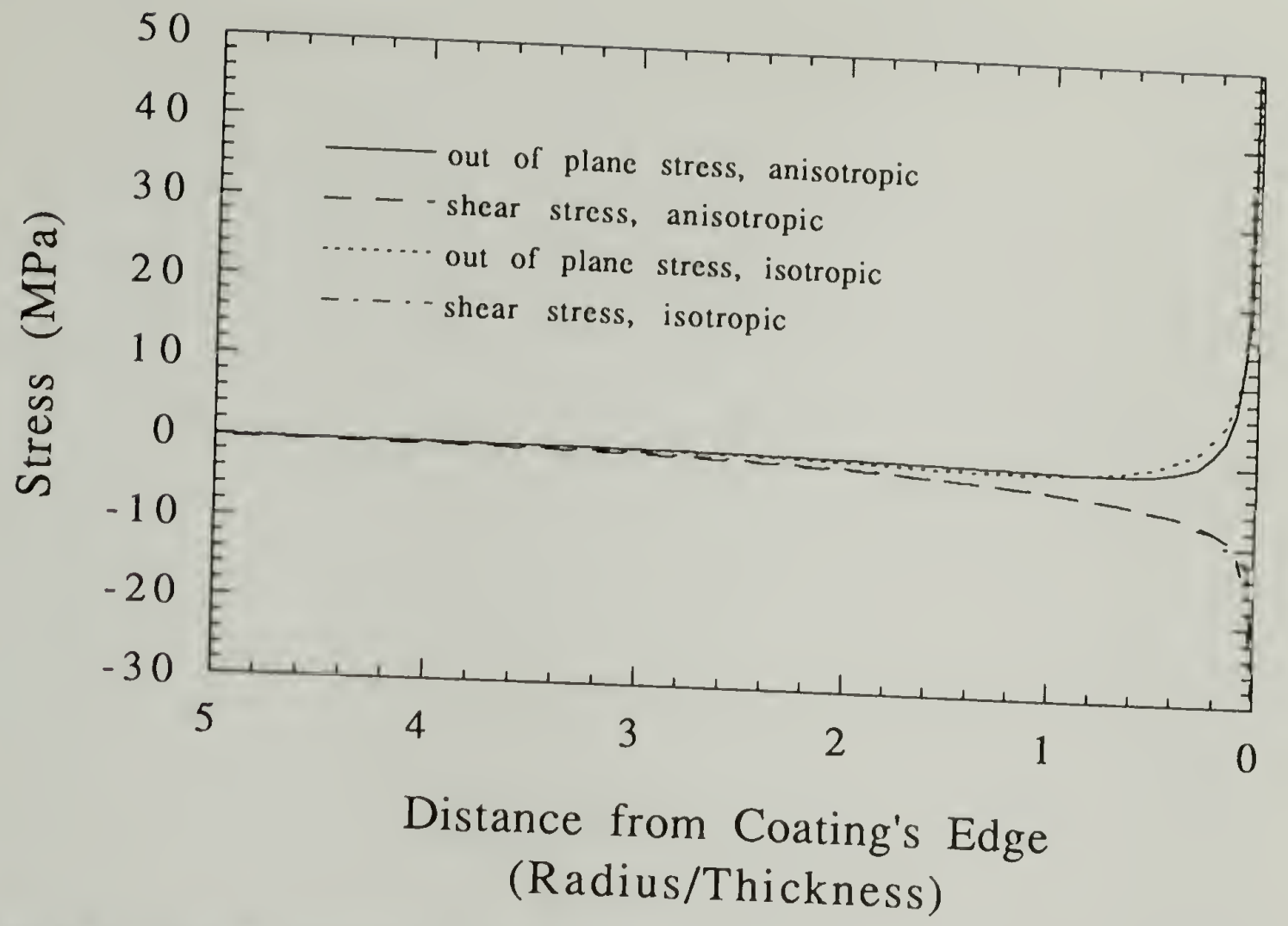

Figure 7.5. Finite element results of interfacial stresses for a thermally loaded PMDA-ODA polyimide coating on a glass substrate.

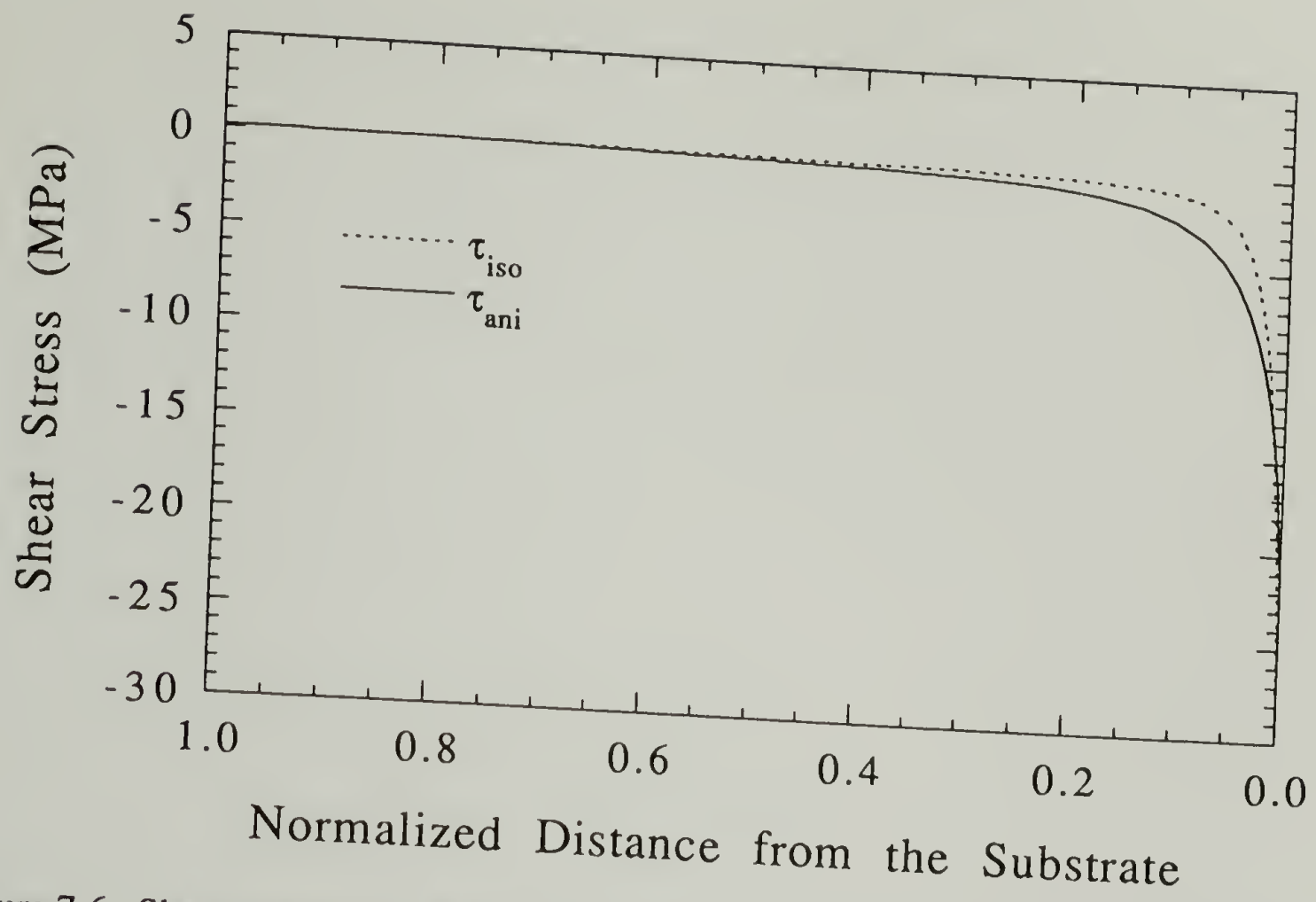

Figure 7.6. Shear stress at the edge of the coating versus film thickness. Isotropic and anisotropic stress distributions are shown.

The effect that a higher in-plane modulus, or higher degree of anisotropy, has in these distributions is shown in Figure 7.7. The in-plane modulus was changed from 3 to 100 GPa in the anisotropic case. However, in order to observe the effect of anisotropy in the coating, shear stress distributions with equal far field in-plane stress need to be compared. The in-plane modulus is, of course, directly proportional to the in-plane stress which means that a large modulus will generate large stresses. The shear stress distribution for the anisotropic case was then scaled to account for the change in the magnitude of the in-plane stress. The shear stress distribution showed a slower decay when the degree of anisotropy was higher (Figure 7.7). It took nearly 50 thicknesses for the shear stress to reach its far-field value.

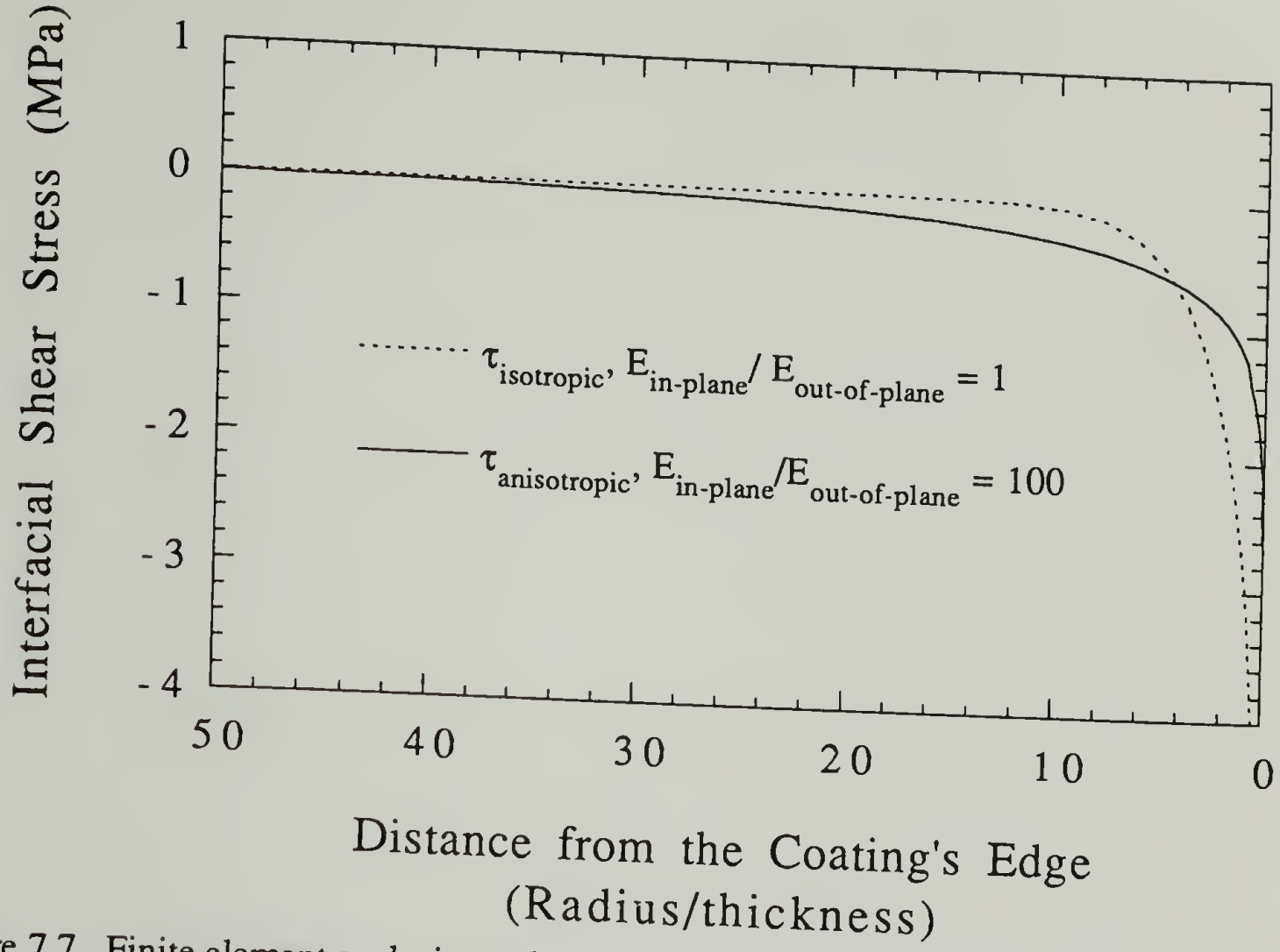

Figure 7.7. Finite element analysis results for a thermally loaded PMDA-ODA coating on a glass substrate. Comparison between coatings with high and low anisotropy.

7.2.2 Comparison with Analytical Solutions

Previous attempts to analyze the effects at the ends of constrained systems have yielded approximate solutions for isotropic stress distributions.[19-22] In one of these studies, it was found that the effects of the applied stress were not significant beyond several film thicknesses away from the edges.[20] The analytical solutions presented in that study, which were based on the principle of least work, did not account for the influence of substrate physical constants in development of stress in the coating. Furthermore, the plots shown in the study could not be reproduced with the information presented. Efforts

have been made to obtain stress distributions at the interface of bi-material structures with finite element analysis.[23]

Finite element analysis results in this study for stress distributions near the edge have been compared with those analytical results from coatings as microelectronic assembly layers.[18] These analytical solutions were derived to determine the stresses in adhesively bonded bi-material assemblies, like those utilized in electronic packaging. The solutions for the stresses are very similar to those obtained by Timoshenko,[5] except for the factor $\chi(x)$ (equation 7.13), which makes this solution satisfactory at the coating's edge. This factor is based on an exponential decay of the square root of the ratio of the axial compliance to the interfacial compliances of the coating and its substrate, k (equation 7.19). The direction parallel to the length of the assembly is x.

Following the convention of reference 19, the in-plane stress of the coating at the coating/film interface is $\sigma_2(x)$ and that of the substrate is $\sigma_1(x)$. $\tau(x)$ is the interfacial shear stress.

$$\sigma_1(x) = \frac{\Delta\alpha\,\Delta T}{\lambda\, h_1}\,\chi\,(x) \tag{7.10}$$

$$\sigma_2(x) = -\frac{\Delta\alpha\,\Delta T}{\lambda\, h_2}\,\chi\,(x) \tag{7.11}$$

$$\tau\,(x) = \frac{\Delta\alpha\,\Delta T}{k\,\kappa}\,e^{-k(l-x)} \tag{7.12}$$

where,

$$\chi\,(x) = 1-e^{-k(l-x)} \tag{7.13}$$

this factor approaches unity at places away from the edges of the assembly. The assembly length is l (exponent) and,

$$\lambda = \lambda' + \frac{h^2}{4D} \tag{7.14}$$

$$\lambda' = \lambda_1 + \lambda_2 \tag{7.15}$$

λ_1 and λ_2 are denoted as the axial compliances of the components.

$$h = h_1 + h_2 \tag{7.16}$$

h_1 and h_2 are the thicknesses of each layer.

$$D = D_1 + D_2 \tag{7.17}$$

D_1 and D_2 are the flexural rigidities of the components

$$D_1 = \frac{E_1 h_1^3}{12\,(1-\nu_1^2)}, \quad D_2 = \frac{E_2 h_2^3}{12\,(1-\nu_2^2)} \tag{7.18}$$

E_1 and E_2 are the elastic moduli of the materials and ν_1 and ν_2, their respective Poisson ratios.

$$k = \sqrt{\frac{\lambda}{\kappa}} \tag{7.19}$$

$$\lambda_1 = \frac{1-\nu_1^2}{E_1 h_1} \tag{7.20}$$

$$\lambda_2 = \frac{1-\nu_2^2}{E_2 h_2} \tag{7.21}$$

$$\kappa = \kappa_1 + \kappa_2 \tag{7.22}$$

κ_1 and κ_2 are regarded as the in-plane shear compliances of the components.

$$\kappa_1 = \frac{2}{3}\,\frac{1+\nu_1}{E_1}\,h_1 \tag{7.23}$$

$$\kappa_2 = \frac{2}{3}\,\frac{1+\nu_2}{E_2}\,h_2 \qquad (7.24)$$

The values utilized for the constants in the evaluation of the stress distributions are given below:

$E_1 = 120$ GPa $\quad E_2 = 3$ GPa $\quad \nu_1 = 0.25$ $\quad \nu_2 = 0.34$

$\Delta T = -100$ K $\quad \Delta\alpha = 25$ ppm/K $\quad l = 1$ $\quad h_1 = 1$ $\quad h_2 = 0.01$

A comparison of the stress distributions generated by equations 7.11 and 7.12, in-plane and shear stress, respectively, are provided in Figures 7.8 and 7.9. It can be observed from Figure 7.8 that the analytical solution yielded a lower value for the far-field in-plane stress. Three dimensional effects are not accounted for in the analytical solution, as it is in a two dimensional solution in Cartesian coordinates. The validity of the far-field value obtained with the finite element approach was verified above with the appropriate Hooke's law equations. The same value was obtained for this stress when the difference in thermal expansion coefficients was changed from 25 ppm/K to 35 ppm/K. For the isotropic case of finite element analysis, the thermal expansion coefficient for the glass substrate was 4 ppm/K and that of PMDA-ODA was 30 ppm/K. The thermal load was -100 K in both cases.

The solutions for the shear stress at the interface, Figure 7.9, show that the distribution is not matched at the edges. Choices of the factor χ (x) or the geometrical difference of the finite element model within this region may be the reason for this difference. Photoelastic measurements on shrunken epoxy slabs bonded to rigid plates have provided experimental stress distributions at the edge similar to those shown in this chapter.[24] An investigation of the influence of thermal loads on stress concentrations at the corners of microelectronic components. [25]

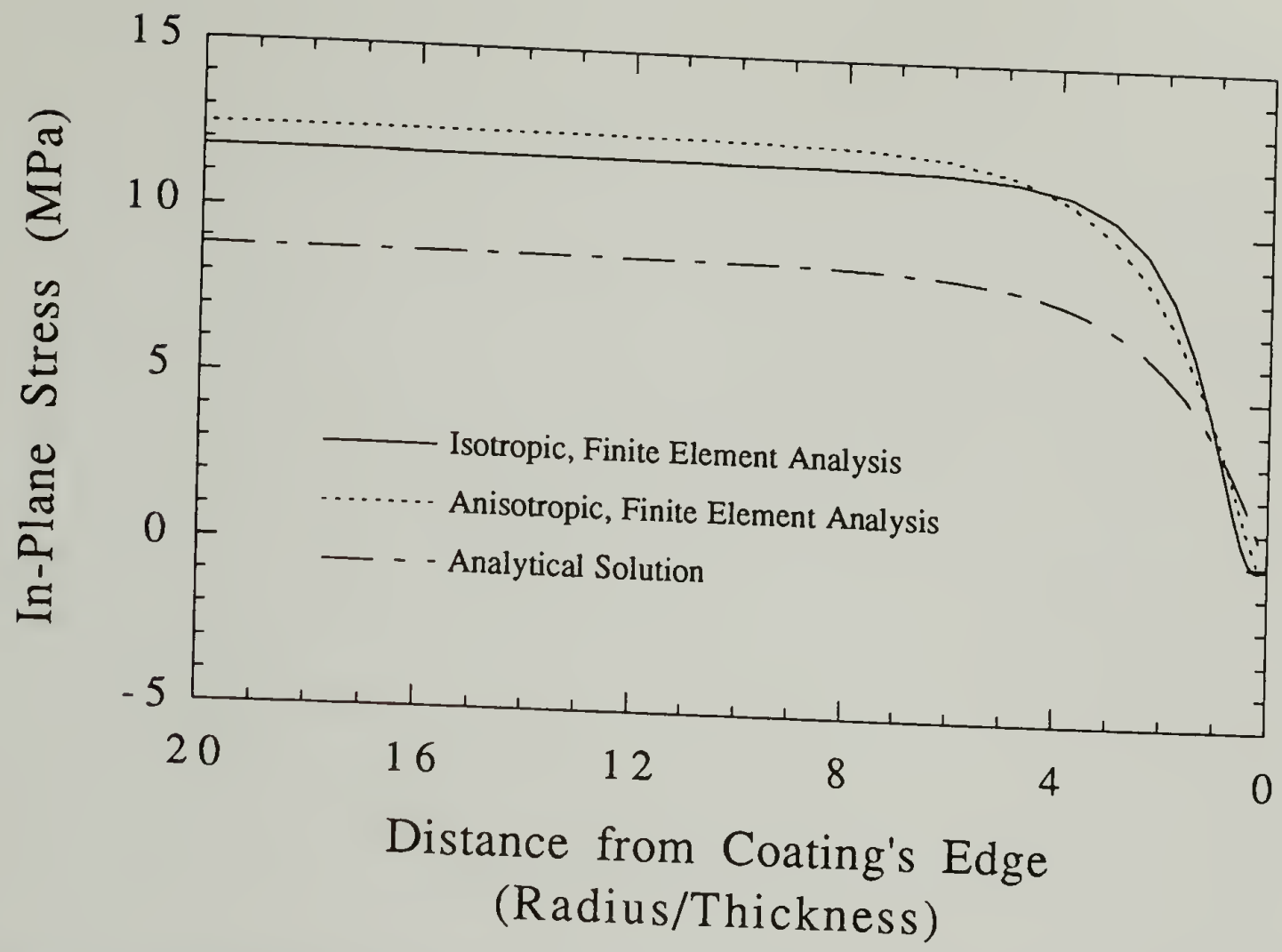

Figure 7.8. Comparison of analytical solution and finite element results for the in-plane stress at a region away from the coating/substrate interface.

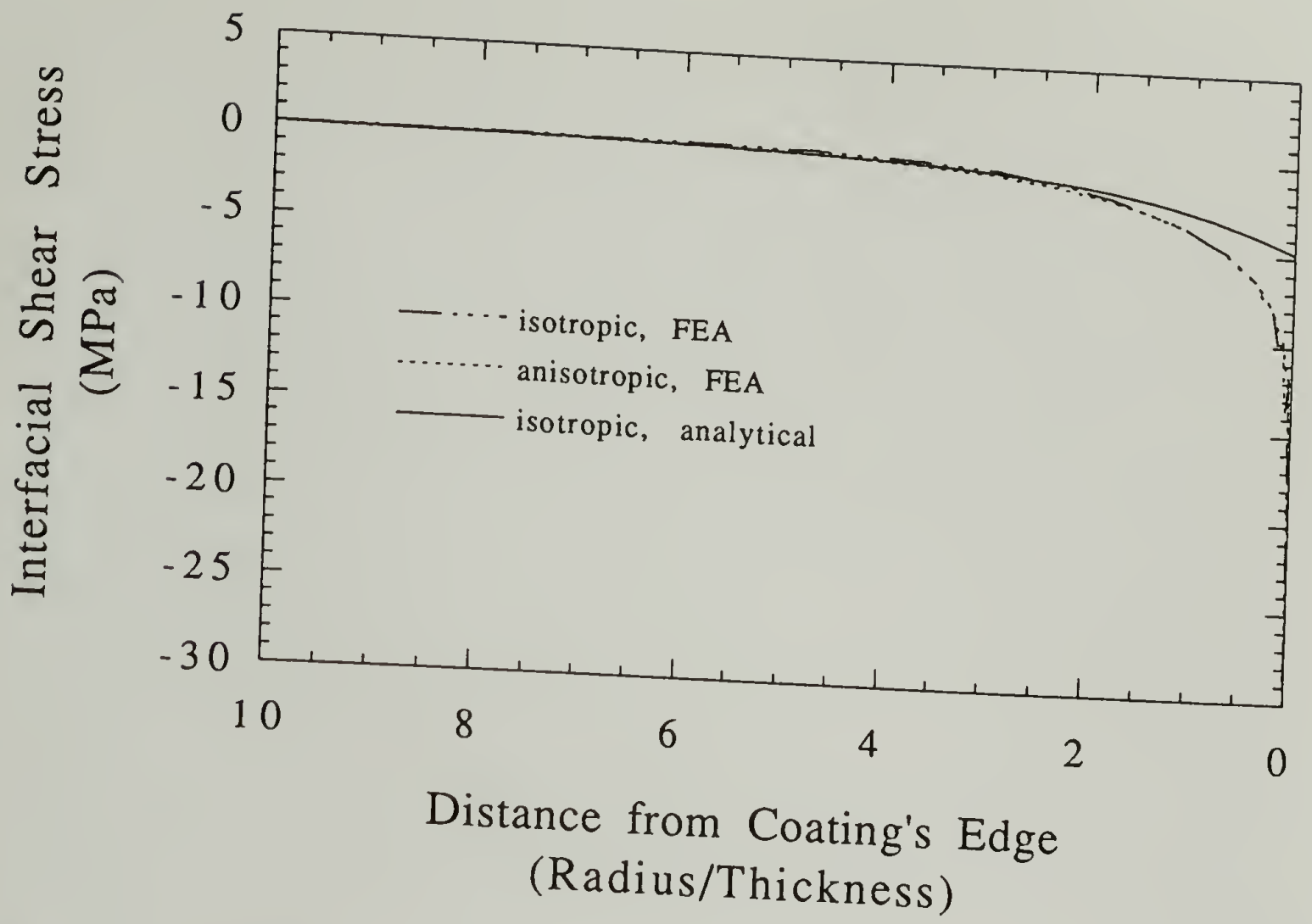

Figure 7.9. Comparison of shear stresses at the interface computed by finite element analysis and analytical solution.

7.3 Conclusions

Finite element analysis, demonstrated that significant contributions from the out-of-plane and shear stresses were observed at the edges of the coatings. These stresses decayed rapidly from the edge and their magnitude was no longer significant after 5 coating thicknesses away from the edge. The rate of decay is initially faster within the first two coating thicknesses. The coating is actually being pushed or sheared away from the substrate is at its edges. Only the in-plane stress is significant away from the edges. Its rate of change is fast within the first 2 thicknesses and it reaches its full value within 5 thicknesses. In the far-field, analytical solutions have yielded a lower in-plane stress than that predicted by finite element analysis or Hooke's law equations. It is suspected that a solution in two dimensions would not provide the same value obtained with finite element results. The difference in thermal expansion coefficients between the coating and its substrate provides for the most significant contribution to the magnitude of the in-plane stress.

The difference between stress distributions for isotropic and anisotropic cases was subtle with the sets of elastic constants utilized. To increase the degree of anisotropy, the modulus was increased from 3 GPa to 100 GPa. The effect was a shear stress distribution that showed a slower decay when the degree of anisotropy was higher.

7.4. References

(1) Plepys, A.R.; Farris, R.J. *Polym.* **1990**, *31*, 1932.

(2) Bauer, C.L.; Farris, R.J. *J. of Coatings Technol.* **1988**, *60*, 51.

(3) Goldfarb, J.L.; Farris, R.J. *J. of Adhesion* **1991**, *35*, 233.

(4) Stoney, G.G. *Proc. Roy. Soc. Lond.* **1909**, *A82*, 172.

(5) Timoshenko, S. *J. Opt. Soc.Am.* **1925**, *11*, 23.

(6) Brenner, A.; Senderoff, S. *J. Res. Natl. Bur. Std.* **1949**, *42*, 105.

(7) Olsen, G.H.; Ettenberg, M. *J. of Appl. Phys.* **1977**, *48*, 2543.

(8) Vilms, J.; Kerps, D. *J. of Appl. Phys.* **1982**, *53*, 1536.

(9) Henein, G.E.; Wagner, W.R. *J. of Appl. Phys.* **1983**, *54*, 6395.

(10) Barnett, D.M.; Townsend, P.H. *J. of Appl. Phys.* **1987**, *62*, 4438.

(11) Maden, M., PhD Dissertation. Dept. of Polym. Sci. and Eng. The University of Massachusetts at Amherst. Amherst, Mass., 1992.

(12) Tong, K., PhD Dissertation. Dept. of Polym. Sci. and Eng. The University of Massachusetts at Amherst. Amherst, Mass., 1993.

(13) Coburn, J.C.; Pottiger, M.T.; Noe, S.C.; Senturia, S.D, submitted to *J. Polym. Sci. B: Phys.*, 1994.

(14) Ree, M.; Nunes, T.L.; Czornyj, G.; Volksen, W. *Polym.* **1992**, *33*, 1228.

(15) Elsner, G. *J. of Appl. Polym. Sci.* **1987**, *34*, 815.

(16) Donnel, L.H. *J. of Appl. Mech.; Brief Notes.* **1962**, 753.

(17) Lekhnitskii, S.G., *Theory of Elasticity of an Anisotropic Elastic Body*; Holden Day, Inc.: San Francisco, 1963.

(18) Maden, M.A.; Tong, K.; Farris, R.J. *Mat. Res. Soc. Symp. Proc.* **1991**, *203*, 129.

(19) Suhir, E. *Mat. Sci. Res.Soc. Symp.Proc.*, Elect. Pack. Mat. Sci. II, Jackson, K.A.; Pohanka, R.C.; Uhlman, D.R.; Ulrich, D.R., ed. **1986**, *72*, 133.

(20) Aleck, J.B. *J. of Appl.Mech.* **1949**, *16*, 118.

(21) Pionke, C.D.; Wempner, G. *J. of Appl. Mech.* **1991**, *58*, 1015.

(22) Herakovich, C.T. *J. of Strain Ana.* **1989**, *24*, 245.

(23) Nakamura, T. *J. of Appl. Mech.* **1991**, *58*, 939.

(24) Durelli, A.J.; Parks, V.J.; del Río, C.J. *Exp. Mech.* **1967**, *Nov.*, 481.

(25) Mark, R. *Exp. Mech.* **1977**, *April*, 121.

CHAPTER 8

EXPERIMENTAL DETERMINATION OF OUT-OF-PLANE DISPLACEMENT AT CONSTRAINED ENDS OF COATINGS

8.1 Phase Measurement Interference Microscopy, A Methodology Overview

This section entails the determination of out-of-plane displacements at the edges of coatings. These displacements, determined experimentally, can be compared with results from finite element calculations of coatings in planar geometries. Measurement of these minute displacements was accomplished with phase-measurement interference microscopy.[1-4] With this technique, vertical displacements within an in-plane region of 0.5 mm x 0.5 mm can be measured with an accuracy of about 5 Å. Surface roughness and other topographical information of interest can also be obtained with this technique. However, the horizontal resolution is limited to about 0.9 microns with our current objective lenses. A description of the technique and its advantages and limitations is provided below.

The equipment is commercially available from Zygo Corporation. (Middlefield, CT). The particular set-up utilized for our study was the Maxim-3D 5800 with Mirau objectives of magnifications 20X, 40X and 100X. The equipment is mounted on a vibration-free table. In the basic system, light from a 1 mW He-Ne laser is focused onto the first beam-splitter that sends one beam to a 512 CID array camera and the other to the objective lens. For the specific case of the Mirau objectives, a beam splitter at the

objective sends one beam to the testing surface and another to a reference surface. The path lengths from the beam-splitter to the test surface and the reference surface is approximately the same. Due to this fact, light with a coherence length of only a few wavelengths can be utilized to create interference. A piezoelectric transducer is utilized for the movement of the reference surface to produce a phase shift from the original phase difference. The phase measurement steps will be explained below in more detail. A schematic of the system is shown in Figure 8.1. From this figure it can be observed that a monitor is linked to the camera to provide a live image of the surface being tested. This image is of course utilized to focus on the test surface and for observation of the interference fringe pattern.

A dynamic phase computation technique is utilized to determine the vertical location of points in the imaging plane. As shown above, a CID array camera is utilized to detect the light intensity at a position of coordinates x,y. This intensity, I, is a combination of a time averaged sum of reflected intensities from the reference and test surfaces and a time-varying component of the interference intensity. These are respectively I_1 and I_2, in equation 8.1 below.

$$I = I_1 + I_2 \cos [\zeta(x,y) + \xi(t)] \tag{8.1}$$

In the second term, $\zeta(x,y)$, is the initial phase change between reflected wavefronts originating from the reference and test surfaces. $\xi(t)$ is the time interval between changes in the positions of the reference surface with respect to the test surface while measuring phase changes. The intensity at each pixel of the camera is integrated over this interval and recorded after phase changes.

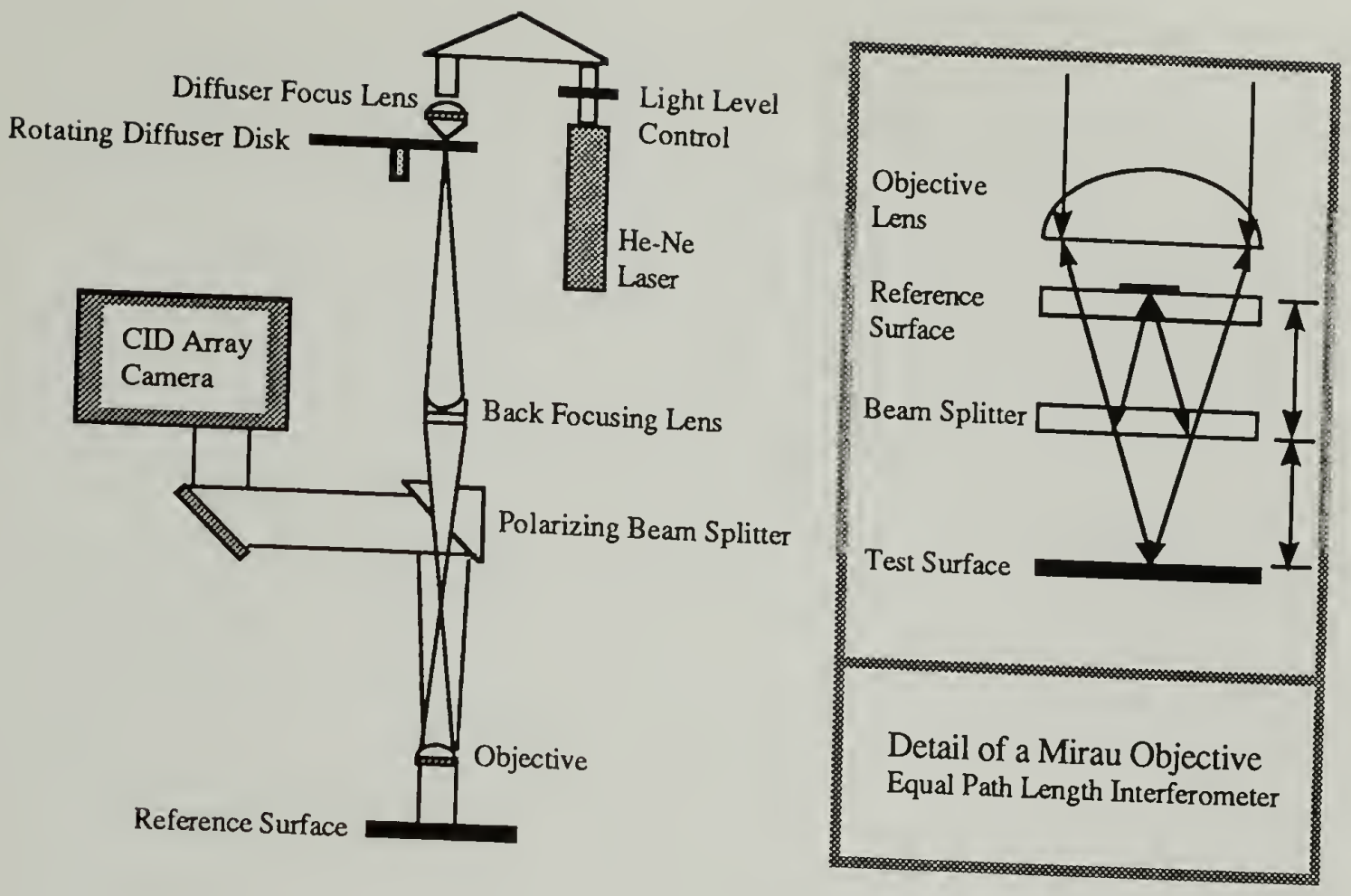

Figure 8.1. Components of a phase measurement interference microscope equipped with a Mirau objective.

A series of five of these intervals are necessary to compute the spatially dependent phase. These intervals are the consequence of shifting the position of the reference surface towards the test surface to obtain a 90° phase shift. This is done for intervals of 90°, 180°, 270°, 360° and 450°. Physically, this is possible with the usage of a piezoelectric transducer. The interference intensities are then integrated over these intervals.

Some precautions need to be taken if the test surface is composed of more than one material, or if this surface is of a thin film on a dissimilar substrate. The first case may arise when measuring step heights (coating thickness) of a coating with different optical constants than those of its substrate. The optical constants n and k, refractive

index and absorption coefficient respectively, need to be entered for the test and reference surfaces in order to avoid phase shift errors when measuring vertical distances of dissimilar materials. These constants can be obtained with ellipsometric measurements. If there is difficulty in obtaining these constants, an offset distance correction can be done instead. These constants change with differences in material, wavelength and objective's numerical aperture. The alternative offset correction entails coating the surface with an opaque specular material, measuring the step height and then correcting for the difference observed when the uncoated surface was measured. In any case the maximum step height that can be measured by our current setup is only about a quarter of the wavelength of the laser light utilized. In our particular case this limits the step height measurements to 1500 Å.

The second case where phase correction is necessary, as stated above, is that where the surface being measured comes from an optically transparent film that is very thin. In this case, light reflected from the film-substrate interface could add or subtract from that reflected from the film-air interface. Phase correction becomes necessary when a value of twice the optical thickness of the film (= refractive index * film thickness) is lower than the interference depth attained by the objective.

8.2 Advantages and Disadvantages of Phase Measurement Interference Microscopy

This technique measures surface texture in terms of width, length, and height. Its horizontal range is from 69 μm square to 6.9 mm square (this is objective dependent); while its vertical range is 1-400,000 Å. Its lateral resolution for a 20x Mirau Lens is 0.96 μm, which is almost equal to its corresponding sampling interval.[5]

Advantages of the technique and equipment are: 1) The capacity to measure film thickness, surface roughness, waviness; 2) The wide range of magnifications and lateral resolutions; 3) Its high vertical resolution; 4) Its easy incorporation as an aid in mechanical deformation measurements; 5) Good software. Disadvantages: 1) Narrow operating temperature: 15-60 °C; 2) Cannot measure films thicker than 1500 Å; 3) Vibration sensitivity; 4) Typical measurement time: 5-15 sec but takes a while to null the interference fringes when measuring step heights; 5) Small working distance for most objectives; 6) Expense of purchasing extra objectives.

8.3 Measurement of Vertical Displacements at The Edges of Coatings

Difficulties were encountered when trying to measure the vertical displacements that occur at the edges of the film. These displacements provide a direct measure of the effect of additional stresses present in this region. Figure 8.1 provides a visual account of this effect. As mentioned in chapter 7, the out-of-plane stresses and shear stresses decay rapidly from the edge of the coating and the only stress present in the far-field is the in-plane normal stress. Thermally induced out-of-plane displacement gradients in electronic assemblies have been previously measured with electro-optic holographic interferometry.[6]

Two methods were considered for measuring these displacements. Atomic force microscopy and phase-measurement interference microscopy. Only phase-measurement interference microscopy is a truly non-contact method. Atomic force microscopy provides better resolution in the plane and is able to go beyond vertical steps higher than 1500 Å. A step height is the vertical increment that is measured between two surface

points. The new two-beam microscopes can measure steps higher than 1500 Å. The interferometer microscope equipment available from our laboratories has this limitation, it cannot measure step heights larger than $\lambda/4$. This was a serious constraint since the lower limit of film thickness required to attain reproducible results was 1 μm. This critical thickness (at the largest temperature change allowed by the instrument's objective lens) was obtained by recording the repeatability of step height measurements with films in the same thickness range as estimated edge displacements for films of differing thicknesses.

Due to this limitation, atomic force microscopy was initially selected for the measurements. However, it was found later that thermal loads, necessary to observe end displacement change in coatings, severely restricted the quality of the information obtained. Also, the effect of the tracing cantilever on the shape of the film edge was uncertain. Figure 8.2 shows an AFM scan of a PMDA-ODA polyimide coating on a glass substrate. One can observe a tendency for the film to peel from its substrate. Energetic calculations, predict that the critical thickness range for self-delamination of polyimide coatings is between 20 and 30 μm.[7] This is above that of the coating shown in Figure 8.2. This indicated that the cantilever probably damaged the edge of the film.

Despite limitations on the magnitude of ΔT allowed by the objective and its small working distance from the sample, final displacement measurements were obtained with phase-measurement interference microscopy. The step height limitation was overcome by measuring the region near the edge only and avoiding the inclusion of data beyond it (height drop and substrate). The film thickness was measured independently with high precision micrometers. Figures 8.3 and 8.4 show the change in the displacement at the edges with imposed temperature change. The coating's edge is the bottom side of the top view shown in the upper left hand corner of this figures. Barely visible in the top view and towards the bottom, there are two hairlines that indicate the location of the surface

profiles shown at the lower left hand corner of the figures. A three dimensional view of the surface is shown at the upper right hand corner of the figures. The legend labeled "yDst" of the profile plot gives the vertical distance in nanometers. This is the vertical distance indicated by the orange and green calipers in the profile plot denote the height of the displacement at the edge of the coating when it is compared to the far-field.The displacement is larger in Figure 8.3 which corresponds to a temperature of 22° C. The displacement at the end decreases as the temperature is raised to 62°C. Figure 8.5 shows a side view of the crest that develops at the edge of the stressed coating.

Figure 8.2. Micrograph of a 2.8 μm PMDA-ODA polyimide film on a glass substrate. Profile obtained with atomic force microscopy.

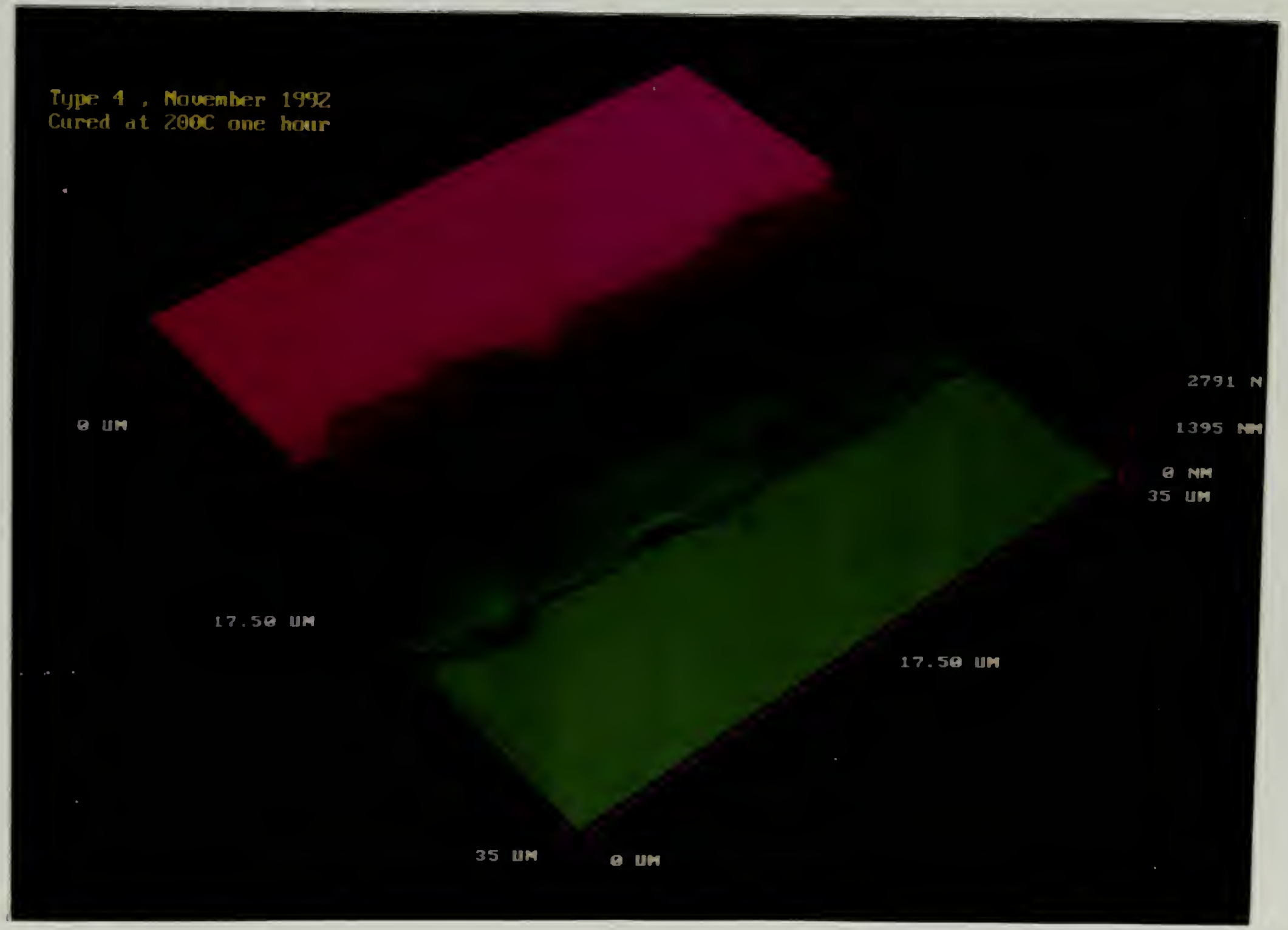
Type 4 , November 1992
Cured at 200C one hour
2791 N
0 UM
1395 NM
0 NM
35 UM
17.50 UM
17.50 UM
35 UM
0 UM

Figure 8.3. Surface map and selected profiles of a 3.0 μm PMDA-ODA coating on a glass substrate at a temperature of 22°C. Phase-measurement interference microscopy.

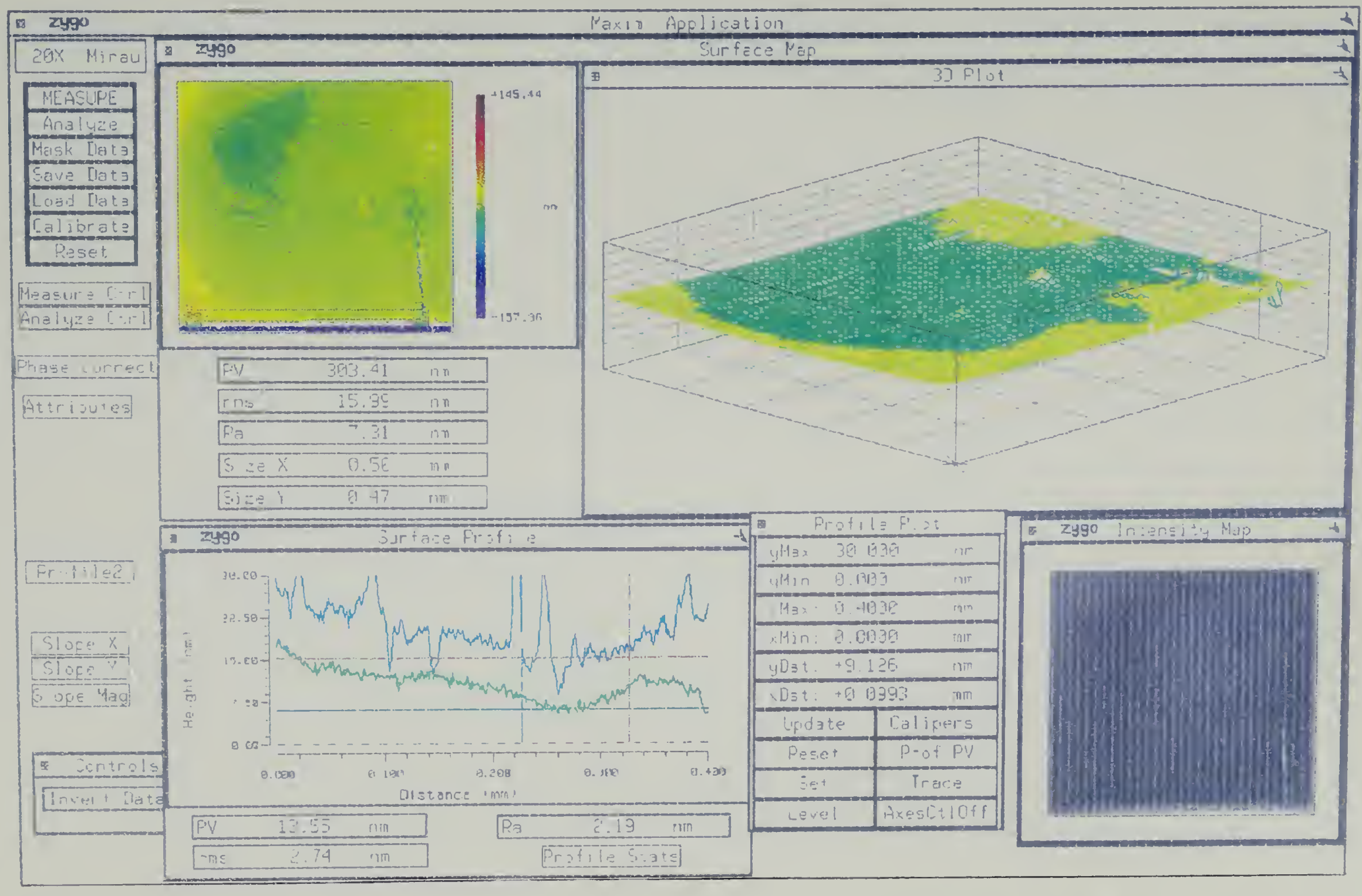
zygo
Maxim Application
20X Mirau
MEASURE
Analyze
Mask Data
Save Data
Load Data
Calibrate
Reset
Measure Ctrl
Analyze Ctrl
Phase Correct
Attributes
zygo
Surface Map
+145.44
-157.96
PV 303.41 nm
rms 15.99 nm
Ra 7.31 nm
Size X 0.56 mm
Size Y 0.47 mm
3D Plot
Profile2
Slope X
Slope Y
Slope Mag
Controls
Invert Data
zygo
Surface Profile
Height (nm)
Distance (mm)
PV 13.55 nm
rms 2.74 nm
Ra 2.19 nm
Profile Stats
Profile Plot
yMax 30.030 nm
yMin 0.003 nm
xMax 0.4030 mm
xMin 0.0030 mm
yDst +9.126 nm
xDst +0.0993 mm
Update
Calipers
Reset
P-of PV
Set
Trace
Level
AxesCtlOff
zygo Intensity Map

1901

Figure 8.4. Surface map and selected profiles of a 3.0 μm PMDA-ODA coating on a glass substrate at a temperature of 62°C. Phase-measurement interference microscopy.

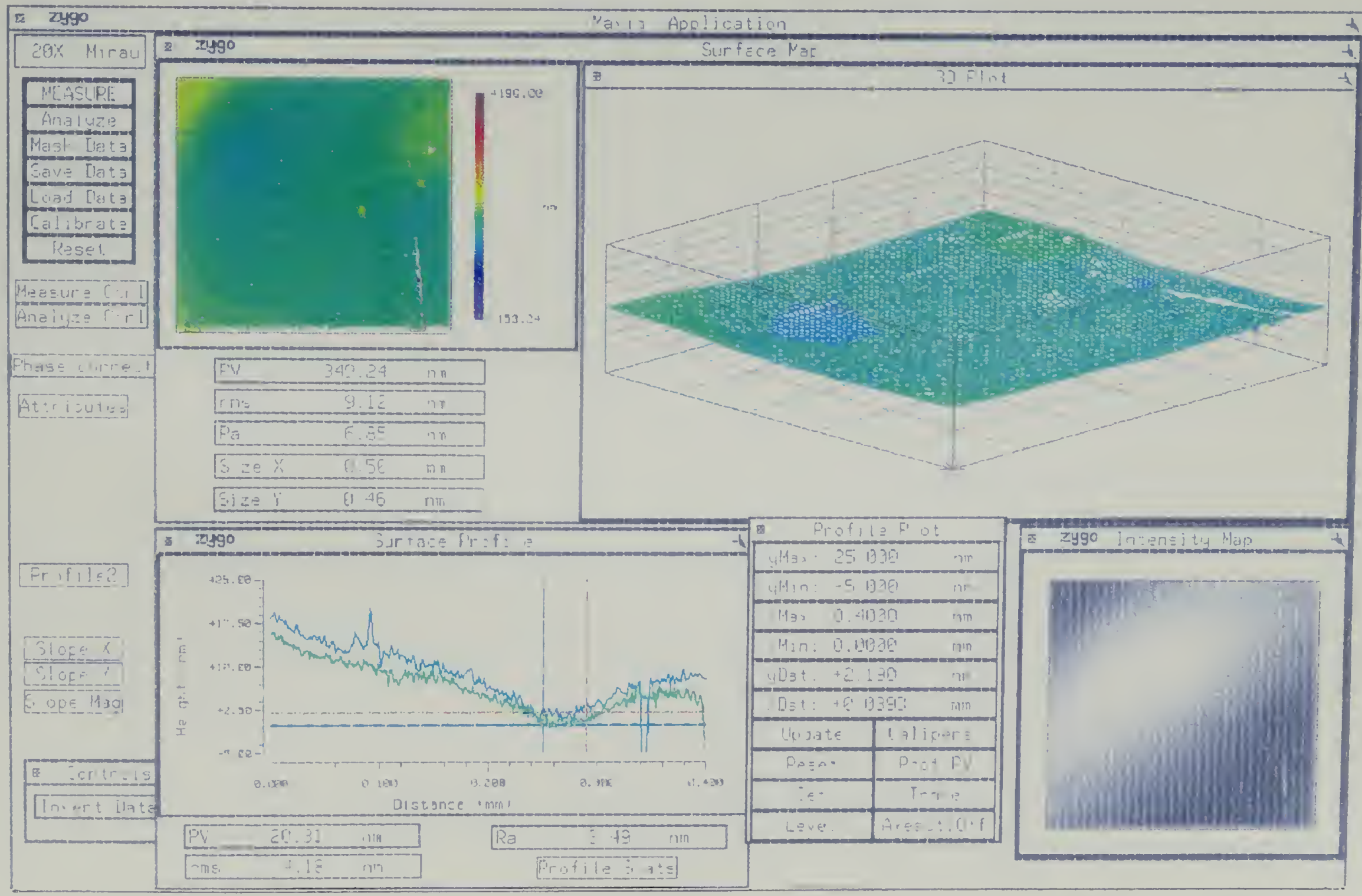
zygo
Main Application
20X Mirau
MEASURE
Analyze
Mask Data
Save Data
Load Data
Calibrate
Reset
Measure Ctrl
Analyze Ctrl
Phase Connect
Attributes
Profiles
Slope X
Slope Y
Slope Mag
Controls
Invert Data
zygo
Surface Map
+196.00
nm
153.04
PV 340.24 nm
rms 9.12 nm
Ra 6.85 nm
Size X 0.56 mm
Size Y 0.46 mm
3D Plot
zygo
Surface Profile
+25.00
+12.50
+0.00
-12.50
Height (nm)
0.000
0.100
0.200
0.300
0.400
Distance (mm)
PV 20.31 nm
rms 4.12 nm
Ra 3.49 nm
Profile Stats
Profile Plot
yMax: 25.030 nm
yMin: -5.000 nm
Max: 0.40300 mm
Min: 0.00000 mm
yDat: +2.130 nm
xDat: +0.03900 mm
Update
Calipers
Peak
Peak PV
Ter
Trough
Level
Area Above
zygo Intensity Map

Figure 8.5. Profile of a 3.0 μm PMDA-ODA coating on a glass substrate at a temperature of 22°C showing a side view of the crest developed at the stressed coating's edge. Phase-measurement interference microscopy.

zygo — Maxim Application

20X Mirau

MEASURE
Analyze
Mask Data
Save Data
Load Data
Calibrate
Reset

Measure Ctrl
Analyze Ctrl

Phase correct

Attributes

Profiles

Slope X
Slope Y
Slope Mag

Controls
Invert Data

zygo — Surface Map

PV	356.7E	nm
rms	26.5c	nm
Ra	13.14	nm
Size X	0.5E	mm
Size Y	0.47	mm

3D Plot

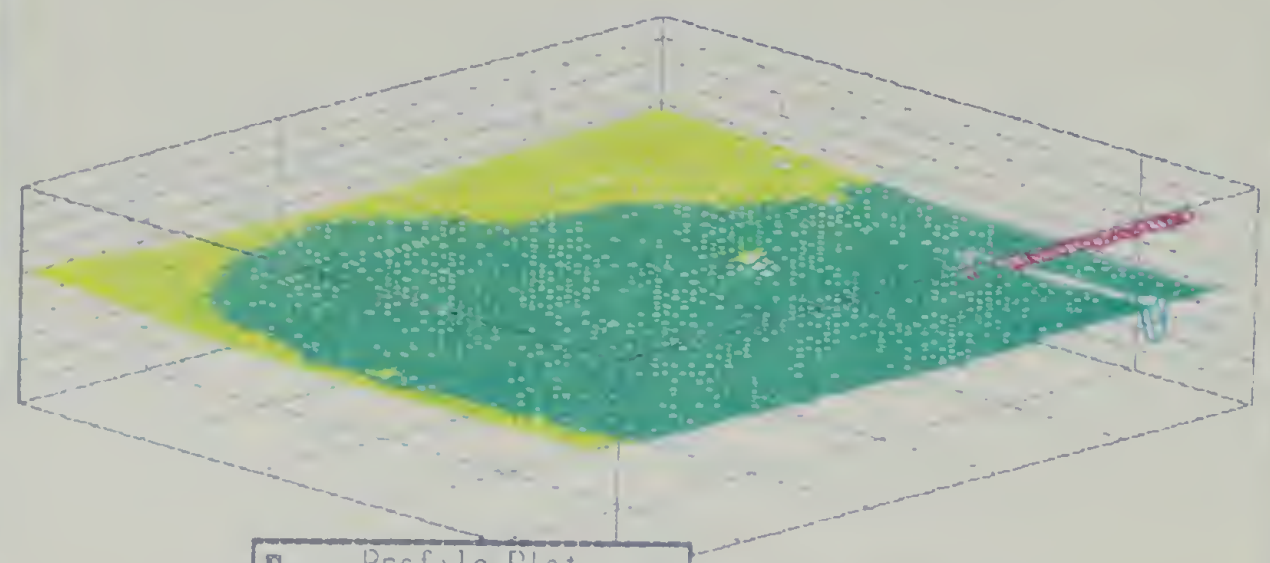

Profile Plot

yMax.	nm
yMin.	nm
xMax	mm
xMin	mm
yDst. +4.126	nm
xDst. +0.0841	mm
Update	Calipers
Reset	Prof PV
Set	Trace
Level	AxesCtlOff

zygo — Surface Profile

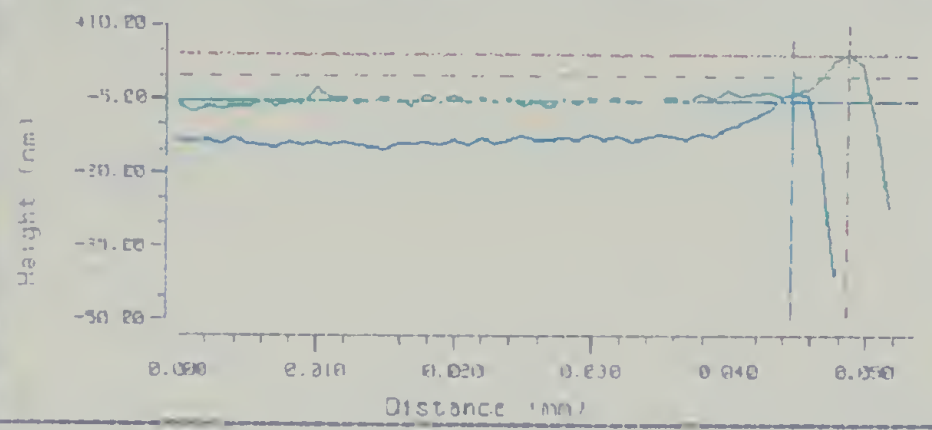

PV	31.12	nm
rms	3.36	nm
Ra	1.33	nm

Profile Stats

zygo — Intensity Map

From Figures 8.3 and 8.4, one can observe that a 69.36 Å displacement was obtained from 3 micron films by decreasing the temperature by 40°C. The results shown in these figures were very reproducible but average values needed to be taken in order to minimize errors involved in the measurement. This was not the case for films thinner than 1 μm. A displacement at the edge is present in the absence of a thermal load because contributions from residual stresses or initial deformation of the surface due to slicing were significant. Slicing was the preferred method for creating a new edge on the coating. Material accumulation at regions of the coating near the edges of the substrate yielded uneven surfaces, unsuitable for analysis. This is believed to be a problem that originates during the spin coating process. A new razor blade was used for every cut. Only a few cuts were of good enough quality for measurement.

The vertical displacement difference obtained was compared with results obtained from finite element analysis. Figure 8.6 shows the finite element analysis results on vertical displacement distributions near the edge of the coating. The anisotropic case shows a larger shrinkage than the isotropic since the thermal expansion coefficient in that direction was higher and the thermal load imposed was negative. The difference between the value of this displacement at the edge and away from it were used to compare with those observed experimentally. This is shown below:

Finite element analysis vertical normalized displacement at the edge for a $\Delta T = -100$ °C:

isotropic coating: -0.04241520

-0.04562870

$\Delta_{iso} = 0.00321350$

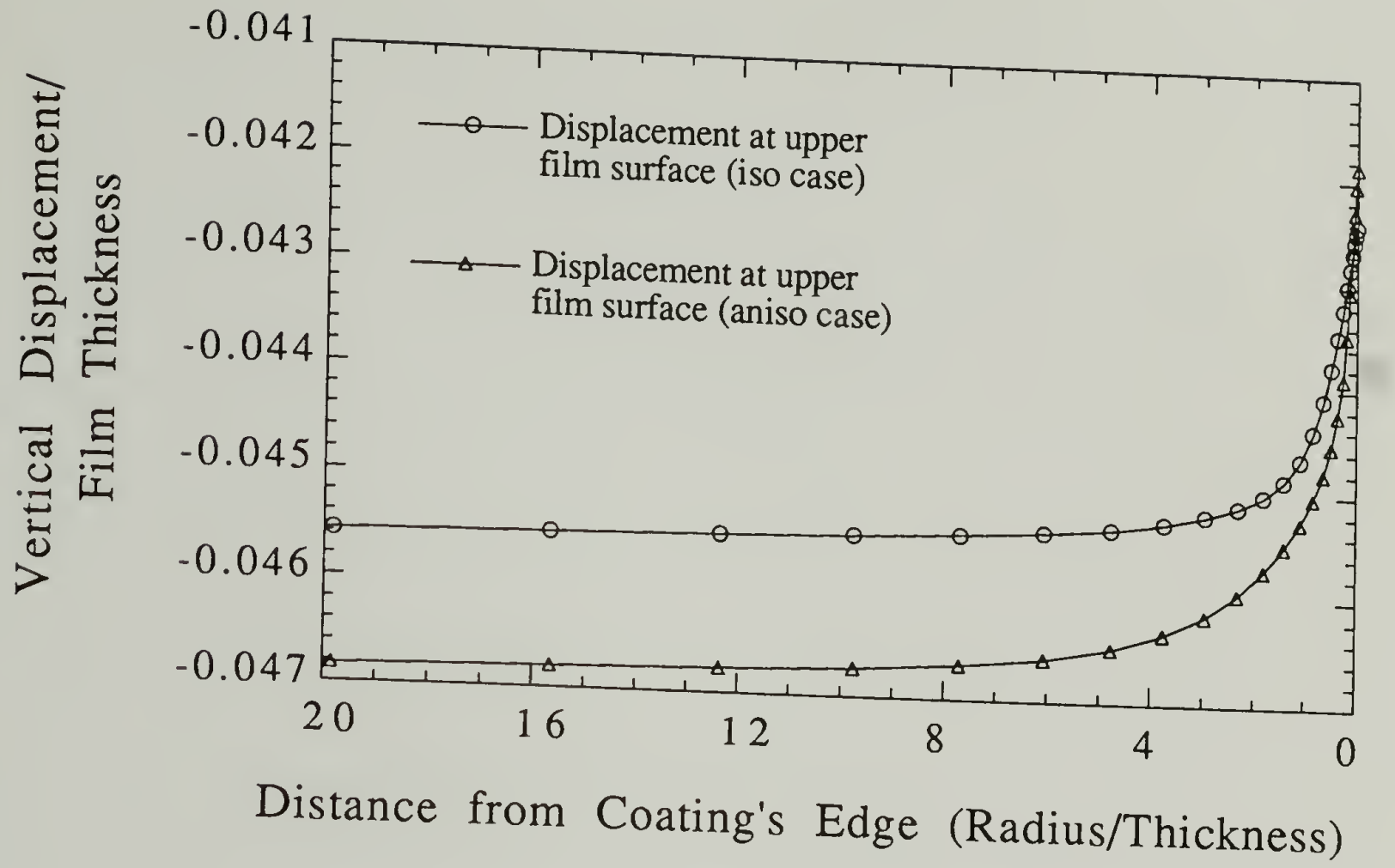

Figure 8.6. Vertical displacements at the upper coating surface versus the distance form its edge. Finite element analysis.

Anisotropic coating: -0.04185310

-0.04685150

Δ_{ani} = 0.00499840

The FEM displacements in thicknesses/°C:

Isotropic = 3.21×10^{-5}

Anisotropic = 5.00×10^{-5}

Phase-measurement interference microscopy experiments, note that these quantities are the averages of several runs:

Observed vertical displacement (meters) / Film thickness (meters)

7.0×10^{-9} m / 3.0×10^{-6} m = 2.33×10^{-3} for a $\Delta T = 38°$ C

The experimental displacement in thicknesses/°C is:

Experiment = 6.14×10^{-5}

This results demonstrate that under thermal loading conditions, the assumption of isotropy would have led to the underestimation of the displacement at the coating's edge. Experiment showed good agreement with finite element analysis and provides validity for this approach.

8.4 Conclusions

Atomic force microscopy and phase-measurement interference microscopy were the two methods considered to obtain vertical displacements at the coating's edge. Due to experimental limitations explained above, phase-measurement interference microscopy was chosen for the measurements. It was shown in this chapter that isotropic conditions did not predict the magnitude of the out-of-plane displacement with accuracy. The vertical displacement value in terms of thicknesses/°C was 3.21×10^{-5} when isotropic conditions were assumed and the experimental value was 6.14×10^{-5}. A better match was obtained by using anisotropic conditions, 5.00×10^{-5}. Agreement between finite element analysis and experiment validated the approach utilized for the calculation of these vertical displacements.

8.5. References

(1) Biegen, J. F.; Smythe, R.A. *Proc. SPIE- Int. Soc. Opt. Eng.* **1988**, *897*, 207.

(2) Perry, D.M.; Moran, P.J.; Robinson, G.M.*J. of the Inst. of Elect. and Rad. Eng.* **1985**, *4*, 145.

(3) White, H.S.; Earl, D.J.; Norton, J.D.; Kragt, H.J. *Anal. Chem.* **1990**, *62*, 1130.

(4) Kragt, H.J.; Earl, D.J.; Norton, J.D.; White, H.S. *J. Electrochem. Soc.* **1989**, *136*, 1752.

(5) Zygo Corporation; Reference manual for the Maxim-3D 5800 High Resolution Phase Measuring Laser Interferometric Microscope. Middlefield, Connecticut. 1993.

(6) Gross, T.S.; Watt, D.W.; Perault, J.A. *Exp. Mech.* **1992**, *Dec.*, 316.

(7) Bauer, C.L., PhD Dissertation. Dept. of Polym. Sci. and Eng. The University of Massachusetts at Amherst. Amherst, Mass., 109, 1988.

CHAPTER 9

SUMMARY

9.1 General Conclusions

Stress development in polymeric materials caused by imposed mechanical or thermal loads is a subject of growing importance. The enhancement of the properties of fibers, self-assembled systems or other high performance polymeric forms is based on the development of extreme anisotropies. It is important to evaluate how material performance can be influenced by the extent of its anisotropy. For the first time, this study analyzes the effect of anisotropy on the stress transfer process of orthotropic polymeric materials using full sets of elastic constants obtained from molecular simulation.

Specifically, stress transfer between anisotropic polymers and isotropic substrates was evaluated in this work. Two cases were examined, one for stress transfer in cylindrical geometries and the other in planar geometries. Examples of the first case are highly anisotropic fibers reinforcing a weaker isotropic polymeric matrix. The second case pertains to the stress development in in-plane oriented films covering a rigid isotropic substrate. Stress transfer which takes place at the ends of fibers or at the edges of coatings is influenced by increases in the degree of material anisotropy. The assumption of isotropic conditions in the analysis of stress transfer situations involving polymers may lead to serious errors.

The development of anisotropy was studied for PMDA-ODA polyimide coatings. Crystallinity and orientational order changes in polyimides and their indirect influence on the stress transfer behavior was studied. A higher crystallinity in these films leads to decreases in expansion coefficients and changes stress transfer behavior. When the discrepancy between the expansion coefficient of the coating and its substrate is large, it results in a significant development of stresses. The degree of crystallinity of these polyimide materials was calculated using wide angle X-ray diffraction and density measurements. Structure and unit cell dimensions were computed for PMDA-ODA polyimide. Previously, determination of structural parameters in these materials was difficult due to the unavailability of highly crystalline samples. Before the development of a technique for obtaining these highly crystalline powders in our laboratories, there was no record of PMDA-ODA polyimides with such a high degree of crystalline order. These samples provided an alternative route to the analysis of conformational distributions by Raman and infrared spectroscopy techniques.

The effect of orientational order in the stress transfer process of PMDA-ODA polyimide coatings was characterized in terms of the difference in properties between their in-plane and out-of-plane directions. A higher in-plane stiffness in a coating stemming from an increased degree of anisotropy in that direction leads to more severe stress conditions at the edges of the coating. When properly scaled and compared to fully isotropic coatings, increased coating anisotropy yielded shear stress distributions with a slower rate of decay from the edge. Stress transfer in continuous coatings above their glass transitions temperatures is only signficant near the edges. Most of the out-of-plane and shear stress decay from the edges of the coating took place within 2 layers of coating and became insignificant within 4-5 thicknesses.

A spectroscopic study of thin polyimide films revealed that molecular anisotropy was higher and molecular packing was lower for films thinner than 150 Å. A high in-plane orientation is still present in thick films. This investigation represents the first time that the orientation of ultra-thin PMDA-ODA polyimide films has been quantitatively characterized. The results are, in part, presented as a new methodology for the characterization of orientational order of high molecular weight polymeric adlayers on metallic substrates. The technique is now being extended to analyze coatings on dielectric substrates.

Elastic constants provided by molecular simulation and that were also used in finite element models, imparted unique insight into the stress analysis of orthotropic bodies. Molecular dynamics simulations of PMDA-ODA polyimide were particularly useful in the determination of anisotropic thermal expansion coefficients. A review of the literature prior to this study indicated no attempts to measure all thermal expansion coefficients of crystalline units in polyimide materials with molecular simulations.

Measurement of out-of-plane displacements near the edges of very thin coatings has been reported here for the first time. Phase measurement interference microscopy was utilized to detect these displacements. These experimentally determined displacements agreed with those obtained by finite element methods.

9.2 Future Studies

This investigation points to future studies in several associated topics. One of these involves the influence of transverse stress development in anisotropic fibers during mechanical and thermal loading which would require experimental investigation. Also, the transverse strain distribution obtained by finite element methods could undergo experimental corroboration with newer emerging technologies in confocal Raman microscopy.

Experimental characterization of failure modes in anisotropic fibers embedded in isotropic matrices needs to be examined. Transverse strengths in single fibers under axial loads needs to be characterized experimentally. The influence of the stress state at the fiber ends on failure modes that are characteristic of anisotropic fibers, like longitudinal splitting, is also worthy of investigation.

Experimental evaluation of out-of-plane elastic constants in polyimide films is important. The techniques used now for this purpose are torsion pendulum and pressure-volume-temperature measurements. Phase measurement interferometric microscopy may also be employed alternatively to determine some of these constants independently.

An experimental evaluation of the in-plane stress development and thermal expansion coefficients development in polyimide films with varying degrees of crystallinity also warrants assessment. Due to increasing interest in the rapid curing of polyimide materials, which increases the crystalline order in films, there is a need to understand how this process influences property development. Holographic interferometry and thermomechanical analysis could yield results with proper experimental implementation.

In this study, for instance, wherever possible, results from molecular simulation–molecular geometry, elastic constants and thermal expansion coefficients–were directly verified experimentally. The success attained with molecular simulation methods in predicting structure and properties of polyimides provides an incentive to explore how chemical substituents on similarly tailored molecules might change material properties. For polyimides, an investigation of the nature of electrostatic intermolecular forces in polyimide materials could represent a significant research investigation. Also, regarding molecular simulation methods, thermal expansion data could be correlated with specific structural rearrangements.

Still another area of potential research interest lies in the orientational order of polyimide films on dielectric substrates. This would involve characterization. Analytical methodologies are currently being developed for just this purpose. The development of a methodology, like that previously developed for metallic substrates, is needed to quantitatively analyze structural information contained in external reflection spectra of films mounted on dielectric substrates. It is expected that the method could utilize information on the in-plane and out-of-plane refractive indices to determine the dipole strength and its orientation with respect to the surface normal.

Influence of segmental rigidity on the stress transfer and adhesion of polymeric coatings to their substrates also investigation. This effect could be important for polyimides. The thickness of poorly packed layers near the substrate may be dependent on this parameter. Similarly, the influence of very thin and poorly packed layers in the stress transfer process needs to be investigated. The layers' compliance may lead to improvements in the accommodation of thermal or residual stresses in electronic multi-component assemblies. As has been shown above, for PMDA-ODA polyimide cured

under the conditions prescribed, films thinner than ~150 Å had poor packing when compared to that of thicker films.

APPENDIX A

X-RAY ANALYSIS

Data treatment for wide-angle X-ray measurements is provided in this appendix. The equations utilized for this purpose are given below. Temperature factor corrections did not show a noticeable effect.

Polarization Correction:

$$P = \frac{1}{2}(1 + \cos^2 2\theta) \qquad (A.1.)$$

Lorentz Correction:

$$L = \frac{1}{4 \sin^2\theta \cos\theta} \qquad (A.2)$$

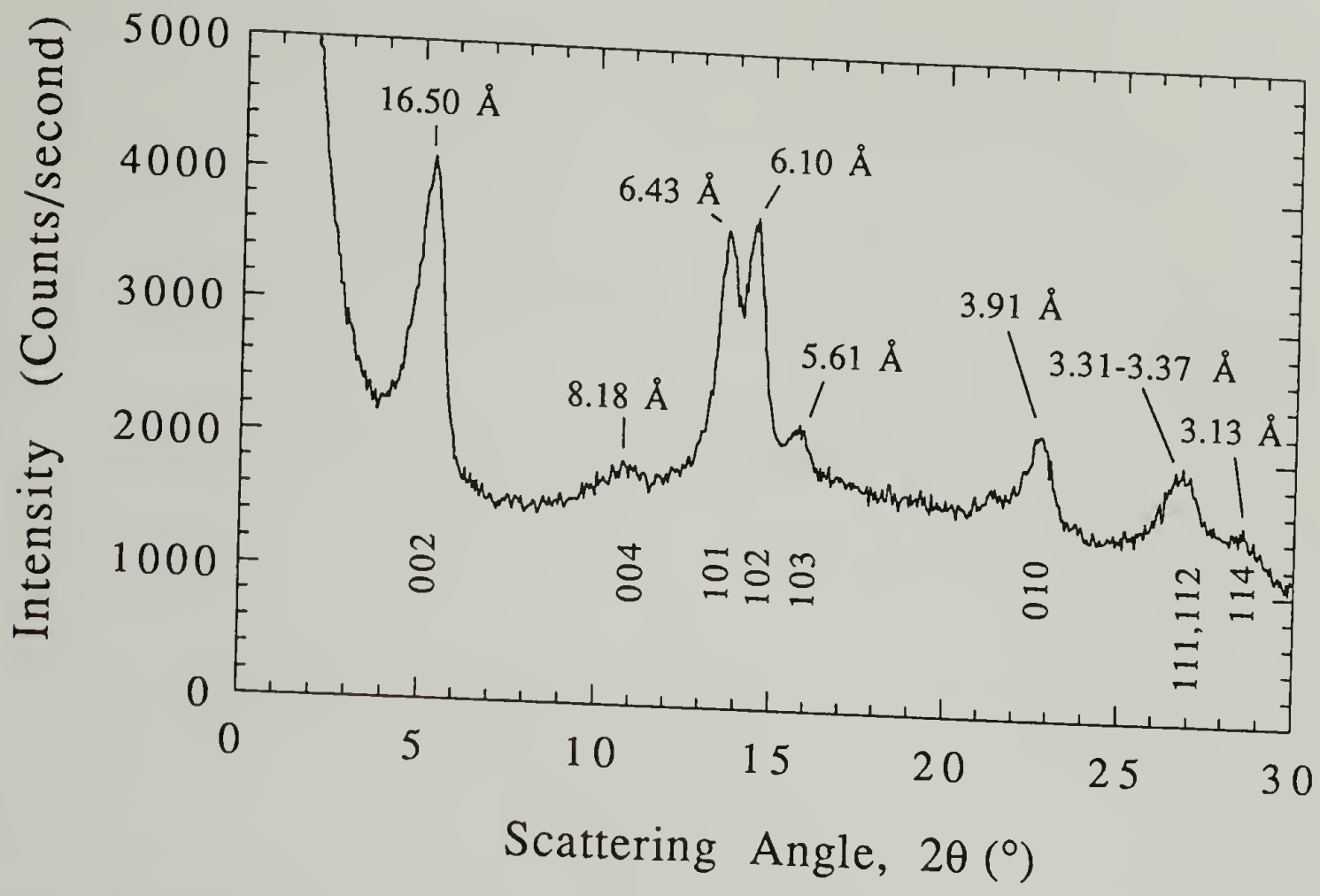

Figure A.1. Reflections of orthorhombic unit cell of PMDA-ODA polyimide.

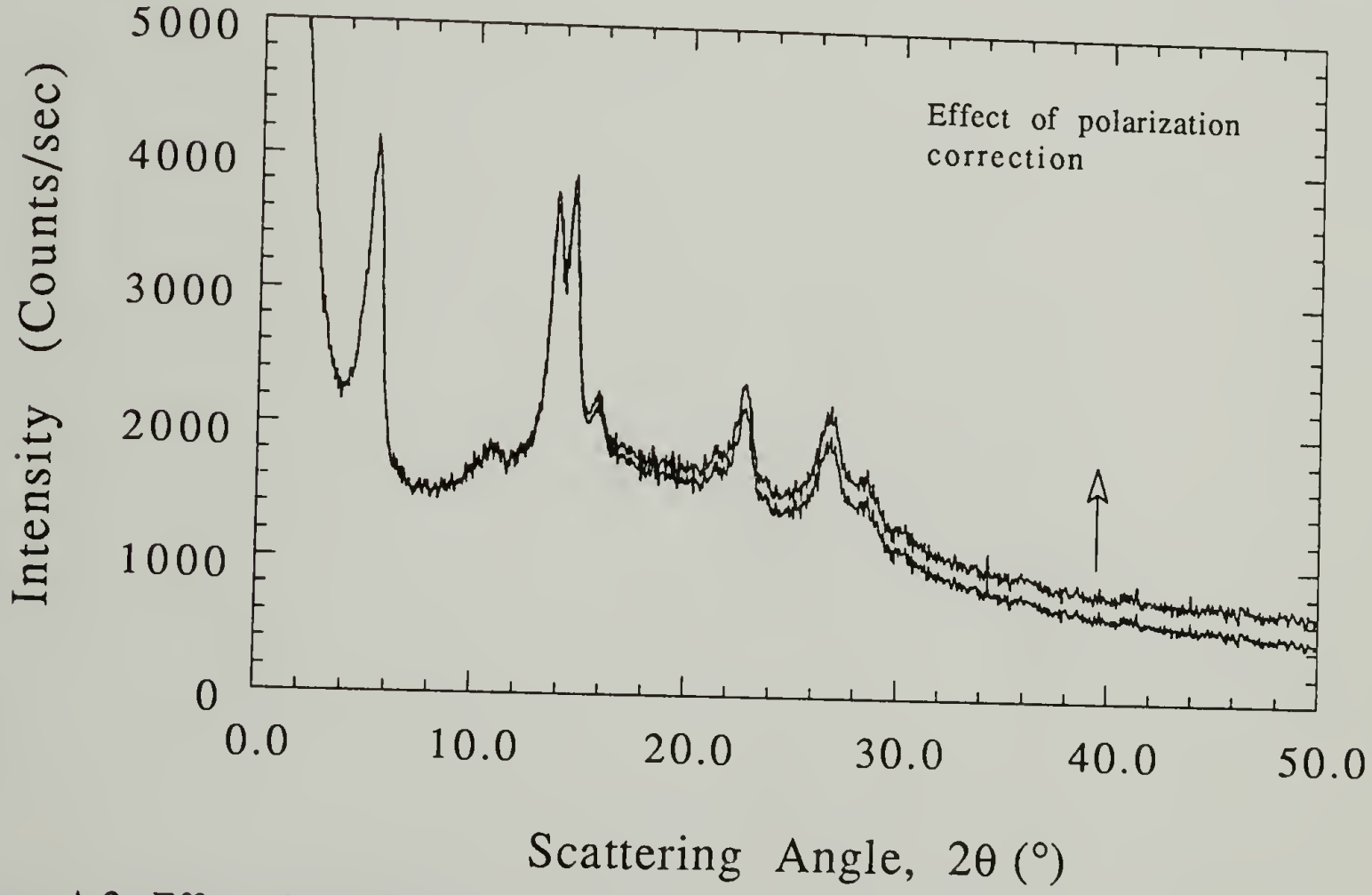

Figure A.2. Effect of polarization correction on the raw data of a diffractometer scan of a PMDA-ODA polyimide powder.

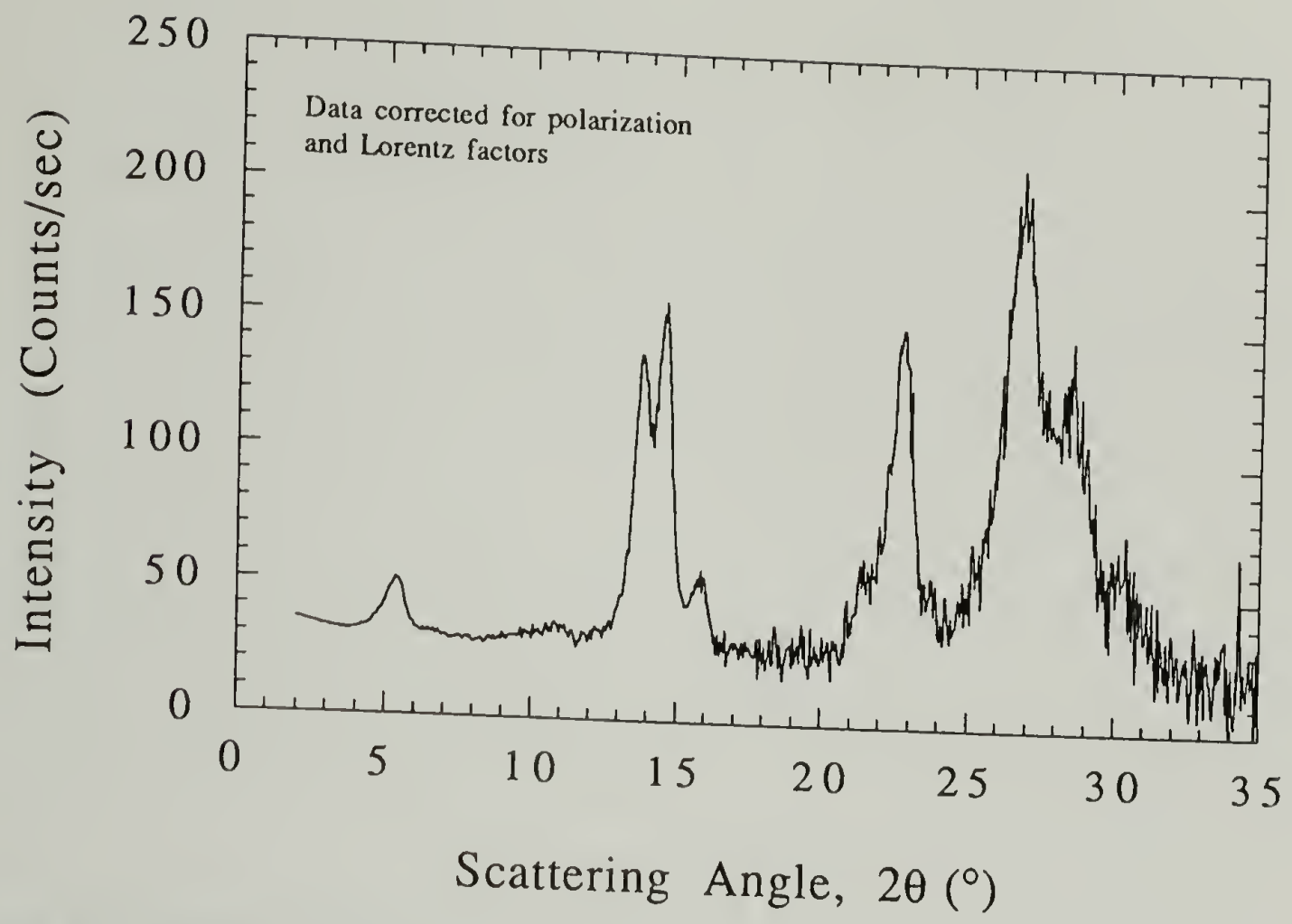

Figure A.3. Effect of polarization and Lorentz corrections on the raw data of a diffractometer scan of a PMDA-ODA polyimide powder.

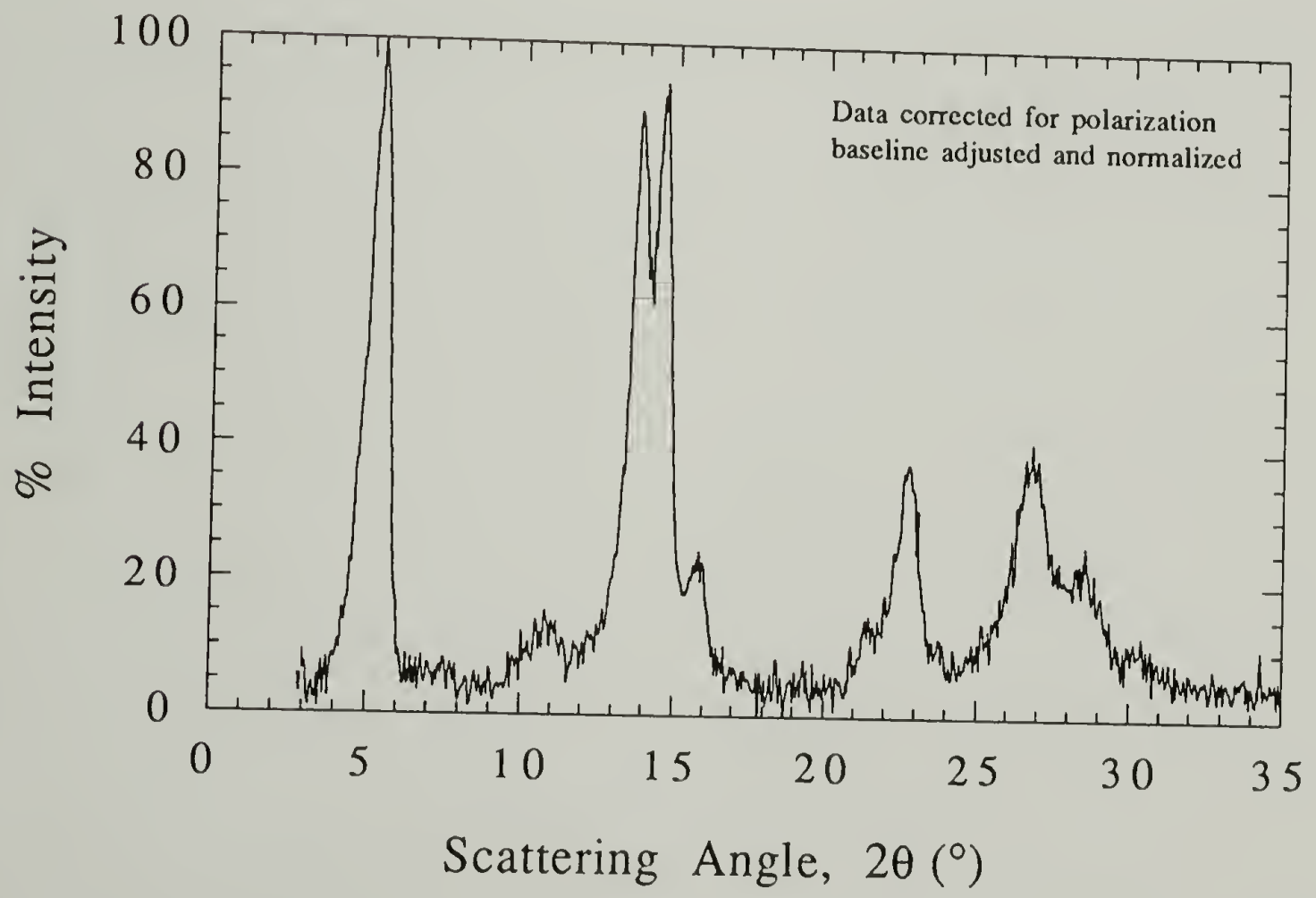

Figure A.4. Crystalline peaks, amorphous background removed, in diffractometer scan of a PMDA-ODA polyimide powder.

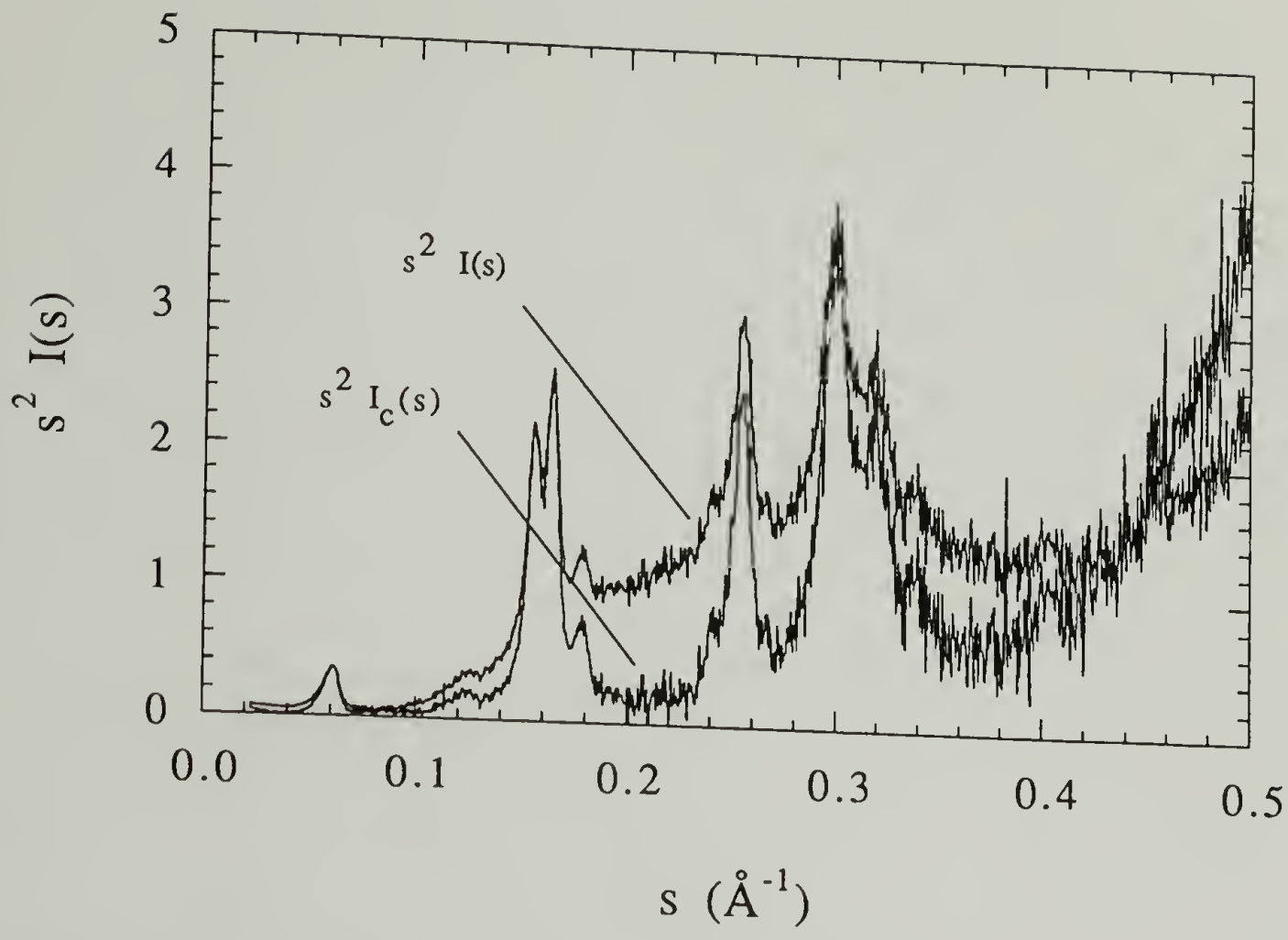

Figure A.5. Curves utilized for the approximation of crystallinity from a diffractometer scan of PMDA-ODA polyimide powder.

APPENDIX B

FILM THICKNESS MEASUREMENTS

Mechanical methods are useful for accurately measuring film thickness above one micron. Two optical and non-destructive methods utilized in this work for measuring film thickness have been incorporated here. The motivation for the creation of this appendix is to point out limitations of these methodologies and to illustrate how measurement errors can easily occur. It is not the intend of this appendix to provide a summary or an introduction to each of these methodologies. The most commonly used technique is ellipsometry. Alternatively utilized is phase-measurement interference microscopy, this method was described in chapter eight and used to measure out of plane displacements at the edges of films.

Ellipsometric measurements were done with a Rudolph Research Ellipsometer AUTOEL®-II using the 6328 Å line (0.2 mW) reflected at a 70° angle with respect to surface normal.

Experimentally, two coefficients are obtained from an ellipsometric measurement, Ψ and Δ. These are given below by equations B.1 and B.2. Equation B.3 is the basic equation of ellipsometry and it represents the ratio of the reflectivity coefficients in the directions parallel and perpendicular to the plane of incidence.

$$\Delta = \delta_{\parallel}^{r} - \delta_{\perp}^{r} \tag{B.1}$$

$$\Psi = \tan^{-1} \frac{\tan \Psi_r}{\tan \Psi_i} \tag{B.2}$$

$$\rho = \frac{r_{\parallel}}{r_{\perp}} = \tan \psi \, e^{j\Delta} \tag{B.3}$$

where ψ is the inverse tangent of the reflectivity ratio in the directions parallel and perpendicular to the plane of incidence and has values between 0° and 90°. Δ is the phase difference for the same directions and its values fall between 0° and 360°.

One of the limitations of ellipsometry is that ψ and Δ are cyclic functions of thickness. This means that for a given substrate-film system there will be a critical value of ψ and Δ after which they will start repeating for different film thickness values. This will take place until the number of cycles approximates the film thickness. Clearly, if this critical value is not known, one could be gathering data for the wrong film thickness. Equation B.4 provides a way to compute the cycle thickness for a particular system of n_f, refractive index of film, and ψ.

$$CYC = \frac{\lambda}{2} \frac{1}{[(n_f)^2 - \sin^2(\psi)]^{1/2}} \tag{B.4}$$

For polyimide films in gold substrates, the cycle thickness was obtained to be 2142 Å and 2007 Å when refractive indices of 1.63 and 1.72 were used respectively. The experimentally obtained value of ψ was 43.60 and λ was 6328 (He-Ne laser). For dielectric substrates, in this case a silicon wafer, the values obtained for the cycle thickness were 1956 Å (n=1.63) and 1852 Å (1.72). The experimental value of ψ was 11.40 for the silicon wafer. Calculations for the values of ψ and Δ for the first cycle up to a film thickness of 2000 Å are shown below in Figures B.1 and B.2.

Figure B.1 illustrates the variation of ψ and Δ as a function of the thickness of a polyimide film cast on gold. The numbers around the cycles indicate film thickness in Å. The curves for two values of the refractive index are shown. These two values of the refractive index corresponds to its limits for the in-plane and out-of-plane directions

(transverse electric and transverse magnetic respectively) in the planar isotropic film. The two values of the refractive index were used to observe its influence in the error involved in the acquisition of the final thickness measurement. It can be observed from the first cycle shown in Figure B.1 that larger errors in the computation of film thickness can be realized between 600 and 1200 Å if the refractive index was not accurately obtained. It can also be ascertained that a slight variation in ψ can affect the measurement severely in the range of 2000 Å and a small error in the measurement of Δ can have equally serious consequences around 500 and 1400 Å. This accuracy is dependent on the nulling capacity (time allowed and precision of mechanism) of the ellipsometer and the number of measurements performed for each location.

The same type of plot as B.1 can be observed in B.2 for a polyimide film on a silicon substrate. The difference arises from the values of the refractive index and absorption coefficient that are obtained for each substrate, either dielectric or metal.

As mentioned in chapter 8, phase-measurement interference microscopy can also measure film thickness if a portion of the substrate surface is utilized as a reference. One can then measure the step height from the substrate's surface to the film surface and obtain the film thickness. The apparatus available from our labs only allows the measurement of step heights below 1500 Å. New double beam interferometers are capable of measuring larger step heights.

Knowledge of the optical coefficients, n and k, is needed to perform a correct measurement of thickness. A phase correction is performed based on the properties of both surfaces. One exception to the rigorous usage of optical coefficients in the measurement of film thickness with phase-measurement interference microscopy is that of a thin polymeric film cast a glass substrate. The refractive index of many polymers is close to 1.5. The refractive index for glass slides is 1.52. The absorption coefficient, k, is

insignificant for either material. Unfortunately, polyimide films on a silicon or gold substrate do not fall into this category, so a full set of optical coefficients needs to be entered to measure film thickness. Values obtained by ellipsometry of optical coefficients for gold and silicon wafers are shown below:

$$n_{gold} = 0.18 \qquad k_{gold} = 19.33$$

$$n_{silwaf} = 3.86 \qquad k_{silwaf} = 0.06$$

Examples of the full step height method (all optical constants taken into account) and the simplified method (no phase shift correction) are provided in Figures B.3 and B.4. A description of the equipment used for these measurements is given in chapter 8.

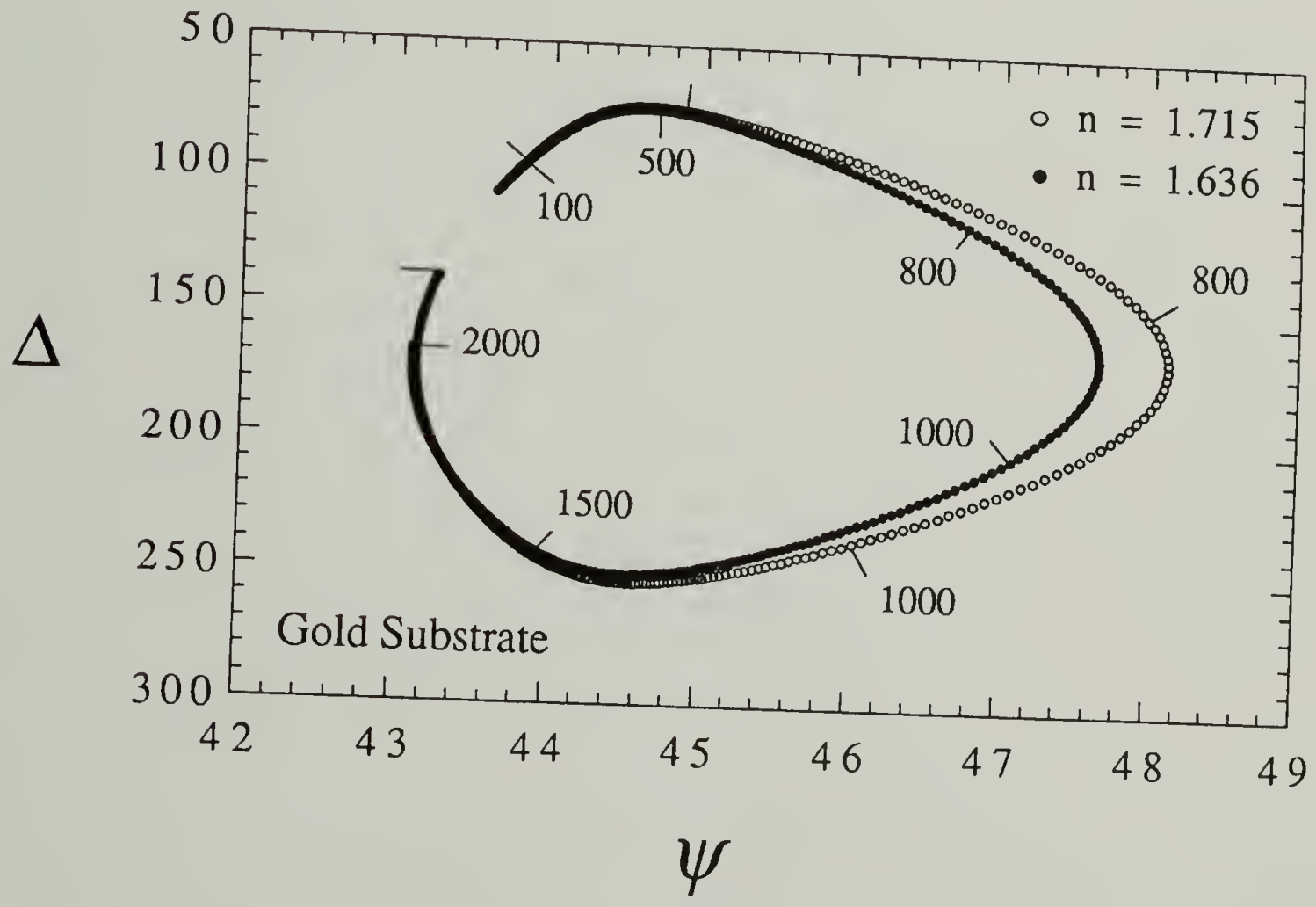

Figure B.1. Polyimide film thickness, as cast on a gold substrate, as a function of ψ and Δ for the in-plane and out-of-plane values of its refractive index.

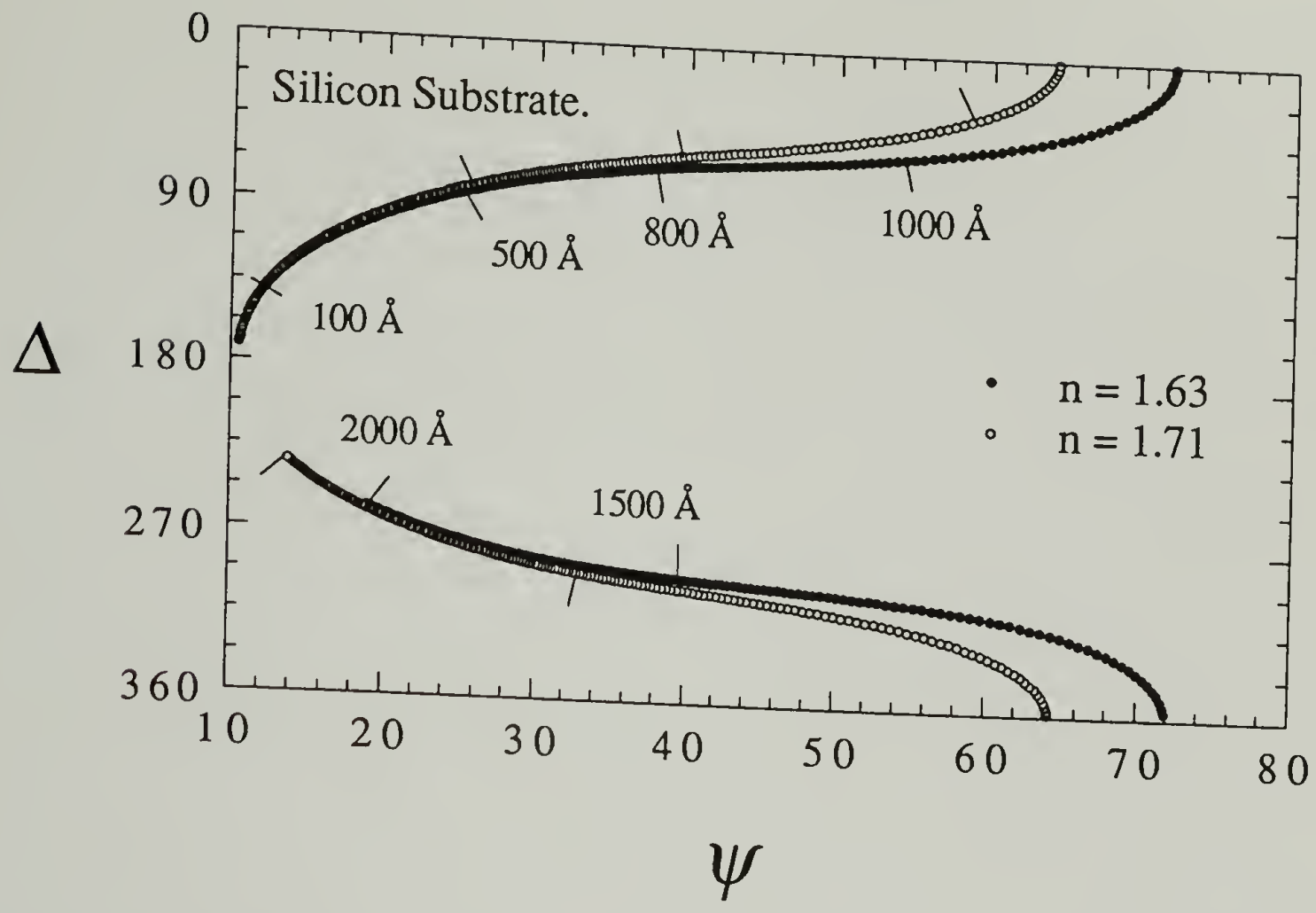

Figure B.2. Polyimide film thickness, as cast on a silicon wafer substrate, as a function of ψ and Δ for the in-plane and out-of-plane values of its refractive index.

Figure B.3. Step height measurement of a polyimide film on a silicon wafer substrate.

Maxim Step Height Application

20X Mirau

MEASURE
Analyze
Mask Data
Calibrate
Save Data
Loac Data
Reset

Measure Ctrl
Analyze Ctrl

Profile Plot

yMax:		A
yMin:		A
xMax:		um
xMin:		um
yDst: +878.1		A
xDst: +76.6		um

Update | Calipers
Reset | Map PV
Set | Trace
Level | AxesCtlOff

Controls

Phase Correction: n and k
Test Region n: 1.6130
Test Region k: 0.4500
Ref Region n: 3.8562
Ref Region k: 0.0553

Steps Map Res

Process
Units
Video Monitor

zygo — Steps Map

Filled Plot

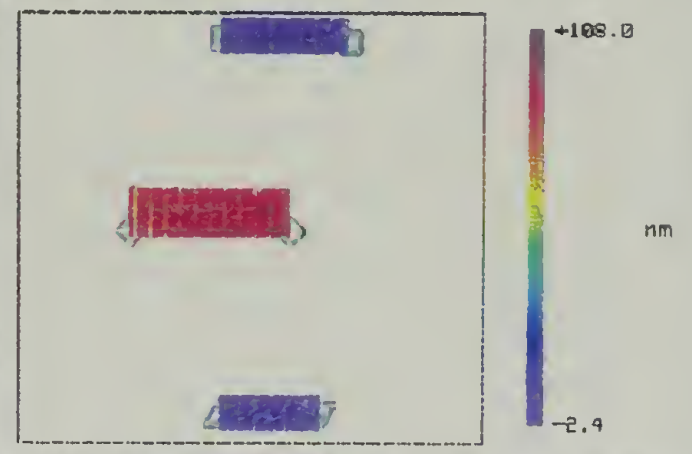

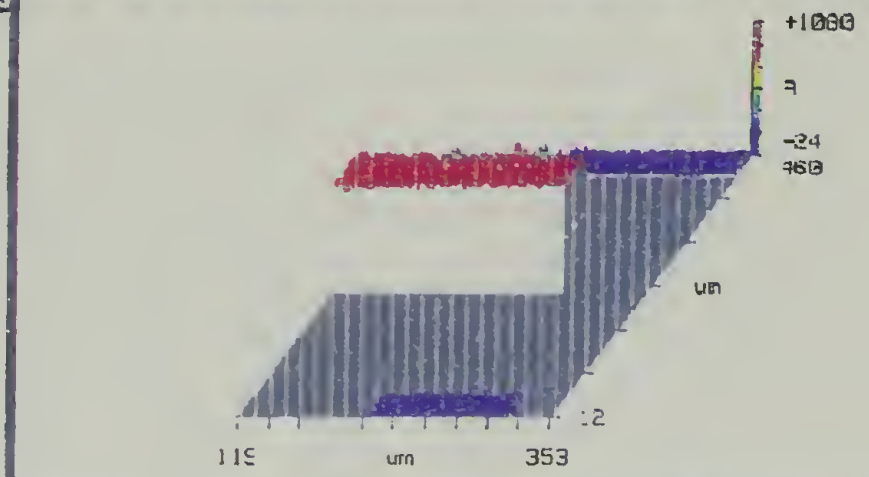

Avg Fit Step	381	A	Avg Height	875	A
Avg Proj Step T	395	A	PV	1104	A
Avg Proj Step R/B	865	A	Scan Direction: Top to Bottom		
			Remove: Plane		

Scan Direction: Top to Bottom
Removed: Plane

zygo — Steps Profile

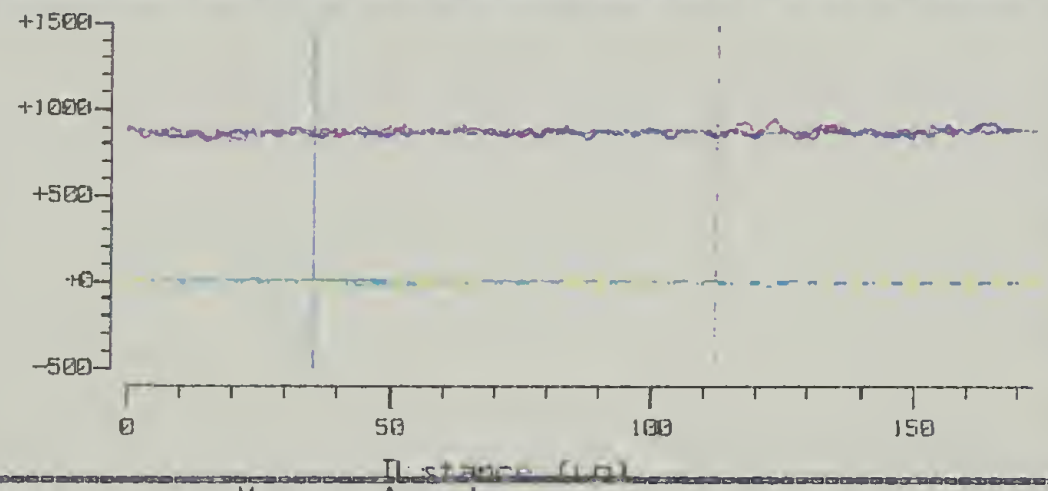

zygo Intensity Map

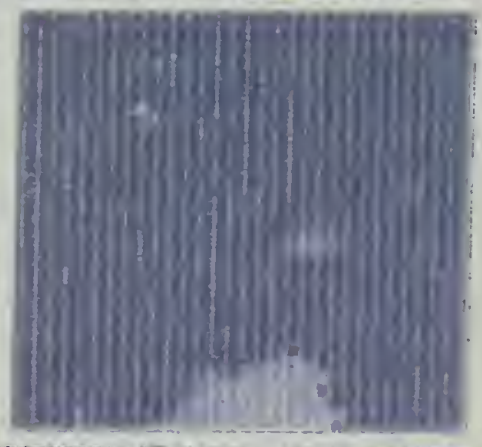

Contrast (Ref) 61
Contrast (Test) 17

Measure Attributes

Thu Jan 20 13:13:55 1994
Objective: 20X Mirau
Sample:Polyimide on Si Wafer #16
File created by: Mario A. Perez
Camera Res: 0.9930 um
Phase Correction: n and k

Figure B.4. Thickness estimation of a polyimide film on glass.

zygo — Maxim 3D Application

20X Mirau

MEASURE
Analyze
Mask Data
Save Data
Load Data
Calibrate
Reset

MTF Map
MTF Profile
PSF Map
Phase Profile
Filled Plot
Oblique Plot
3D Plot

Slope X
Slope Y
Slope Mag

zygo — Surface Map

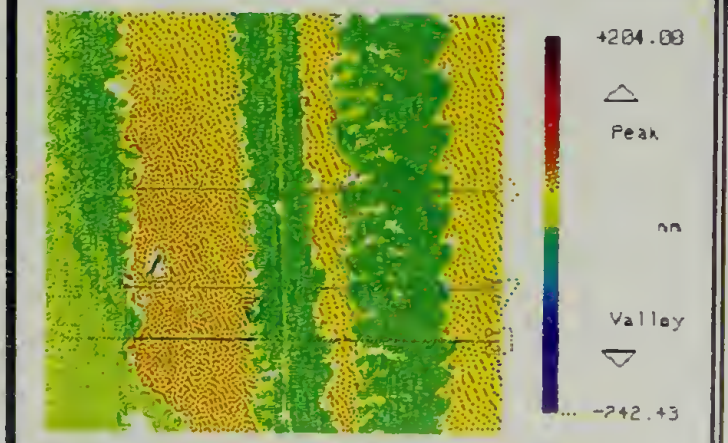

PV	446.43	nm
rms	25.63	nm
Ra	24.70	nm
Size X	0.47	mm
Size Y	0.44	mm

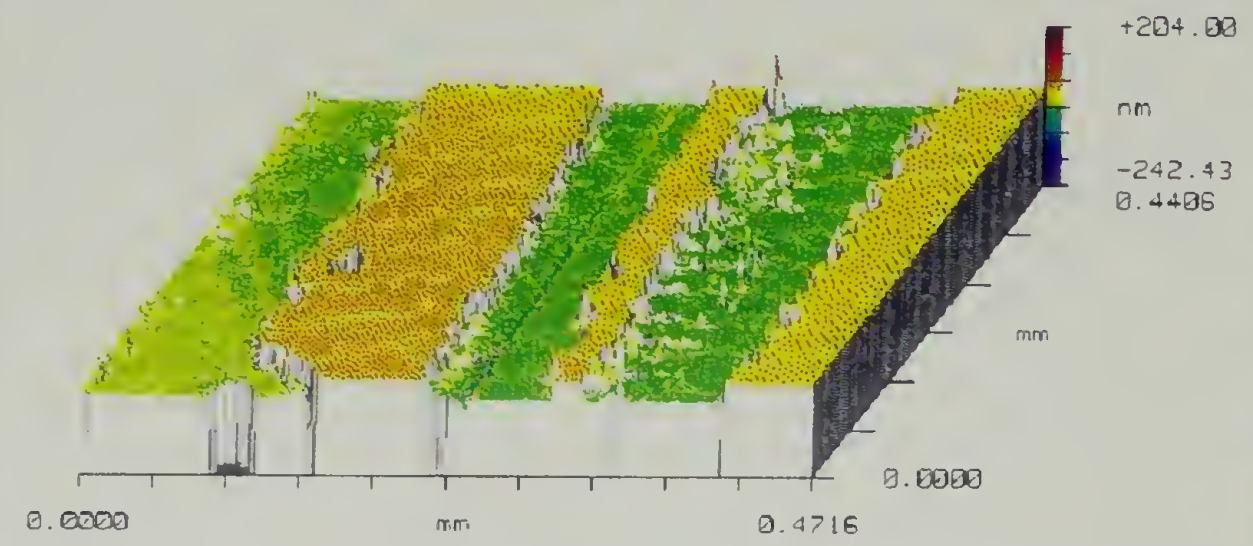

Removed: Plane
Trimmed: 0

Filter: Off
Filter Type:

zygo — Surface Profile

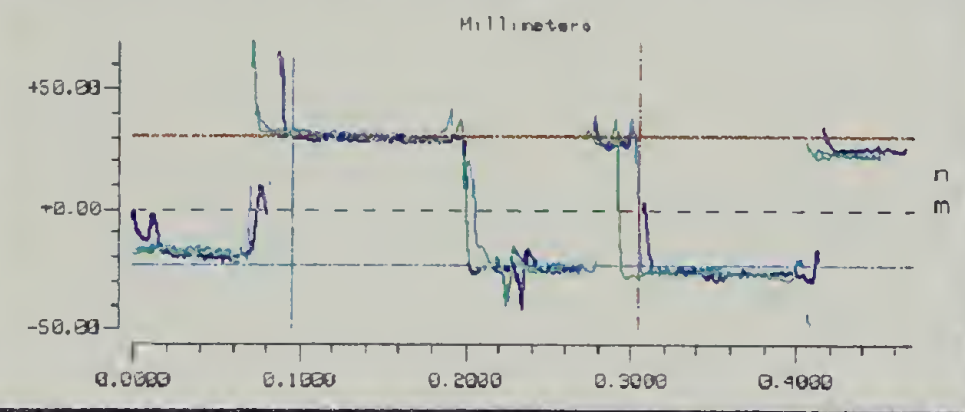

zygo — Surface Map

Remove: Plane
Trim: 0
Filter: Off
Filter Type: Average
Filter Window Size: 15

Profile Plot

yMax:		nm
yMin:		nm
xMax:		mm
xMin:		mm
xDst:	0.2087	mm
yDst:	+54.16	nm

Update | Calipers
Reset | ProfilePV
Set | Trace
Level | Axes 3

zygo Intensity Map

APPENDIX C

ALTERNATIVE SOLUTION FOR POLYIMIDES WITH THREE DIMENSIONAL ANISOTROPY

In the case of monolayer films with higher dimensional anisotropies, vectorial solutions may be appropriate and the specific directions of the transition moments would be necessary for describing the directionality of molecular assemblies. For example if one knows that vectors M_1 and M_2 are in the same plane that contains the chain axis, then the chain axis equation can be described vectorially as a linear combination of M_1 and M_2. Figure C.1 shows the transition geometry utilized for these calculations. In this figure, M_1 and M_2 are respectively the vectors representing the transition moment directions for the symmetric and asymmetric carbonyl stretches. M_3 is the C-N-C out-of-plane bending. M_1 and M_2 are in the same plane. M_1 is ~ 29° from the axis of the planar zigzag. $\theta_1 = 90°$, $\theta_2 = 59°$, $\phi_1 = 31°$ and $\phi_2 = 26°$. Figure C.2 shows a vectorial description of the transition moment directions.

The purpose of these calculations is to provide a solution for θ_c. Based on that geometry, the transition moments may be given by equations C.1 and C.2:

$$\vec{M}_1 = (\sin\theta_1 \cos\psi, \sin\theta_1 \sin\psi, \cos\theta_1) \qquad (C.1)$$

$$\vec{M}_2 = (0, -\sin\theta_2, \cos\theta_2) \qquad (C.2)$$

From the dot product of these two vectors, equation C.3, and equation C.4, one of the unknown angles, ψ, can be obtained. ϕ_1 and ϕ_2 are the known transition moment angles described in Figure C.2. θ_1 and θ_2 are the angles that M_1 and M_2 respectively make with the plane normal as computed with equation 5.27.

$$\vec{M}_1 \cdot \vec{M}_2 = |\vec{M}_1| \; |\vec{M}_2| \cos \phi_2 \tag{C.3}$$

$$\sin \psi = \frac{\cos \phi_2 - \cos \theta_2 \cos \theta_1}{-\sin \theta_2 \sin \theta_1} \tag{C.4}$$

A linear combination of the two vectors that describe the chain axis is given by equations C.4 and C.5.

$$\vec{C} = \vec{M}_1 + a \vec{M}_2 \tag{C.4}$$

$$\vec{C} = (\sin \theta_1 \cos \psi, \sin \theta_1 \sin \psi - a \cdot \sin \theta_2, \cos \theta_1 + a \cdot \cos \theta_2) \tag{C.5}$$

One can now determine "a" using equations C.5, and C.7. θ_c can be subsequently measured using equation C.8.

$$\vec{M}_1 \cdot \vec{C} = |\vec{M}_1| \; |\vec{C}| \cos \phi_1 \tag{C.6}$$

$$\vec{M}_1 \cdot \vec{C} = |\vec{M}_1|^2 + a \cdot \vec{M}_1 \cdot \vec{M}_2 \tag{C.7}$$

$$\vec{C} \cdot \vec{Z} = |\vec{C}| \; |\vec{Z}| \cos \theta_c \tag{C.8}$$

There are two unique solutions for θ_c. The validity of either one can be checked with results from other techniques, such as electron diffraction.

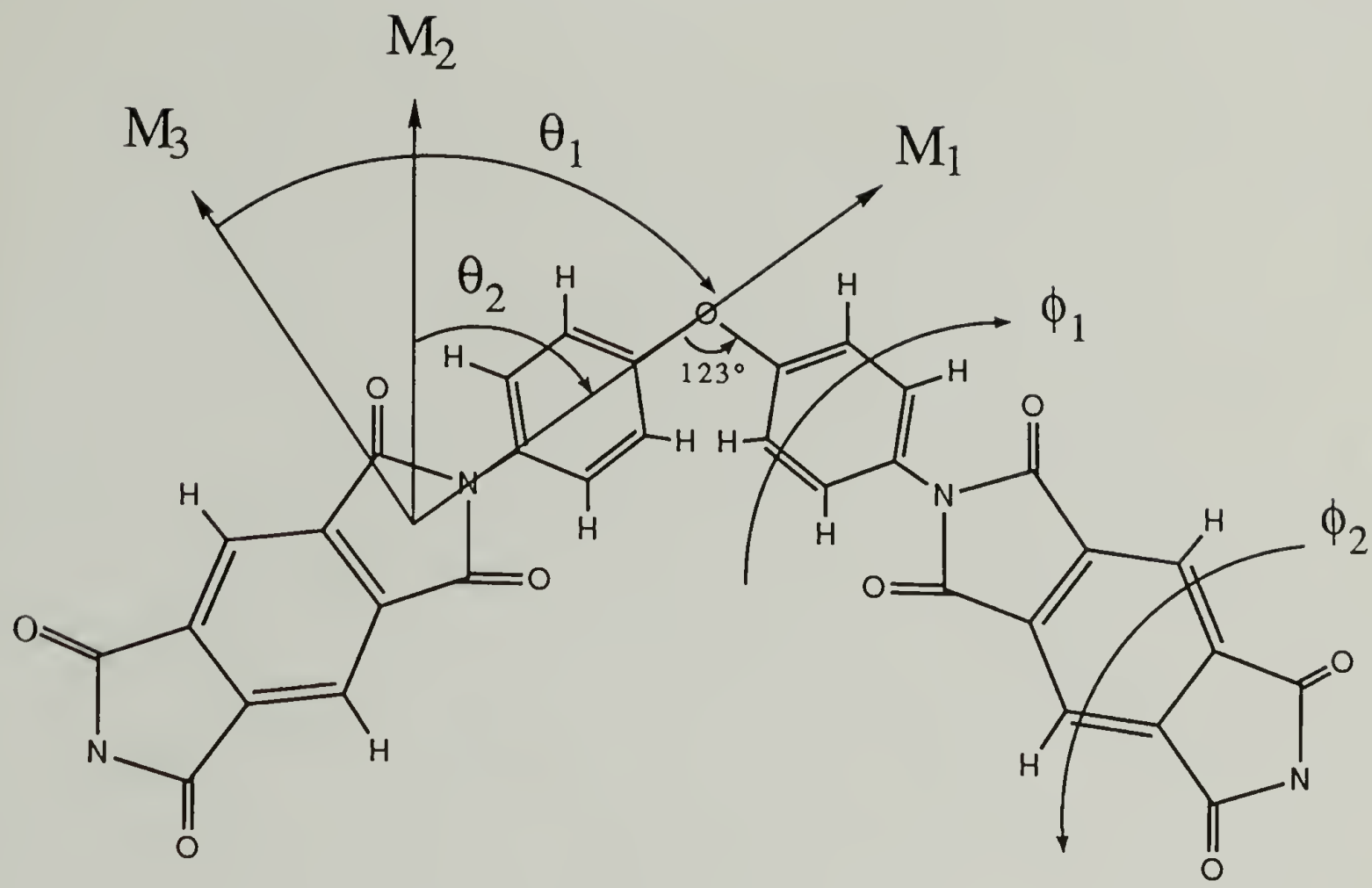

Figure C.1. Transition moment orientation and some geometrical parameters for a PMDA-ODA polyimide of an ideal conformation as it would be observed within a crystal.

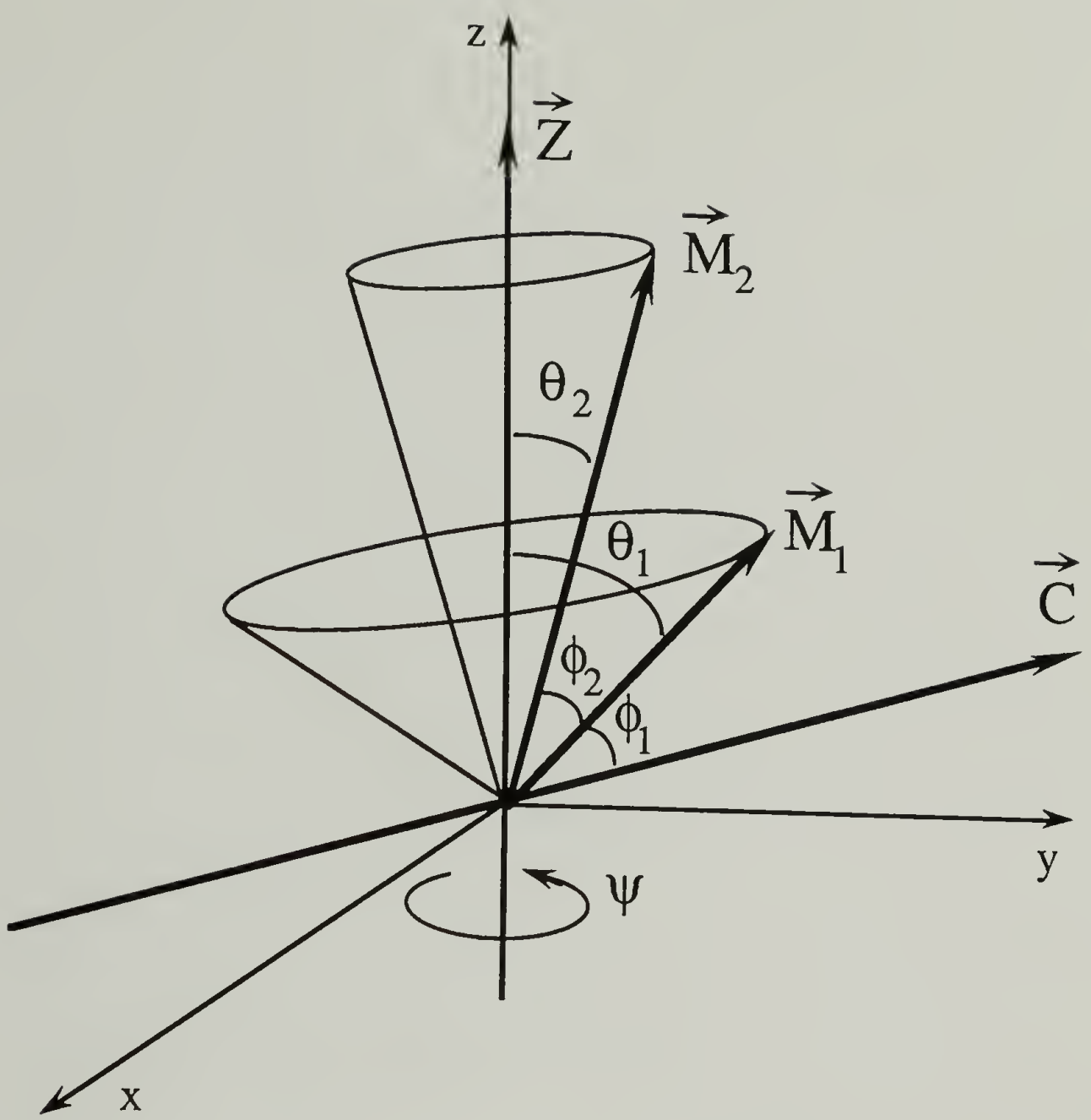

Figure C.2. Vectorial representation of the transition moments with respect to the plane normal and the chain axis direction.

BIBLIOGRAPHY

1. Aboelfotoh, M.O.;Feger, C.;Castellano, A.; Kaufman, R.; Molis, S. *Appl.Phys.Lett.* **1993**, *62*, 2286.

2. Agarwal, B.D.; Lifshitz, J.M.; Broutman, L.J. *Fibre Sci. Technol.* **1974**, *7*, 45.

3. Aleck, J.B. *J. of Appl.Mech.* **1949**, *16*, 118.

4. Allara, D.L.; Baca, A.; Pryde, C.A. *Macromol.* **1978**, *11*, 1215.

5. Allara, D.L.; Nuzzo, R.G. *Langmuir* **1985**, *1*, 50.

6. Allen, S.R.; Farris, R.J. *Mat. Res. Soc. Symp.* **1989**, 34.

7. Allen, S.R.; Farris, R.J. *Polym.* **1990**, *31*, 1467.

8. Anwer, A.; Lovell, R.; Windle, A.H. in *Computer Simulation of Polymers*; edited by R.J. Roe. Prentice Hall. Englewood Cliffs: N.J., 41, 1991.

9. Archer, R.R., *Growth Stresses and Strains in Trees*; Springer Series in Wood Science. Springer-Verlag: N.Y., 73 and 209, 1986.

10. Avery, W.B.; Herakovich, C.T. *J. of Appl. Mech.* **1986**, *53*, 751.

11. Barnett, D.M.; Townsend, P.H. *J. of Appl. Phys.* **1987**, *62*, 4438.

12. Bauer, C.L., PhD Dissertation. Dept. of Polym. Sci. and Eng. The University of Massachusetts at Amherst. Amherst, Mass., 109, 1988.

13. Bauer, C.L.; Farris, R.J. *J. of Coatings Technol.* **1988**, *60*, 51.

14. Bessonov, M.I.; Koton, M.M.; Kudryavtsev, V.V.; Laius, L.A., *Polyimides: Thermally Stable Polymers;* Consultants Bureau: New York., 177, 1987.

15. Bicerano, J. *Computational Modeling of Polymers*; Marcel Dekker, Co.: N.Y., 1992.

16. Biegen, J. F.; Smythe, R.A. *Proc. SPIE-Int. Soc. Opt. Eng.* **1988**, *897*, 207.

17. Blundell, D.J. *Polym.* **1992**, *33*, 3773.

18. Boehme, R.F.; Cargill III, G.S. into *Polyimides: Synthesis, Characterization and Applications*; Ed. K.L.Mittal. Plenum Press: N.Y., 1, 461, 1984.

19. Boese, D.; Lee, H.; Yoon, D.Y.; Swalen, J.D.; Rabolt, J.F. *J. of Polym. Sci., Part B: Polym. Phys.* **1992**, *30*, 1321.

20. Boogh, L.C.N.; Meier, R.J.; Kausch, H.H.; Kip, B.J. *J. Polym. Sci., Part B: Phys.* **1992**, *30*, 325.

21. Brenner, A.; Senderoff, S. *J. Res. Natl. Bur. Std.* **1949**, *42*, 105.

22. Buontempo, J.T.; Rice, S.A. *J. of Chem. Phys.* **1993**, *98*, 5825.

23. Burkert, U.; Allinger, N. L., *Molecular Mechanics; ACS Monographs*: Washington D.C., 74, 1982.

24. Burnett, D.S., *Finite Element Analysis: From Concepts to Applications*; Addisson-Wesley Publishing Co.:N.Y., 766, 1987.

25. Carrara, A.S.; McGarry, F.J. *J. Compos. Mater.* **1968**, *2*, 222.

26. Cha, C.Y.; Samuels, R.J. *Antec* **1993**, 2896.

27. Chen, S.T.; Wagner, H.H. *J. of Elect.Mat.* **1993**, *22*, 797.

28. Chow, T.S.; Liu, C.A.; Penwell, R.C. *J. of Polym. Sci.: Polym. Phys.* **1976**, *14*, 1311.

29. Choy, C.L.;Wong, S.P.;Young, K. *J. Polym. Sci.: Polym. Phys. Ed.* **1984**, *22*, 979.

30. Christensen, R.M. *Mechanics of Composite Materials*; Wiley: N.Y., 1979.

31. Coburn, J.C.; Pottiger, M.T., *Fourth Int. Tech. Conf. on Polyimides. Session VI. Applications,* 1991, 3.

32. Coburn, J.C.; Pottiger, M.T.; Noe, S.C.; Senturia, S.D., *Stress in Polyimide Coatings*, submitted to *J. Polym. Sci. B: Polym. Phys.*, 1994.

33. Coburn, J.C.; Pottiger, M.T., in *Advances in Polyimide Science and Technology*; Feger, C.; Kohjasteh, M.M.; Htoo, M.S., ed., Technomic Pub. Co. Inc.: Lancaster, 360, 1991.

34. Coburn, J. C.; Pottiger, M. T. *Antec* **1993**, 656.

35. Collier, J.R., *Polymer Orientation Induced by Solvent Removal. J. of MRL at the Pennsylvania State University*. University Park, PA. ,1981.

36. Colthup, N. B.; Daly, L. H.; Wiberley, S. E. *Introduction to Infrared and Raman Spectroscopy;* Third edition ed.; Academic Press: N.Y., 1990.

37. Conte, G.; D'Ilario, L.; and Pavel, N.V. *Journal of Polym. Sci. Polym. Phys. Ed.* **1976**, *14*, 1553.

38. Cox, H.L. *British J. of Appl. Phys.* **1952**, *3*, 72.

39. Dluhy, R.A. *J. Phys. Chem.* **1986**, *90*, 1373.

40. Donnel, L.H. *J. of Appl. Mech.; Brief Notes.* **1962**, 753.

41. Dupont, Data Manual for Kevlar® 49 Aramid", E.I. Dupont de Nemours Co., 1986.

42. Durelli, A.J.; Parks, V.J.; del Río, C.J. *Exp. Mech.* **1967**, *Nov.*, 481.

43. Elsner, G. *J. of Appl. Polym. Sci.* **1987**, *34*, 815.

44. Elsner, G.; Kempf, J.; Bartha, J.W.; Wagner, H.H. *Thin Solid Films* **1990**, *185*, 189.

45. Factor, B.J.; Russell, T.P.; Toney, M.F. *Phys. Rev. Lett.* **1991**, *66*, 1181.

46. Factor, B.J.; Russell, T.P.; Toney, M.F. *Macromol.*, **1993**, *26*, 2847.

47. Fan, C.F.; Hsu, S.L. *J. Pol. Sci., Part B: Polym. Phys.* **1989**, *27*, 337.

48. Fan, C.; Hsu, S.L., *Macromol.* **1989**, *22*, 1474.

49. Fan, F.C.; Hsu, S.L. *J. of Polym. Sci. Part B: Polym. Phys.* **1992**, *30*, 603.

50. Fan, F.C.; Hsu, S.L. *J. of Polym. Sci. Part B: Polym. Phys.* **1992**, *30*, 619.

51. Farris, R.J. Personnal Communication. Jan/1991.

52. Farris, R.J.; Madden, M.A. in *Advances in Polyimide Science and Technology;* ed. by Feger, C., Khojasteh, M.M., Htoo, M.S. Technomic Pub. Co. Inc. Lanc.Basel, 1993, 644.

53. Feger, C., Khojasteh, M.M., Htoo, M.S. *Advances in Polyimide Science and Technology;* Technomic Pub. Co. Inc.: Lanc.Basel, 1993.

54. Fina, L.J.; Tung, Y. *Appl. Spect.* **1991**, *45*, 986.

55. Fletcher, R.; Powell, M.J.D. *The Computer Journal* **1963**, *6*, 163.

56. Galiotis, C.; Young, R.J.; Yeung, P.H.J.; Batchelder, D.N. *J. Mat. Sci.* **1984**, *19*, 3640.

57. Gasteiger, J.; Marsili, M. *Tetrahedron* **1980**, *36*, 3219.

58. Gericke, A.; Michailov, A.V.; Hühnerfuss, H. *Vib. Spect.* **1993**, *4*, 335.

59. Goldfarb, J.L.; Farris, R.J. *J. of Adhesion* **1991**, *35*, 233.

60. Goldfarb, J.L.; Farris, R.J. *J. of Adhesion Sci. & Technol.* **1993**, *7*, 8.

61. Greenler, R.G., *J. of Chem. Phys.* **1966**, *44*, 310.

62. Gribov, L. A. *Intensity Theory for Infrared Spectra of Polyatomic Molecules*; Academy of Sciences of USSR Press: Moscow. 79, 1963.

63. Gross, T.S.; Watt, D.W.; Perault, J.A. *Exp. Mech.* **1992**, Dec., 316.

64. Hansen, W.N. *J. of the Opt. Soc. of Am.* **1968**, *58*, 380.

65. Hansen, W.N. *Advances in Electrochemistry and Electrochemical Engineering*; Ed. R.H. Muller; John Wiley & Sons: New York. Vol. 9, Ch 1, 1973.

66. Heavens, O.S. *Optical Properties of Thin Solid Films* ; Dover Publ.: New York, 1965.

67. Henein, G.E.; Wagner, W.R. *J. of Appl. Phys.* **1983**, *54*, 6395.

68. Herakovich, C.T. *J. of Strain Ana.* **1989**, *24*, 245.

69. Herminghaus, S.; Boese, D.; Yoon, D.Y.; Smith, B.A. *Appl. Phys. Lett.* **1991**, *59*, 1043.

70. Higuchi, S.; Tsuyama, H.; Tanaka, S.; Kamada, H. *Spectrochim. Acta* **1974**, *30A*, 463.

71. Hobson, R.J.; Windle, A.H. *Polym.* **1993**, *34*, 3582.

72. Holister, G.S.; Thomas, C. *Fibre Reinforced Materials*, Elsevier Pub. Co.: N.Y., 1966.

73. Hunter, C. A.; Sanders, J. K. M. *J. Am. Chem. Soc.* **1990**, *112*, 5525.

74. Hsueh, C.H.; Becher, P.F. *J. of Mat. Sci. Lett.*, **1991**, *10*, 1165.

75. Ishida, H.; Wellinghoff, S.T.; Baer, E.; Koenig, J.L. *Macromol.* **1980**, *13*, 826

76. Ishino, Y.; Ishida, H. *Appl. Spect.* **1992**, *46*, 504.

77. Ishino, Y.; Ishida, H. *Langmuir* **1988**, *4*, 1341.

78. Jahankhani, H.; Galiotis, C. *J. of Comp.Mat.* **1991**, *25*, 609.

79. Jennings, R., PhD Dissertation. Dept. of Polym. Sci. and Eng. The University of Massachusetts at Amherst., 53, 1993.

80. Jennings, B.; Farris, R.J. *J. of Polym. Sci.: Part B: Polym. Phys.* **1994**, *32*, 1457.

81. Johnson, C.; Xu, H.; Wunder, S.L.; Houlihan, F.M.; Chin, E. *J. of Polym. Sci., Part B: Polym. Phys.* **1992**, *30*, 1409.

82. Jungnickel, B.J. *Polym. Eng.and Sci.* **1987**, *27*, 1021.

83. Kazaryan, I.G.; Tsvankin, D. Y.; Ginzburg, B.M.; Tuichiev, S.; Korzahvin,L.N.; Frenkel, S. Y. *Polym. Sci. USSR* **1972**, *14*, 1344.

84. Kochi, M.; Yonezawa, T.; Yokota, R.; Mita, I., *Advances in Polyimide Science and Technology;* ed. by Feger, C., Khojasteh, M.M., and Htoo, M.S. Technomic Pub. Co. Inc.: Lanc.Basel, 1993, 375.

85. Knott, T. W.; Herakovich, C.T. *J. of Compos. Mater.* **1991**, *25*, 732.

86. Kragt, H.J.; Earl, D.J.; Norton, J.D.; White, H.S. *J. Electrochem. Soc.* **1989**, *136*, 1752.

87. Kurmar, S.S.; Fartash, A.; Grimsditch, M.; Schuller, I.K.; Kumar, R.S. *Macromol.* **1993**, *26*, 6184.

88. Laius, L.A. *Polym. Sci. USSR* **1974**, *16*, 2435.

89. Lebedev, G.A. *Polym. Sci. USSR* **1975**, *17*, 1338.

90. LeFévre, R. J.; Sundaram, A.; Sundaram, K. M. *Bull. Chem. Soc. Japan* **1962**, *35*, 690.

91. Lekhnitskii, S.G. *Theory of Elasticity of an Anisotropic Body*; MIR Publishers: Moscow, 70, 1981.

92. Lekhnitskii, S.G. *Theory of Elasticity of an Anisotropic Elastic Body*; Holden-Day, Inc.: San Francisco., 1963.

93. Leyrer, R.J.; Wegner, G.; Wettling, W. *Ber. Bunsenges. Phys. Chem.* **1978**, 82, 697.

94. Linde, H.G. *J. of Appl. Polym. Sci.* **1990**, *40*, 2049.

95. Lukasheva, N.V.; Milevskaya, I.S.; Baklagina, Y. G. *Polym. Sci. USSR* **1989**, *31*, 471.

96. Lukasheva, N.V.; Zubkov, V.A.; Milevskaya, I.S.; Baklagina, Y.G.; Strunnikov, A.Y. *Polym. Sci. USSR* **1987**, *29*, 1453.

97. Maden, M. A.; Farris, R.J., *4th Int. Tech. Conf. on Polyimides. Sess. IV: Mechanical Aspects*; Ellenville, N.Y., **1991**, 1.

98. Maden, M., PhD Dissertation. Dept. of Polym. Sci. and Eng. The University of Massachusetts at Amherst. Amherst, Mass., 1992.

99. Mark, R. *Exp. Mech.* **1977**, *April*, 121.

100. Matzat, Von E. *Acta Cryst.* **1972**, *B28*, 415.

101. Mayo, S. L.; Olafson, B.D.; Goddard III, W.A. *J.Phys.Chem.* **1990**, *94*, 8897.

102. McGarry, F.J.; Moalli, J.E. *Polym.* **1991**, *32*, 1811.

103. McIntyre, J. D.E.*Advances in Electrochemistry and Electrochemical Engineering*; Ed. R.H. Muller; John Wiley & Sons: New York. Vol. 9, Ch 2, 1973.

104. Molis, S.E.; Saraf, R.; Hodgson, R.T.*Antec* **1991**, 1700.

105. Moonen, J.A.H.M.; Roovers, W.A.C.; Meier, R.J. Kip, B.J. *J. Polym. Sci., Part B: Phys.* **1992**, *30*, 361.

106. Nairn, J. A. *A Variational Mechanics Analysis of the Stresses Around Breaks in Embedded Fibers*. Submitted *Mech. of Mater.*

107. Nakagawa, K. *J. of Appl. Polym. Sci.* **1990**, *41*, 2049.

108. Nakamura, T. *J. of Appl. Mech.* **1991**, *58*, 939.

109. Netravali, A.N.; Sachse, W. *Polym. Comp.* **1991**,*12*, 370.

110. Noe, S.C., PhD Dissertation. Dept. of Mat. Sci. Eng. Massachusetts Institute of Technology. Cambridge, Mass., 1992.

111. Noyan, I.C.; and Cohen, J.B. *Residual Stress: Measurement by Diffraction and Interpretation;*. Springer-Verlag: N.Y., 218, 1987.

112. Ojeda, J. R.; Martin, D. C. *Macromol.* **1993**, *26*, 6557.

113. Okuyama, K.; Sakaitani, H.; Arikawa, H. *Macromol.* **1992**, *25*, 7261.

114. Olsen, G.H.; Ettenberg, M. *J. of Appl. Phys.* **1977**, *48*, 2543.

115. O'Mahoney, C. A.; Williams, D. J.; Colquhoun, H. M.; Mayo, R.; Young, S. M.; Askari, A.; Kendrick, J.; Robson, E. *Macromol.* **1991**, *24*, 6527.

116. Outwater, J.O., *Mod. Plast.* **1956**, *March*, 1956.

117. Pacansky, J.; England, C.; Waltman, R.J. *J. Polym. Sci. Part B:Phys.* **1987**, *25*, 901.

118. Parikh, A.N.; Allara, D.L. *J. Chem. Phys.* **1992**, *96*, 927.

119. Perez, M. A.; Ren, Y.; Farris, R. J.; Hsu, S. L. *Submitted for publication.* **1994**.

120. Perez, M.A.; Hsu, S.L.; Farris, R.J. *Polymer Prepr., Am. Chem. Soc.* **1993**, *69*, 22.

121. Perry, D.M.; Moran, P.J.; Robinson, G.M. *J. of the Inst. of Elect. and Rad. Eng.* **1985**, *4*, 145.

122. Petersen, C.S. *Acta Chem Scand.* **1969**, *23*, 2389.

123. Pionke, C.D.; Wempner, G. *J. of Appl. Mech.* **1991**, *58*, 1015.

124. Plepys, A.R.; Farris, R.J. *Polym.* **1990**, *31*, 1932.

125. *Polygraf*™, Reference Manual, 1993.

126. Poon, T. W.; Saraf, R. F.; Silverman, B. D. *Macromol.* **1993**, *26*, 3369.

127. Pottiger, M.T.; Coburn, J.C. *Antec* **1993**, 1925.

128. Prest, Jr., W.M.; Luca, D.J. *J. Appl. Phys.* **1979**, *50*, 6067.

129. Prest, Jr, W.M.; Luca, D.J. *J. of Appl. Phys.* **1980**, *51*, 5170.

130. Rao, V.; Drzal, L.T. *Polym.Comp.* **1991**, *12*, 48.

131. Ree, M.; Nunes, T.L.; Czornyj, G.; Volksen, W. *Polymer* **1992**, *33*, 1228.

132. Robinson, I.M.; Galiotis, C.;Batchelder, D.N.; Young, R.J. *J. of Mat. Sci.* **1991**, *26*, 2293.

133. Robinson, I.M.; Young, R.J.; Galiotis, C.; Batchelder, D.N. *J. of Mat. Sci.* **1987**, *22*, 3642.

134. Roe, R.J. *Computer Simulation of Polymers*; Prentice Hall. Englewood Cliffs: N.J., 1991.

135. Rosen, B.W. *Mechanics of Composite Strengthening in Fiber Composite Materials*, ASM Pub., 1964.

136. Russell, T. P.; Brown, H.R. *J. of Polym. Sci. Phys., Part B: Phys.* **1987**, *25*, 1129.

137. Russell, T.P.; Gugger, H.; Swalen, J.D. *J. of Polym. Sci.: Polym. Phys. Ed.* **1983**, *21*, 1745.

138. Rutledge, G.C.; Suter, G.C. *Polymer* **1991**, *32* , 2179.

139. Sakurada, I.; Kaji, K. *J. Polym. Sci.: Part C* **1970**, *31*,57.

140. Saraf, R.F.; Tong, H.; Poon, T.W.;Silverman, B.D.; Ho, P.S.; Rossi, A.R. *J. of Appl. Polym. Sci.* **1992**, *46*, 1329.

141. Schmid, E.D.; Brosa, B. *The J. of Chem. Phys.* **1972**, *56*, 6267.

142. Silverman, B. D. *Macromol.* **1989**, *22*, 3768.

143. Snyder, R.W.; Thomson, B.; Bartges, B.; Czerniawski, D.; Painter, P.C. *Macromol.* **1989**, *22*, 4166.

144. Sroog, C.E. *Macromol. Rev.* **1976**, *11*, 161.

145. Stewart, W.C.; Leu, J.; Jensen, K.F. *Mat. Res. Soc. Symp. Proc.* **1989**, *153*, 285.

146. Stoney, G.G. *Proc. Roy. Soc. Lond.* **1909**, *A82*, 172.

147. Streitwieser, Jr.; Heathcock, C.H. *Introduction to Organic Chemistry*; Macmillan Publishing Co, Inc.: N.Y.,1073, 1976.

148. Strunnikov, A. Yu.; Mikhailova, N.V.; Sidorovich, A.V. *Polym. Sci. USSR* **1990**, *32*, 1.

149. Suhir, E., *Mat. Sci. Res.Soc. Symp.Proc.*, Elect. Pack. Mat. Sci. II, Jackson, K.A.; Pohanka, R.C.; Uhlman, D.R.; Ulrich, D.R., ed.,**1986**, *72*, 133.

150. Takahashi, N.; Yoon, D.Y.; Parrish, W. *Macromol.* **1984**, *17*, 2583.

151. Tiller, A.R. *Macromol.* **1992**, *25*, 4605.

152. Timoshenko, S. *J. Opt. Soc.Am.* **1925**, *11*, 23.

153. Timoshenko, S.; Goodier, J.N., *Theory of Elasticity*; McGraw-Hill Book Co.: New York., 343, 1951.

154. Tissington, B.; Pollard, G.; Ward, I. M. *J. of Mat. Sci.* **1991**, *26*, 82.

155. Tong, K., PhD Dissertation. Dept. of Polym. Sci. and Eng. The University of Massachusetts at Amherst. Amherst, Mass., 1993.

156. Treloar, L.R.G. *Polym.* **1960**, *1*, 95.

157. Treloar, L.R.G. *Polym.* **1960**, *1*, 279.

158. Van Eijk, M.C.P.; Leblans, P.J.R.; Meier, R.J.; Kip, B.J. *J. Mat. Sci. Lett.* **1990**, *9*, 1263

159. Varsanyi, G. *Vibrational Spectra of Benzene Derivatives*; Academic Press: New York, 1974.

160. Venkatesh, G.M.; Shen, D.Y.; S.L.Hsu *J. of Polym. Sci.: Polym. Phys. Ed.* **1981**, *19*, 1475.

161. Vilms, J.; Kerps, D. *J. of Appl. Phys.* **1982**, *53*, 1536.

162. Walls, D.J. *Antec* **1993**, 1919.

163. Wellinghoff, S.T.; Ishida, H.; Koenig, J.L.; Baer, E. *Macromol.* **1980**, *13*, 834.

164. White, H.S.; Earl, D.J.; Norton, J.D.; Kragt, H.J. *Anal. Chem.* **1990**, *62*, 1130.

165. Whitney, J.M.; Drzal, L.T.; *Axisymmetric Stress Distribution Around an Isolated Fiber Fragment. Toughened Composites, ASTM STP 937*, Norman J. Johnston, Ed., Am. Soc. for Test. and Mat., Philadelphia, 179, 1987.

166. Yang, X.; Hsu, S.L. *Macromol.* **1991**, *24*, 6680.

167. Yen, Y.; Wong, J.S. *J. of Phys. Chem.* **1989**, *93*, 7208.

168. Young, R.J.; Day, R.J.; Zakikhani, M. *Mat. Res. Soc. Sym. Proc.* **1989**, *34*, 351.

169. Young, J.T.; Tsai, W.H.; Boerio, F.J. *Macromol.* **1992**, *25*, 887.

170. Young, J.T.; Boerio, F.J. *J. of Surf.and Interf. Anal.* **1993**, *20*, 341.

171. Zygo Corporation; Reference manual for the Maxim-3D 5800 High Resolution Phase Measuring Laser Interferometric Microscope. Middlefield, Connecticut. 1993.